

Characterization of natural fractures of the Upper Devonian Duvernay Formation in the Kaybob
Area, Alberta

by

Guido Agustin Garcia Rodriguez

A thesis submitted in partial fulfillment of the requirements for the degree of

Master of Science

Department of Earth and Atmospheric Sciences

University of Alberta

© Guido Agustin Garcia Rodriguez, 2023

Abstract

The organic-rich mudstones of the Upper Devonian Duvernay Formation constitute an unconventional reservoir in the Western Canada Sedimentary Basin, developed for over a decade using hydraulic fracturing technology. Integrating natural fracture characterization with lithofacies analysis, mechanical properties examination, and regional structural study can define the mechanical stratigraphy of mudrocks, reconstruct stress fields, and elucidate basin-scale fluid flow during fracturing. Determining the geometry, orientation, and fracture intensity of natural fractures is crucial for fracture modeling, horizontal well placement, and optimizing hydraulic fracturing and production operations.

This study focuses on characterizing natural fractures in the Duvernay Formation in the Kaybob area. It seeks to determine fracture intensity, controlling factors of fracture propagation, and the relative timing of fracturing in the Upper Devonian organic-rich mudrocks beneath the Alberta Basin. Objectives include analyzing lithofacies, mechanical properties, type, geometry (height, length, aperture), orientation, intensity/spacing of natural fractures, and fracture structural settings. Results on fracture morphology and distribution in the Duvernay Formation are compared to descriptions and structural analyses of fractures in the Upper Devonian Perdrix Formation in the Front Ranges and Foothills of the Nordegg area, serving as an outcrop analog of the Duvernay Formation. The aim is to correlate phases and timing of fracturing in these areas.

The research is based on the description and analysis of approximately 418 meters of core, core tests, and well logs in seven vertical wells, as well as around 4.4 kilometers of Formation Micro-Imager (FMI) logs in four horizontal wells in the Kaybob area. 3D structural

modeling (90 km x 90 km) and facies modeling (2 km x 2 km to 10 km x 12 km) were conducted to interpret the lateral distribution of lithofacies and fractures in the Duvernay, Majeau Lake, and Leduc Formations.

Seven lithofacies are identified in the Duvernay Formation core, with three constituting nearly 95% of the total thickness. Facies F2 exhibits ductile behavior with low calcite content, high illite, and total organic carbon (TOC), and low elastic and strength parameters (UCS, YM, TSTR). Facies F3 displays moderate stiffness and strength with intermediate calcite, illite, TOC, and elastic and strength parameters. Facies F5 shows stiff behavior with high calcite content, low illite, TOC, and high elastic and strength parameters. The lower fracture intensity in facies F2 and F5 can be related to more ductile mechanical properties of facies F2, which are not favorable for fracture propagation, and higher thickness of beds in facies F5.

Analysis of drilling-induced fractures and breakouts in FMI logs helped determine the orientation of the present-day maximum horizontal stress (SH_{max}) as $N53^{\circ} \pm 2^{\circ}$, with $SH_{max} > S_v$. Tensile calcite-filled vertical fractures (#2003) in the Duvernay Formation form three main sets oriented parallel, orthogonal, and at approximately 20° to SH_{max} . Open and subhorizontal fractures and polished slip faces are subordinate. Fracture intensity in mudrocks varies from approximately 1 to 1.6 fract/m in vertical wells and from around 3 to 4.5 fract/m and m^2/m^3 in horizontal wells. The highest fracture intensity occurs in thinly bedded organic- and carbonate-rich mudrocks of facies F3 compared to more ductile organic-rich biosiliceous mudrocks of facies F2 and stronger and stiffer carbonate-rich nodular mudrocks of facies F5.

Hydrocarbon generation and fluid expansion are significant mechanisms for fracture development in shales. In the study area, thermal maturity organic-rich mudrocks, fluid pressure, and burial depth of the Duvernay Formation increase from the northeast to the southwest. Estimated fracture intensity from vertical wells similarly increases from the northeast to the southwest. Proposed phases of fracturing in the Duvernay Formation during burial and uplift are based on fracture characterization and regional data on fracturing in Upper Devonian carbonate rocks of the West Shale Basin.

Fracture intensity in organic-rich mudrocks of the Perdrix Formation is higher than in the mudrocks of the Duvernay due to increased deformation in the Front Ranges. Two deformation phases are identified, involving subhorizontal calcite-filled tensile fractures and bedding-orthogonal tensile and transtensional fractures during the Laramide orogeny, and NNW-SSE open subvertical fractures likely during Eocene extension.

The detailed investigation of natural fractures in the Duvernay and Perdrix Formations in core, image logs, and outcrops provides geoscientists and engineers with crucial information for fracture modeling. This information can enhance exploration, drilling, and production practices of the source rock reservoir in the Western Canada Sedimentary Basin.

Preface

My thesis comprises six chapters. The first chapter serves as the introduction, aimed at explaining the research goal. The second chapter contains the geologic background, discussion on the tectonic structure and evolution of the Alberta Basin, the stratigraphy and facies distribution of Upper Devonian deposits in the West Shale Basin, the mechanical properties of the rocks, and published data on natural fractures in the Duvernay Formation and its outcrop analog, the Perdrix Formation.

The third chapter presents the methods employed and the available dataset, which includes Formation Micro-Imager (FMI) logs from four horizontal wells, core data from seven vertical wells obtained from the Alberta Energy Regulator (AER) website (<https://www.aer.ca/>), well logs obtained from the geoSCOUT database, structural surfaces obtained from the 3D Provincial Geological Framework Model of Alberta, version 2, compiled by the Alberta Geological Survey in 2019, available at the website: <https://ags.aer.ca/publication/3d-pgf-model-v2>, and outcrop data from the Perdrix Formation collected during a field trip.

The fourth chapter presents the results, encompassing lithofacies descriptions of the Duvernay Formation, 3D facies modeling in different areas within Kaybob, the mechanical and petrophysical properties of the main lithofacies, as well as an analysis of fractures in vertical and horizontal wells, and fractures in the Perdrix Formation.

Lastly, the fifth and sixth chapters are dedicated to the discussion and conclusions.

Acknowledgements

I would like to express my sincere gratitude to the following individuals and organizations for their invaluable support and contributions to this research:

Dr. Elena Konstantinovskaya, my dedicated supervisor, for generously sharing her extensive knowledge, providing constructive feedback, and offering invaluable guidance in the fields of geomechanics and structural geology. Her mentorship has been instrumental in the successful completion of this study.

The exam committee, Professor Nicholas Harris and Stephen Johnston, for kindly accepting evaluating my thesis and providing very helpful suggestions and comments that helped to improve the initial manuscript.

Professor Nicholas Harris for supervision of this research study on facies description and analysis, and Daniel Shaw for sharing the data on sequence stratigraphy analysis of the Duvernay Formation.

Pat Fothergill, whose expertise in interpreting fractures from image logs and insightful feedback on my presentations significantly enhanced the clarity and precision of this study.

Byron Veilleux and Murray Gilhooly, for their expert consulting on core logging, facies description, and structural interpretation of core samples.

Charles Berg and Mark Cooper, for their advice and consulting about fractures.

Tian Dong, for providing hardness measurements from well 100/02-22-063-20W5/00.

An anonymous energy company, for sharing and permission displaying image log data.

Schlumberger, for providing an academic license of Petrel to the University of Alberta.

geoLOGIC systems ltd., for their contribution of data and software used in this study.

NSERC, for their financial support through grants RGPIN 2019 04397 and DGEGR 2019 00186. This funding has been crucial in enabling the progress of this research project.

CRC and AER teams for support when studying and sampling core, for providing well reports used in this study.

Finally, I extend my heartfelt appreciation to my loving family and friends in Argentina, as well as my new family in Canada, for their unwavering support and encouragement throughout this challenging journey. Your belief in me has been a constant source of inspiration.

Thank you to all these individuals and organizations for their significant contributions to the successful completion of this research.

Table of Contents

Abstract.....	ii
Preface.....	v
Acknowledgments.....	vi
Chapter 1: INTRODUCTION.....	1
Chapter 2: GEOLOGIC BACKGROUND.....	4
2.1. Stratigraphy and facies distribution of Upper Devonian deposits in the West Shale Basin...5	
2.2. Paleogeography of the Duvernay Formation	12
2.3. The tectonic structure of the Alberta Basin	15
2.4. Tectonic evolution of the Alberta Basin	19
2.5. Geochemistry, thermal maturity and burial history of the Duvernay Formation.....	24
2.6. Mechanical properties of Duvernay shales	29
2.7. Present-day stress field in the Alberta Basin	31
2.8. Natural fractures: classifications, kinematic types and formation settings in shales	36
2.9. Natural fractures in the Duvernay Formation.....	40
2.10. Upper Devonian Perdrix Formation.....	42
Chapter 3: DATA AND METHODS.....	46
3.1. Data sources.....	46
3.1.1 Database.....	47
3.2. Methods and Workflow.....	52
3.2.1. Core and microscopic description of lithofacies and fractures of the Duvernay Formation.....	52
3.2.2. FMI interpretation of bedding and fractures of the Duvernay Formation.....	56
3.2.3. Petrophysical and geomechanical parameters of the Duvernay Formation	60
3.2.4. 3D models of the Duvernay Formation in selected areas, Kaybob area	65
3.2.5. Field structural methods	67

Chapter 4: RESULTS.....	70
4.1. Lithofacies of the Duvernay Formation	70
4.1.1. F1 Relatively coarse-grained carbonate-rich organic-poor silty mudstones	70
4.1.2. F2 Planar-laminated clay-bearing organic-rich biosiliceous mudstones	71
4.1.3. F3 Planar-laminated clay-bearing organic-rich mudstones, locally with thinly layered light-grey carbonate-rich silty interbeds.....	71
4.1.4. F4 Fossiliferous bioturbated wackestones.....	71
4.1.5. F5 Carbonate-rich nodular mudstones.....	72
4.1.6. F6 Clay-rich fissile mudstones.....	72
4.1.7. F7 Discontinuous pyrite-rich lens-shaped aggregates and laminae.....	72
4.2. 3D structural and facies models of the Duvernay Formation in the Kaybob Area	79
4.2.1. 3D Structural model of the Duvernay Formation	79
4.2.2. The 3D facies models of the Duvernay Formation	85
4.3. Petrophysical properties of main lithofacies of the Duvernay Formation	96
4.4. Mechanical properties of main lithofacies of the Duvernay Formation	103
4.5. Fractures in the Duvernay Formation in core of vertical wells	108
4.5.1. Natural fractures (NFs)	109
4.5.2. Drilling-Induced fractures (DIFs).....	118
4.5.3. Fracture intensity (P10).....	120
4.6. Fractures in horizontal wells interpreted from FMI logs	124
4.6.1. Orientation of natural fractures	125
4.6.1.1. Well A N144°E	126
4.6.1.2. Well B N03°E.....	128
4.6.1.3. Well C N01°E.....	129
4.6.1.4. Well D N343°E	130
4.6.1.5. Orientation of resistive and conductive natural fractures.....	132
4.6.1.6. Summary of orientation of natural fractures.....	134
4.6.2. Fracture distribution and intensity P10, P32.....	135
4.6.2.1. Well A N144°E	135
4.6.2.2. Well B N03°E	141

4.6.2.3. Well C N01°E	145
4.6.2.4. Well D N343°E	151
4.6.3. Drilling-induced fractures and borehole breakouts orientation.....	153
4.7. Composition, structural elements and fractures in the Perdrix Formation	155
Chapter 5: DISCUSSION.....	174
5.1. Relationship between lithofacies, mechanical properties and rock composition	174
5.2. Controlling factors for fracture development	177
5.3. Relationship between fracture intensity, thermal maturity, fluid pressure, and burial depth of the Duvernay Formation in the Kaybob area of the West Shale Basin	180
5.4. Orientation of natural fractures in the Duvernay Formation and present-day horizontal stresses.....	183
5.5. Natural fractures in the Duvernay and Perdrix Formations and phases of deformation.....	186
5.6. Fracture intensity and spacing of extensional fractures in the Duvernay Formation and its analogs.....	187
5.7. Suggested future work.....	189
Chapter 6: CONCLUSIONS.....	190
References.....	192
Appendix A: Additional petrophysical logs	220
Appendix B: Elastic and strength parameters for additional wells	225

List of Tables

Table 2.1. Code, names and UWI shown in Fig. 2.7 after Shaw, (2020); Shaw and Harris, (2022).....	15
Table 3.1. Summary of well and core data used in this study. 1-7, vertical wells with core of the Duvernay Formation; A-D, horizontal wells; C1-C5, vertical wells between wells C and 5. TVT, True vertical thickness. Well logs: GR, gamma ray; DTC and DTS, compressional and shear wave sonic; RHOB, bulk density; PEF, photoelectric factor; CALI, caliper; and ROP, rate of penetration. Core data include core description, thin sections and hardness measurements obtained in this study. See Table 3.2 for petrophysical and geomechanical testing reports used in this study and available at AER website	49
Table 3.2. List of core testing reports used on this study with available analyses. Data can be requested at the AER website. Analysis description abbreviations: GM: Geomechanics; YM: Young’s Modulus; PR: Poisson’s ratio; GRI: Shale gas analysis; DB: Bulk density; GAD: Grain density; K: Permeability; POR: Porosity measurements; RE: Rock Evaluation; TOC: Total Organic Carbon; XDR: X-ray diffraction; RM: Rock mechanics; TCT: Triaxial compressive test; ACV: Acoustic velocity; DEP: Dynamic elastic properties; GS: Gas saturation; SO: Oil saturation; SW: Water saturation; EP: Effective porosity; PET: Petrology; TRA: Tight rock analysis; TP: Total porosity; UC: Unconfined compression; TSP: Thin sections petrographics; ELAN: Elemental analysis.....	51
Table 3.3. Parameters of the 3D models build up around the horizontal wells in the Duvernay Formation, Kaybob area. See Fig. 3.2 for the location of the models.....	66
Table 3.4. List of samples collected for studying fractures in the Perdrix shale.....	68
Table 4.1. Summary characteristics of the lithofacies of the Duvernay Formation based on core description in seven vertical wells 1-7 (Table 3.1, Fig. 4.6).....	73
Table 4.2. Summary of petrophysical properties of mudrocks of the Duvernay Formation based on data of core petrophysical testing (AER reports) in six vertical wells 1, 3-7 (Fig. 4.6, Table 3.1) and average values estimated for lithofacies F2, F3 and F5 based on core data in all six wells (Table 4.1). The shown values correspond to average values \pm standard deviation. No petrophysical core data is available for well 2 (Table 3.1).....	97
Table 4.3. Summary of ranges of values of selected well logs and estimated profiles of mechanical properties in lithofacies F1-F7 of mudrocks of the Duvernay Formation analyzed in seven vertical wells 1-7 (Table 3.1, Fig. 4.6). Well logs: GR, gamma ray; RHOB, bulk density; DTSH and DTCO, shear and compressional slowness, respectively. Estimated profiles: YMs and YMd, static and dynamic Young’s Moduli, respectively; UCS, unconfined compressive strength. See Table 4.1 for facies description.....	104
Table 4.4. Core-based Tensile Strength, Facies, and Wells used on Fig. 4.29.....	108
Table 4.5. Fracture intensity P10 values (fract/m) in core of the Duvernay Formation per well after application of the Terzaghi’s correction. See Table 3.1 and Fig. 4.6 for the wells’ name and location.....	121
Table 4.6. Fracture intensity P10 (fract/m) estimated in core of the Duvernay Formation per facies after normalization by facies thickness and application of the Terzaghi’s correction. See Table 4.1 for facies composition.....	123

Table 4.7. Orientation (strike azimuth and dip angle) of bedding, Borehole Breakouts (BO), Drilling-induced fractures (DIFs) and sets of natural fractures (Set 1 to 3) for each horizontal well. Number of fractures per set and per well are shown.....128

Table 4.8. Strike of resistive and conductive fractures per set in four horizontal wells.....134

Table 4.9. Mean fracture intensity P10 and P32 estimated in each horizontal well in total and for intervals with different values of GR log. See Table 4.1 and text for the facies definition.....137

Table 4.10. Mean P10 values for each set of fractures per horizontal well.....139

Table 5.1. Comparison of fracture intensity P10 (fract/m) and P32 (m^2/m^3) estimated from core and image logs in mudrocks of the Duvernay and Perdrix Formations and their analogs in the United States. See text for the source reference papers.....189

List of Figures

Fig. 2.1. Simplified geology and main tectonic features of the Alberta Basin and tectonic domains of the basement, after Pana et al., (2021). The location of the Western Canada Sedimentary Basin is shown in the inset map, after Waldron et al., (2016). Black polygon indicates the location of the Kaybob area; black line A-A' delineates the location of the cross-section of Figure 2.8; black lines 12 and 13 correspond to the location of 2D seismic lines of Fig. 2.9.A.....	4
Fig. 2.2. Stratigraphic chart of Upper Devonian sedimentary succession in central Alberta, Western Canada Sedimentary Basin (Switzer et al., 1994; Alberta Geological Survey, 2019: https://ags.aer.ca/publications/Table_of_Formations_2019.html). The sequence stratigraphy boundaries and depositional sequences (DS1-DS3) are shown after Knapp et al. (2019); Shaw and Harris (2022).....	6
Fig. 2.3. Schematic depositional model of the Woodbend Group in the Central Alberta, after Fothergill et al. (2014), Switzer et al. (1994), and Dunn et al. (2012)	8
Fig. 2.4. Map of lithofacies of Upper Devonian Duvernay Formation and contours of reefs of the Woodbend Group, after Switzer et al. (1994; 2008). Faults of the deformation front of the Canadian Rocky Mountains are shown after Hamilton et al. (1999). The shapefiles were downloaded from the AGS website http://www.ags.gov.ab.ca/publications/ . The location of the study area in the Kaybob area is shown by red polygon. The black star shows the location of the well from Fig. 2.5. The inset map shows the location of the map in the Western Canada Sedimentary Basin. Coordinate system UTM NAD83 zone 11 N.....	9
Fig. 2.5. Log plot for well MURPHY SAXON 1-28-61-23 displaying tracks from the left to the right: subdivisions of the Duvernay Formation, measured depth (m, KB), spectral gamma, gamma, and deep resistivity logs, interpretation of lithofacies, measured TOC and sequence stratigraphic interpretation, after Shaw (2020). The location of the well is shown in Fig. 2.4.....	10
Fig. 2.6. Late Devonian paleogeography, approximately 375 m. a. after Blakey (2013). In red, the area of study is highlighted. AB: Alberta; SK: Saskatchewan; MB: Manitoba	12
Fig. 2.7. Depositional model proposed for the Duvernay Formation in the Kaybob Area, focusing on two stages: A) the construction of the Grosmont Platform, and B) the subsequent flooding of the Grosmont Platform, after (Shaw, 2020; Shaw and Harris, 2022). See name and UWI of wells in Table 2.1. The red circle shows the location of well 4 that is studied in this thesis.....	15
Fig. 2.8. The WSW-ENE regional structural cross-section across the Canadian Rocky Mountains Fold and Thrust Belt, Foothills and the Alberta Basin, modified after Reiter and Heidbach (2014) and Hamilton et al. (1999), Map No: 236.....	18
Fig. 2.9. Examples of the subsurface high-angle normal faults in the Alberta Basin. A) Normal faults mapped in the Peace River Arch area displace Precambrian basement and Paleozoic sedimentary cover, after (Hope et al., 1999). The red star shows the interval with the Duvernay Formation. Precamb: Precambrian; Woodbd: Woodbend; Wab: Wabamun. B) Schematic illustration of fold and fracture zones developed in the sedimentary cover above a steep normal fault in basement, based on physical modeling experiment, after (Withjack et al., 1990).....	19

Fig. 2.10. Paleogeographic reconstruction for the Late Devonian (380 Ma), after Scotese (2016). Screenshot from the animation taken from https://www.youtube.com/watch?v=g_iEWvtKcuQ	20
Fig. 2.11. Paleogeographic reconstruction for the Early Cretaceous (100 Ma), after Scotese (2016). Screenshot from the animation taken from https://www.youtube.com/watch?v=g_iEWvtKcuQ	21
Fig. 2.12. Paleogeographic map for the Cadomin-Getting strata in the Alberta Basin, after (Smith, 1994). The chain of erosional highlands (Keg River, Red Earth, Wainwright, Pembina) may correspond to the location of forebulge extended NW-SE in the foreland basin and associated with lithosphere flexure and tectonic loading of the proto-Rockies (Pana, 2021).....	22
Fig. 2.13. Conceptual model of the formation of the foreland basin by isostatic flexure of the continental lithosphere in response on the emplacement of the orogenic belt, after Price (1994). Df, Di, final and initial depth of basement.....	23
Fig. 2.14. A) Top of the Duvernay Formation after (Lyster et al., 2017). B) Mean simulated TOC (wt%) in the Duvernay Formation, after (Lyster et al., 2017). The red polygon outlines the area of study.	25
Fig. 2.15. Map of thermal maturity zones of the Duvernay Formation of peak oil (Tmax of ~435 °C), peak wet gas (Tmax of ~450 °C), and peak dry gas (Tmax of ~460 °C) maturity, after (Yeates et al., 2022). Filled circles shows the Nuclear Magnetic Resonance and Tmax measurements (see legend). WGMH, Willisden-Green maturity high.....	26
Fig. 2.16. Burial history for the Eastern Foothills (EF), Peace River Arch (PRA), West Shale Basin (WSB), East Shale Basin (ESB) and Rimbey Meadowbrook Trend (RMT), after Stacey et al. (2020). Burial curves are shown for the Swan Hills Formation in the WSB (Duggan et al., 2001) and ESB (Laflamme, 1990), Leduc Formation in the Rimbey Meadowbrook Trend (Amthor et al., 1993), Wabamun Group in the WSB (Green and Mountjoy, 2005) and in the PRA (Mountjoy and Halim-Dihardja, 1991), and the Exshaw Formation in the Eastern Foothills (Price, 1994). Two main episodes of subsidence are associated with the Antler phase of deformation in the latest Devonian – Mississippian and Laramide Orogeny in the Late Cretaceous to Paleocene.....	28
Fig. 2.17. Mean simulated pressure gradient (kPa/m) in the Duvernay Formation, after (Lyster et al., 2017). The red polygon shows the study area	29
Fig. 2.18. Anderson (1951) fault classification system, after (Wikel, 2011; Tyiasning and Cooke, 2016).....	32
Fig. 2.19. Map of state of stress in the Western Canada Sedimentary Basin, Alberta, after (Lundstern and Zoback, 2020). The black lines indicate the orientations of maximum horizontal stress (SHmax), while the background with different colors represents the relative stress magnitudes parameter $A \square$. Location of the Kaybob area is highlighted by the red circle.....	33
Fig. 2.20. A) Orientation of maximum horizontal stress (SHmax) in the Western Canada Sedimentary Basin, Alberta, after (Reiter et al., 2014). The location of study area is highlighted by the red circle. B) Location of induced earthquakes triggered by hydraulic fracturing in the Duvernay Formation shown by red circles, after (Schultz et al., 2020). The focal mechanisms of the most significant four events are displayed from left to right: the event of 12 January 2016 with a magnitude of 4.1 Mw, the event of 23 January 2015 with a magnitude of 3.6 Mw, the	

event of 13 June 2015 with a magnitude of 3.9 Mw, and the event of 4 March 2019 with a magnitude of 3.7 Mw. The earthquake mechanisms correspond to dextral strike slip or oblique normal displacement along the near N-S high-angle faults. See references in the text.....35

Fig. 2.21. Schematic model showing N-S strike-slip fault system involving a master vertical fault in the basement that evolves upwards into a series of transtensional faults forming a negative flower structure in overlying Paleozoic sedimentary units, Fox Creek area, after Wang et al. (2017).....36

Fig. 2.22. Mohr circle illustration showing different failure modes in a normal faulting stress regime, after Ferrill et al. (2017). σ_1 = maximum principal effective stress, σ_2 = intermediate principal effective stress, and σ_3 = minimum principal effective stress.....37

Fig. 2.23. Different type of mode of formation of fractures modified from Siddique et al., (2021), Rice (1968).....38

Fig. 2.24. Upper Devonian stratigraphy of the Frontal Ranges of the Rocky Mountains and correlation with the sub-surface units in the Western Canada Sedimentary Basin from MacKay et al., (2018) after McLean and Mountjoy, (1993).....43

Fig. 2.25. A A) Geological map of the Nordegg area in the Central Alberta Rocky Mountain and Foothills belts, after (Pana and Elgr, 2013). The outcrops studied are located in the Hoodoo Creek and Wapiti Creek, marked with a red star. B) Structural cross-section of Nordegg area, after Langenberg et al, (2002); Begin and Veilleux (2011).44

Fig. 3.1. Workflow chart of data and methods used in studying natural fractures of the Upper Devonian Duvernay and Perdrix Formations. QC = Quality Control; V. W. = Vertical Wells; H. W. = Horizontal wells.46

Fig. 3.2. Depth structural map of the top of the Duvernay Formation (m, bsl) in the Kaybob area. A-D, wellhead location of four horizontal wells (red circles). 1-7, wellhead location of vertical wells, in which core was described (black circles). C-1 to C5, wellhead location of vertical wells (blue circles) used in 3D lithofacies and petrophysical models (white rectangles). The pairs of wells 4 and B and wells 7 and D belong to common well pads, respectively. The blue polygons depict simplified geometry of the Leduc Reefs. TVDSS, bsl, True vertical depth below sea level. See Table 3.1 for the list of the wells.....48

Fig. 3.3. Terzaghi’s angular correction applied for linear fracture intensity for different fracture sets. α is the angle between the core axis (line of observation) and orientation of a fracture set. Fractures of set 1 will be less likely to be seen in the core, as they are sub parallel to the core axis. Terzaghi correction of fracture intensity will be higher for set 1 than for set 2.....54

Fig. 3.4. Different types of drilling-induced fractures, after Li and Schmitt (1998); Zhang et al., (2010). The double-headed arrows reflect the orientation of the maximum horizontal stress SHmax, parallel to the strike of the fractures. SHmax for scallop type is inferred.....56

Fig. 3.5. A) Fractures (black) and bedding (green) intersecting a cylindrical surface (horizontal borehole) within a rock mass. B) Unrolled borehole trace map with fracture and traces of slightly inclined bedding. Modified from Wang, (2005).....57

Fig. 3.6. Changes in fracture intensity estimated using different sampling rate. Track 1, FMI dynamic log with picked sinusoids of fractures; Track 2, orientation of natural fractures (true dip azimuth and dip angle); Tracks 3-5, linear fracture intensity P10 estimated with 0.5 m, 1 m, 1.5

m and 2 m of step and window size, respectively. The red rectangles highlight the intervals of high variability of fracture intensity depending on a window and step size.....58

Fig. 3.7. Orientation of borehole breakouts and drilling-induced tensile fractures relative to orientation of remote principal stresses (maximum and minimum) and hoop stresses (σ_{θ} max and σ_{θ} min), modified after Reinecker et al. (2003).....59

Fig. 3.8. Schematic wellbore cross-section of a horizontal well oriented NW-SE, displaying orientation of borehole breakouts and drilling-induced fracture (DIF) relative to remote regional stresses in the Kaybob area.....60

Fig. 3.9. Cross-plot of core porosity (%) vs core permeability (mD, Log scale) estimated based on petrophysical testing reports for core samples of the Lower Ireton, Duvernay and Majeau Lake Formations in wells 3 and 6 (Tables 3.1, 3.2, Fig. 3.9). See text for the equation.....62

Fig. 3.10. Estimated profiles of petrophysical and geomechanical parameters (solid lines) and XRD and geomechanical core testing data and hardness measurements obtained in this study (dots) in Well 6. U. Duv., Upper Duvernay.65

Fig. 4.1. A) Light-grey faintly laminated to massive silty mudstones, facies F1 (3260.18m, well 3). B) Thin section of a weakly laminated carbonate-rich silty mudstone (photo taken from CRC report R8955, 3526.03m, well 7). See Fig. 4.6 and Table 3.1 for the name and location of the wells.....74

Fig. 4.2. A) Faintly planar-laminated clay-bearing mudstones of facies F2 (3279.12m, well 3). B) F2 thin section, showing faint planar-laminated structure of the organic-rich mudstone with a few bioclasts (photo of thin section is taken from CRC report R8955, 3537.75m, well 7). C) Planar laminated mudstones with thinly layered light-grey carbonate-rich silty interbeds of facies F3 (3061.18m, well 5). D) F3 thin section, displaying the alternation of organic/clay-rich and carbonate-rich interbeds (3190.93m, well 4). See Fig. 4.6 and Table 3.1 for the name and location of the wells.....75

Fig. 4.3. A) Fossiliferous wackestones, facies F4 (3287.60m, well 3). B)-D) F4 thin section: B) carbonate-rich fossiliferous wackestones with Styliolinids (3528.4m, well 7). C) Close up view of Styliolinids (3528.4m, well 7). D) Close up view of a transversal section of Styliolinids (3260.24m, well 6). See Fig. 4.6 and Table 3.1 for the name and location of the wells.....76

Fig. 4.4. A) Nodular mudstone, facies F5 (3304.82m, well 3). B) F5 thin section of mudstone nodule showing faint lamination to massive structure and fossils fragments (photo taken from CRC report R8955, 3541.70m, well 7). See Fig. 4.6 and Table 3.1 for the name and location of the wells.....77

Fig. 4.5. A) Clay-rich fissile mudstones, facies F6 (3198.69m, well 4). B) F6, close up view of A) fissility in the mudstone. C) Discontinuous pyrite-rich lens-shaped aggregates and laminae, facies F7 (3203.45m, well 4). D) F7, thin section showing pyrite-rich laminae in carbonate-rich mudstone of the Perdrix Formation (sample ‘W-06-S2’ collected at the outcrop of the Wapiti Gap, Nordegg area, Alberta). See Fig. 4.6 and Table 3.1 for the name and location of the well and Fig. 4.64 for the outcrop location.....78

Fig. 4.6. Structural surface of the top of the Duvernay Formation (NAD 83 UTM zone 11 N). The white circles define top picks of the Duvernay Formation imported from the 3D Provincial Geological Framework Model of Alberta (2019) that were used for building the surface.

Wellhead location of wells analyzed in this study: A-D, four horizontal wells (red circles). 1-7, seven vertical wells, in which core was described (black circles). C-1 to C5, wellhead location of vertical wells (blue circles) used in 3D lithofacies and petrophysical models (white rectangles). The pairs of wells 4 and B and wells 7 and D belong to common well pads, respectively. Top picks from the studied wells were added to generate the surface. Blue polygons delineate the simplified geometry of the Leduc reefs. TVDSS, bsl, True vertical depth below sea level. See Table 3.1 for the name and location of the wells.....79

Fig. 4.7. Structural surface of the top of the Beaverhill Lake Group (NAD 83, UTM zone 11 N). The white circles define top picks of the Beaverhill Lake Group imported from the 3D Provincial Geological Framework Model of Alberta, 2019 used for building the surface. The black circles indicate the location of wellheads of the vertical wells (1-7), in which core was studied (Table 3.1); top picks from these wells were added to generate the surface. The blue polygons depict simplified geometry of the Leduc reefs. TVDSS, bsl, True vertical depth below sea level. See Table 3.1 for the name and location of the wells.....81

Fig. 4.8. Isopach map of Duvernay and Majeau Lake Formation. Note the increase of thickness of the Duvernay Formation towards the center of the basin and pinching out of the mudrocks around the Leduc Reefs. The red lines indicate the location of the cross-section displayed in Fig. 4.9 and Fig. 4.10. See Table 3.1 for the name and location of the wells.....82

Fig. 4.9. Estimated thickness of facies F1-F7 as percent of total thickness of the Duvernay Formation based on core description in seven vertical wells 1-7 (see Table 3.1 and Fig. 4.6). Note the greater thickness of F2 and F3 compared to other facies. See Table 4.1 for the facies description.....83

Fig. 4.10. Cross-section SW-NE of the 3D structural model, Kaybob Area. Surfaces and top picks were imported from the 3D Provincial Geological Framework Model of Alberta, 2019 <https://ags.aer.ca/publication/3d-pgf-model-v2> and modified to include the picks from the studied wells. See Fig. 4.8 for the cross-section location. Squares indicate well top picks. The Beaverhill Lake Group is below the Duvernay and Leduc Formations.....84

Fig. 4.11. Cross-section NW-SE of the 3D structural model, Kaybob Area. Surfaces and top picks were imported from the 3D Provincial Geological Framework Model of Alberta, 2019 <https://ags.aer.ca/publication/3d-pgf-model-v2> and modified to include the picks from the studied wells. See Fig. 4.8 for the cross-section location. Squares indicate well top picks. The Beaverhill Lake Group is below the Duvernay and Leduc Formations.....84

Fig. 4.12. Map of modelled facies of the Duvernay Formation in 3D model A along the horizon at the depth where the horizontal well A was landed. Red circle and line, wellhead location and trajectory of horizontal well A. Black circle, wellhead location of vertical well 1, in which core was described. The distance between well 1 and well A is 5.2 km. Table 3.1 for name of the wells within the Kaybob area. See Table 4.1 for facies description. The red circle within the inset map shows the location of wells A, 1 and model A.....85

Fig. 4.13. Cross-section NW- SE along horizontal well A in 3D model A, displaying modelled facies of the Duvernay Formation. The well was landed mostly in organic-rich facies F2 and F3 of the upper Duvernay Member. Thin black line indicates GR log along well A trajectory. Formation tops: U.Duv., Upper Duvernay; M. Duv., Middle Duvernay; L.Duv., Lower Duvernay; Blk., Beaverhill Lake. See Fig. 4.6, 4.12 and Table 3.1 for location of the well, Table 4.1 for facies description.....87

Fig. 4.14. Map of modelled facies of the Duvernay Formation in 3D model B along the horizon at the depth where the horizontal well B was landed. Red circle and line, wellhead location and trajectory of horizontal well B. Black circle, wellhead location of vertical well 4, in which core was described. See Table 3.1 name of the wells within the Kaybob area. See Table 4.1 for facies description. The red circle within the inset map shows the location of wells B, 4 and model B.....88

Fig. 4.15. Cross-section S-N along horizontal well B in 3D model B, displaying modelled facies of the Duvernay Formation. The well was landed mostly in organic-rich facies F2 and F3 of the upper Duvernay Member. Facies interpretation (left track) and gamma ray log (right track) are shown in vertical well 4 located in the same well pad as well B. Thin black line indicates GR log along well B trajectory. Formation tops: U.Duv., Upper Duvernay; M. Duv., Middle Duvernay; L.Duv., Lower Duvernay; Blk., Beaverhill Lake. See Fig. 4.6, 4.14 and Table 3.1 for location of the wells, Table 4.1 for facies description.....89

Fig. 4.16. Map showing modelled facies of the Duvernay Formation in 3D model C along the horizon at the depth where the most of the horizontal wells in the area were landed. C-1 to C-5, wellhead location of vertical wells (blue circles) used in 3D facies model C. Red circles and lines, wellhead location and trajectory of other horizontal wells drilled in the area. Black circle, wellhead location of vertical well 5, in which core was described. See Table 3.1 for name of the wells within the Kaybob area. See Table 4.1 for facies description. The red circle within the inset map shows the location of wells C, C1-C5 and model C.....90

Fig. 4.17. 3D view of the Duvernay facies interpreted in model C. Facies of the Duvernay Formation interpreted in wells C-1 to C-5 based on well logs data and in well 5 based on core description are used in 3D facies model C. Labels C1-C5 and 5 indicate location of vertical wells at the top of the Duvernay Formation (yellow circles). Red lines, location and trajectory of horizontal wells drilled the area. Horizontal wells in the area are landed in organic-rich facies F2 and F3. See Fig. 4.6 and Table 3.1 for the location of the model and name of the wells within the Kaybob area. See Table 4.1 for facies description.....91

Fig. 4.18. Cross-section N-S along horizontal well C in 3D model C, displaying modelled facies of the Duvernay Formation. The well was landed mostly in organic-rich facies F2 and F3 at the base of the upper Duvernay Member. Thin black line indicates GR log along well C trajectory. Formation tops: U.Duv., Upper Duvernay; M. Duv., Middle Duvernay; L.Duv., Lower Duvernay; Blk., Beaverhill Lake. See Fig. 4.6, 4.16 and Table 3.1 for the location of the well, Table 4.1 for facies description.....92

Fig. 4.19. Map showing modelled facies of the Duvernay Formation in the 3D model D along the horizon at the depth where the horizontal well D in the area was landed. Red circles and line, wellhead location of horizontal well D with its trajectory. Black circle, wellhead location of vertical well 7, in which core was described. See Table 3.1 name of the wells within the Kaybob area. See Table 4.1 for facies description. The red circle within the inset map shows the location of wells D, 7 and model D.....93

Fig. 4.20. Cross-section SE-NW along horizontal well D in 3D model D, displaying modelled facies of the Duvernay Formation. The horizontal well D was landed mostly in organic-rich facies F2 and F3. Facies interpretation (left track) and gamma ray log (right track) are shown for vertical well 7 located in the same well pad as well D (see Table 3.1, Fig. 4.6). Thin black line indicates GR log along the well trajectory. Formation tops: U.Duv., Upper Duvernay; M. Duv.,

Middle Duvernay; L.Duv., Lower Duvernay; Blk., Beaverhill Lake. See Fig. 4.6, 4.19 and Table 3.1 for the location of wells, Table 4.1 for facies description.....95

Fig. 4.21. Sequence stratigraphy boundaries, lithofacies, gamma ray (GR), bulk density (RHOB), estimated profiles of petrophysical parameters (solid lines) and XDR core testing data (dots) in well 3 (see Tables 3.1, 4.1, Fig. 4.6). PHIT, total porosity; kmax, horizontal permeability; TOC, total organic carbon; Sg, So and Sw, fluid saturation. Formation tops: U. Duv., Upper Duvernay; M.D., Middle Duvernay; L. Duv., Lower Duvernay; MLK., Majeau Lake; BLK, Beaverhill Lake. SB, sequence boundary, MFS; maximum flooding surface; MRS, maximum regressive surface.....98

Fig. 4.22. Sequence stratigraphy boundaries, lithofacies, gamma ray (GR), bulk density (RHOB) logs, estimated profiles of petrophysical parameters (solid lines) and XDR core testing data (dots) in well 7 (see Tables 3.1, 4.1, Fig. 4.6). PHIT, total porosity; kmax, horizontal permeability; TOC, total organic carbon; Sg, So and Sw, fluid saturation. Formation tops: U. Duv., Upper Duvernay; M.D., Middle Duvernay; L. Duv., Lower Duvernay; BLK., Beaverhill Lake. SB, sequence boundary, MFS; maximum flooding surface; MRS, maximum regressive surface.....99

Fig. 4.23. Box plot diagrams showing petrophysical properties of facies F2 of the Duvernay mudrocks per well in six vertical wells 1, 3-7 (see Table 3.1, Fig. 4.6). A) TOC (wt.%). B) Gas saturation Sg (%). C) Oil saturation So (%).100

Fig. 4.24. Box plot diagrams showing petrophysical properties of facies F3 of the Duvernay mudrocks per well in six vertical wells 1, 3-7 (see Table 3.1, Fig. 4.6). A) TOC (wt.%). B) Gas saturation Sg (%). C) Oil saturation So (%).101

Fig. 4.25. Box plot diagrams showing petrophysical properties of Facies F5 of the Duvernay mudrocks per well in six vertical wells 1, 3-7 (see Table 3.1, Fig. 4.6). A) TOC (wt.%). B) Gas saturation Sg (%). C) Oil saturation So (%). See legend on Fig. 4.23.....102

Fig. 4.26. Cross-plots of GR vs Illite (left) and GR vs Calcite (right) in facies F1-F7 of the Duvernay Formation based on XRD analysis of core in well 7. See Fig. 4.6 and Table 3.1 for the location of well 7, Table 4.1 for facies description.....105

Fig. 4.27. Well 3. Lithofacies, sequence stratigraphy boundaries, well logs of Gamma Ray, Photoelectric Factor (PEF), Bulk Density (RHOB), Shear (DTSH) and Compressional (DTCO) Slowness, and estimated profiles of Young's Modulus (YM), Poisson's Ratio (PR), Unconfined Compressional Strength (UCS) and Hardness measurements in the mudrocks of the Duvernay Formation. Labels d, DYN, dynamic; s, static. On the right, photos of lithofacies: F3 (A); F7 (B); F4 (C); F5 (D); F1 (E); F2 (F).....106

Fig. 4.28. Well 7. Lithofacies, sequence stratigraphy boundaries, well logs of Gamma Ray (GR), Photoelectric Factor (PEFZ), Bulk Density (RHOB, RHOZ), Shear and Compressional Slowness (DTSH, DTCO), Deep (AT90), Medium (AT60) and Shallow (AT20) Resistivity, Caliper (HCAL), and estimated profiles of Young's Modulus (YM), Poisson's Ratio (PR), Unconfined Compressional Strength (UCS), and Hardness measurements in the mudrocks of the Duvernay Formation. Labels DYN, dynamic; s, static.....107

Fig. 4.29. Box-plot diagram showing the average values of Tensile Strength (TSTR) in facies F1, F2, F3 and F5 of the Duvernay Formation based on core data in wells 4, 6 and 7. See Table 3.1 and Fig 3.2 for name and location of studied vertical wells, Table 4.1 for the facies composition, Table 4.4 for TSTR values from different wells used on this figure.....108

Fig. 4.30. Calcite-filled subvertical (A), inclined (B), and horizontal (C) fractures in core samples of the Duvernay Formation, well 7, depth 3522.55 for (A), well 6, depth 3360.30 m for (B), well 6, depth 3371.61 m for (C). Sparse crystals of anhydrite (pink arrows) in the mudrocks are highlighted in C. See Table 3.1 and Fig. 4.6 for the wells' name and location.....109

Fig. 4.31. Thin sections of fractures in the Duvernay Formation: A) Subvertical mineralized fracture with calcite and pyrite, showing blocky texture (well 1, 3435.01 m) B) Partially mineralized horizontal fracture filled with calcite (well 3, 3284.29 m). C) Subvertical mineralized fracture with crystals of calcite (10 – 100 μm) and kerogen (well 7, 3522.65 m). The fracture is crossed by a younger open subhorizontal fracture. D) Mineralized inclined fracture showing two different stages of calcite growth, one with smaller calcite crystals (< 80 μm) at the walls of the fracture, and another one with larger calcite crystals (up to 300 μm) in the center of the fracture (well 3, 3285.12 m). Bedding in A-D is subhorizontal. Parallel nicols in A-C, crossed nicols in D. See Table 3.1 and Fig. 4.6 for the wells' name and location. Abbreviations: Cal: Calcite; Krg: Kerogen.....110

Fig. 4.32. Vertical fractures in mudrocks of the Duvernay Formation: A) Vertical calcite-filled fracture propagated in F3 and limited by rock strength contrast between facies F2 and F3 (well 3, 3280.54 m). B) Vertical calcite-filled fracture fading into the mudstones at the top and bottom tips of the fracture, facies F3 (well 3, 3282.14 m). C) Thin-section of a tensile vertical calcite-filled fracture crossing microlaminae of carbonate- and organic-rich mudrocks (well 4, 3190.93 m). Parallel nicols. See Table 3.1 and Fig. 4.6 for the wells' name and location.....112

Fig. 4.33. Histogram of fracture aperture size of calcite-filled fractures in mudrocks of the Duvernay Formation. About half of measured fractures are characterized by aperture between 0.1 and 0.2 mm. Total number of samples 46.....113

Fig. 4.34. Transtensional calcite-filled fractures in the Duvernay Formation: A) Core sample with a splay of inclined calcite-filled complex fractures characterized by repeating segments of shear (S) and tensile (T) deformation (well 3, 3285.19 m). B) Schematic representation of the influence of bed competence on deformation during fracture propagation, with tensile dilational jogs forming in carbonate-rich beds and shear deformation in ductile organic-rich beds, modified from Sibson (2000). C) Core sample with another splay of inclined calcite-filled complex fractures, showing shear deformation in organic-rich beds and tensile deformation in carbonate-rich beds (well 3, 3284.30 m). D) Thin-section of a splay of calcite-filled fractures in facies F3 (well 3, 3285.12 m). E) Thin-section of one branch of the splay of fractures in facies F3 showing shear deformation in organic-rich laminae and calcite-filled tensile deformation in carbonate-rich laminae (well 3, 3285.12 m). Parallel nicols in B and D. See Table 3.1 and Fig. 4.6 for the wells' name and location.....114

Fig. 4.35. Fractures in the Duvernay mudrocks in thin sections: A) Scanned thin section showing several branches of a transtensional complex splay of fractures. The red squares indicate the location of figures B and C. B) Calcite-filled fracture showing tension gashes in carbonate-rich beds and shear displacement in organic-rich beds. Open horizontal fractures along the bedding are displaced by high-angle transtensional fracture (well 3, 3284.29 m). C) Several sub-vertical calcite-filled fractures, showing shear deformation in organic-rich beds and tensile deformation in carbonate-rich beds (well 3, 3284.30 m). D) Calcite-filled tension gash showing blocky texture (well 3, 3284.49 m). E) Calcite and pyrite-filled tension gash showing blocky texture and different grain-size of calcite filling (well 3, 3284.29 m). Nicols parallel in B-E. See Table 3.1 and Fig. 4.6 for the wells' name and location.....116

Fig. 4.36. Polished slip faces (PSF) in the mudrocks of the Duvernay Formation: A) Side-view of the core sample, showing location of PSF along pyrite-rich laminae of 3 mm thick in bituminous mudrock. B) Top (map) view of the PSF, showing the mirror-like face with striae highlighted by white dotted lines (well 1, 3448.40 m). See Table 3.1 and Fig. 4.6 for the wells' name and location.....117

Fig. 4.37. Petal drilling-induced fractures observed in core samples of mudrocks of the Duvernay Formation in the Kaybob area: A) Well 3, 3268.42 m (side view). B) Well 3, 3268.42 m. C) Well 4, 3197.80 m. D) Well 4, 3197.80 m (side view). See Table 3.1 and Fig. 4.6 for the wells' name and location.....119

Fig. 4.38. Drilling-induced irregular crack networks observed in core samples of mudrocks of the Duvernay Formation in the Kaybob area: A) open cracks in carbonate nodules of facies F5 (well 4, 3208.65 m). B) open and rock-flour filled cracks in facies F1 (well 7, 3539.26 m). C) Open cracks replicating the shape of the carbonate nodules at the edge of the core, with several subhorizontal cracks, facies F5 (well 7, 3567.80 m). See Table 3.1 and Fig. 4.6 for the wells' name and location.....120

Fig. 4.39. Fracture intensity P10 (fract/m) in core of the Duvernay Formation per well after application of the Terzaghi's correction. See Table 3.1 and Fig. 4.6 for the wells' name and location.....121

Fig. 4.40. Distribution of fracture intensity P10 in core of Duvernay Formation extrapolated between seven vertical wells 1-7. Background is the structural map (TV DSS) of the top of the Duvernay Formation. See Table 3.1 and Fig. 4.6 for the wells' name and location.....122

Fig. 4.41. Histogram of fracture intensity P10 (fract/m) estimated in core of the Duvernay Formation per facies after normalization by facies thickness and application of the Terzaghi's correction. See Table 4.1 for facies composition.....123

Fig. 4.42. Depth structural map of the top of the Duvernay Formation (bsl). Location of four horizontal wells, in which FMI image logs were studied, is shown. The blue polygons depict simplified geometry of the Leduc Reefs. Rose diagrams show the strike of each set of fractures per well and the total number of fractures per well (N). See Table 4.1 for the number of fractures per set and per well.125

Fig. 4.43. Example of interpreted FMI log in well A. Three sets of subvertical natural fractures of variable orientation are marked by circles of different colors. Borehole breakout (BO) is shown by black polygons. Most of the fractures represented as sinusoids that cross the borehole entirely. See Fig. 4.42 for well location.....126

Fig. 4.44. Stereographic equal area projection of three sets of natural fractures (NF) and bedding picked in well A plotted as poles to planes (true dip azimuth and true dip angle, upper hemisphere). See Fig. 4.42 for well location.....127

Fig. 4.45. Example of interpreted FMI log in well B. Set 1 of the NE-SW-striking subvertical natural fractures is marked with oval of blue color. Drilling-induced fractures (DIF) are outlined by red circle. See Fig. 4.42 for well location.....128

Fig. 4.46. Stereographic equal area projection of set 1 of natural fractures and bedding picked in well B and plotted as poles to planes (true dip azimuth and true dip angle, upper hemisphere). See Fig. 4.42 for well location.....129

Fig. 4.47. Example of interpreted FMI log in well C. See Fig. 4.42 for well location.130

Fig. 4.48. Stereographic equal area projection of three sets of natural fractures and bedding picked in well C plotted as poles to planes (true dip azimuth and true dip angle, upper hemisphere). See Fig. 4.42 for well location.....	130
Fig. 4.49. Example of interpreted FMI log in well D. Set 1 and 2 of subvertical natural fractures are marked with blue and green circles. See Fig. 4.42 for well location.....	131
Fig. 4.50. Stereographic equal area projection of three sets of natural fractures and bedding picked in well D plotted as poles to planes (true dip azimuth and true dip angle, upper hemisphere). This well shows the lower number of fractures (N=14). See Fig. 4.42 for well location.	132
Fig. 4.51. Rose diagrams and stereographic equal area projection (upper hemisphere) showing poles to planes of natural fractures (true dip angle, true dip azimuth) and strike of resistive (upper row) and conductive (lower row) fractures for each horizontal well.....	133
Fig. 4.52. Rose diagrams and stereographic equal area projection (upper hemisphere) showing poles to planes of natural fractures (true dip angle, true dip azimuth) and strike of three main sets of natural fractures determined in four horizontal wells A-D from image log analysis. See Fig. 4.42 for well location.....	134
Fig. 4.53. Cross-section along well A. Surfaces of the tops of the Upper (U.Duv), Middle (M. Duv) and Lower Duvernay (L. Duv) Members are modeled based on the well tops in neighboring vertical wells. The GR log and histograms of fracture intensity P10 are shown along well A trajectory. P10 is shown for all fractures (a) and by fracture type (b-d): discontinuous conductive (b), continuous conductive (c), and resistive (d). Red circle highlights the interval of maximum curvature of the borehole trajectory, close to the heel of the well. Blue circles depict location of resistive fractures clustered in intervals of carbonate-rich facies with low GR (150 < GR <200 gAPI).....	136
Fig. 4.54. Log plot for well A showing interpreted dynamic (track 1) and static (track 2) FMI logs, orientation of interpreted structures (track 3), fracture intensity P10 (track 4) and P32 (track 5), GR log (track 6), Rate of Penetration (ROPS) log (track 7), and borehole deviation (track 8). The blue rectangles define segments with dominant resistive fractures (mineralized), low GR and ROPS. The red rectangle depicts an interval of the maximum curvature of the borehole trajectory with dominant conductive fractures (open).....	138
Fig. 4.55. Cross-section along well A. Surfaces of the tops of the upper Duvernay Member (U.Duv) and Beaverhill Lake Group (Bvrhl_lk) are modeled based on the well tops in vertical wells. The GR log and histograms of fracture intensity P10 are shown along the well trajectory. P10 is shown for three sets of natural fractures of different orientation (Table 4.10).....	140
Fig. 4.56. Cross-section along well B. Surfaces of the tops of the Middle Duvernay (M. Duv.) and Lower Duvernay (L. Duv.) Members are modeled based on the well tops in vertical well 4. The GR log and histograms of fracture intensity P10 are shown along well B trajectory. P10 is shown for all fractures (a) and by fracture type (b-d): discontinuous conductive (b), continuous conductive (c), and resistive (d). The GR log and core-based interpreted facies in vertical well 4 of the same well pad are shown.	142
Fig. 4.57. Log plot for well B showing interpreted dynamic (track 1) and static (track 2) FMI logs, orientation of interpreted structures (track 3), fracture intensity P10 (track 4) and P32 (track 5), GR log (track 6), borehole deviation (track 7) and calipers (track 8). The purple and pink sinusoids displayed in track 1 correspond to discontinuous and continuous conductive fractures.	

The red rectangle corresponds to a segment with dominant conductive fractures (open) in carbonate rich facies (GR < 200 gAPI).144

Fig. 4.58. Cross-section along well C. Surface of the top of the middle Duvernay Member (M. Duv.) is modeled based on the well tops in neighboring vertical wells. The GR log and histograms of fracture intensity P10 are shown along well C trajectory. P10 is shown for all fractures (a) and by fracture type (b-d): discontinuous conductive (b), continuous conductive (c), and resistive (d).....146

Fig. 4.59. Log plot for well C showing interpreted dynamic (track 1) and static (track 2) FMI logs, orientation of interpreted structures (track 3), fracture intensity P10 (track 4) and P32 (track 5), GR log (track 6), borehole deviation (track 7), and calipers (track 8). The red rectangle shows a segment with dominant conductive fractures (open) of lower resistivity.....148

Fig. 4.60. Cross-section along well C. Surfaces of the tops of the Upper Duvernay (U. Duv.) and Middle Duvernay (M. Duv.) are modeled based on the well tops in vertical wells. GR log and histograms of fracture intensity P10 are shown along the well C trajectory. P10 is shown for determined three sets of fractures of different orientation (Table 4.10).150

Fig. 4.61. Cross-section along well D. Surfaces of the tops of the Upper Duvernay (U. Duv.), Middle Duvernay (M. Duv.) and Lower Duvernay (L. Duv.) members are modeled based on the well tops in vertical well 7 from the same well pad. The GR log and histograms of fracture intensity P10 are shown along well D trajectory. P10 is shown for determined three sets of fractures of different orientation (Table 4.10). The GR and facies interpreted for vertical well ‘7’ are shown on the right.....152

Fig. 4.62. Rose diagrams and stereographic equal area projection (upper hemisphere) showing poles to planes (true dip angle, true dip azimuth) and strike of drilling-induced fractures in horizontal wells B and C. The red dots shows true dip azimuth and true dip angle, and the grey histograms show the strike of the fractures. See Fig. 4.42 for well location.....153

Fig. 4.63. Rose diagrams, stereographic equal area projection (upper hemisphere) and interpretation schemes of orientation of borehole breakouts (BO) in horizontal wells A and D. True dip angle and true dip azimuth of fractures are shown in black dots; strike is displayed in grey histograms. HAZI, borehole azimuth. See Fig. 4.42 for well location.....154

Fig. 4.64. A) Google Earth map of Front Ranges and Foothills in the Nordegg area with projected main thrust faults (white lines), after the AER dataset (Hamilton et al., 1999), with location of the Hoodoo Creek (52°16’20.59” N, 116°27’ 21.23” W) and Wapiti Gap (52°29’10.99” N, 116°24’29.59” W) outcrops (red stars). The red line indicates the location of the cross-section B. B) Photo of the outcrop across the Hoodoo Creek.....156

Fig. 4.65. Organic-rich shales of the Perdrix Formation, Hoodoo Creek (A-B) and Wapiti Gap (C-D). A) Outcrop photo, bedding planes (S0) are highlighted by white dashed lines. The red-dashed lines indicate cleavage (S1). B) Stereographic equal area projection of bedding of the Perdrix Formation in the Hoodoo Creek, plotted as planes (black lines, strike and dip angle) and poles to planes (orange dots, dip azimuth and dip angle, lower hemisphere). The orange line depicts the azimuth of strike and dip angle of mean bedding plane determined from high-density pole to plane location. Red color contours indicate density of pole to planes. C) Outcrop photo of organic-rich shale of the Perdrix Formation in the Wapiti Gap (W-04-S1), D) Thin section of interbedded organic-rich shale and limestone (W-06-S1). Calcite-filled tensile fractures in carbonate-rich beds that stop in the shale beds.....157

- Fig. 4.66.** Structural elements in the organic-rich shales of the Perdrix Formation, Hoodoo Creek: A) Bedding (S0 white-dashed lines), subvertical cleavage (S1 red-dashed lines) and intersection lineation (Li blue dots). B) Stereographic equal area projection of cleavage plotted as planes (black lines, strike azimuth and dip angle) and poles to planes (blue dots, dip azimuth and dip angle, lower hemisphere). The blue line is the mean strike azimuth and dip angle of the cleavage. Density contours for the poles to planes S1 are highlighted by red color. C) Stereographic equal area projection of mean plane and pole of bedding (orange line and dot) and cleavage (blue line and dot), and trend azimuth and plunge of intersection lineation (red dots), lower hemisphere.....158
- Fig. 4.67.** A) Scanned thin section of organic-rich shale of the Perdrix Formation (HC-01-S1) with strong subvertical cleavage and a network of open fractures. B) Thin-section of vertical cleavage (HC-01-S1). Open subhorizontal fractures are connected with subvertical fractures, creating a lattice pattern. Some of these fractures are partially mineralized and filled with blocky crystals of calcite.....159
- Fig. 4.68.** High-density subhorizontal calcite-filled fractures in the Perdrix organic-rich shales above the thrust fault zone: outcrop photo, frontal view (A) and thin section, sample HC-12-S2 (B). Thick calcite and quartz veins developed along the thrust fault zone. Subhorizontal veins are orthogonal to the subvertical cleavage S1. Late subvertical fractures cut through subhorizontal veins.....160
- Fig. 4.69.** Deformation elements in the Perdrix shales along the dextral strike-slip fault, the Hoodoo Creek: A) Shear zone along the subvertical dextral strike-slip fault, map view. The organic-rich shales of the Perdrix Formation display sigmoidal schistosity S2 consistent with the dextral displacement along the shear zone. B) Calcite lens and calcite-filled fractures (red circle) in the shear zone. C) Stereographic equal area projection planes (lines) and poles to planes (dots) of mapped thrusts (black) and strike-slip faults (blue), lower hemisphere. The red lines indicate the mean strike azimuth and dip angle of the thrusts and strike-slip faults. Contours are built in poles to planes, with red colors indicating higher intensity of pole to planes. D) Drag folds within the shear zone. E) Stereographic equal area projection of trend and plunge of axes of drag folds (red dots) and strike (black lines) with poles to planes of schistosity S2 (blue dots) in the dextral strike-slip shear zone, lower hemisphere.....161
- Fig. 4.70.** Slickenlines and mirror planes developed in drag folds in the deformed organic-rich shales of the Perdrix Formation within the dextral strike-slip shear zone, Hoodoo Creek.162
- Fig. 4.71.** Open subvertical NNW-SSE fractures (joints) with plumose structure (A) and calcite-filled fractures (B-C) in organic-rich shales of the Perdrix Formation, Hoodoo Creek. Low-angle calcite-filled fractures are orthogonal to the subvertical cleavage S1 and characterized by slickenlines (C) indicating updip shear slip to the SE. The white-dashed lines (B) highlight the fractures.....163
- Fig. 4.72.** Tensile calcite-filled fractures in organic-rich shales of the Perdrix Formation, Hoodoo Creek, thin sections, nicols parallel: A) oblique fracture partially filled with blocky calcite and pyrite. B) horizontal and subvertical fractures orthogonal and parallel to subvertical cleavage S1, respectively. Subvertical fracture is partially filled with calcite and kerogen. Abbreviations: Cal = Calcite, Py = Pyrite, Krg = Kerogen.....164
- Fig. 4.73.** Tensile calcite-filled fractures in the mudrocks of the Perdrix Formation, Hoodoo Creek: A-B). Top (A) and side (B) view of carbonate-rich and organic-rich mudstones. The

carbonate-rich beds experienced boudinage with calcite veins formed between boudins. C) Calcite-filled fractures with height > 50 cm crossing bed boundary between carbonate-rich mudstones and organic-rich shales. The calcite-filled veins start in the carbonate-rich mudrocks, where they have larger aperture, and propagate into the shales across the bed boundary. D) subhorizontal tension gashes (calcite-filled fractures) with height < 5 cm propagated within the mudstone bed.....165

Fig. 4.74. Conjugate tensile calcite-filled fractures in organic-rich shales of the Perdrix Formation, Hoodoo Creek. Conjugate sets of fractures form left-lateral (A) and right-lateral (B) semi-brittle shear zones are highlighted by red arrows. (C) Slab of organic-rich shales detached from the outcrop. The axis (white arrows) bisecting the acute angle between the conjugate tensile fractures is oriented in the outcrop NW-SE, trend and plunge N128°/05°.....166

Fig. 4.75. Horizontal, vertical tensile and extensional shear fractures in thinly interbedded carbonate-rich mudrocks and organic-rich shales of the Perdrix Formation, Hoodoo Creek, thin sections, nicols parallel (HC-03-S1): Extensional shear fracture (red-dashed line) cut through the beds with ~1 mm of normal displacement. The shear fracture postdates (displaces) horizontal tensile fractures (blue arrows), and it predates (is crossed by) subvertical tensile fractures (green arrow).....167

Fig. 4.76. Several generations of calcite-filled fractures, cleavage and pressure shadows around pyrite in thin sections of the Perdrix shales, the Hoodoo Creek, nicols parallel: A) Cross-cutting relationship of calcite-filled fractures. The younger transtensional fracture with a shear component of displacement (2) displaces the older tensile fracture (1), splits and propagates along the wall of the older fracture (1), sample HC-12-S4. B) Detail of thin section A. C) Subhorizontal calcite-filled tensile fractures oriented perpendicular and at low angle to subvertical cleavage (S1= red line). The dissolution along the cleavage planes results in apparent shift of segments of the orthogonal veins highlighted by the red arrow, sample HC-06-S1. D) Subvertical pressure shadows filled with fibrous calcite around the pyrite crystal, growing parallel to subvertical cleavage S1, in the direction orthogonal to the main compressive stress.....168

Fig. 4.77. Outcrop photo (A) and thin section, sample HC-08-S1 (B) of subhorizontal stylolites in fossiliferous carbonate-rich mudstone and wackstone of the Perdrix Formation, Hoodoo Creek. Dissolution along the stylolites results in an apparent shift of subvertical calcite-filled veins. The red arrows point out the stylolites.....169

Fig. 4.78. Orientation of calcite-filled and open tensile fractures of set 2 and conjugate transtensional semibrittle fracture sets 1 and 3 in organic-rich shales of the Perdrix Formation, Hoodoo Creek. Mean strike azimuth and dip angle of three sets of fractures (lines) and poles to planes (dots) are plotted on stereographic equal area projection, lower hemisphere. Density contours of poles to planes are highlighted by red color. No bedding rotation is applied.....170

Fig. 4.79. The map view of the top of carbonate-rich mudstone bed of the Perdrix Formation, Hoodoo Creek. The red lines highlight mapped open fractures. The black lines and circles A and B indicate the scanlines used for the estimation of fracture intensity P10 and P21, respectively. The small white circles are plotted at the intersections of fractures with the circular scanline.....172

Fig. 4.80. The map view of the top of carbonate-rich mudstone bed of the Perdrix Formation, Hoodoo Creek. The red lines highlight mapped calcite filled fractures. The black lines and circles A and B indicate the scanlines used for the estimation of fracture intensity P10 and P21. The small white circles are plotted at the intersections of fractures with the circular scanline173

Fig. 5.1 Box-plot diagram of average values of static Young’s Modulus (A), bulk density, RHOB (B), Unconfined Compressional Strength, UCS (C), and Hardness (D) in three main lithofacies F2, F3, F5 of the Duvernay Formation based on core and log data in seven vertical wells 1-7. See Table 3.1 and Fig. 3.2 for name and location of studied seven vertical wells, Table 4.1 for the facies composition.....176

Fig. 5.2. Cross-plots of log-based estimated Unconfined Compressional Strength (UCS) (MPa) and static Young’s Modulus (GPa) vs core-based mineral composition of mudrocks of the Duvernay Formation for three main lithofacies F2, F3 and F5 in well 7. The mineral content of Calcite (%), Illite (%), and Total Organic Carbon (TOC) (wt.%) is obtained from the XRD core data of the Duvernay Formation in well 7. See Table 4.1 for lithofacies definition. See Table 3.1 and Fig. 3.2 for well’s name and location.....177

Fig. 5.3. Fracture height classification, after Gale et al., (2014); Hooker et al., (2013). A) Perfect bed-bounded fractures. B) Top-bounded fractures. C) Hierarchical fractures. D) Unbounded fractures.179

Fig. 5.4. Conjugate fractures formed under transitional tensile behavior conditions, modified from (Davies and Raynolds, 1996).....185

Chapter 1: INTRODUCTION

The characterization of natural fractures in source rock reservoirs, integrated with the analysis of lithofacies, mechanical properties and regional structural studies, helps to define mechanical stratigraphy of mudrocks and reconstruct deformation phases, resulting in burial and maturation or uplift and erosion experienced by the rocks, and basin-scale fluid flow (Engelder, 2004; Jamison, 2016; Hooker et al., 2017). Fracture orientation and morphology is used to determine orientation of stresses and stress regime during fracturing (Engelder and Gross, 1993; Ferrill et al., 2022). Determination of height, length, aperture, orientation of natural fractures and fracture intensity in lithofacies with different mechanical properties is an essential information for fracture modeling, horizontal well placement, optimization of hydraulic fracturing and production operations (Hyman et al., 2016; Welsh et al., 2019; Nelson, 2001; 2020). Simulation of interaction between natural and hydraulic fractures can help to constrain vertical and lateral propagation of complex fracture networks, evaluate stimulated rock mass volume and analyze fluid migration through the fracture network (Weng et al., 2011; Weng, 2015; Ramanathan et al., 2015; Faskhoodi et al., 2020; Konstantinovskaya et al., 2021; Li et al., 2023). Additionally, naturally fractured organic-rich shales were studied as potential targets of CO₂ sequestration, geothermal energy extraction, and waste storage (Cutright, 2011; Schaef et al., 2014; Hazra et al., 2022; Yuan et al., 2023).

Natural fractures in source rock reservoirs have been studied based on the description of core in vertical wells and interpretation of image (FMI) logs in horizontal wells (Coyle, 2011; Gale et al., 2014).

The organic-rich shale of the Upper Devonian Duvernay Formation is a source rock and one of the unconventional shale resources in the Western Canada Sedimentary Basin that has been developed by the hydraulic fracturing technology since 2011 (Preston et al., 2016). Recent studies have shown the presence of recoverable resources of 1.3 billions barrels of crude oil and close to 22.2 trillion cubic feet of natural gas (USGS, 2019).

Prior investigations of natural fractures in the Duvernay Formation in the Western Canada Sedimentary Basin based on core data have revealed the presence of various types of fractures, including open and calcite-filled tensile fractures of various orientation (vertical, sub-vertical, inclined, irregular/complex, and horizontal), shear fractures and polished-slip faces

(Davies et al., 2014; Soltanzadeh et al., 2015; Currie, 2021). Intervals of polished-slip faces record fault zones, particularly thrust displacement, that occur in the subsurface of the Alberta Basin as far as 100-150 km to the northeast of the deformation front in the Foothills of the Canadian Rocky Mountains (Davies et al., 2014). Through the analysis of image logs, three main sets of fractures were determined in the mudrocks of the Duvernay Formation in the Kaybob area (Fothergill et al., 2014), which are oriented parallel, orthogonal and a slight angle to the regional present-day maximum horizontal stress SHmax. However, geometry, lateral and vertical distribution of natural fractures, tensile fracture intensity and spacing in lithofacies of different mechanical properties, timing and deformation phases of fracturing in the Duvernay Formation are still poorly understood.

This study aims to characterize natural fractures of the Duvernay Formation in the Kaybob area to determine fracture intensity, controlling factors of fracture propagation, and relative timing of fracturing of the Upper Devonian organic-rich mudrocks in the subsurface of the Alberta Basin. The objectives of this study include the analysis of lithofacies, mechanical properties of the rocks, geometry, orientation and intensity/spacing of natural fractures, and fracture structural settings. The results on fracture morphology and distribution in the Duvernay Formation in the subsurface are compared to description and structural analysis of fractures in the Upper Devonian Perdrix Formation in the Front Ranges and Foothills of the Nordegg area, an outcrop analog of the Duvernay Formation, aiming to correlate phases and timing of fracturing in these areas.

The research is based on the description and analysis of ~418 m of core, core tests and well logs in seven vertical wells, ~4.4 km of image logs in four horizontal wells in the Kaybob area. Lithofacies, natural fractures and drilling-induced fractures are described in seven vertical wells. Well logs were used to estimate continuous profiles of porosity, predict permeability, and estimate dynamic and static elastic and strength parameters, which were validated with core petrophysical and geomechanical testing data. Orientation and intensity of natural fractures, drilling-induced fractures and borehole breakouts were interpreted in FMI logs in four horizontal wells. 3D structural (90 km x 90 km) and facies (2 km x 2 km to 10 km x 12 km) modeling was carried out to interpret lateral distribution of lithofacies and fractures in the Duvernay, Majeau Lake and Leduc Formations.

A better understanding of fractures and mechanical stratigraphy of the Duvernay Formation can help to enhance exploration, drilling, and production practices of the source rock reservoir in the Alberta Basin.

Chapter 2: GEOLOGIC BACKGROUND

The Alberta Basin is part of the Western Canada Sedimentary Basin (WCSB), which extends for about 1800 km from the NW to the SE in front of the Cordillera Fold and Thrust Belt (Fig. 1). The metamorphic and igneous rocks of the Canadian Shield are exposed to the northeast and east of the basin (Switzer et al., 1994). The Bow Island Arch separates the Alberta Basin from the Williston Basin (part of the Western Canada Sedimentary Basin). The study area (~8000 km²) is located in the Kaybob area to the NE of Edmonton (Fig. 2.1).

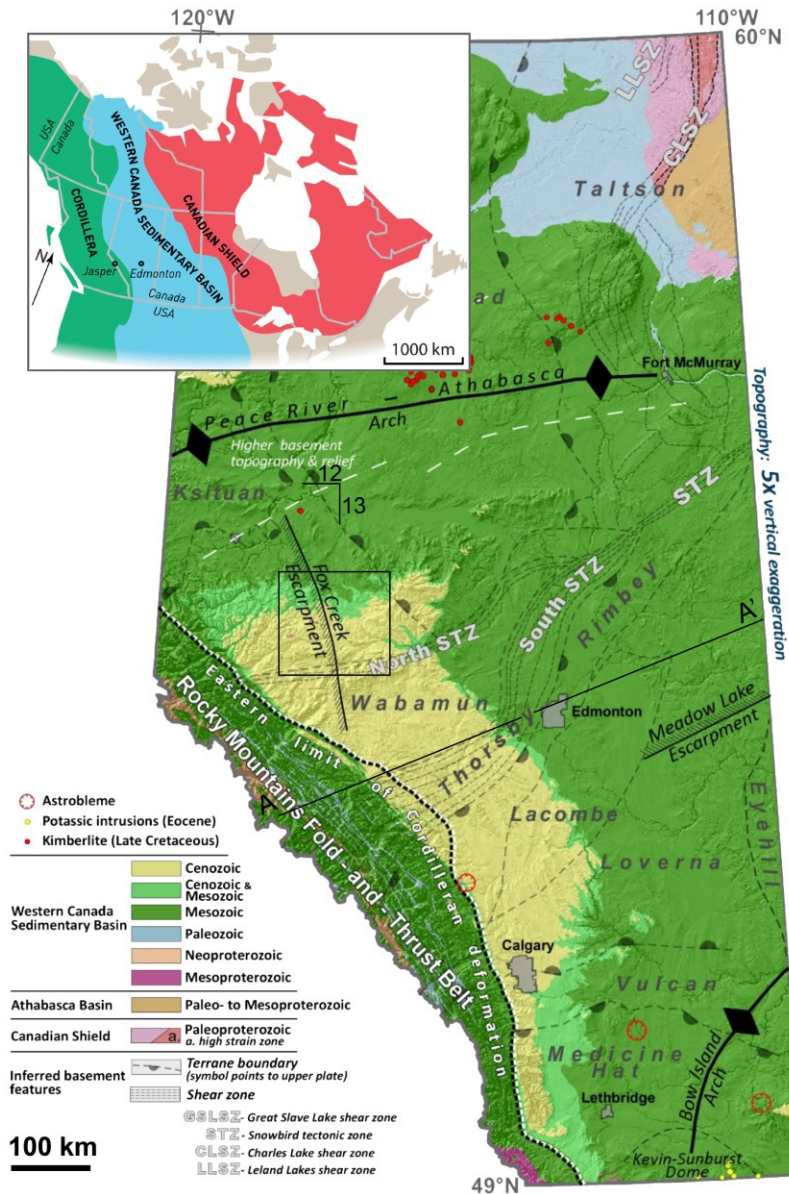


Fig. 2.1. Simplified geology and main tectonic features of the Alberta Basin and tectonic domains of the basement, after Pana et al., (2021). The location of the Western Canada Sedimentary Basin is shown in the inset map, after Waldron et al., (2016). Black polygon indicates the location of the Kaybob area; black line A-A' delineates the location of the cross-section of Figure 2.8; black lines 12 and 13 correspond to the location of 2D seismic lines of Fig. 2.9.A.

The Formation of the Canadian Cordillera involved the collision and accretion of allochthonous terranes and it was divided into five different morpho-geographic belts (Morger and Price, 2002) (Fig. 2.1). The Omineca Belt constitutes the suture zone between the collision of the Intermontane Superterrane and the North American Cordilleran miogeocline, while the Coast Belt constitutes the suture zone between the Insular Superterrane and Intermontane Superterrane (Price, 1994).

2.1. Stratigraphy and facies distribution of Upper Devonian deposits in the West Shale Basin

The Ireton, Duvernay, Majeau Lake, Leduc and Cooking Lake Formations constitute the Woodbend Group (Fig. 2.2).

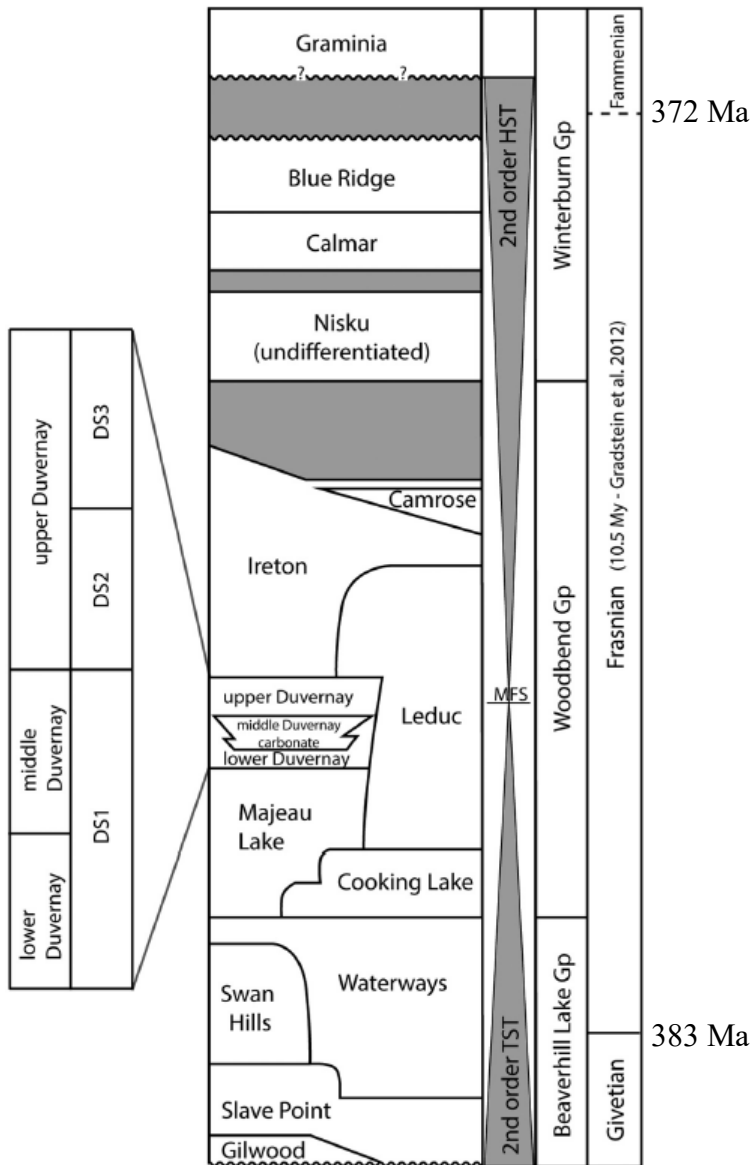


Fig. 2.2. Stratigraphic chart of Upper Devonian sedimentary succession in central Alberta, Western Canada Sedimentary Basin (Switzer et al., 1994; Alberta Geological Survey, 2019; https://ags.aer.ca/publications/Table_of_Formations_2019.html). The sequence stratigraphy boundaries and depositional sequences (DS1-DS3) are shown after Knapp et al. (2019); Shaw and Harris (2022).

The Cooking Lake Formation is found at the base of the Woodbend Group, and it overlies the Beaverhill Lake Group (Figs 2.2 and 2.3). It consists of tan limestones, which grade from calcilulites to calcarenites. Along the Leduc Rimbey-Meadowbrook trend, the limestones are dolomitized. The limestones include varied lithologies with different type of fossils, including gastropods, ostracods, crinoids, brachiopods, stromatoporoids and stromatolitic carbonaceous laminae (Andrichuk, 1958). The thickness is variable, ranging from 60 m to 90 m.

The Majeau Lake Formation is a time-equivalent of the upper portion of the Cooking Lake Formation, and corresponds to basinal deposits (Switzer et al., 1994). In the West Shale Basin, the Majeau Lake Formation overlies the Beaverhill Lake Group. It is composed of a lower deep-water limestone unit, present in the West Shale Basin, and an upper shaly unit present in both West and East Shale Basin (Switzer et al., 1994). The thickness is highly variable, ranging from 1 m to 150 m (Pollock, 1967).

The Leduc Formation consists of the fossiliferous carbonate-rich reef deposits of the Woodbend Group (Switzer et al., 1994). It is composed of a wide variety of facies, including limestones, skeletal mudstones, boundstones, floatstones and muddy skeletal packstones and wackestones, with stromatoporoids as the main reef builder (Wendte and Stoakes, 1982). When fully developed, the thickness of the reefs can reach 275 m – 300 m (Switzer et al., 1994).

The Duvernay Formation is composed of organic-rich mudstones that overlie the organic-lean mudstones of the Majeau Lake Formation and underlie the basin-filling clinoforms formed by organic-lean shales of the Ireton Formation (Fig. 2.3). The Duvernay Formation is a lateral facies of the carbonate-rich Leduc Reefs (Switzer et al., 1994). It has been informally divided into three members: the upper, middle and lower Duvernay Members. The upper and lower Duvernay Members are composed of siliceous mudstones with variable organic content, while the middle Duvernay Member is mostly made of carbonate-rich mudstones (Andrichuk, 1961; Dunn and Humenjuk, 2014; Stoakes, 1980; Stoakes and Creaney, 1985). The organic-rich shales of the Duvernay Formation are distributed in West and East Shale Basins (Fig. 2.4). Thickness of the Duvernay ranges from about 2 m to 99 m in the West Shale Basin and from 35 m to 60 m in the East Shale Basin (Knapp et al., 2017; Knapp et al., 2019; Galvis Portilla, 2022). In the Kaybob area of the West Shale basin, the thickness increases to the center of the basin and to the S – SW, close to the Leduc Reefs (Switzer et al., 1994; AGS, 2019; Shaw, 2020).

The Ireton Formation (Fig. 2.3) overlies the Duvernay and partially Leduc Formations (Oliver and Cowper, 1965). The Ireton Formation has been informally divided in two (Andrichuk and Wonfor, 1954; Belyea, 1964) or three members (McCrossan, 1961) based on lithology: Upper, Middle and Lower Ireton. The Lower Ireton (25 m – 35 m) is composed of massive and compact limestone, accompanied by minor layers of calcareous shale inclusions,

which are intermixed with gray-green calcareous shale (Oliver and Cowper, 1965). The Middle Ireton (110 m – 130 m) consists of calcareous, fissile, grey-green shale with occasional fine-grained nodular limestone with a rhythmic bedding. The Upper Ireton (15 m – 20 m) is composed of alternating layers of calcareous shale and fossiliferous limestone dolomitized in the upper part of the member. The limestone deposits vary from massive to nodular, fragmentary, partly coquinoid, and partly made up of intact brachiopod shells (Oliver and Cowper, 1965).

The total thickness of the Woodbend Group can reach up to 300 m, where about 75% of it is contributed by the Ireton Formation (Switzer et al., 1994).

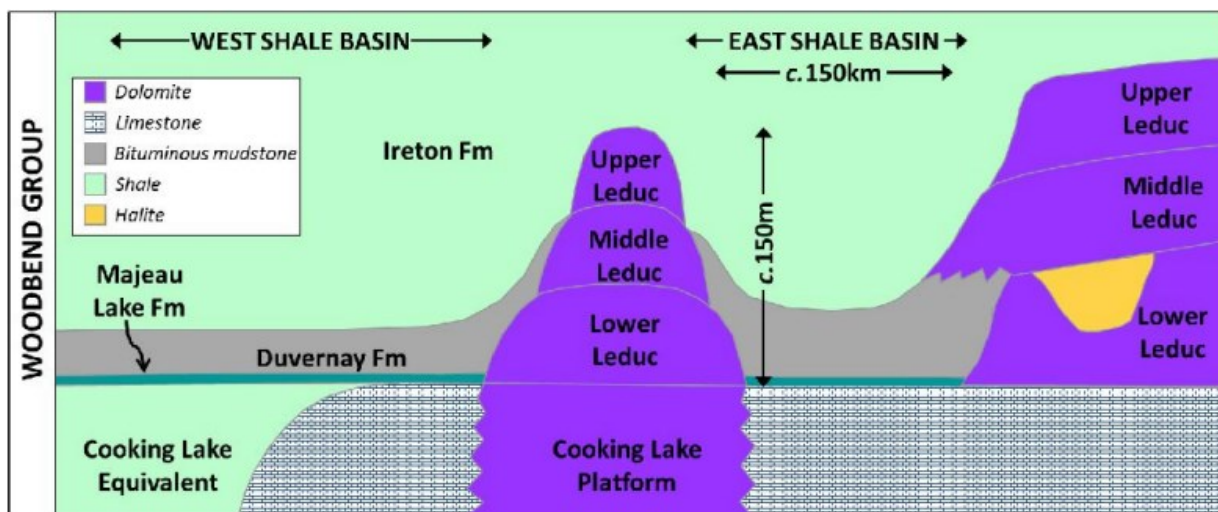


Fig. 2.3. Schematic depositional model of the Woodbend Group in the Central Alberta, after Fothergill et al. (2014), Switzer et al. (1994), and Dunn et al. (2012).

Sequence stratigraphy is a valuable tool for foreseeing how sedimentary bodies are distributed in space and understanding the relationships between them (Knapp et al., 2017). Catuneanu et al., (2009) defined a sequence as “a succession of strata deposited during a full cycle of change in accommodation or sediment supply”. Three third-order depositional sequences DS1-DS3 are recognized in the Duvernay Formation (Fig. 2.5), bounded by sequence stratigraphy boundaries SB0-SB3 (Knapp et al., 2019; Shaw and Harris, 2022). The depositional sequences are distinguished by different facies stacking patterns. Five lithofacies were described in the Duvernay Formation including planar-laminated silt, wavy-laminated sand and silt, bioturbated silt, fossiliferous and carbonate-rich nodular wackestones (Knapp et al., 2017; Shaw, 2020; Shaw and Harris, 2022). Also, five lithofacies in the Duvernay were identified by other

authors (Venieri et al., 2021) using core data and well logs, including a) organic rich black siliceous mudstones, b) carbonate-rich mudstones, wackestones, and packstones, c) organic-poor clay-rich mudstones, d) organic-rich clay-rich mudstones, and e) interbedded silica-rich and carbonate-rich mudstones.

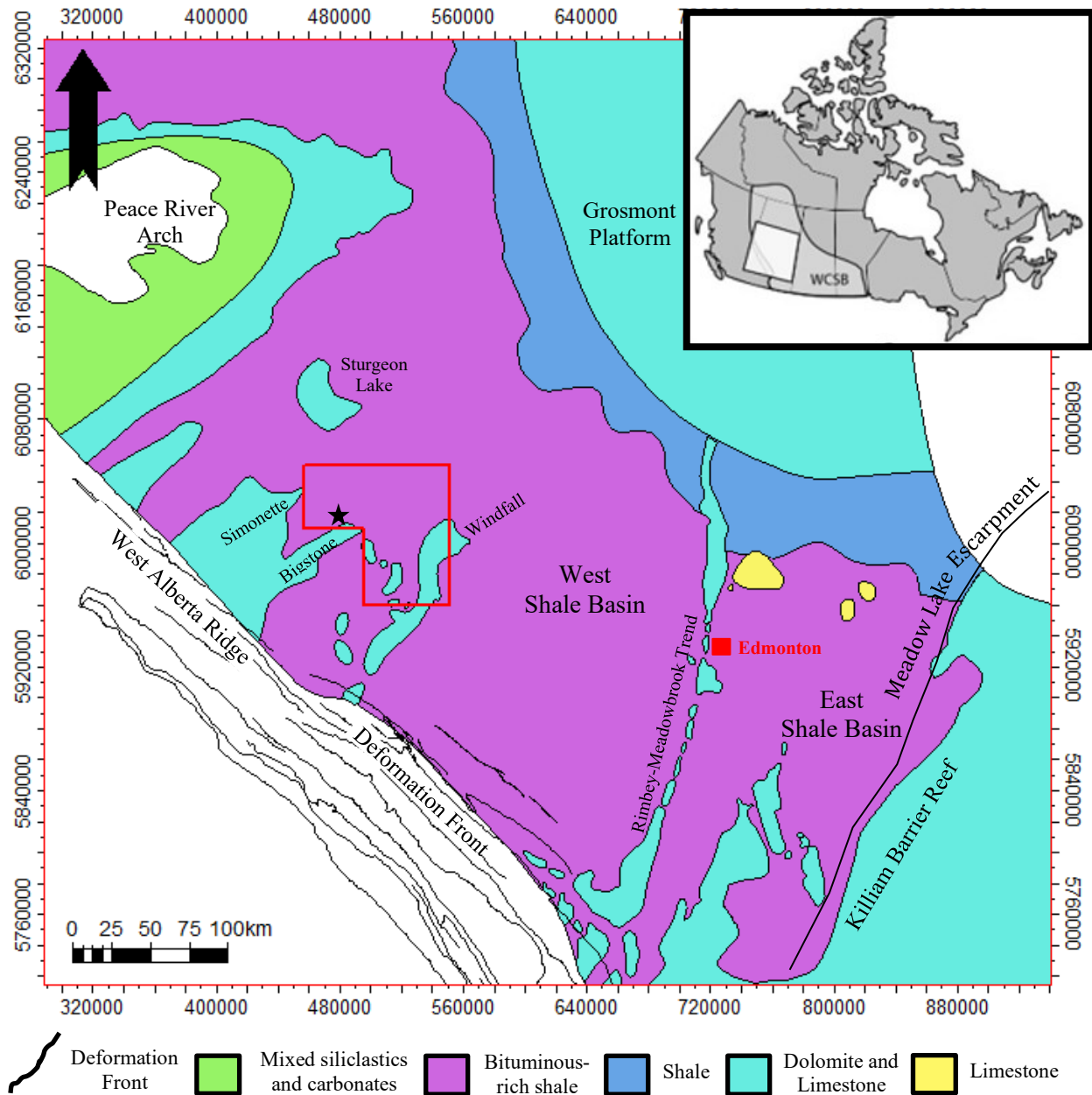


Fig. 2.4. Map of lithofacies of Upper Devonian Duvernay Formation and contours of reefs of the Woodbend Group, after Switzer et al. (1994; 2008). Faults of the deformation front of the Canadian Rocky Mountains are shown after Hamilton et al. (1999). The shapefiles were downloaded from the AGS website <http://www.ags.gov.ab.ca/publications/>. The location of the study area in the Kaybob area is shown by red polygon. The black star shows the location of the well from Fig. 2.5. The inset map shows the location of the map in the Western Canada Sedimentary Basin. Coordinate system UTM NAD83 zone 11 N.

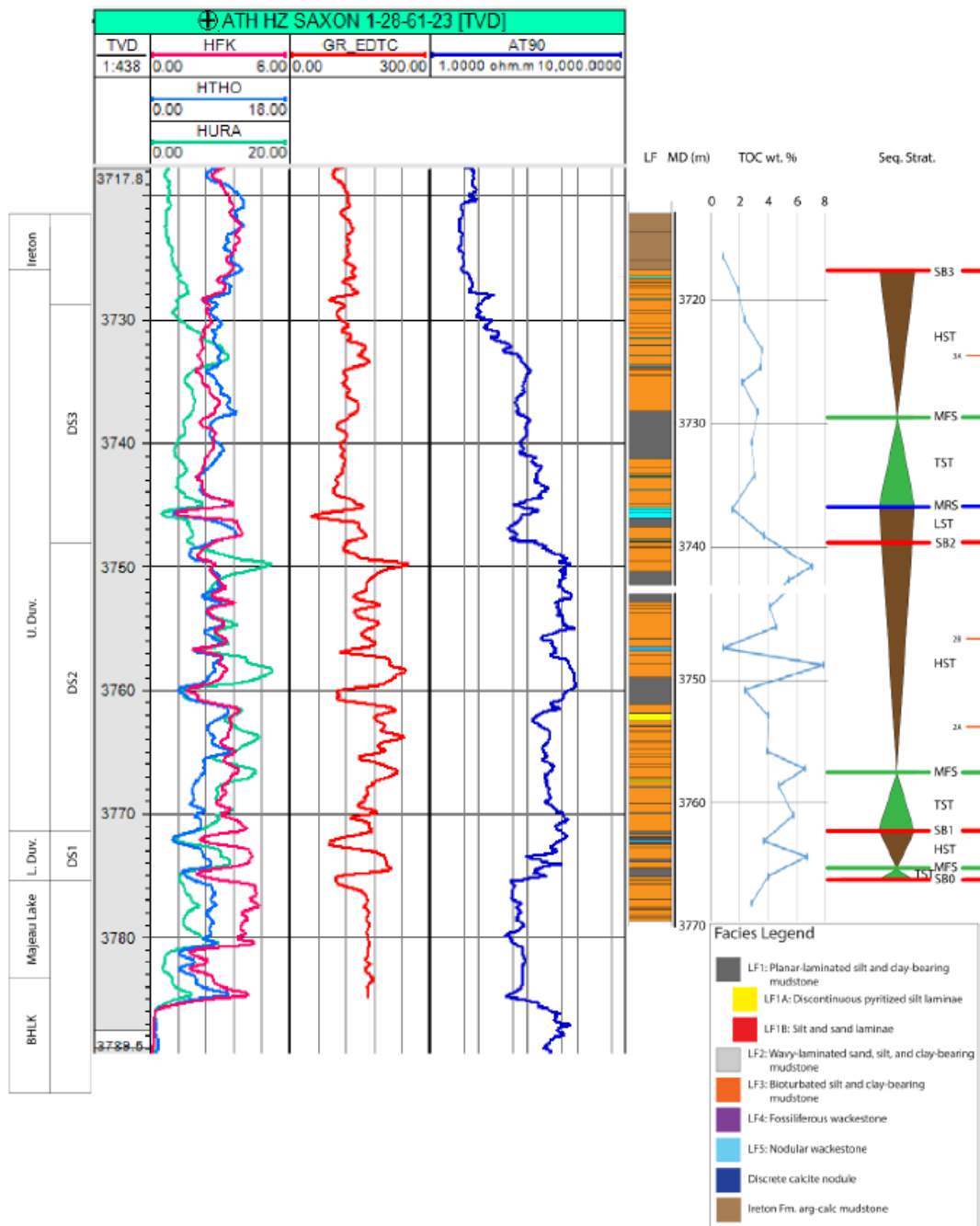


Fig. 2.5. Log plot for well MURPHY SAXON 1-28-61-23 displaying tracks from the left to the right: subdivisions of the Duvernay Formation, measured depth (m, KB), spectral gamma, gamma, and deep resistivity logs, interpretation of lithofacies, measured TOC and sequence stratigraphic interpretation, after Shaw (2020). The location of the well is shown in Fig. 2.4.

Highstand systems tracts (HST), transgressive systems tracts (TST) and lowstand systems tracts (LST) were described in the Duvernay Formation (Knapp et al., 2019; Shaw and Harris, 2022). The LSTs are limited by sequence boundaries (SB) at the bottom and maximum regressive surfaces (MRS) at the top. The TSTs are bounded by SB or MRS at the bottom and maximum flooding surface (MFS) at the top. The HSTs are bounded by MFS at the bottom and SB at the top. Highstand deposits include coarse-grained, carbonate-rich, organic-poor bioturbated facies; transgressive deposits are described as fine-grained, biosiliceous, organic-rich facies; and lowstand deposits mainly composed of detrital, clay-rich, bioturbated facies (Shaw and Harris, 2022). Depositional sequences DS1 and DS2 are composed of transgressive systems tracts (TST), which are overlain by highstand systems tracts (HST). Depositional sequence DS3 is composed of three systems tracts interpreted as lowstand systems tract (LST) followed by transgressive systems tract (TST) and highstand systems tract (HST) (Shaw and Harris, 2022).

The distribution of these facies is not homogeneous across the Kaybob area. Carbonate-rich nodular wackestones are commonly found close to the Grosmont platform slope in the northeast of the area and nearby the Leduc reefs in the southwest. Organic-rich planar-laminated mudstones are dominant in the center of the Kaybob area (Fig. 2.4 and 2.7), while bioturbated facies are more abundant closer to the reefs (Shaw and Harris, 2022). During the Duvernay deposition, the depocenter was in the middle of the Kaybob area, between Simonnette, Bigstone, Windfall and Sturgeon Lake reefs (Shaw, 2020).

2.2. Paleogeography of the Duvernay Formation

The Duvernay Formation was deposited in the Late Devonian (Frasnian), when the global sea level was high (Johnson and Klapper, 1985; Savoy and Mountjoy, 1995; Haq and Schutter, 2008) and a large epicontinental sea covered most of the western Canada (Fig. 2.6). Other organic-rich black shales found in North America, such as the Muskwa Formation, New Albany Shale, Woodford Shale, Chattanooga, and Rhinestreet are time-equivalent to the Duvernay Formation (Campbell, 1946; Schieber, 1998a; Lash and Blood, 2006; Ferri et al., 2011; Harris et al., 2018).

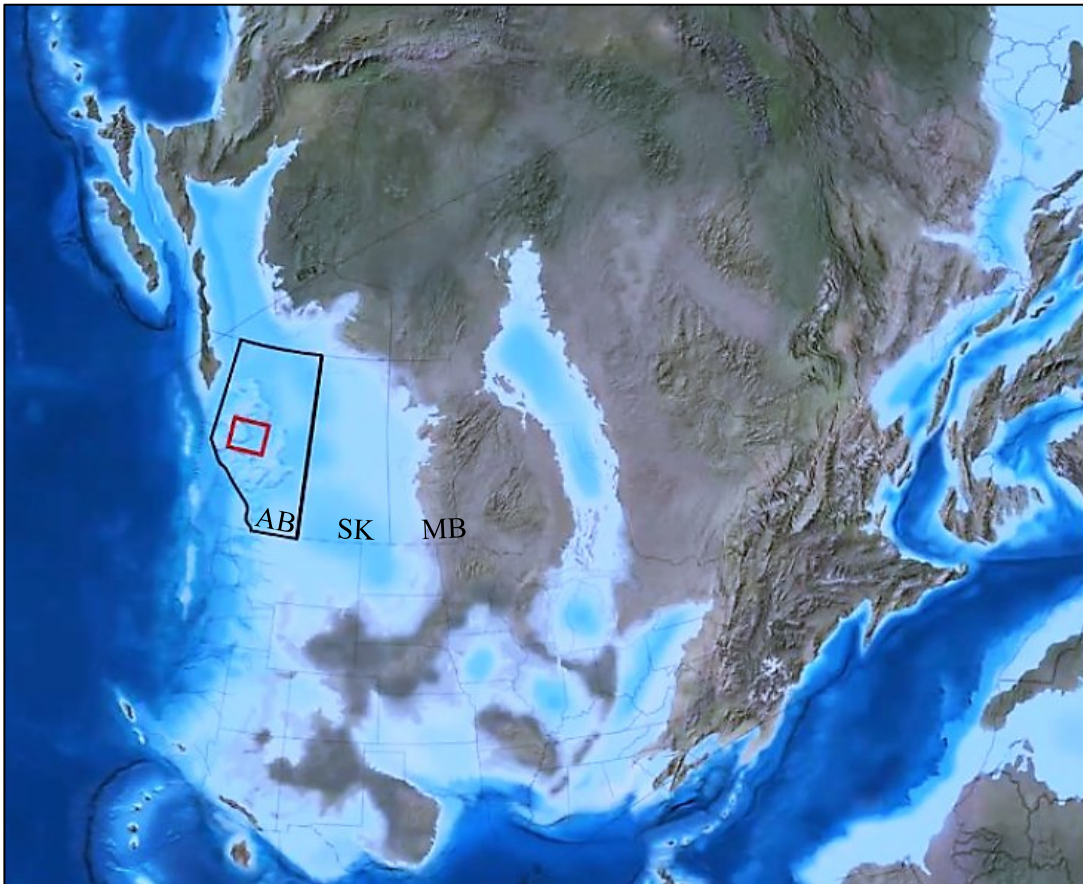


Fig. 2.6. Late Devonian paleogeography, approximately 375 m. a. after Blakey (2013). In red, the area of study is highlighted. AB: Alberta; SK: Saskatchewan; MB: Manitoba.

The sedimentary rocks of the Duvernay formation were deposited in the Alberta basin, located on the western margin of North America. At that time, carbonate platforms and reefs dominated the area, with basinal shales accumulated in the inter-reef areas. These reefs acted as a barrier to water circulation during the Devonian, which created the favorable conditions for organic matter preservation (Fothergill et al., 2014). Several significant tectonic structures

influenced the deposition of the sediments, including the Peace River-Athabasca Arch, the West Alberta Ridge, the Rimbey Arc, and the Meadow Lake Escarpment (Fig. 2.4) (Switzer et al., 1994). The Peace River Arch was a landmass positioned northwest of the Alberta Basin and surrounded by Leduc reefs (Dix, 1990). The Rimbey Arc, a paleobathymetric high trending from northeast to southwest, acted as a linear boundary composed of Leduc reefs separating the East and West Shale Basins during the Frasnian (Switzer et al., 1994; Rokosh et al., 2012; Preston et al., 2016). The Meadow Lake Escarpment was a pre-Devonian uplift that during the Frasnian formed the base of the Killiam Barrier Reef at the eastern boundary of the East Shale Basin and represented the farthest limit of Duvernay deposition (Switzer et al., 1994; Oldale and Munday, 1994). The increase in the sea level was favorable for the accumulation of organic-rich facies of the Upper Devonian Duvernay Formation in the Kaybob area (Shaw and Harris, 2022). At the same time, marine shales were deposited in British Columbia and Northwest Territories, while dolomites and evaporites were deposited in Saskatchewan and Manitoba (Ziegler, 1967; Switzer et al., 1994; Weissenberger, 1994). The Duvernay Formation marks the time of accumulation and preservation of organic-rich shale facies. This reflects a major change in the stratification and oxygenation of basinal waters during the maximum transgressive stage of the Woodbend Group (Shaw, 2020).

According to depositional models for the Upper Duvernay Formation (Knapp et al., 2017; Shaw, 2020; Shaw and Harris, 2022), depositional sequence DS1 (Fig. 2.7) corresponds to the development of the Grosmont Platform, where sediments prograded to the southwest, in the direction perpendicular to the platform. Depositional sequences DS2 and DS3 correspond to the early-flooded phase of the platform, where sediments prograded from the Grosmont Platform in the direction parallel to the platform, towards the southeast (Shaw and Harris, 2022). The Grosmont Platform construction stage was characterized by the development of shallow-water carbonate platforms. These platforms were formed through the accumulation of carbonate sediments in a relatively high-energy environment. The deposition of carbonate mud, skeletal fragments, and microbial buildups contributed to the construction of these platforms. The Flooded Platform stage was characterized by a transition to a flooded platform setting. Rising sea levels led to the submergence of the carbonate platforms, resulting in the deposition of fine-grained sediments composing organic-rich mudstones and shales. These sediments were

deposited in a lower-energy environment characterized by reduced oxygen levels. The controlling factors of the distribution of facies are related to the paleogeography and the changes in the relative sea level (Shaw and Harris, 2022).

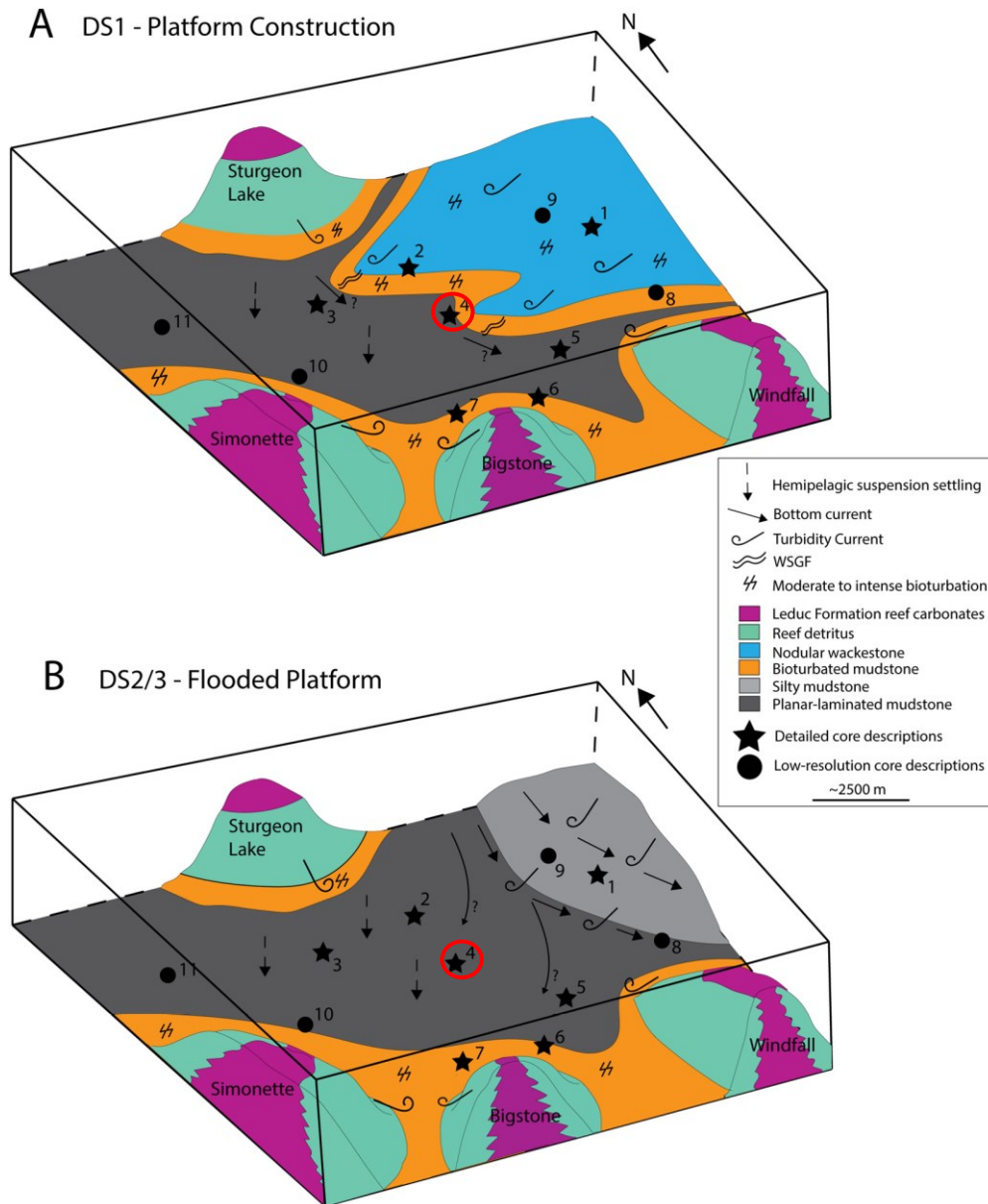


Fig. 2.7. Depositional model proposed for the Duvernay Formation in the Kaybob Area, focusing on two stages: A) the construction of the Grosmont Platform, and B) the subsequent flooding of the Grosmont Platform, after (Shaw, 2020; Shaw and Harris, 2022). See name and UWI of wells in Table 2.1. The red circle shows the location of well 4 that is studied in this thesis.

Code	Well Name	UWI
1	MURPHY TWOCK	100/04-21-064-16W5/00
2	MURPHY 04-32A KAYBOB	100/04-32-064-20W5/00
3	CPEC MCKINLEY	100/04-19-064-22W5/00
4	SCL HZ KAYBOB	100/02-22-063-20W5/00
5	TQN FOXCK	103/16-25-061-19W5/00
6	CPEC KAYBOBS	100/06-16-060-20W5/00
7	MURPHY SAXON	100/01-28-061-23W5/00
8	Bounty Wind	100/11-34-061-15W5/00
9	APL(98) Kaybob	100/14-09-065-17W5/00
10	Murphy Simon	100/01-12-064-25W5/00
11	CVE HZ KARR	102/09-25-065-27W5/00

Table 2.1. Code, names and UWI shown in Fig. 2.7 after Shaw, (2020); Shaw and Harris, (2022).

2.3. The tectonic structure of the Alberta Basin

The Alberta Basin is composed of Cenozoic, Mesozoic, and Paleozoic deposits, separated from the Precambrian basement with an angular unconformity. The Precambrian basement below the Paleozoic-Cenozoic sedimentary succession of the Western Canada Sedimentary Basin is heterogeneous, and includes different terrains (Chacko et al., 2000; Aulbach et al., 2004; Corrigan et al., 2005; Hajnal et al., 2005) separated by the crustal lineaments (Sami and James, 1993; Ross et al., 2000). Some of the lineaments likely influence tectonic structure, heat flow distribution and tectonic evolution of the sedimentary cover (Burwash et al., 1994; Yeates et al., 2022).

The sedimentary succession of the Alberta Basin dips at $\sim 5^\circ$ to the W-SW (Fig. 2.8) below the Foothills and Rocky Mountains (Switzer et al., 1994). The thickness of the sedimentary cover of the basin increases from the Canadian Shield in the northeast to the

southwest, reaching ~5500 meters below the Foreland fold-and-thrust belt (Hamilton et al., 1999; Reiter and Heidbach, 2014). In the study area (Fig.2.1), the average elevation is 850 meters above sea level, and thickness of the sedimentary cover varies from ~3500 meters in the WSW to ~2500 m in the NE (Hope et al., 1999, Wright et al., 1994). The change in thickness across the basin can be explained through a combination of processes of subsidence, uplift and erosion occurred during different phases of deformation that are considered in section 2.5.

The high-angle normal and strike-slip faults are interpreted in the Precambrian basement and Paleozoic deposits of the sedimentary succession of the Alberta Basin based on the interpretation of 2D and 3D seismic surveys (Hope et al., 1999; Barrett, 2014; Wang et al., 2017; Corlett et al., 2018; Schultz et al., 2017; Eaton et al., 2018; Konstantinovskaya et al., 2021). The normal faults were interpreted in 2D seismic lines in the Peace River Arch area (Hope et al., 1999), referred as the Dawson Creek Graben Complex (Barclay et al., 1990). These faults strike NW-SE and NE-SW and form a series of grabens and halfgrabens (Fig. 2.9.A and B). The normal faults in the Peace River Arch area are subvertical and offset the Precambrian basement, Paleozoic and, locally, Triassic units for about 20-40 ms TWT with syn-depositional thickness changes, likely remaining active from the Devonian through to Triassic (Hope et al., 1999). To the south of Calgary, the high-angle NW-SE striking normal faults were interpreted in subsurface of the southern Alberta Basin (Lemieux, 1999; Hope et al., 1999). These faults displace the basement and the sedimentary succession up to the Upper Cretaceous Second White Specks Formation for about 110 m to 235 m and may be related to younger period of extension during the pre-Belly River (Campanian) time (Lemieux, 1999; Hope et al., 1999).

The high-angle normal and transtensional strike-slip faults were interpreted in 3D seismic surveys in the Kaybob (Fox Creek) area (Wang et al., 2017; Eaton et al., 2018; Konstantinovskaya et al., 2021). These faults are generally characterized by the NE-SW, NW-SE and N-S strike and in some cases interpreted as transtensional strike-slip fault systems. According to this interpretation, a master strike-slip fault in the basement is subsequently replaced by a series of transtensional faults, giving rise to a negative flower structure in the Paleozoic rocks, including units of the Swan Hills Group and Duvernay Formation.

The geometry and kinematics of the normal faults that displace the Precambrian basement and lower interval of sedimentary cover are consistent with formation of the faults under an extensional or transtensional tectonic regime (Gibbs, 1984; Peacock et al., 2016). It was suggested that some of the high-angle normal faults might have been associated with reef growth and other morphological features of the platform such as channels and embayments (Corlett et al., 2018). The example of the Gold Creek Gas Field shows that normal faults may also form in Upper Devonian-Mississippian carbonate rocks above Leduc reef structures as a result of structural sagging and reef collapse with negative relief of the top Wabamun structure reaching up to 160 m (Barrett, 2014). The mechanism of the collapse is interpreted to be differential compaction within the underlying Upper Devonian Leduc reef.

A variety of salt and carbonate dissolution features are present in the Alberta basin, and karst topography is present on several erosional surfaces (Pana et al., 2021). Dissolution of Devonian upper Elk Point Group salt has occurred around reefs of similar age. The timing of dissolution varies and has been interpreted from seismic and subsurface well information. Dissolution of Devonian salt is also interpreted at the sub-Mesozoic unconformity that controls, to some extent, the variation in the thickness of overlying Cretaceous strata as well as the relief on post-Cretaceous surfaces in the eastern and northeastern Western Canada Sedimentary Basin (Pana et al., 2021).

The NW-SE striking low-angle to flat blind thrust faults were interpreted in the sedimentary succession in the western segment of the Western Canada Sedimentary Basin, closer to the deformation front (Xiao and Unsworth, 2006; Hart et al., 2007; Riazi and Eaton, 2020). The detachment occurs at the lower interval of the Upper Cretaceous Kaskapau Formation, causing fault-related folds in the Cardium Formation and overlying units (Hart et al., 2007). The displacement is < 25 ms and several fault splays diverge from the main detachment fault. Another low-angle detachment level in the western Alberta Basin is associated with siltstones the Mississippian Banff Formation, along which thrusts faults propagate and cut upward into the Debolt and Mountney Formations with vertical offset of 30 m – 200 m (Riazi and Eaton, 2020)

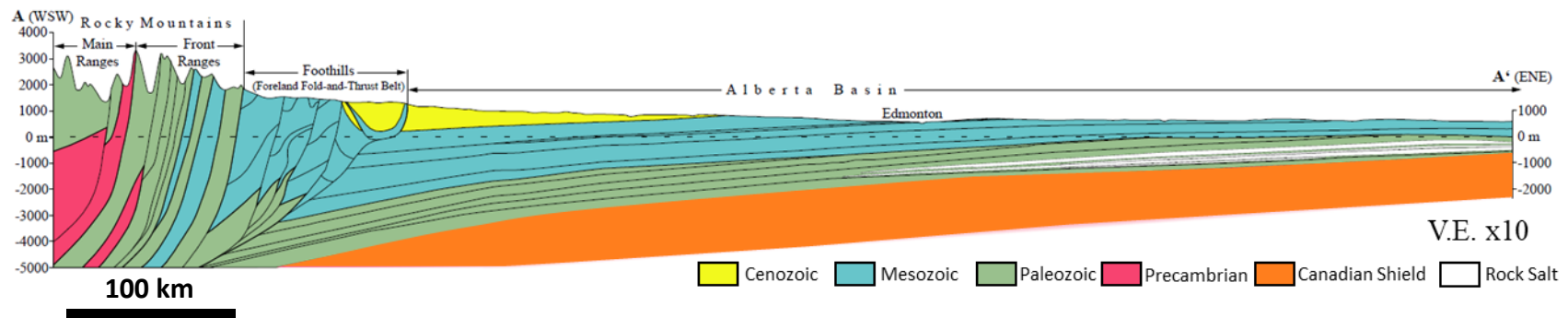


Fig. 2.8. The WSW-ENE regional structural cross-section across the Canadian Rocky Mountains Fold and Thrust Belt, Foothills and the Alberta Basin, modified after Reiter and Heidbach (2014) and Hamilton et al. (1999), Map No: 236.

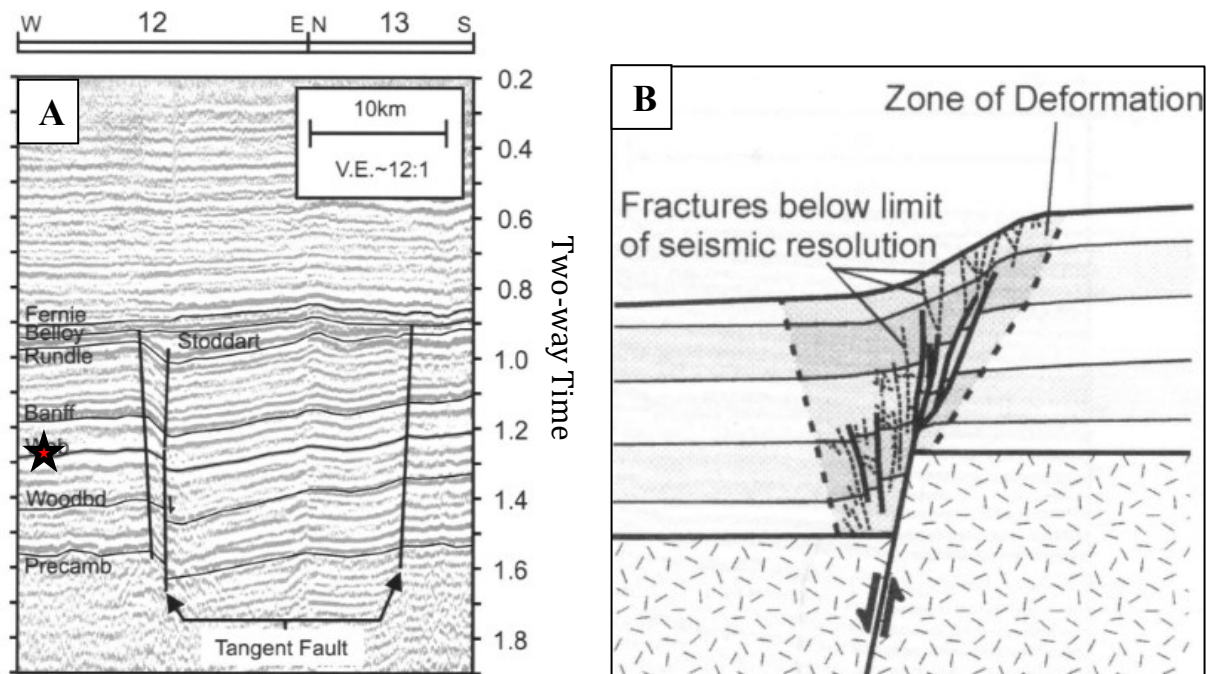


Fig. 2.9. Examples of the subsurface high-angle normal faults in the Alberta Basin. A) Normal faults mapped in the Peace River Arch area displace Precambrian basement and Paleozoic sedimentary cover, after (Hope et al., 1999). The red star shows the interval with the Duvernay Formation. Precamb: Precambrian; Woodbnd: Woodbend; Wab: Wabamun. B) Schematic illustration of fold and fracture zones developed in the sedimentary cover above a steep normal fault in basement, based on physical modeling experiment, after (Withjack et al., 1990).

2.4. Tectonic evolution of the Alberta Basin

The Paleozoic to Middle Devonian sedimentary succession of the Alberta Basin was accumulated on the passive continental margin (Figs 2.6, 2.10), formerly recognized as Cordilleran miogeocline (Price, 1994; Pana et al., 2021). The isostatic subsidence of the lithosphere in the passive margin occurred in response to the loading of the overlying sedimentary cover and gradual increase of the cumulative thickness of lithified lower Paleozoic sedimentary deposits (Price, 1994). Early phases of deformation occurred in the Cordilleran margin during the Late Silurian, Early and Middle Devonian (Root, 2001). During the Devonian to Mississippian, general tectonic settings in western Canada are interpreted as regional extension related to slab rollback caused back-arc and intra-arc spreading (Nelson et al., 2002).

During the Antler orogeny (Late Devonian to Mississippian), the Alberta Basin is interpreted to have been transformed into a distal foreland basin (Root, 2001). The Antler fold and thrust belt and foreland basin development may have occurred along the length of the Canadian portion of the ancient Cordilleran continental margin during the Devonian and Mississippian (Root, 2001). The mid-Paleozoic (Late Devonian) increase in the subsidence rate in the basin may have been influenced by a combination of flexural loading by thrust sheets and foreland basin strata and horizontal in-plane stresses associated with the Antler convergent tectonics (Root, 2001). Synchronously, a large sea level rise relative to the cratonic platform resulted in the flooding of interior basins of North America (Fig. 2.10) (Bond and Kominz, 1991).

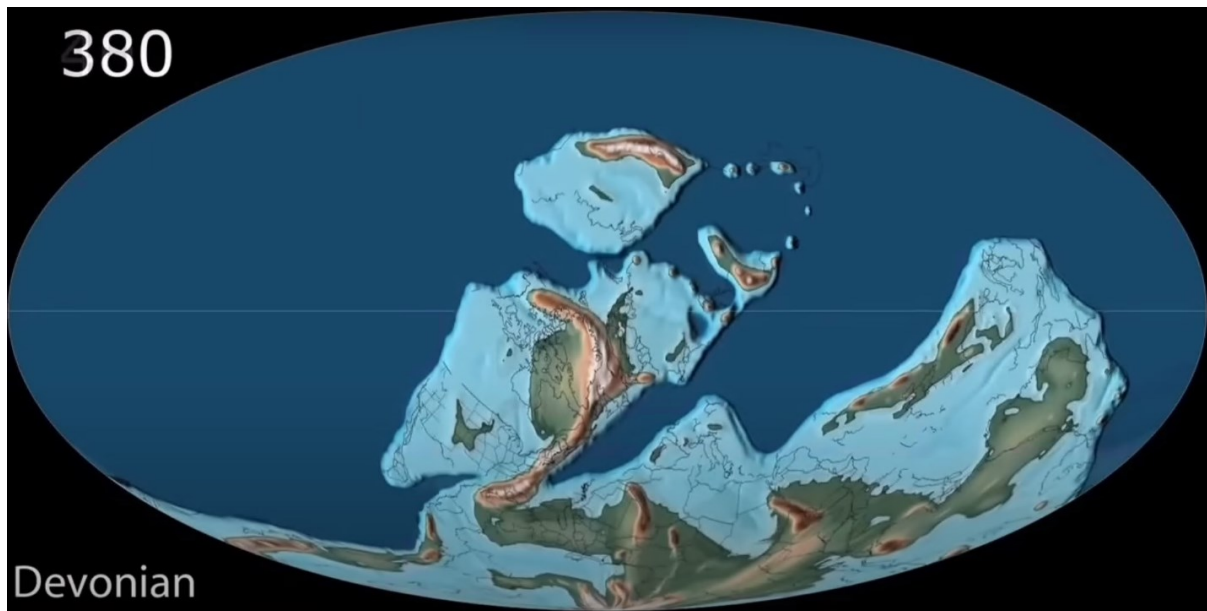


Fig. 2.10. Paleogeographic reconstruction for the Late Devonian (380 Ma), after Scotese (2016).

Screenshot from the animation taken from https://www.youtube.com/watch?v=g_iEWvtKcuQ

During the Columbian Orogeny (Middle Jurassic to Early Cretaceous), the Alberta Basin developed into a foreland basin (Fig. 2.11) due to the depression of the passive margin continental lithosphere by the Cordilleran deformation front (Pana et al., 2001; Pana et al., 2021). The change in tectonic settings is marked by the basin-scale sub-Oxfordian angular unconformity (Issler et al., 1999; Douglas and Stockmal, 1989; Pana, 2021).

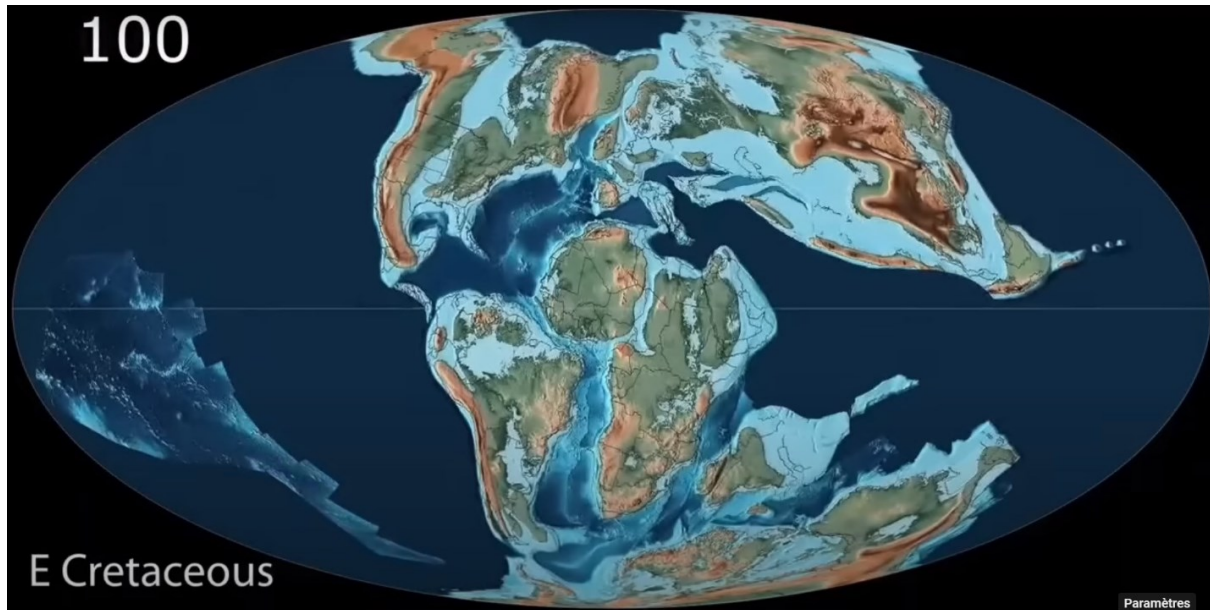


Fig. 2.11. Paleogeographic reconstruction for the Early Cretaceous (100 Ma), after Scotese (2016). Screenshot from the animation taken from https://www.youtube.com/watch?v=g_iEWvtKcuQ

During the Early Cretaceous, the forebulge development related to lithosphere flexure and tectonic loading of the proto-Rockies resulted in formation of regional sub-Cadomin unconformity (Pana, 2021). The location of the forebulge in the foreland basin formed in the Valanginian can be mapped as erosional highland areas in the Lower Mannville Cretaceous deposits known as sub-Cadomin-sub-Mannville unconformity (Pana, 2021). The Devonian, Mississippian, Triassic and Jurassic beds are exposed in the Keg River, Red Earth, Wainwright, Pembina highlands that form a zone of eroded highlands in the Lower Mannville paleogeography extending from the NW to the SE at a distance of ~250-325 km from the present-day deformation front (Smith, 1994; Hayes et al., 1994) (Fig. 2.12).

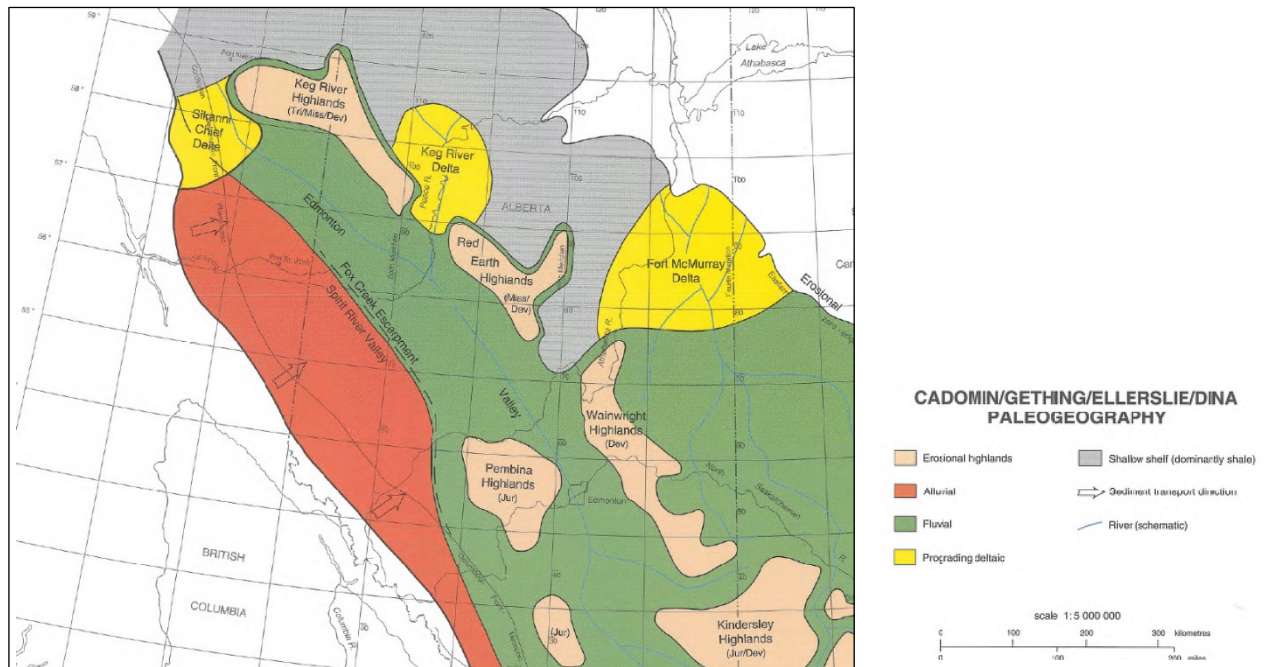


Fig. 2.12. Paleogeographic map for the Cadomin-Getting strata in the Alberta Basin, after (Smith, 1994). The chain of erosional highlands (Keg River, Red Earth, Wainwright, Pembina) may correspond to the location of forebulge extended NW-SE in the foreland basin and associated with lithosphere flexure and tectonic loading of the proto-Rockies (Pana, 2021).

During the Laramide orogeny (Late Cretaceous to Paleocene), the Alberta Basin developed as a foreland basin in front of the orogenic belt of the Rocky Mountains and Foothills. Shortening and thrusting in the orogenic belt occurred in tectonic pulses from the west to the east as supported by the $^{40}\text{Ar}/^{39}\text{Ar}$ dating of the fault rocks (Pana, 2021). Five pulses took place during the Cretaceous, including: 1) Valanginian (136-133 Ma), 2) Barremian - Aptian (128-123 Ma), 3) Albian - Cenomanian (113 – 96 Ma), 4) Santonian - Coniacian (87 – 85 Ma), 5) Campanian – Maastrichtian (79 – 68 Ma) and one in the Paleocene (64 – 55 Ma). The Southern Rocky Mountain Trench shear zone, the Walker Creek fault zone, and the Valmont strain zone are interconnected and were active during various strike-slip movements related to the previous described pulses (Pana, 2021). The Northern Rocky Mountain Trench, which is the continuation of the Southern Rocky Mountain Trench shear zone, is characterized by more than 450 km of right-lateral displacement during the Late Cretaceous and Early Paleocene (Roderick, 1967; Price, 1994). Transpressional settings are also reconstructed by the post-Eocene dextral strike-

slip reactivation of pre-existing normal faults in the Southeastern British Columbia. The brittle dextral strike-slip faults cut the Eocene extensional shear zones (Finley, 2020). The orientation of shortening in the eastern margin of the Canadian Rockies during the Laramide orogeny is NE-SW/ E-W, based on structural indicators in main thrust sheets that are oriented NW-SE/N-S (Dahlstrom, 1970; Jones and Workum, 1978; Spratt et al., 2004).

The subsidence of the Alberta foreland basin (Fig. 2.13) resulted from the isostatic flexure of the North America lithosphere under the weight of the foreland fold-and-thrust belt emplaced during the Laramide orogeny (Price, 1973; 1994; Wright et al., 1994; Switzer et al., 1994). The Alberta foreland basin was shaped through the downward bending of the Canadian Shield caused by the weight of the overlying lithosphere, coupled with isostatic lithosphere flexure (Leckie and Smith, 1992; English and Johnston, 2004) and accumulation of sediments transported from the Canadian Cordillera (Gabrielse and Yorath, 1989).

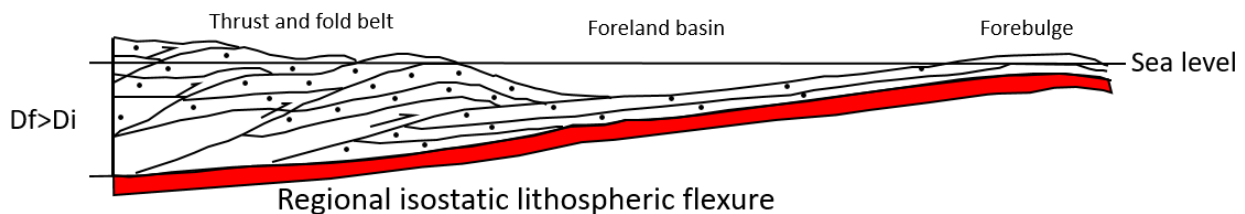


Fig. 2.13. Conceptual model of the formation of the foreland basin by isostatic flexure of the continental lithosphere in response on the emplacement of the orogenic belt, after Price (1994). D_f , D_i , final and initial depth of basement.

The maximum burial of the sedimentary cover in the Alberta Basin occurred at ~ 60 Ma, as discussed in section 2.4 (Issler et al., 1999). It was followed by an uplift linked to Laramide orogeny at around 48 Ma as reconstructed from the analysis of the vitrinite reflectance data (Kalkreuth and McMechan 1988; Woodland and Bell 1989; Issler et al. 1999). During the Tertiary, the tectonic uplift in the eastern edge of the Foothills consisted of about 3 km, and the amount of erosion ranged from approximately 500-900 m in the east to around 1400 m to 3000 m in the west of the basin (Magara, 1978; Nurkowski, 1984; Woodland and Bell, 1989; Kalkreuth and McMechan, 1988, 1996). The amount of erosion was interpreted from organic maturation indices based on the moisture content of coals from the Belly River Group, Horseshoe Canyon and Wapiti Formations and Scollard Member of the Paskapoo Formation.

The sedimentary beds of different ages are exposed at the present-day erosional surface in the Alberta Basin (Hamilton et al., 1999), e.g., Upper Cretaceous deposits in the west and Lower Cretaceous beds in the east of the basin. In the NE, close to the erosional boundary with the Canadian Shield, Devonian formations are exposed (Issler et al., 1999; Hamilton et al., 1999). Non-marine Neogene fluvial and Quaternary glaciogenic deposits, and postglacial sediments are characterized by variable thickness and distribution (less than 1 m to 360 m) (Atkinson et al., 2020).

2.5. Geochemistry, thermal maturity and burial history of the Duvernay Formation

The depth of top of the Duvernay Formation ranges from 600 m in the NE area of the East Shale Basin to 5000 m in the W-SW area of the West Shale Basin (Fig. 2.14.A).

The total organic carbon (TOC) content in the mudrocks of the Duvernay Formation is highly variable depending on facies distribution. TOC of the net thickness of the Duvernay Formation was estimated using geophysical well logs (Lyster et al., 2017) using Passey's method (Passey et al., 1990). The TOC lowest values (0.2 to 1 wt.%) are typical in the northeast of the West and East Shale basins, close to the Grosmont Platform (Fig. 2.14.B). The higher TOC values (3-5 wt.%) are interpreted along the NW-SE median line in the West Shale Basin. In the Kaybob area, the TOC is high, ranging from 2.6 wt.% to 5 wt.%.

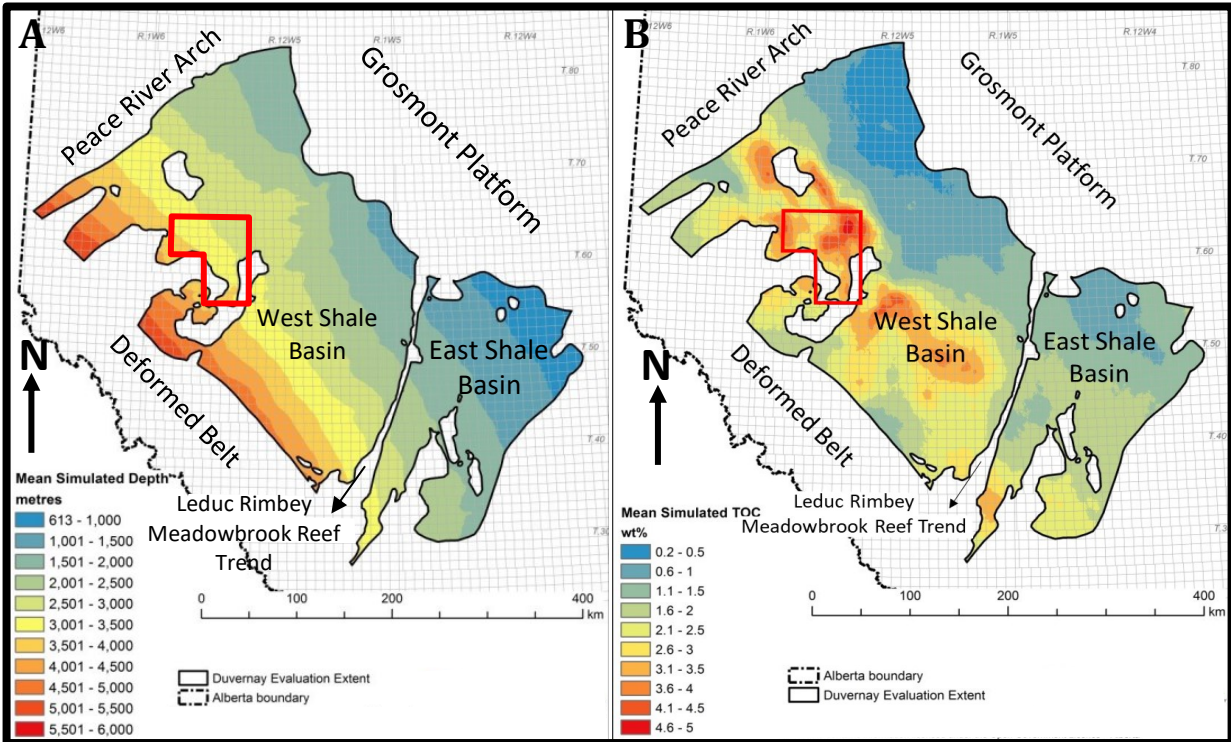


Fig. 2.14. A) Top of the Duvernay Formation after (Lyster et al., 2017). B) Mean simulated TOC (wt%) in the Duvernay Formation, after (Lyster et al., 2017). The red polygon outlines the area of study.

The vitrinite reflectance (R_o) of the organic matter of the Duvernay Formation ranges from 0-0.8% in the east-northeast, close to the Grosmont carbonate platform to 1.21-2% in the west-southwest, close to the deformation front (Rokosh et al., 2012). The general trend of increasing R_o values to the southwest correlates with the amount of subsidence (Fig. 2.14.A) and different degree of thermal maturity of the Duvernay shales (Fig. 2.15). Thermal maturity of the organic-rich shales generally increases from immature in the east-northeast to oil and condensate zone in the middle of the basin to dry gas in the west-southwest (Rokosh et al., 2012, Preston et al., 2016, Lyster et al., 2017). However, there is an anomaly in the general maturity trend. The recent study of NMR spectroscopy and Rock-Eval Tmax data indicate there is an increase in maturity of the shales of the Duvernay Formation within the Willesden-Green area (Yeates et al., 2022), the origin of which is poorly understood. The Willisden-Green high maturity anomaly may be related to the fluid migration controlled by the Snowbird Tectonic Zone in Precambrian

basement. Another possibility is that the Kaybob and Willesden-Green areas of high maturity might have different burial histories, although that remains arguable (Yeates et al., 2022).

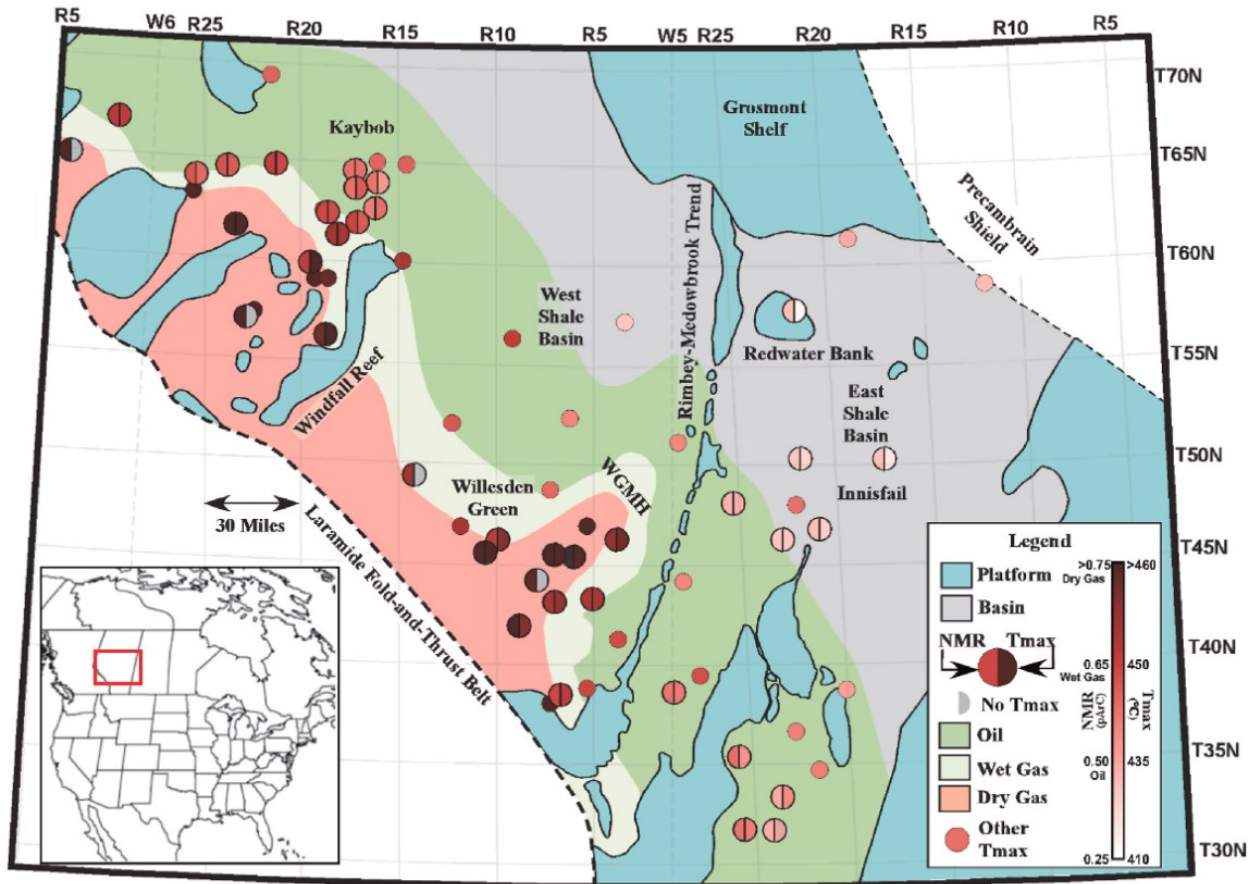


Fig. 2.15. Map of thermal maturity zones of the Duvernay Formation of peak oil (T_{max} of ~ 435 °C), peak wet gas (T_{max} of ~ 450 °C), and peak dry gas (T_{max} of ~ 460 °C) maturity, after (Yeates et al., 2022). Filled circles shows the Nuclear Magnetic Resonance and T_{max} measurements (see legend). WGMH, Willisden-Green maturity high.

This increase in maturity of the Duvernay shales is usually associated with the structural trend of the burial to a greater depth towards the WSW (Fig. 2.14.A) (Rokosh et al., 2012; Yeates et al., 2022).

The burial history of the Devonian rocks in the Alberta Basin (Fig. 2.16) was reconstructed based on studies of isotope and geochemical composition of fluids in Middle-Upper Devonian dolomites (Green and Mountjoy, 2005; Stacey et al., 2020). The burial and basin fluid flow occurred during several main deformation phases described in section 2.5. The

early (shallow) burial phase (0 - 1500 m) is related to the Antler tectonic phase from the Late Devonian to the Mississippian. Temperatures of 45°C to 75°C typical for pervasive dolomitization would have been reached during the late Devonian to Jurassic, at burial depths of about 700 m to 1500 m (Green and Mountjoy, 2005). The intermediate phase (~ 1500 – 2500 m) is associated with the Columbian orogeny from the Late Jurassic to Early Cretaceous. The later (deep) burial phase (> 2500 m) is related to the Laramide Orogeny from the Late Cretaceous to Paleocene (Fig. 2.16). The maximum burial in the Alberta Basin occurred at about 60 Ma based on the results of apatite fission track analysis for Cretaceous, Paleozoic and Precambrian borehole samples along two major transects through the Western Canada Sedimentary Basin (Issler et al., 1999). The Duvernay Formation in the center of the West Shale Basin reached the oil window (60°C - 150°C) at about 70-80 Ma ago and the gas window (120°C - 150°C) at about 50 Ma ago based on the basin modeling (Creaney et al., 1994; Wang et al., 2018). Burial history curves in Devonian rocks shows deeper subsidence in the West Shale Basin, compared to the East Shale Basin and Peace River Arch (Figs 2.14, 2.16). In the eastern Foothills, the amount of subsidence was even higher (Fig. 2.16) than in the West Shale Basin, reaching up to 9 km during the Laramide Orogeny (Price, 1994).

Two main different stages of fracturing were interpreted in carbonate rocks of the Leduc, Swan Hills Formation and Wabamun Group that have occurred during different burial phases (Green and Mountjoy, 2005; Stacey et al., 2020). The first stage of fracturing is related to the early relatively shallow (1000 m – 1500 m) burial during the Antler orogeny (Late Devonian-Mississippian). The second stage of fracturing is associated with intermediate (1500 m – 2500 m) and deep (> 2500 m) burial during the Columbian and/or Laramide orogeny (Green and Mountjoy, 2005; Stacey et al., 2020). Based on normal geothermal gradient (30°C/km), the temperatures during the shallow burial would range between 25° C - 75° C, while the deep burial would be between 80° C - 190° C (Green and Mountjoy, 2005).

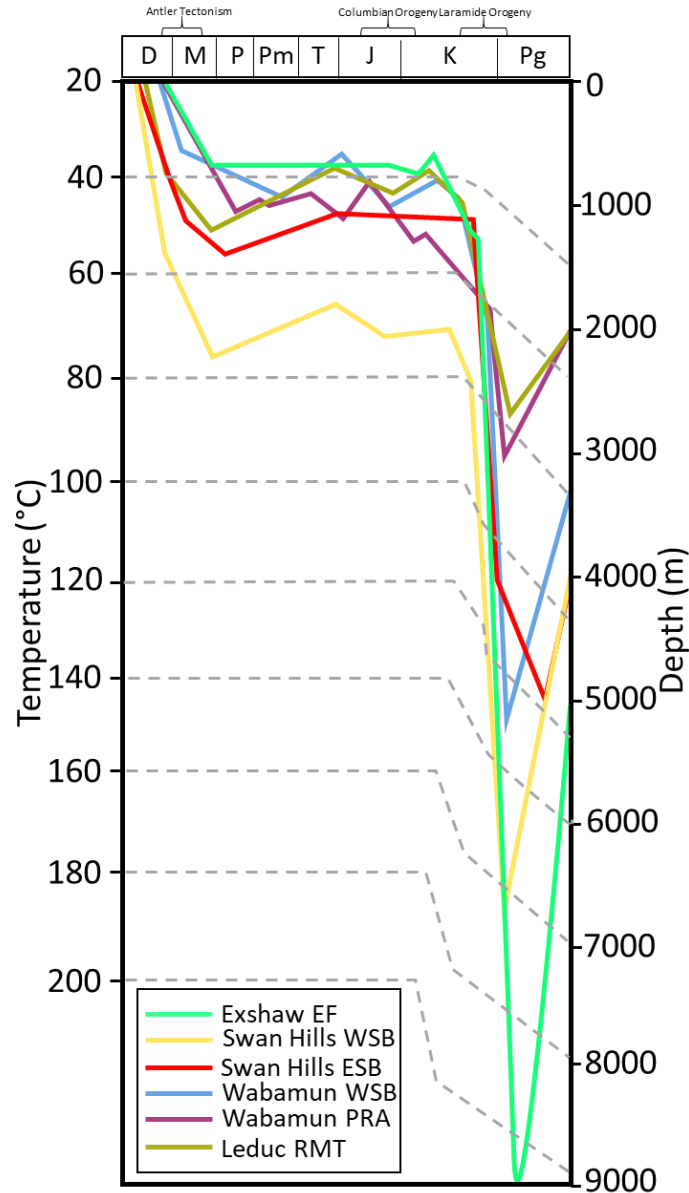


Fig. 2.16. Burial history for the Eastern Foothills (EF), Peace River Arch (PRA), West Shale Basin (WSB), East Shale Basin (ESB) and Rimbey Meadowbrook Trend (RMT), after Stacey et al. (2020). Burial curves are shown for the Swan Hills Formation in the WSB (Duggan et al., 2001) and ESB (Laflamme, 1990), Leduc Formation in the Rimbey Meadowbrook Trend (Amthor et al., 1993), Wabamun Group in the WSB (Green and Mountjoy, 2005) and in the PRA (Mountjoy and Halim-Dihardja, 1991), and the Exshaw Formation in the Eastern Foothills (Price, 1994). Two main episodes of subsidence are associated with the Antler phase of deformation in the latest Devonian – Mississippian and Laramide Orogeny in the Late Cretaceous to Paleocene.

The hydrocarbon generation in the Duvernay shale likely contributed to the generation of overpressure in the Kaybob area. In the West Shale basin, the formation pressure of the Duvernay Formation is highly variable, going from high overpressure in the west (pressure gradient up >20 kPa/m), to hydrostatic in the east (pressure gradient <10 kPa/m) (Eaton and Schultz, 2018; Lyster et al., 2017). In the area of study, the pressure gradient varies from >20 kPa/m in the west to 10-16 kPa/m in the east (Fig. 2.17).

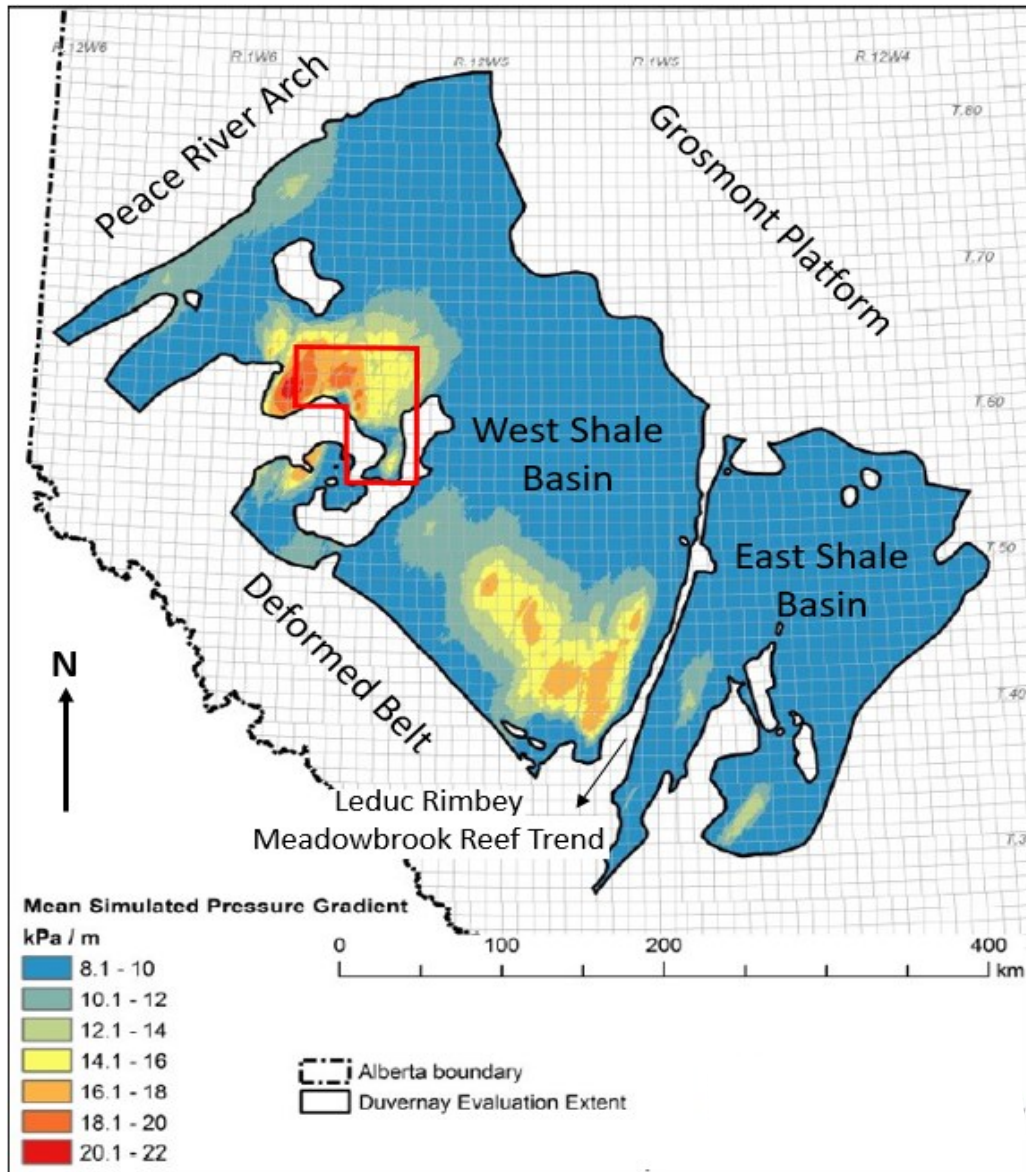


Fig. 2.17. Mean simulated pressure gradient (kPa/m) in the Duvernay Formation, after (Lyster et al., 2017). The red polygon shows the study area.

2.6. Mechanical properties of Duvernay shales

The mechanical properties of the rocks, together with in-situ stress and pore pressure represent the parameters that control formation and propagation of natural fractures. The contrast between relatively more stiff and more ductile beds in the organic-rich shales, including the Duvernay Formation, control fracture height (Helgesen and Aydin, 1991; Younes et al., 2011; Philipp et al., 2013; Ferrill et al., 2014; Gale et al., 2014; Mackay et al., 2018). Bed thickness is a contributing factor in vertical fracture propagation and fracture intensity (Narr and Suppe, 1991). With the increase of thickness, fracture spacing increases and fracture intensity decreases (Ladeira and Price, 1981). Emplacement of fractures in the deformed beds can be strongly related to the structural position of beds, e.g., in the fold hinge zone, on the steep and shallow dipping fold limbs, or cut by a fault zone (Murray, 1968; Jamison, 2016).

The mechanical properties of rocks that are estimated from the core testing data or from well logs include elastic parameters (Young Modulus and Poisson Ratio) and strength parameters (Unconfined Compressional Strength UCS, tensile strength and angle of internal friction). The dynamic elastic parameters are estimated from the compressional and shear velocity and density data, the static elastic parameters are estimated from the laboratory triaxial tests at the formation pressure settings. In this work, Young's Modulus, Poisson's Ratio and Unconfined Compressional Strength are considered.

The mechanical properties of the sedimentary rocks of Duvernay Formation vary depending on the content of organic matter, carbonate, biogenic silica and siliciclastic components (Dong et al., 2018; Venieri et al., 2019). The upper and lower Duvernay Member, which are characterized by higher content of clay and organic matter show lower values of Young's Modulus and UCS, in contrast to the middle Duvernay Member that is characterized by the higher carbonate content (Soltanzadeth et al., 2015; MacKay et al., 2018; Konstantinovskaya et al., 2021). Previous studies have shown a correlation between rock composition and mechanical properties of rocks of the Duvernay Formation. According to Dong et al. (2018), clay is the main factor that affects the geomechanical properties in the Duvernay, which makes the rock more ductile. Young's Modulus and clay percentage show a negative correlation, meaning that the increase in clay content decreases the stiffness of the rock (Fox and Soltanzadeh, 2015). Carbonate minerals, like calcite, have the opposite effect on rocks that are stiffer with higher content of carbonates. As a result, the elastic and strength parameters, such as Young Modulus

(YM) and Unconfined Compressional Strength (UCS), will be higher in carbonate-rich facies and lower in clay-rich facies. Poisson's Ratio have a positive correlation with the calcium from ECS log reading and carbonate from core XRD measurements and tends to be lower in the upper and lower clay-rich Duvernay Members, if compared to the middle carbonate-rich Member (Venieri et al., 2019). Another component that affects the mechanical properties of shales is biogenic silica, which is represented by the radiolarians, sponges and diatoms preserved in the Duvernay mudrocks. The biogenic silica content has positive correlation with hardness of the Duvernay shales, while the detrital silica is characterized by a negative correlation with hardness of the rocks (Dong et al., 2017).

The amount and thermal maturity of the organic matter affects the mechanical properties of shales (Mba and Prasad, 2010; Emmanuel et al., 2016; Dong et al., 2017). An increase in organic matter in an immature shale will make the rock more ductile (Aoudia et al., 2010; Eliyahu et al., 2015; Labani and Rezaee, 2015, Dong et al., 2018). However, there is no clear evidence of the effect of organic matter on geomechanical properties at high maturity levels in the Duvernay mudrocks (Dong et al., 2018).

2.7. Present-day stress field in the Alberta Basin

Understanding the present-day and paleo-stress field of the study area is essential for understanding of orientation and distribution of natural fractures in the subsurface. Changes in the stress regime and/or in orientation of the principal stresses at different tectonic phases can cause the emplacement of distinct sets of fractures through time and/or may result in shear or tensile reactivation of pre-existing natural fractures (Morris et al., 1996).

Anderson (1951) proposed three tectonic regimes based on the orientation of three principal stresses: σ_1 , the maximum principal stress; σ_2 , the intermediate principal stress; and σ_3 , the minimum principal stress. Two present-day principal stresses are horizontal (S_{Hmax} and S_{Hmin}) and one is vertical (S_v). The tectonic regime is normal faulting when vertical stress is σ_1 $S_v > S_{Hmax} > S_{Hmin}$; strike-slip faulting if vertical stress is σ_2 $S_{Hmax} > S_v > S_{Hmin}$; and reverse faulting when vertical stress is σ_3 $S_{Hmax} > S_{Hmin} > S_v$ (Fig. 2.18). The magnitudes of the present day principal stresses are estimated by different techniques, including the analysis of earthquake focal mechanisms and recent fault movement in different locations of North America (Lundstern and

Zoback, 2020). The maps of present-day tectonic regime were generated by interpolation of data on magnitude of present-day principal stresses (Fig. 2.19) using the generalized parameter A_ϕ (Simpson, 1997; Lund Snee and Zoback, 2018). The parameter A_ϕ of faulting regime is defined mathematically by:

$$A_\phi = (n + 0.5) + (-1)n(\phi - 0.5),$$

$$\phi = (\sigma_2 - \sigma_3)/(\sigma_1 - \sigma_3),$$

where σ_1 , σ_2 , and σ_3 are the magnitudes of the maximum, intermediate, and minimum principal stresses, respectively, and n is 0 for normal faulting, 1 for strike-slip faulting, and 2 for reverse faulting.

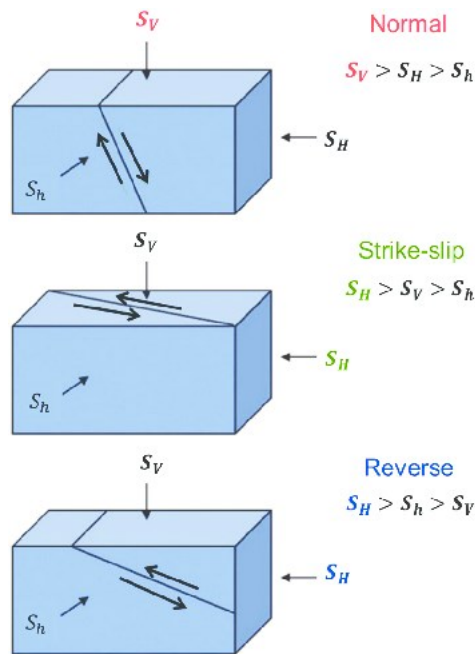


Fig. 2.18. Anderson (1951) fault classification system, after (Wikel, 2011; Tyiasning and Cooke, 2016). S_H and S_h , present-day maximum and minimum horizontal stresses, S_v , vertical stress.

The present-day stress regime in the Western Canada Sedimentary Basin (Fig. 2.19) changes from normal fault regime in Saskatchewan to strike-slip in the Alberta Basin and thrust

fault regime in the Foothills of the Rocky Mountains (McLellan, 1989; Bell and Grasby, 2012; Cui et al., 2013; Reiter et al., 2014; Shen et al., 2019; Lundstern and Zoback, 2020).

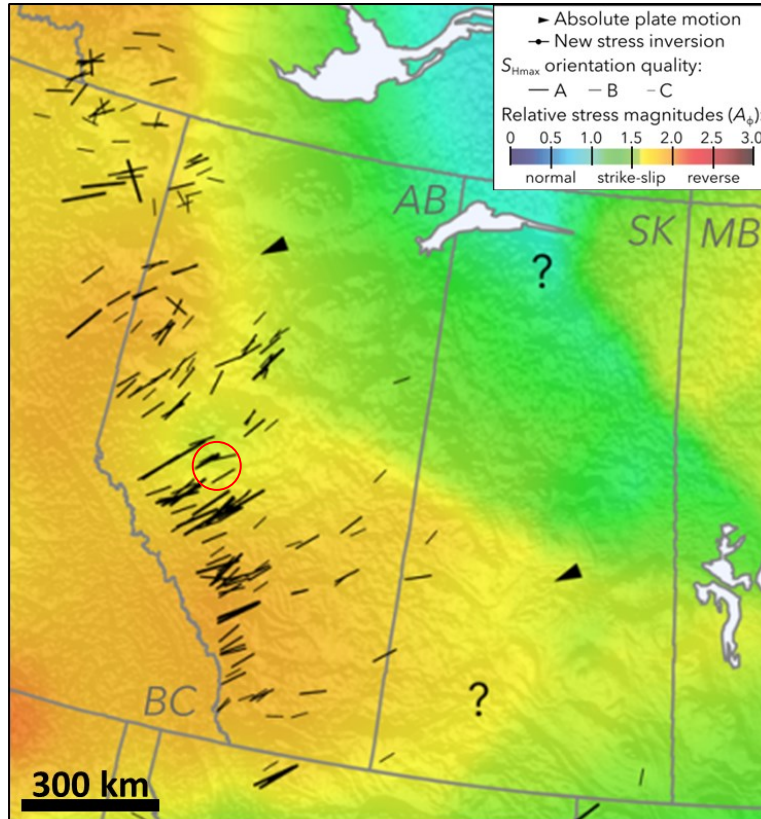


Fig. 2.19. Map of state of stress in the Western Canada Sedimentary Basin, Alberta, after (Lundstern and Zoback, 2020). The black lines indicate the orientations of maximum horizontal stress (S_{Hmax}), while the background with different colors represents the relative stress magnitudes parameter A_ϕ . Location of the Kaybob area is highlighted by the red circle.

Studies from overcoring measurements, hydraulic fractures, bed-slip movements and borehole breakouts show that stress regime varies with depth in the Western Canada Sedimentary Basin, a result of increased crustal loading (Bell and Babcock, 1986). From the surface to about 350 meters deep, the stress-regime correspond to thrust faulting as $S_{Hmax} > S_{hmin} > S_v$; from 350 meters to 2500 meters deep, the stress-regime is strike-slip faulting as $S_{Hmax} > S_v > S_{hmin}$; below 2500 meters, the stress-regime correspond to normal faulting as $S_v > S_{Hmax} > S_{hmin}$. These absolute values of elevation may change depending on the location in the western, central or eastern part of the Alberta Basin.

The Kaybob area is characterized by the present-day strike-slip tectonic regime ($S_{Hmax} > S_v > S_{Hmin}$) with S_{Hmax} oriented NE-SW $N45^\circ E \pm 5^\circ$ (Bell and Bachu, 2003; Bell and Grasby, 2012; Reiter et al., 2014; Shen et al., 2019) (Fig. 2.20). This information has been derived from the analysis of extensive collections of data, which include breakouts and borehole tensile failures during drilling, hydraulic fracturing, seismic focal mechanisms, and geological markers. Some of the preexisting faults in the Alberta Basin are reactivated under the present-day stress settings during hydraulic fracturing operations in the West and East Shale Basins (Wang et al., 2018; Schultz et al., 2020; Schultz and Wang, 2020; Wang et al., 2020; Konstantinovskaya et al., 2021, Li et al., 2023) or waste water disposal close to the deformation front (Kienan et al., 2021; Li et al., 2021). These faults are locally interpreted as a negative flower structure (Fig. 2.21). The earthquakes mechanisms of induced seismicity correspond to the dextral strike slip fault or oblique normal displacement along the near N-S high-angle faults and to the NW-SE thrust faults (Eaton and Mahani, 2015; Wang et al., 2017; Kao et al., 2018; Schultz et al., 2020; Wang et al., 2020; Shultz and Wang, 2020; Li et al., 2021).

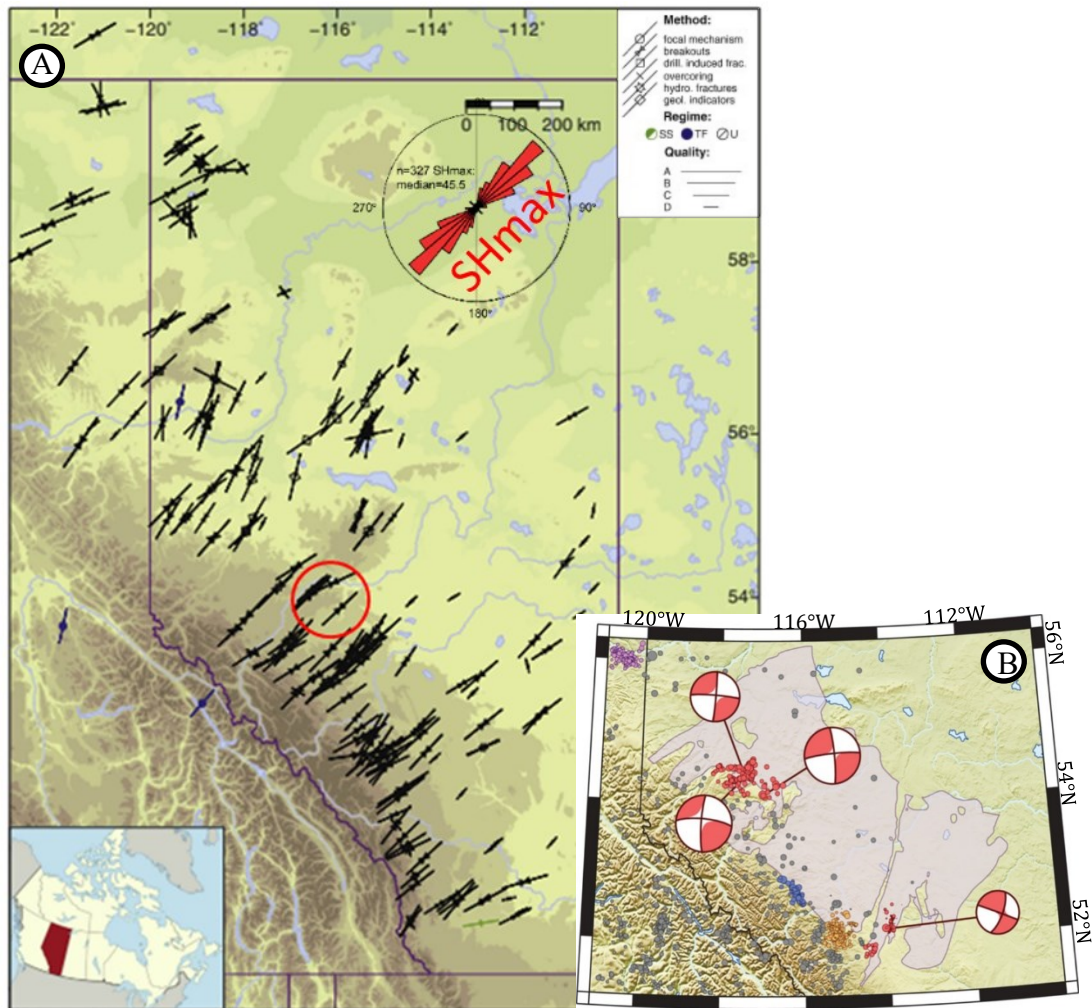


Fig. 2.20. A) Orientation of maximum horizontal stress (SHmax) in the Western Canada Sedimentary Basin, Alberta, after (Reiter et al., 2014). The location of study area is highlighted by the red circle. B) Location of induced earthquakes triggered by hydraulic fracturing in the Duvernay Formation shown by red circles, after (Schultz et al., 2020). The focal mechanisms of the most significant four events are displayed from left to right: the event of 12 January 2016 with a magnitude of 4.1 Mw, the event of 23 January 2015 with a magnitude of 3.6 Mw, the event of 13 June 2015 with a magnitude of 3.9 Mw, and the event of 4 March 2019 with a magnitude of 3.7 Mw. The earthquake mechanisms correspond to dextral strike slip or oblique normal displacement along the near N-S high-angle faults. See references in the text.

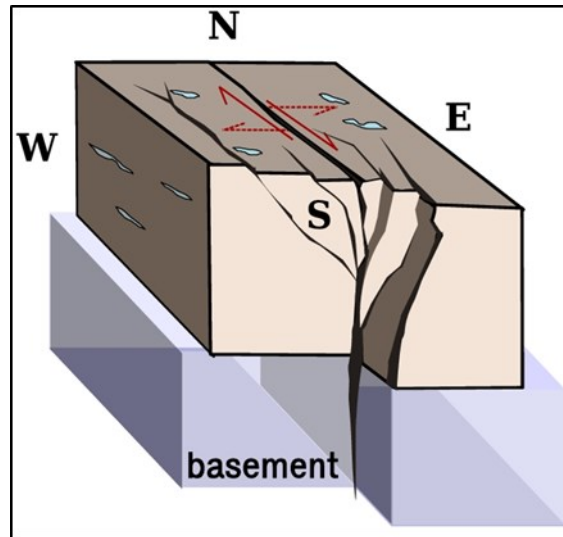


Fig. 2.21. Schematic model showing N-S strike-slip fault system involving a master vertical fault in the basement that evolves upwards into a series of transtensional faults forming a negative flower structure in overlying Paleozoic sedimentary units, Fox Creek area, after Wang et al. (2017).

2.8. Natural fractures: classifications, kinematic types and formation settings in shales

Natural fractures represent discontinuities in rocks formed in the opening mode (joints) or in shear mode (shear fractures) with low-scale displacement and limited length (Davis and Reynolds, 1996). The shear fractures can be differentiated from faults as faults have generally higher length (> 10 m) and displacement along a fault plane (> 40 cm). Fractures can occur at different scales, from small-scale to large-scale fractures that can affect substantial regions. They result from strains caused by concentrated stress around imperfections, and physical discontinuities.

Natural fractures can be characterized by composition, orientations, size, intensity, relationship to bedding, structural position (structural curvature, fault zone), kinematic type of opening, origin (e.g., related to phases of burial and hydrocarbon generation, uplift and unloading, tectonic deformation such as folding and faulting).

There are different kinematic types of natural fractures that form two main groups of tensile and shear fractures and transitional types of transtensional and transpressional fractures (Bratton, 2006; Davis and Reynolds, 1996; Ferrill et al., 2017) (Fig. 2.22). Tensile fractures form perpendicular to the minimum principal stress σ_3 and open normal to the fracture with no displacement parallel to the fracture walls. Shear fractures form at an acute (30°) angle to σ_1 , with displacement parallel to the fracture surface. Slickensides and polish slip faces are usually seen on the shear fracture surface. Hybrid transtensional failure involves fractures that are partly tensile and partly shear. These fractures form at 16° to σ_1 , when effective stress σ_3 is tensile and the confining pressure has a value greater than 3 times tensile strength but less than 5 times tensile strength (Davis and Reynolds, 1996). Compactive shear failure corresponds to the combination of stylolite with a shear component of displacement. Compactive fractures (stylolite) are perpendicular to σ_1 , and the fracture surface contains the σ_2 and σ_3 orientations. They involve the loss of volume without displacement.

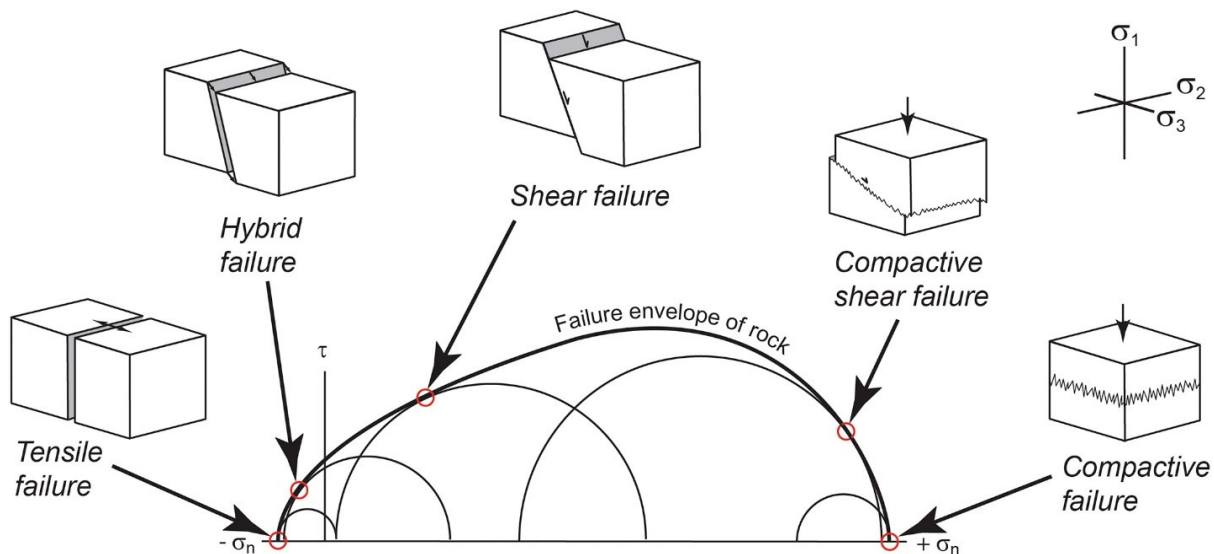


Fig. 2.22. Mohr circle illustration showing different failure modes in a normal faulting stress regime, after Ferrill et al. (2017). σ_1 = maximum principal effective stress, σ_2 = intermediate principal effective stress, and σ_3 = minimum principal effective stress.

The classification of natural fractures based on their mode of formation was developed by Rice (1968). The fractures of Mode I group, also known as ‘opening mode’, form under tensile stress normal to the plane of the crack. The fractures of Mode II or ‘sliding mode’ group form under the settings when shear stress acts parallel to the plane of the crack, perpendicular to the

crack front. The fractures of Mode III or ‘tearing mode’ group form when shear stress acts parallel to the plane of the crack and the crack front (Fig. 2.23).

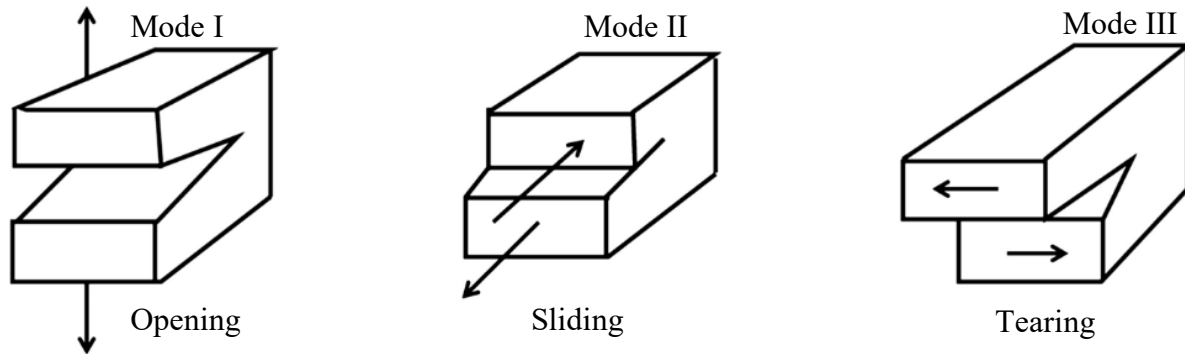


Fig. 2.23. Different type of mode of formation of fractures modified from Siddique et al., (2021), Rice (1968).

Fractures in core that was extracted from subsurface can either be natural (open joints with plume structures or mineralized veins) or artificial, formed as drilling-induced fractures, or unloading fractures opened along bedding, when core is extracted to the surface and dried out. The microstructure of filled fractures (veins) may vary from fibrous, blocky, elongated-blocky, and stretched. This depends on several factors such as growth direction (syntaxial, antitaxial, bitaxial, uniaxial (Durney, 1973), fracture location (localized, delocalized), opening trajectory, fracture type (intergranular, transgranular), and mineralization filling type (e.g., calcite, quartz) (Bons et al., 2012), and relative motion of the fracture wall rocks during fracture opening and filling (Passchier and Trouw, 2005).

Natural fractures can have different origin. Fractures can form during the burial and tectonic loading and during the uplift and unloading (Engelder, 1985; Davis and Raynolds, 1996). During the burial, tectonic compaction or compaction of the overburden generates the increase in pore pressure with depth that results in the decrease of effective principal stresses and may lead to shear fracturing. If the minimum effective principal stress decreases to become negative, tensile failure occurs, and tectonic or hydraulic joints form at depth. During the uplift, the principal stresses and differential effective stress decrease that is not favorable for fracturing. However, at depths 3 km and less, a decrease in the vertical load during an uplift and erosion will cause expansion in vertical direction and contraction in the horizontal direction based on the

Poisson effect (Twiss and Moores, 1992). As the rocks are not free to change horizontal dimensions, the horizontal stresses decrease sufficiently to offset the Poisson contraction, according to Hook's law and tensile fractures would form. Thermal contraction of a rock associated with the decrease of temperature that accompanies erosion and uplift in the rocks near the surface competes and generally overwhelms the Poisson effect (Twiss and Moores, 1992) and contributes to the formation of unloading and release joints. For example, formation of tensile fractures in shales and siltstones of the Devonian Catskill Delta of the Appalachian Plateau, New York was attributed to the processes of burial, tectonic loading and unloading during the Alleghanian orogeny (Engelder, 1985).

Both shear and tensile fractures can form as a result of tectonic deformation related to high-strain zones close to faults and folds. High density of tensile fractures was interpreted along the zone of structural curvature in the Antelope structure formed by the Devonian Sanish-Bakken rocks in the Williston Basin, North Dakota (Murray, 1968). In the hinge zone of a fold, tension fractures are common among other minor structures (Davis and Reynolds, 1996). For example, strong correlation between forelimb structural position and density of tensile fractures and its effect on hydrocarbon production was shown for the folds in the Upper Triassic dolomites in the Foothills of northeastern British Columbia (Butler and Cooper, 2018).

However, there are several examples of Devonian shales where subvertical fractures detected in core are related to more penetrative regional deformation and distant from large-scale tectonic structures (Gale et al., 2014). In numerous cases, the formation of fracture networks does not rely on folds and faults.

The burial and thermal maturation of organic-rich mudrock can result in formation of tensile natural fractures. As an organic-rich mudrock is buried to a greater depth (~3000 m) with elevated temperature (50°C to 150°C) and pressure (30 MPa to 100 MPa), the kerogen breaks down into liquid and gas phases (Tissot and Welte, 1978). This breakdown of the kerogen results in an increase in volume of fluids due to hydrocarbon generation, which causes an increase in formation pressure (Luo and Vasseur, 1996, Chaney, 1950; Hedberg, 1974; Spencer, 1983). It seems that the highest joint densities occur in the black organic-rich shales, whereas lower joint densities occur in the grey organic-lean shales. For example, Lash et al. (2004) concluded that

the preferential jointing in the Upper Devonian Marcellus organic-rich shales of the Appalachian Plateau reflects an extended hydrocarbon generation history during burial and thermal maturity.

Tensile fractures are prone to develop in rocks under the overpressure as high formation pressure results in decrease of effective stresses. Sequential cracking and rhythmic plumose ornamentation in joints interpreted by Bahat and Engelder (1984) at Watkins Glen, New York can be explained by the rhythms of fluid-pressure buildup and fracture-induced release. Even small changes in stress can exceed rock's resistance, leading to fracture initiation.

Natural fractures in shales can be related to uplift, unloading, and exposure to the surface (Voight and St. Pierre, 1974; Narr and Currie, 1982; Engelder, 1985; Davis and Reynolds, 1996; English, 2012). Uplift and unloading involve the removal of overlying rocks or reduction of pressure on the rocks, which can cause the shales to experience tensile fracturing. There are many examples of fractures in shales created due to unloading. The Antrim shale in the Michigan basin was affected by late glacial unloading events, which influenced fracture generation (Budai et al., 2002). The shallower part of the Devonian New Albany shale in the Illinois Basin is another example of fractures related to unloading, as they have shown higher fracture development compared with the same shale in the deeper location (Strapoć et al., 2010). In the Alberta Basin and in the subsurface below the central Alberta Foothills, the region-wide tectonic uplift and unloading during the Laramide orogeny resulted in opening of natural fractures in the Cardium Formation (Currie and Nwachukwu, 1974). Fractures in the buried Cardium sandstone opened at depths ranging from 2590 m in the foreland and 3657 m in the western Foothills, close to the area below the front range of the Rocky Mountains. The foreland was affected by 1200 m – 1350 m of uplift and 450 m to 900 m of erosion of sediments, while in the Foothills the total uplift exceeded 3600 m. The study of fluids inclusion in minerals filling of fractures suggests that fractures initiated at depth and were open progressively as a result of tectonism, uplift and erosional unloading (Currie and Nwachukwu, 1974). During the Laramide orogeny, different sets of fractures were formed in folded and faulted units of the Cardium sandstone in the central Alberta Foothills as a result of horizontal shortening and thrusting (Jamison, 2016).

2.9. Natural fractures in the Duvernay Formation

Natural fractures were previously described in the Duvernay mudstones from core data and image logs in the West and East Shale Basins (Davies et al., 2014; Fothergill et al., 2014; Fox and Soltanzadeh, 2015; Soltanzadeh et al., 2015; Currie, 2021). Slickensides, polished slip faces, cleavage, non-mineralized, mineralized, vertical, sub-vertical, inclined, irregular/complex, and horizontal (bedding-parallel) natural fractures in the Duvernay Formation have been described in the core of the Duvernay shales.

Subvertical fractures studied in the core of the Duvernay Formation are more frequently filled with calcite (Currie, 2021). Open natural fractures with plume ornamentation or fringe cracks on the walls of joints were described (Currie, 2021).

Three main statistically significant sets of subvertical fractures were determined in the Kaybob area from image logs analysis in two horizontal wells (Fothergill et al., 2014). These sets of fractures are oriented 055°, 130° and 075°, being parallel, orthogonal and at low angle to SHmax, respectively (Fothergill et al., 2014). Mackay et al., (2018) determined the presence of subvertical natural fractures oriented 045° and 135°, being parallel and orthogonal to the SHmax based on the analysis of acoustic image logs from a vertical well in the West Shale Basin. Currie, (2021) described fractures from core of vertical wells, with fracture height ranging from less than 10 centimeters to more than 100 centimeters.

In the Duvernay Formation, there are intervals with rock properties and mineralogy where fractures are more prone to develop. Rocks that are either too ductile or too strong tend to have a lesser number of fractures (Fox and Soltanzadeh, 2015; Soltanzadeh et al., 2015). According to Soltanzadeh et al. (2015), the cutoffs for fracture occurrence in the Duvernay shales are approximately 20–30 (scaled by (1/GPa) x 100) of the plane-strain Young's Modulus and approximately 66–90% of the clay-based mineralogical brittleness index. The upper Member of the Duvernay Formation is characterized by the higher presence of natural fractures than the lower and middle Duvernay (Soltanzadeh et al., 2015). On the other hand, the middle Duvernay Member has lower fracture intensity, with calcite-filled fractures concentrated within carbonate nodules (Mackay et al., 2018).

Bed thickness affects the presence and distribution of fractures in non-deformed beds (Huang and Angelier, 1989). The middle Duvernay Member is composed of the carbonate-rich mudrocks that act as a thick mechanically strong unit with thicker beds (~15 cm – 30 cm), which results in larger fracture spacing and lower fracture intensity (Mackay et al., 2018). In contrast, within the upper and lower Duvernay Members, bed thickness is lower and the fracture spacing is lower compared to the middle Duvernay Member.

In general, fractures are characterized by larger spacing with the increase of bed thickness. The relationship between these two variables can be explained by the Michaelis and Menten non-linear equation applicable for clastic and carbonate rocks (Michaelis and Menten, 1913):

$$S = \frac{at}{b + t}$$

Where:

S = median fracture spacing

a = maximum median fracture spacing

b = constant which is numerically equal to the bed thickness when $s = 0.5a$

t = bed thickness

2.10. Upper Devonian Perdrix Formation

The Upper Devonian Perdrix Formation is the outcrop equivalent of the Duvernay Formation, exposed in the Front Ranges of the Rocky Mountains. It is a part of the Fairholme Group (Fig. 2.24). The Perdrix Formation overlies dark grey wackestones and mudstones of the Maligne or Flume Formations (where Maligne is absent) and underlies argillaceous mudstones and siliciclastic shales of the Mount Hawk Formation (McLean and Mountjoy, 1993) (Fig. 2.18). The Perdrix Formation is composed of organic-rich shales that contain between 1 % to 6 % of organic matter (Hopkins, 1972). The main facies consists of dark-grey finely laminated shales

with argillaceous limestone interbeds (McLean and Mountjoy, 1993). Organic-rich shales of the Perdrix Formation are lateral facies of the carbonate buildups of the Cairn Formation, which is comparable to the Lower Leduc Member and Cooking Lake Formation in the subsurface of the Western Canada Sedimentary Basin. The amount of skeletal wackestones, packstones and carbonate nodules in the Perdrix Formation increases close to the reef buildups. The thickness of the Perdrix Formation ranges from 80 m to 140 m (McLaren, 1955; Mountjoy and Mackenzie, 1973).

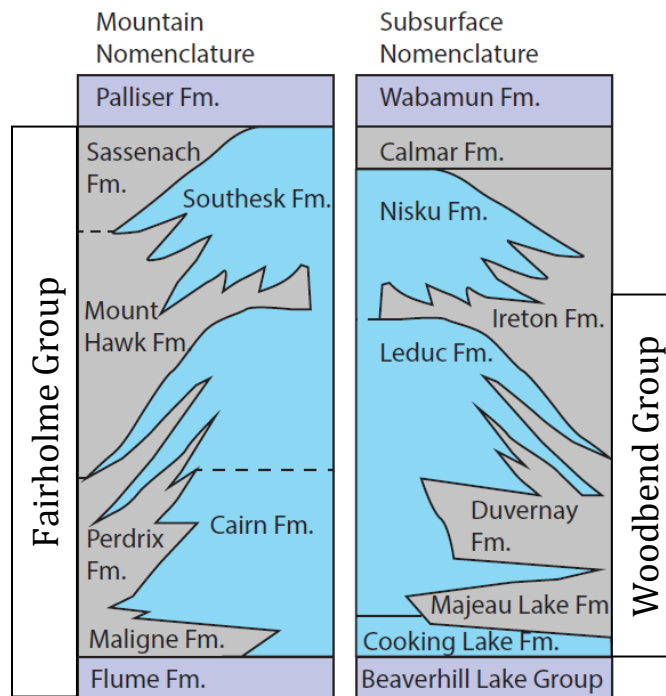


Fig. 2.24. Upper Devonian stratigraphy of the Frontal Ranges of the Rocky Mountains and correlation with the sub-surface units in the Western Canada Sedimentary Basin from MacKay et al., (2018) after McLean and Mountjoy, (1993).

The area of outcrop study is located in the Front Ranges and inner Foothills of the Canadian Rockies (Figs 2.2, 2.25), where Paleozoic, Mesozoic and Tertiary deposits form several thrust sheets (Jones and Workum, 1978; Begin and Veilleux, 2011).

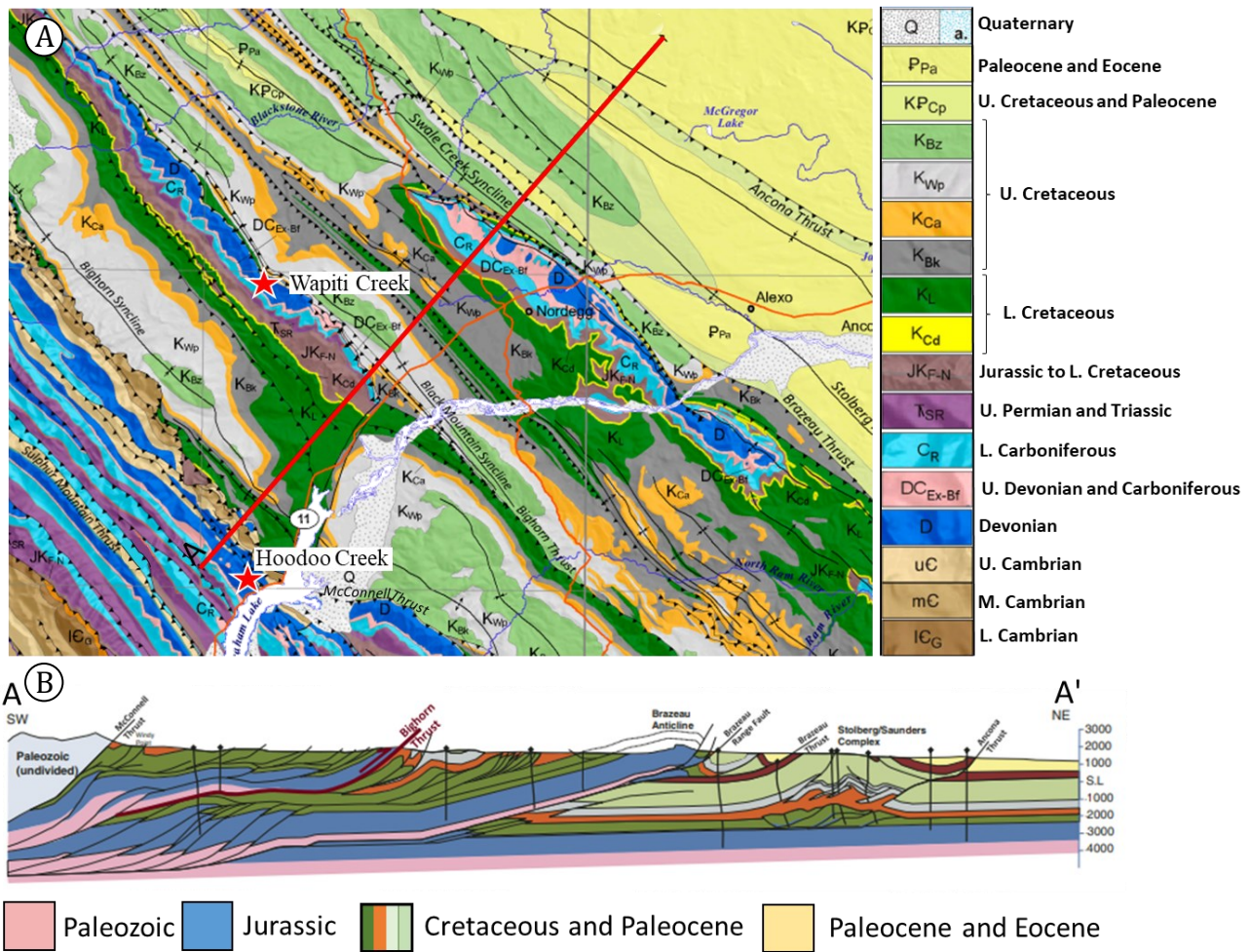


Fig. 2.25. A) Geological map of the Nordegg area in the Central Alberta Rocky Mountain and Foothills belts, after (Pana and Elgr, 2013). The outcrops studied are located in the Hoodoo Creek and Wapiti Creek, marked with a red star. B) Structural cross-section of Nordegg area, after Langenberg et al, (2002); Begin and Veilleux (2011).

The NW-SE striking main thrust faults in the area include the Brazeau Thrust, Bighorn Thrust, the McConnell Thrust and the Surphur Mountain Thrust. These faults dips to the southwest showing a concave upward in profile and tens of kilometers of NE-SW displacement (Price and Mountjoy, 1970; Jones and Workum, 1978; Begin and Vielleux, 2011). In the southwestern Foothills of Alberta, the NW-SE striking Brazeau Thrust fault shows a displacement of > 20 kms, displacing Cambrian rocks over Mesozoic Rocks (Langenberg et al., 2002; Xiao and Unsworth, 2006). The Bighorn Thrust, located in the inner Foothills, has exposed and displaced reef facies of the Southesk and Cairn Formation and Shaly facies of the Mount Hawk, Perdrix and Flume Formations over Cretaceous rocks in the Wapiti Creek area (Spratt et

al., 2004; Begin and Veilleux, 2011). The McConnell Thrust fault is the eastern thrust sheet of the Front Ranges and shows a maximum displacement of 40 km based on 2D kinematic restoration along balanced cross-sections in the Rocky Mountains (Price and Mountjoy, 1970). It is mostly composed of Paleozoic rocks, including the Perdrix Formation. K/Ar Dating on illite from the footwall has shown an age of 77 Ma (Convey et al., 1994; Vrolijk et al., 1994). The McConnell Thrust fault has been dated with $^{40}\text{Ar}/^{39}\text{Ar}$ method as 51 and 54 Ma, that corresponds to late (overprint?) Eocene deformation phase (Pana, 2021). The Surphur Mountain Thrust displaces Paleozoic rocks (including the Perdrix shales) over Jurassic rocks in the Abraham Lake area (Begin and Vielleux, 2011; Pana, 2021). The Surphur Mountain Thrust has been dated with $^{40}\text{Ar}/^{39}\text{Ar}$ method as Campanian, 76 Ma (Pana, 2021).

Natural fractures were previously described before in the Perdrix Formation (MacKay et al., 2018; Konstantinovskaya and Bahramiyarahmadi, 2020; Galvis Portilla, 2022). Fractures in shales are more often orthogonal to the bedding and filled with calcite or open, with fracture height controlled by the changes in mechanical properties and lithology of hosted rocks. In the sedimentary succession, the mudrocks of the Perdrix Formation are characterized by mechanically weak behaviour. However, the black mudstones can locally be interbedded with relatively carbonate-rich mudrocks. Vertical fractures are clustered in these strongly cemented carbonate beds. The carbonate-rich layers contain thick, well-cemented, bedding-parallel and bedding orthogonal fractures. The Perdrix Formation was studied in this research to describe the correlation between composition and properties of organic-rich shales and carbonate-rich interbeds and spatial distribution, orientation, and density of natural fractures. However, the Upper Devonian strata exposed in the Canadian Rockies experienced folding and faulting during the Laramide orogeny that is not necessarily typical for the rocks in the subsurface of the Alberta Basin. The fracture orientation and intensity in the Perdrix Formation is expected to be different with the intensity in the Duvernay Formation, as shortening and tectonic uplift in the fold-and-thrust belt likely affected the deformed rocks, creating sets of fractures that are not necessarily developed in the subsurface.

Chapter 3: DATA AND METHODS

The data and methods involved in this study are used to characterize natural fractures in different lithofacies of the Upper Devonian Duvernay Formation interpreted in core in 7 vertical wells and FMI logs in 4 horizontal wells of the Kaybob area (Fig. 3.1). Additionally, natural fractures in the Perdrix Formation, an outcrop stratigraphic and lithological analog of the subsurface Duvernay Formation, were studied near Nordegg, in the Front Ranges of the Canadian Rocky Mountains.

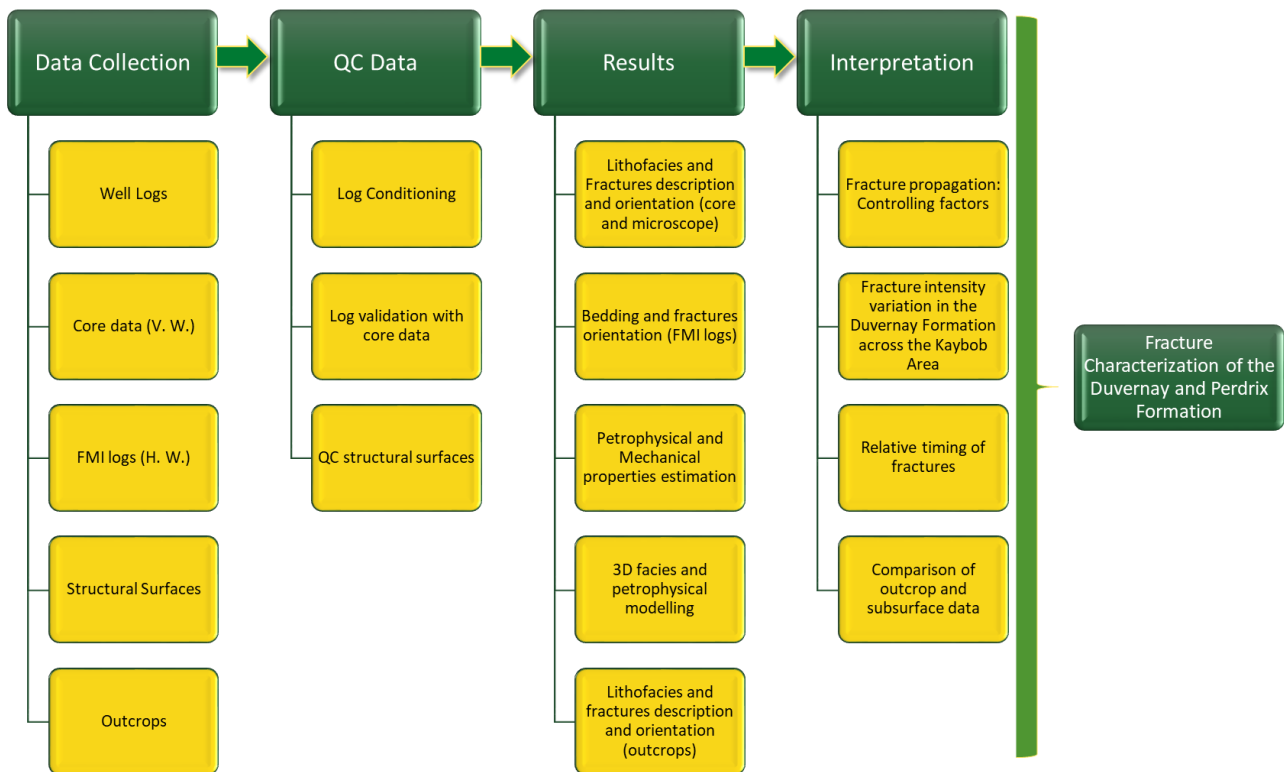


Fig. 3.1. Workflow chart of data and methods used in studying natural fractures of the Upper Devonian Duvernay and Perdrix Formations. QC = Quality Control; V. W. = Vertical Wells; H. W. = Horizontal wells.

3.1. Data sources

Well data including well location, trajectory, well tops and well logs were obtained from the geoScout database through the research agreement between the University of Alberta and geoLOGIC Systems Ltd. Core logging and sampling was conducted at Core Research Center, Alberta Energy Regulator (AER). The reports of core petrophysical and geomechanical testing

were obtained from AER (<https://www.aer.ca/>). The Fullbore Formation Microimager (FMI) logs were donated by an anonymous energy company through a confidential agreement with Microseismic Consortium.

Additional information on well tops and surfaces of the Ireton, Duvernay and Leduc Formations and Beaverhill Lake Group in the Kaybob area were collected from 3D Provincial Geological Framework Model of Alberta, version 2 compiled by Alberta Geological Survey in 2019 available at website: <https://ags.aer.ca/publication/3d-pgf-model-v2>. The digital topography data used in 3D modeling were downloaded from the website <http://www.geogatis.gc.ca/> published by the Government of Canada. The shapefiles of lithofacies of the Upper Devonian formations and faults of the Rocky Mountains deformation front that represent digitized data of the Geological Atlas of the Western Canada Sedimentary Basin (1994) were downloaded from AGS website <http://www.ags.gov.ab.ca/publications/>. The shared data on lithofacies and sequence stratigraphy that have already been determined and described in a series of wells in the area by Daniel Shaw (Shaw, 2020) are considered as a main background.

Thin sections of collected core and outcrop samples were prepared at the thin section laboratory and scanned at the Digital Image Facility, Earth and Atmospheric Sciences Department, University of Alberta. The description of thin sections was complemented by the description of thin sections of core samples in studied wells available in CRC AER reports.

The data of present-day stress orientation, stress regime and pore pressure were obtained from the website of World Stress Map (<https://www.world-stress-map.org/>) and previous publications (Bell et al., 2012; Heidbach et al., 2010; Reiter et al., 2014; Lyster et al., 2017; Shen and Schmitt, 2019; Schultz et al., 2020).

The regional geological cross-sections, geological maps papers and reports on the facies of the Upper Devonian facies were used to determine the field work study area (Bégin and Veilleux, 2017; Langenberg and Erdmer, 1992, Hamilton et al., 1999; Spratt et al., 2004; Mountjoy and Price, 1974; Douglas, 1955; Workum and Hedinger, 1992).

3.1.1 Database

The study of the core of the Duvernay Formation was conducted for seven (Table 3.1) vertical wells (1-7) in the Kaybob area (Fig. 3.2). The choice of studied vertical wells penetrating the Duvernay Formation (Table 3.1) included the following parameters: 1) available core; 2) the proximity, preferably at the same well pad, to the location of the horizontal wells, in which FMI data were studied; 3) available petrophysical and geomechanical testing reports. These wells were used to describe core and interpret lithofacies and fractures, build lithofacies and petrophysical models around horizontal wells (see section 3.2.3 for more information).

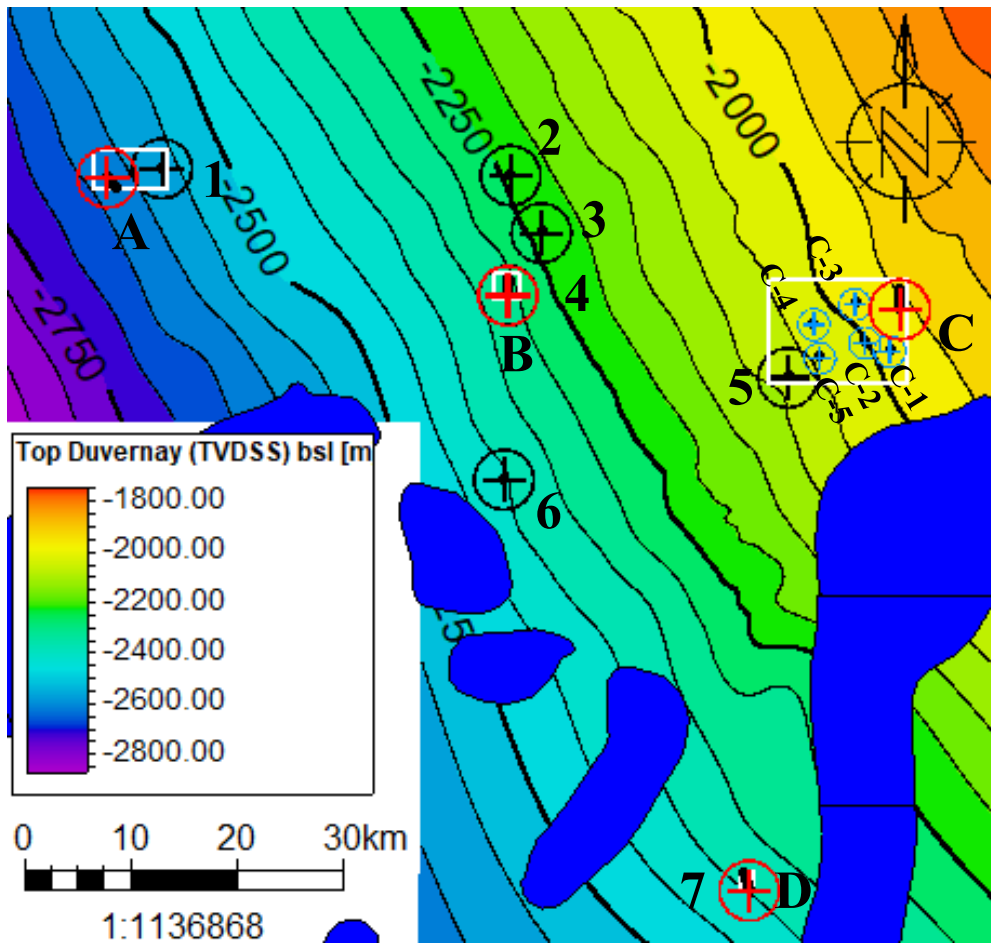


Fig. 3.2. Depth structural map of the top of the Duvernay Formation (m, bsl) in the Kaybob area. A-D, wellhead location of four horizontal wells (red circles). 1-7, wellhead location of vertical wells, in which core was described (black circles). C-1 to C-5, wellhead location of vertical wells (blue circles) used in 3D lithofacies and petrophysical models (white rectangles). The pairs of wells 4 and B and wells 7 and D belong to common well pads, respectively. The blue polygons depict simplified geometry of the Leduc Reefs. TVDS, bsl, True vertical depth below sea level. See Table 3.1 for the list of the wells.

Data from these wells includes wellhead location and well trajectory, formation tops, core data and a suit of well logs (Table 3.1). The well logs used in this study include logs of natural radioactivity gamma ray (GR), compressional and shear wave sonic (DTC, DTS), density (RHOB), neutron porosity (NPHI), photoelectric factor (PEF), resistivity, caliper. The core intervals studied in 7 wells included the base of the Ireton Formation and generally full length of the Duvernay Formation (Table 3.1). The core intervals with fractures in the Duvernay Formation in five wells (1, 3, 4, 6, 7) were sampled, and thin sections were prepared.

The study of the FMI logs was carried out for 4 horizontal wells A-D within the Kaybob area (Fig. 3.2, Table 3.1). Both interpreted pdf files and not interpreted digital (.dlis) files were provided. The original .dlis files were interpreted in this study with a guidance from the interpretations in pdf files carried out by interpreters of Schlumberger.

Well logs of 5 additional vertical wells (C1-C5) were analyzed (Fig. 3.2, Table 3.1)) to interpret lithofacies of the Duvernay Formation based on core description conducted in well 5 and build 3D lithofacies and petrophysical models in the area between well 5 and well C.

Code	Well Name	Top and bottom of studied core interval (m)	Top and TVT of the Duvernay Formation (m)	GR	DTC DTS	RHOB	PEF	Resistivity	CALI	ROP	FMI logs	Core data
1	KIWETINOHK WAHIGAN 7- 17-63-23	3426.06 - 3462.45	3425.33 - 53.41	✓	✓	✓	✓	✓	✓			✓
2	SCL HZ KAYBOB 2- 22-63-20	3068.00 - 3141.21	3084.85 - 53.08	✓	✓	✓	✓	✓	✓			
3	CPEC KAYBOBS 11- 26-62-20	3257.00 - 3323.00	3263.22 - 56.49	✓	✓	✓	✓	✓	✓	✓		✓
4	CHEVRON HZ KAYBOBS 2- 9-62-20	3180.00 - 3214.00	3191.46 - 62.23	✓	✓	✓	✓	✓	✓			✓

5	CPEC FOXCK 1-18-61-17	3056.50 - 3122.00	3050.79 - 48.91	✓	✓	✓	✓	✓	✓	✓		✓
6	CPEC KAYBOBS 6- 16-60-20	3344.00 - 3423.00	3350.54 - 59.14	✓	✓	✓	✓	✓	✓	✓		✓
7	CHEVRON 100 PINE CK 6-15- 56-18	3508.00 - 3572.14	3499.56 - 66.37	✓	✓	✓	✓	✓	✓	✓		✓
A	CHEVRON WAHIGAN 4- 12-63-24		3483.65 - 52.41	✓					✓	✓	✓	
B	CHEVRON HZ KAYBOBS 2- 16-62-20		3189.50 - 62.25	✓					✓		✓	
C	CHEVRON HZ CHICKDEE 3- 8-62-16		2868.53 - 57.16	✓					✓		✓	
D	CHEVRON 100 PINE CK 4-22- 56-18		3501.30 - 66.45	✓					✓		✓	
C1	WESTCOAST FINA HSOUND 10- 19-61-16		2890.40 - 50.9	✓	✓			✓	✓			
C2	OUTLIER RES CHICKDEE 3- 25-61-17		2929.10 - 55.8	✓	✓				✓			
C3	FINA AMOCO HB PASSCK 7- 2-62-17		2882.20 - 62.5	✓	✓	✓		✓				
C4	AUINTANA ET AL H SORIND 6-33- 61-17		2931.00 - 61.5	✓	✓			✓				
C5	FINA AMOCO HB PASSCK 7- 21-61-17		2945.00 - 61.2	✓	✓	✓		✓				

Table 3.1. Summary of well and core data used in this study. 1-7, vertical wells with core of the Duvernay Formation; A-D, horizontal wells; C1-C5, vertical wells between wells C and 5. TVT, True vertical thickness. Well logs: GR, gamma ray; DTC and DTS, compressional and shear wave sonic; RHOB, bulk density; PEF, photoelectric factor; CALI, caliper; and ROP, rate of penetration. Core data include core description, thin sections and hardness measurements obtained in this study. See Table 3.2 for petrophysical and geomechanical testing reports used in this study and available at AER website.

Well	Report	Analysis description
1	R_10512	GM
	R_10994	YM, PR, GRI, DB, GAD, K, POR, RE, TOC
	G_14424	XRD
3	G_10989	TOC, RE, XRD
	R_10414	RM, TCT, DB, YM, PR, ACV, DEP, GRI, K, POR, GS, GAD, SO, SW
4	R_8578	DB, EP, GS, GM, SO, K, PET, PR, RE, RM, TRA, TOC, TP, TCT, UC, SW, XRD, YM
5	R_8747	TCT, DEP, GS, GM, GAD, SO, K, PR, POR, GRI, SW, YM, ACV
	R_8909	K, POR, GAD, SW, SO, GS, XRD, TOC, RE, TM
	R_8910	TRA, POR, K, EP, SW, GS, SO, GAD, GM, YM, PR, TCT
6	R_10735	GM, TCT, YM, PR, XDR
7	R_8955	GM, TCT, YM, PR, TRA, SW, GS, SO, TP, K, POR, RE, TOC, XRD, TSP, ELAN
	R_10934	UC

Table 3.2. List of core testing reports used on this study with available analyses. Data can be requested at the AER website. Analysis description abbreviations: GM: Geomechanics; YM: Young's Modulus; PR: Poisson's ratio; GRI: Shale gas analysis; DB: Bulk density; GAD: Grain density; K: Permeability; POR: Porosity measurements; RE: Rock Evaluation; TOC: Total Organic Carbon; XDR: X-ray diffraction; RM: Rock mechanics; TCT: Triaxial compressive test; ACV: Acoustic velocity; DEP: Dynamic elastic properties; GS: Gas saturation; SO: Oil saturation; SW: Water saturation; EP: Effective porosity; PET: Petrology; TRA: Tight rock analysis; TP: Total porosity; UC: Unconfined compression; TSP: Thin sections petrographics; ELAN: Elemental analysis.

3.2. Methods and Workflow

This section provides an overview of the methods and workflow employed for analyzing different datasets to characterize natural fractures in the Duvernay and Perdrix Formations.

The workflow (Fig. 3.1) includes the following steps. 1) Data collection involved obtaining well data and well logs, core sampling and description in vertical wells, core petrophysical and geomechanical testing reports; FMI logs in horizontal wells; structural and topography depth surfaces; outcrop sampling and description. 2) Quality control of data considered depth check and conditioning of well logs, depth check of core data, comparison of well tops and depth structural surfaces of the Ireton, Duvernay and Leduc Formations and

Beaverhill Lake Group in the Kaybob area. 3) Results section aimed the description of lithofacies and fractures composition and orientation of the Duvernay Formation based on core logging and thin section study, interpretation of bedding and fracture orientation based on FMI logs, estimation of petrophysical and mechanical properties, 3D facies and petrophysical modeling, description of lithofacies and fractures of the Perdrix Formation in outcrops. 4) Interpretation included analysis of factors that control lateral and vertical fracture propagation, fracture intensity variation in the Duvernay Formation across the Kaybob area, relative timing of different sets of fractures, comparison of fractures analyzed in outcrops and subsurface. These steps helped to characterize natural fractures of the Duvernay and Perdrix Formations, which is the main objective of this research study.

3.2.1. Core and microscopic description of lithofacies and fractures of the Duvernay Formation

To analyze the distribution of fractures depending on rock composition and fabric in different lithofacies of the Duvernay Formation, both lithofacies and fractures were described in core at the base of the Ireton and in the Duvernay Formations in seven vertical wells 1-7 of the Kaybob area (Fig. 3.2, Table 3.1).

The macroscopic core description included parameters of rock color, siliciclastic grain size, fabric, sedimentary structures, presence of carbonate and anhydrite material, trace and body fossils, bitumen stain, pyrite occurrence, composition and orientation of fractures. The presence of carbonate material in shales was assessed by treatment of core with 10% hydrochloric acid (HCl). Sequence stratigraphy surfaces were interpreted in studied wells 1-7 using core facies description, well log analysis and previous results (Knapp, 2016; Wong et al., 2016; Knapp et al., 2017, 2019; Harris et al., 2018; Shaw, 2020). Lithofacies were identified in core based on the sedimentological analysis and guidance with petrophysical logs and mechanical properties. The lithofacies described in core and supported by well log analysis were used to build discrete facies logs in vertical wells.

The description of natural fractures included several parameters: type of fracture (open or healed), fracture filling (vein composition), presence of slickensides and/or plume structures,

fracture height, aperture and orientation relative to the core axis and bedding, and fracture spacing in the core. These parameters were observed, recorded and analyzed. The composition of veins was determined using HCl and using a steel nail to distinguish different minerals based on their hardness from Mohr's scale. The dip angle of fractures in core was measured relative to the core axis in vertical wells by using a protactor. The density porosity curves were estimated in the studied wells before core description to highlight core intervals with potential presence of fractures as a part of standard steps of fracture description on core (Nelson, 2001).

Linear fracture intensity (P10) was estimated in core as a number of fractures per core length unit (m). Fracture intensity was corrected using Terzaghi's angular correction method for directional bias (Fig. 3.3).

To calculate corrected fracture intensity, the following equation was applied:

$$Fc = \frac{F}{\sin(\theta)}$$

where:

Fc: corrected fracture intensity (number of fractures/m)

F: observed fracture intensity without correction (number of fractures/m)

θ : angle between the core axis (line of observation) and fracture set orientation (Fig. 3.3).

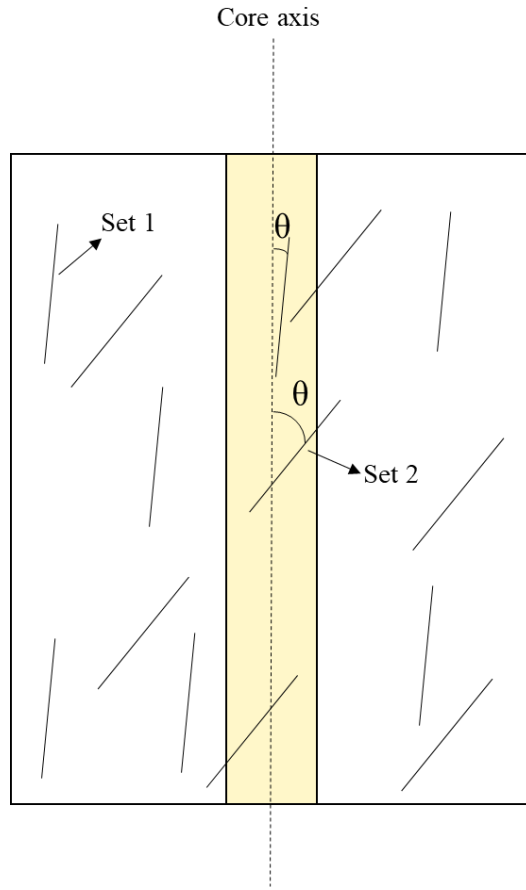


Fig. 3.3. Terzaghi's angular correction applied for linear fracture intensity for different fracture sets. θ is the angle between the core axis (line of observation) and orientation of a fracture set. Fractures of set 1 will be less likely to be seen in the core, as they are sub parallel to the core axis. Terzaghi correction of fracture intensity will be higher for set 1 than for set 2.

More advanced methods for fracture intensity correction in core were proposed by different authors. Narr (1996) included fracture height and borehole diameter to Terzaghi's equation. Berg (2019) considered fracture height and γ (gamma), which is the angle between a line perpendicular to the borehole within the fracture plane and the fracture length axis. These approaches are generally used for fracture intensity correction of natural fractures of a rectangular shape. Berg (2021) also developed an equation that is applicable for fracture intensity estimation of natural fractures of a variable, not only rectangular, shape. As described below, software used in this study to estimate linear fracture intensity in FMI logs applies Terzaghi correction. To be consistent in estimation of linear fracture intensity in core and in image logs, Terzaghi correction was used in the analysis of fractures in the core.

The cored intervals with fractures were sampled to prepare thin sections to study natural fractures. The core samples were cut perpendicular to bedding. Thin sections were scanned using a Nikon Super Coolscan 5000 ED scanner, which enables the observation of features at the millimeter scale. A Nikon Trinocular microscope and camera were used to observe mm- to μm -scale features. The microscopic description included the parameters of rock composition and fractures similar to those analyzed during core logging. The relative timing of observed fracture sets was interpreted based on cross-cutting relationship between fracture sets. The kinematic type of fracture (shear, tensile or transtensional) and growth direction (syntaxial or antitaxial) was interpreted based on the fracture geometry, orientation crystal fibers, and presence of a median line (Davis and Reynolds, 1996).

The natural fractures observed in the core were distinguished from drilling-induced fractures based on the proposed criteria (Nelson, 2001; Lorenz and Cooper, 2018; Kulander et al., 1990; Chatterjee and Mukherjee, 2023). Natural fractures can be open, partially or fully mineralized, may have grooves or slickenlines. Natural fractures are generally enclosed within the core with both ends terminate within the core and do not intersect the core edge; they form one or more parallel sets (Nelson, 2001). The drilling-induced or unloading fractures are usually open. Drilling-induced fractures have different shapes including petal, petal-centreline, saddle, cup and scallop (Fig. 3.4). Petal fractures occur when there is a notable difference between the magnitudes of the maximum and minimum horizontal stress. As this difference decreases, the fractures transition from petal fractures to petal-centerline fractures, eventually progressing to the cup/disc type (Li and Schmitt, 1998). A petal centerline fracture is a transverse fracture found at a shallower depth, and as the depth increases, it transforms into a centerline or longitudinal fracture relative to the drill core. Disc/cup-shaped fractures primarily develop in fine-grained fissile rocks as a result of removal of overburden pressure (Nelson, 2001, Chatterjee and Mukherjee, 2023). Although these fractures tend to have a predominantly (sub)horizontal orientation in a (sub)vertical core, their alignment can be influenced by inclined beds, cross-beddings, and rock anisotropy (Chatterjee and Mukherjee, 2023). These fractures usually show a change in strike or dip at the edge of the core (Nelson, 2001).

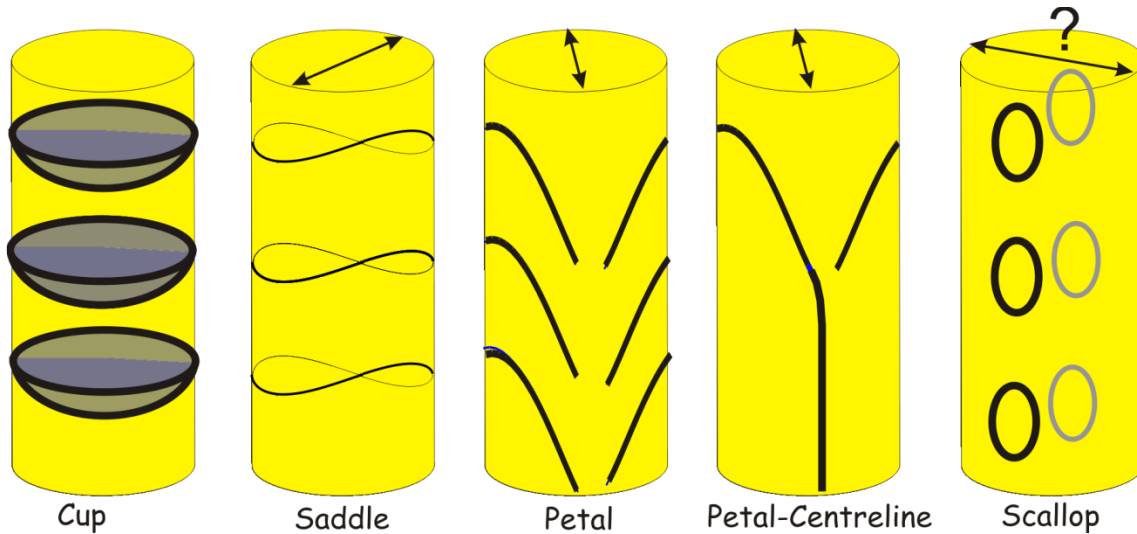


Fig. 3.4. Different types of drilling-induced fractures, after Li and Schmitt (1998); Zhang et al., (2010).

The double-headed arrows reflect the orientation of the maximum horizontal stress SH_{max} , parallel to the strike of the fractures. SH_{max} for scallop type is inferred.

3.2.2. FMI interpretation of bedding and fractures of the Duvernay Formation

Interpretation of bedding, natural fractures, drilling-induced fractures (DIFs) and borehole breakouts in the Duvernay Formation in FMI logs was carried out in TechlogTM (<https://www.software.slb.com/products/techlog>) for four horizontal wells A, B, C, and D of the Kaybob area (Fig. 3.2, Table 3.1). Magnetic declination as a difference between magnetic north and true north was previously applied during the processing of raw image log files by Schlumberger consulting service. Terzaghi's correction for directional bias of linear fracture intensity was applied in the software during fracture intensity interpretation.

The bedding was interpreted in FMI logs as full sinusoids, where clearly visible. As bedding in the Duvernay Formation of the Kaybob area is subhorizontal dipping to the SW at about 3° - 6° (Fig. 3.2), it is subparallel to the lateral segments of horizontal wells. The subhorizontal bedding is expressed in the FMI logs of horizontal wells as high-amplitude sinusoids (Fig. 3.5). If the borehole intersects non-planar bedding structures (e.g. wavy laminae) or carbonate concretions, the bedding expression in the FMI log is more complex (Glover and Bormann, 2007). The interpretation of bedding orientation was used to correlate the intervals of fracture intensity with disruptions in bedding orientation that may indicate the presence of deformation zones with higher strain of the rocks (Nelson, 2020).

Natural fractures were interpreted as full or partial sinusoids depending on whether a fracture crosses the borehole in full diameter or only partially (Fig. 3.5). Orientation of structural elements interpreted in FMI logs was projected on upper hemisphere in Schmidt stereonet and rose diagrams. Different type of natural fractures were identified including resistive fractures, continuous conductive fractures, and discontinuous conductive fractures. Resistive fractures are mineralized fractures, while conductive fractures are open fractures that cross the borehole entirely (continuous) or partially (discontinuous).

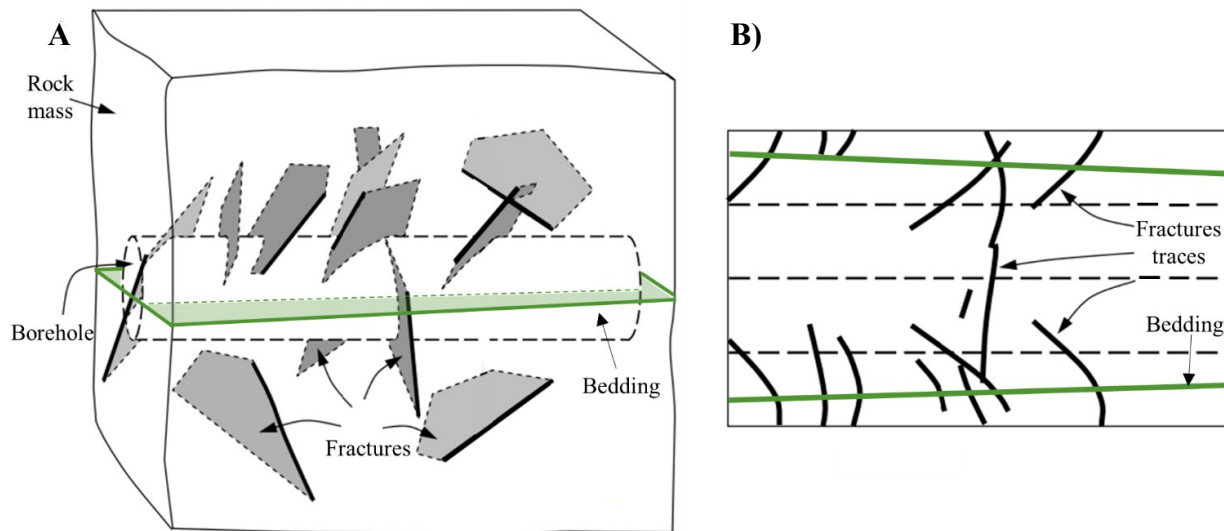


Fig. 3.5. A) Fractures (black) and bedding (green) intersecting a cylindrical surface (horizontal borehole) within a rock mass. B) Unrolled borehole trace map with fracture and traces of slightly inclined bedding. Modified from Wang, (2005).

Linear fracture intensity P10 (number of intersections per unit of length, fr/m) and volumetric fracture intensity P32 (area of fractures per unit of volume, m^2/m^3) were estimated based on fracture interpretation in the FMI logs. Fracture intensities P10 and P32 were calculated with a step and window size of 0.5 meters. The chosen step and window size results in more accurate estimation of P10 and P32 compared to larger sampling steps (Fig. 3.6).

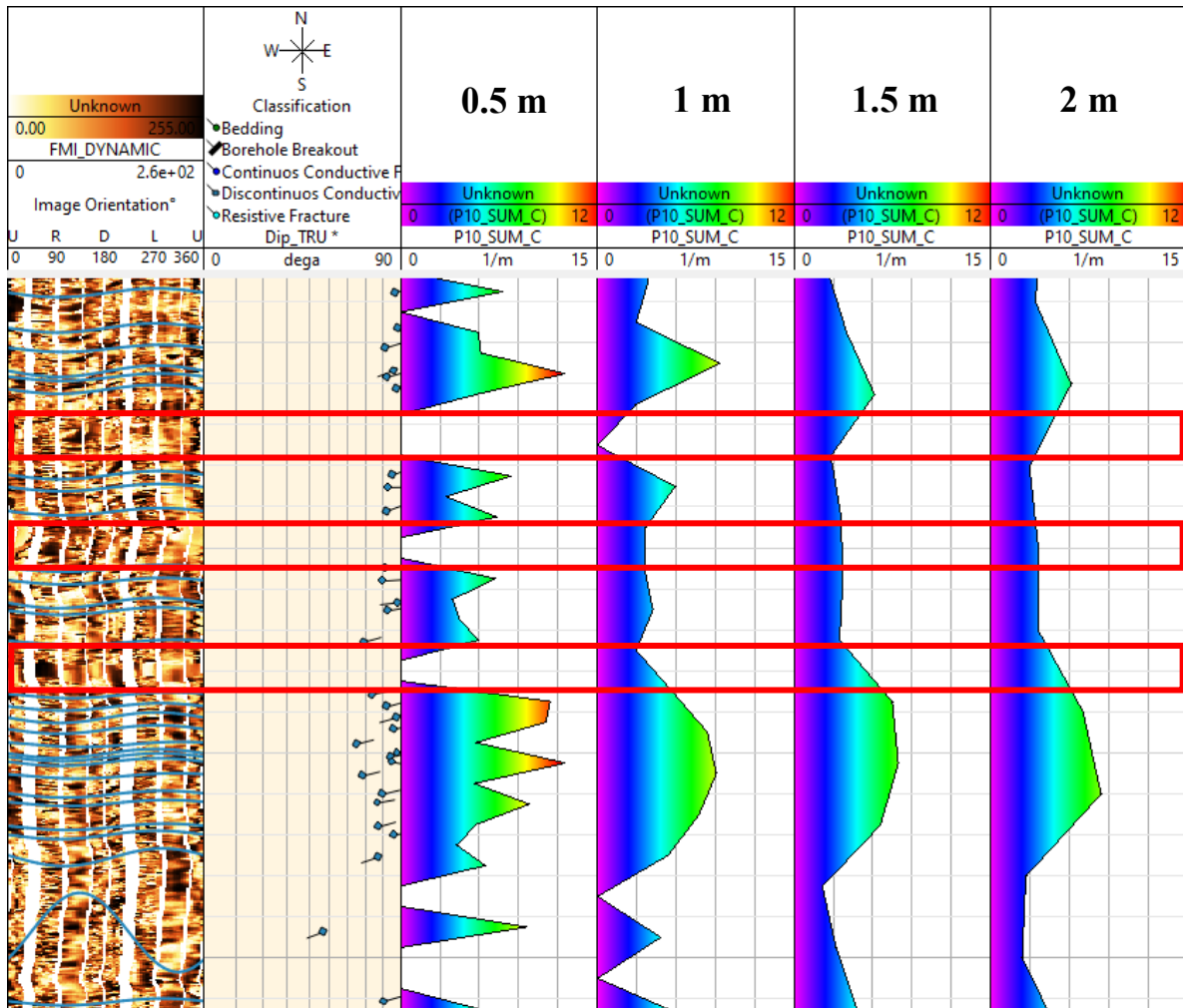


Fig. 3.6. Changes in fracture intensity estimated using different sampling rate. Track 1, FMI dynamic log with picked sinusoids of fractures; Track 2, orientation of natural fractures (true dip azimuth and dip angle); Tracks 3-5, linear fracture intensity P10 estimated with 0.5 m, 1 m, 1.5 m and 2 m of step and window size, respectively. The red rectangles highlight the intervals of high variability of fracture intensity depending on a window and step size.

Borehole breakouts occur as symmetric features of shear failure at borehole walls that are aligned with the orientation of the minimum principal stress (Fig. 3.7) acting remotely around the borehole (Haimson and Song, 1993; Schmitt et al., 2012; Zoback et al., 1985, 2003). Drilling-induced fractures (DIFs) are formed when minimum principal stress exceeds the tensile strength of rocks at the wellbore wall (Reiter et al., 2014). DIFs are oriented perpendicular to the minimum principal stress and parallel to the maximum principal stress (Reiter et al., 2014, Aadnøy and Bell, 1998; Tingay et al., 2008; Zoback et al., 2003).

Orientation of DIFs and borehole breakouts helped to interpret the orientation of the regional horizontal stress (S_{Hmax}) and relative magnitude of the minimum and maximum principal stresses acting around the borehole as described in Results. The regional data for the Western Canada Sedimentary Basin indicate that present-day stress field is characterized by NE-SW orientation of maximum horizontal stress S_{Hmax} ($N45^{\circ}E \pm 5^{\circ}$), and strike-slip fault regime $S_{Hmax} > S_v > S_{Hmin}$ (Bell et al., 2012; Heidbach et al., 2010, Reiter et al., 2014, Shen and Schmitt, 2019; Lund Snee and Zoback, 2020). Under these settings, the minimum and maximum principal stresses acting around a horizontal well that is oriented NW-SE, parallel to S_{Hmin} , are represented by vertical (lithostatic) stress S_v and S_{Hmax} , respectively (Fig. 3.8). Hence, the orientation of borehole breakouts in horizontal wells on the top and bottom of a horizontal well oriented NW-SE indicate that $S_v < S_{Hmax}$. The subvertical NE-SW DIFs cross-cutting the NW-SE horizontal well are consistent with the orientation parallel to S_{Hmax} and perpendicular to S_{Hmin} (Fig. 3.8).

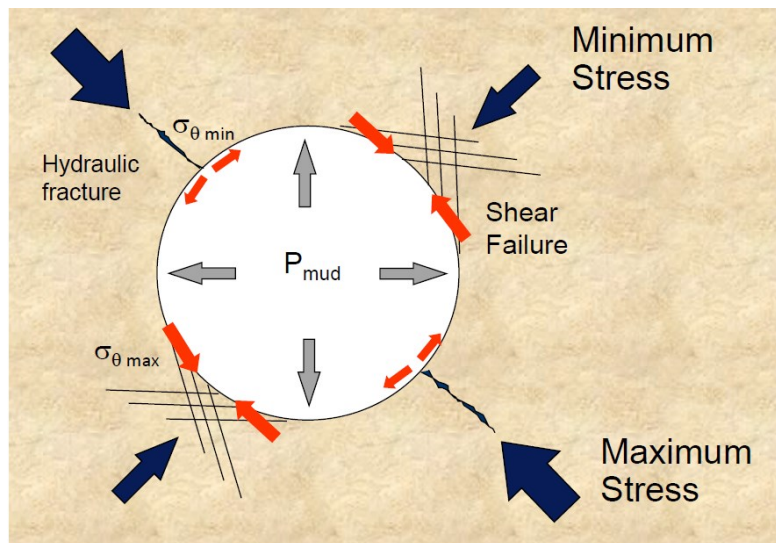


Fig. 3.7. Orientation of borehole breakouts and drilling-induced tensile fractures relative to orientation of remote principal stresses (maximum and minimum) and hoop stresses ($\sigma_{\theta \max}$ and $\sigma_{\theta \min}$), modified after Reinecker et al. (2003).

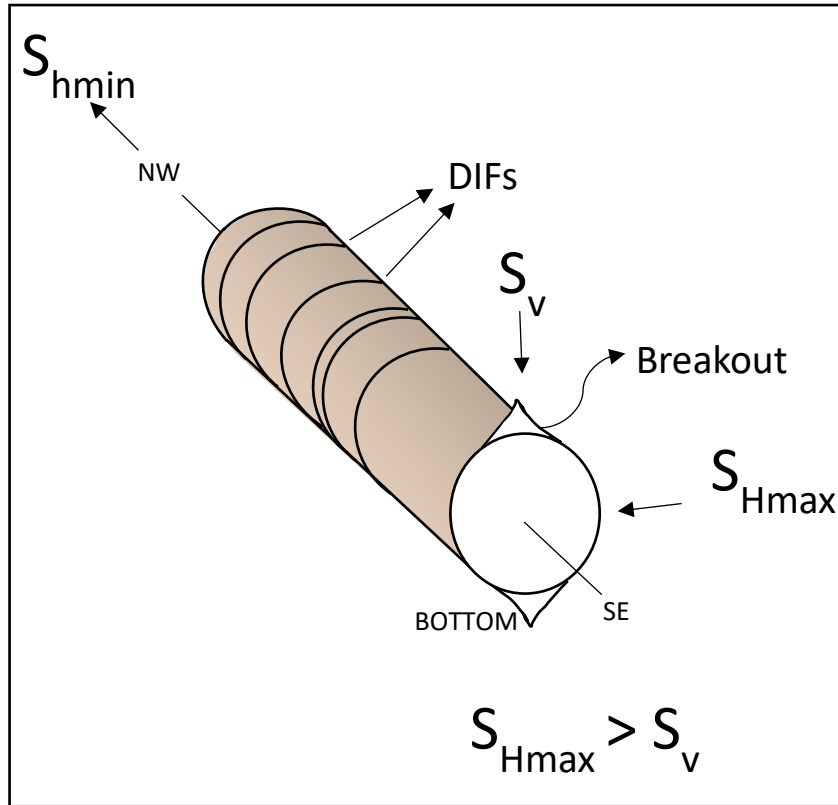


Fig. 3.8. Schematic wellbore cross-section of a horizontal well oriented NW-SE, displaying orientation of borehole breakouts and drilling-induced fracture (DIF) relative to remote regional stresses in the Kaybob area.

3.2.3. Petrophysical and geomechanical parameters of the Duvernay Formation

The aim of this subsection is to describe the approaches used in the analysis of the petrophysical and mechanical properties of the Duvernay Formation in vertical wells 1-7 of the Kaybob area (Fig. 3.2, Table 3.1). The well logs were conditioned, and adjusted for depth inconsistency. The estimated log-derived petrophysical properties included total porosity, permeability and TOC (Total Organic Carbon) content.

Total porosity (ϕ) is the total void space of the rock. The density porosity was estimated using the density equation:

$$\phi_d = (\rho_{matrix} - \rho_{log}) / (\rho_{matrix} - \rho_{fluid})$$

where:

ϕ_d : Total density porosity (v/v)

ρ_{matrix} : Density of matrix (2.65 gr/cm³ for sandstone, 2.71 gr/cm³ for limestone, 2.85 gr/cm³ for dolomite)

ρ_{log} : Bulk density of log reading (gr/cm³)

ρ_{fluid} : Density of fluid (0.6 gr/cm³ for gas and 0.8 gr/cm³ for oil)

Permeability (K) is the ability of the rock to transmit fluids (water, oil, gas). The log-derived permeability was estimated from the total porosity log, using the following equation:

$$K = 10^{((0.5861971 * Phit) - 7.146905)}$$

Where:

$Phit$ = Total porosity (v/v)

K = Permeability (mD)

This equation was determined in this study based on the correlation between core porosity and core permeability data available in petrophysical testing reports for core samples of the Lower Ireton, Duvernay and Majeau Lake Formations in wells 3 and 6 (Tables 3.1, 3.2, Fig. 3.9).

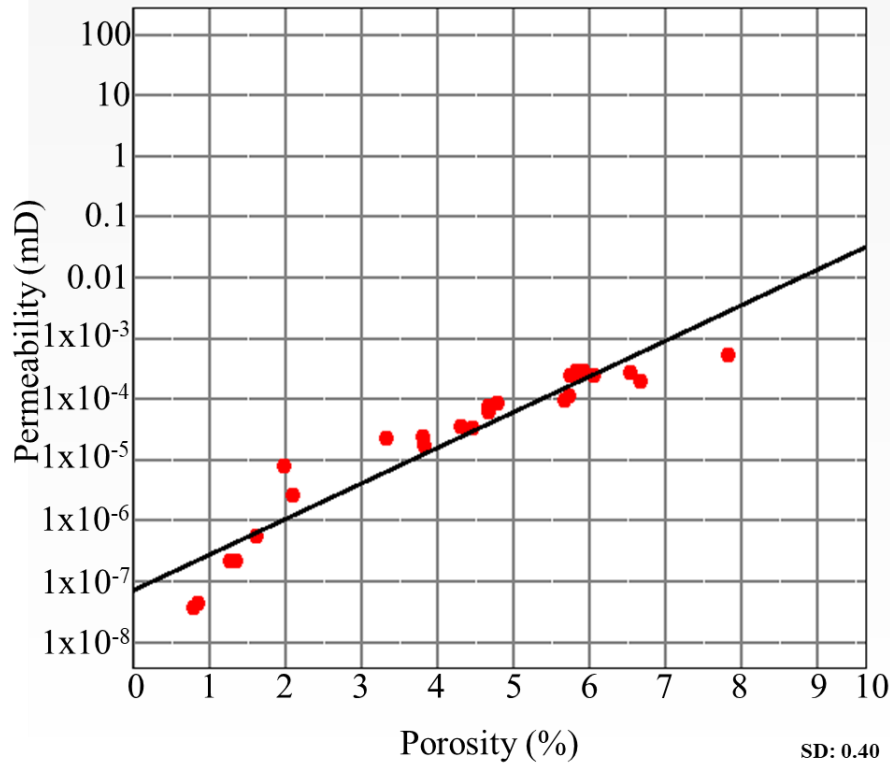


Fig. 3.9. Cross-plot of core porosity (%) vs core permeability (mD, Log scale) estimated based on petrophysical testing reports for core samples of the Lower Ireton, Duvernay and Majeau Lake Formations in wells 3 and 6 (Tables 3.1, 3.2, Fig. 3.9). See text for the equation.

TOC is the amount of organic carbon present in a rock. It was calculated from the Gamma Ray log using a modified equation from Zhang, (2015), developed for the Duvernay Formation in the Kaybob area:

$$TOC_{GR} = \frac{GR - 50}{350 - 50} * 7$$

Where:

TOC_{GR} : TOC calculated from GR (wt.%)

GR : Gamma Ray (gAPI)

The Young's modulus is an elastic constant equal to the ratio of longitudinal stress to longitudinal strain. The Poisson's ratio is the ratio of the transverse strain (normal to the applied

load) to the axial strain (in the direction of the applied load). Density, compressional and shear wave sonic logs were utilized to estimate the dynamic Young's modulus (YM) and Poisson Ratio (PR) using established equations (Zoback, 2010).

$$YM_{dyn} = \frac{\rho V_s^2 (3V_p^2 - 4V_s^2)}{V_p^2 - V_s^2}$$

$$PR_{dyn} = \frac{V_p^2 - 2V_s^2}{2(V_p^2 - V_s^2)}$$

Where:

ρ : density (gr/cm³)

V_s : Shear wave velocity (m/s)

V_p : Compressional wave velocity (m/s)

YM_{dyn} : Dynamic Young's Modulus (MPa)

PR_{dyn} : Dynamic Poisson's ratio (unitless)

The static Young's modulus and Poisson's ratio were estimated from the dynamic parameters by applying the following equations previously obtained from core data of the Duvernay Formation in the Kaybob area (Konstantiovskaia et al., 2021):

$$YM_{st} = 43.248 \ln (YM_{dyn}) - 132.09$$

$$PR_{st} = 0.9939 * PR_{dyn} - 0.0157$$

Where:

YM_{st} : static Young's modulus (GPa)

PR_{st} : static Poisson's ratio (unitless)

YM_{dyn} : dynamic Young's modulus (GPa)

PR_{dyn} : dynamic Poisson's ratio (unitless)

The unconfined compressive strength (UCS) refers to the maximum amount of axial compressive stress that a cylindrical material sample can endure under atmospheric conditions. The UCS was estimated from the static Young's modulus using modified Plumb's equation (Plumb, 1994):

$$UCS = 4.242 * YM_{st}$$

Where:

UCS : unconfined compressional strength (MPa)

YM_{st} : static Young's modulus (GPa)

The log-derived profiles of petrophysical and geomechanical parameters were calibrated by the core testing data in wells 1, 3, 4, 5, 6, and 7 available from core testing reports (Fig. 3.10) and hardness measurements obtained in this study (Fig. 3.10, Appendix A and B). The core data of fluid saturation was used to estimate average and range values of fluid saturation for each well and for main lithofacies (F2, F3 and F5). The depth interval of core location in the analyzed wells was corrected using the density log and core density data (Fig. 3.10). The depth shift for core data generally did not exceed 2-5 m.

To calibrate the unconfined compressive strength profiles, core hardness measurements were conducted in this study in wells 1, 3, 4, 5, 6 and 7. Additionally, the previously published measured hardness data for well 2 (Dong et al., 2018) was used in this study. Hardness measurements in core were taken by measuring 3-5 points at approximately every 50 centimeters using Proceq Bambino 2 Hardness Tester. The average value for each measured interval was estimated and used for validation of unconfined compressive strength profiles.

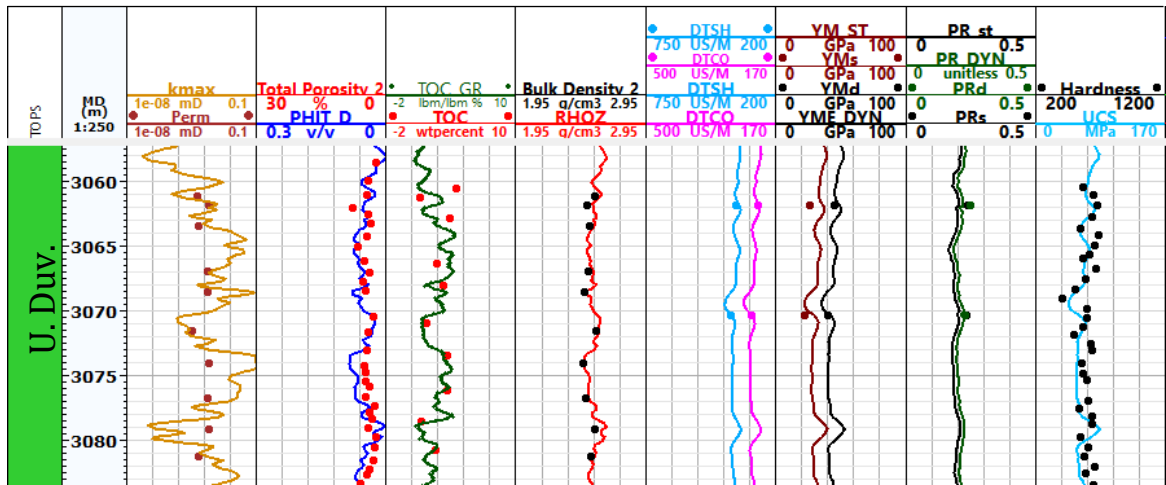


Fig. 3.10. Estimated profiles of petrophysical and geomechanical parameters (solid lines) and XRD and geomechanical core testing data and hardness measurements obtained in this study (dots) in Well 6. U. Duv., Upper Duvernay.

3.2.4. 3D models of the Duvernay Formation in selected areas, Kaybob area

The 3D models (A, B, C and D) of the Duvernay Formation in the Kaybob area (Fig. 3.2) were built in the selected polygons around studied horizontal wells A-D (Fig. 3.2). 3D modeling was conducted to analyze lateral and vertical distribution of lithofacies in the Duvernay Formation based on core description and well log analysis in neighboring vertical wells. The modeling was carried out in PetrelTM (<https://www.software.slb.com/products/petrel>) using well tops and depth surfaces of the top Ireton, Duvernay, and Leduc Formations and Beaverhill Lake Group. The original dataset of well tops and depth surfaces from the 3D Provincial Geological Framework Model of Alberta was modified by adding well tops of seven vertical wells 1-7 used in this study, in which core of the Duvernay Formation was described (Table 3.1). As no seismic data is available in this study, faults were not incorporated in the model. Sequence stratigraphy surfaces that were interpreted using core description and well logs analysis were incorporated in the models. As top of the Majeau Lake Formation was not interpreted in all wells, the combined thickness of the Duvernay and Majeau Lake Formations was mapped using the surfaces of the tops of the Duvernay Formation and Beaverhill Lake Group.

The structural grid of the 3D models was generated with lateral cell size 50 x 50 m for 3D Model C and 25 x 25 m for the others (Table 3.3). The number of layers is 105 for 3D model A, 120 for 3D model B, 195 for 3D model C, and 150 for 3D model D. The total number of cells in the geomechanical grid is 4.26×10^6 for 3D model A, 8.3×10^3 for 3D model B, 4.01×10^7 for 3D model C, and 4.53×10^5 for 3D model D. The choice of lateral cell size was made taking into account the length of lateral section of horizontal wells. The layering was conducted to obtain cell height that would assure detailed interpretation of facies in the Duvernay Formation. Fewer layers were generated in the overlying and underlying units with more homogeneous composition. Both gridding and layering were conducted to keep the total number of cells in the grid less than 1×10^6 , ensuring a practical processing time.

	Model A	Model B	Model C	Model D
Lateral cell size	25 x 25 m	25 x 25 m	50 x 50 m	25 x 25 m
Number of layers	105	120	195	150
Number of cells	4.26×10^6	8.3×10^3	4.01×10^7	4.53×10^5
Area	3.5 km x 7 km	2.2 km x 2.3 km	10 km x 13 km	1.1 km x 1.8 km
Thickness of the model	48 m	62 m	62 m	66 m
Average cell height	0.52 m	0.57 m	0.32 m	0.44 m

Table 3.3. Parameters of the 3D models build up around the horizontal wells in the Duvernay Formation, Kaybob area. See Fig. 3.2 for the location of the models.

Facies and property modelling of Gamma Ray, Bulk Density and Resistivity was carried out in four 3D models for selected areas around the studied horizontal wells A-D (Fig. 3.2). The lithofacies discrete logs were derived from core description and recorded well logs in vertical wells 1-7 and were subsequently upscaled into the models. The area of the 3D model around horizontal well C was extended to include additional vertical wells C1-C5 (Table 3.1) to increase the accuracy of the model because of the greater (~13 km) distance between the location of vertical well 5 with core testing data and horizontal well C (Fig. 3.2). Facies for vertical wells C1-C5 were estimated based on well log analysis and the comparison with the cored well 5, in which lithofacies from core were described.

Sequential indicator simulation (SIS) algorithm (Alabert, 1987) was used for modeling of facies and petrophysical properties between the vertical wells in the 3D models. The SIS algorithm is a stochastic modeling technique that operates on a pixel-based level, utilizing upscaled cells as the foundation for modeling the distribution of facies types.

3.2.5. Field structural methods

The fieldwork was conducted in Frontal Ranges of the Canadian Rocky Mountains, within the McConnel, Bighorn and Brazeau Thrusts in the Nordegg area. The fieldwork aimed to observe carbonate-rich and carbonate-poor shale facies of the Perdrix Formation and analyze distribution of fractures in units with variable content of carbonate material. The field observations are compared to the results of fracture analysis in the Duvernay Formation in the subsurface.

Structural measurements of bedding, cleavage, intersection lineation, faults and fractures were collected using measuring tape and Brunton compass. The described parameters for each fracture set included fracture type (open or healed), fracture mineral filling, fracture dip azimuth and dip angle, height, and aperture. Several geological parameters that are known to control fracture spacing in subsurface rock units (Nelson, 2001) were documented, including composition, grain size, porosity, bed thickness, structural position. Additionally, fracture behavior at intersection with bedding surfaces was analyzed.

Fracture intensity is estimated along selected observation lines along the cross-sections and within circles on the bedding surfaces (Mauldon et al., 2001). The structural position of the site of fracture intensity measurements was analyzed. Fracture intensity may vary depending on the strain of the rocks in a given structural position, e.g., on the fold limb or fold hinge zone and distance to a fault (Nelson, 2001). In addition, fracture type vary depending on their relationship with the structure (Stearns, 1968). Type 1 fractures are described as tensile fractures oriented perpendicular to the fold axis, and the Type 2 fractures are tensile but parallel to the fold axis and perpendicular to bedding.

Samples of the Perdrix shale with mineralized fractures (generally calcite veins) were collected for fluid inclusion study (Table 3.4). 11 open thin sections were prepared from samples

collected at 7 different observation points. Thin sections were described using a Nikon Trinocular microscope.

Sample	Location	Stop N°	Brief description
HC-01-S1	Hoody Creek, Nordegg	01	Black fissile shale
HC-03-S1	Hoody Creek, Nordegg	03	Calcite vein from the shear zone
HC-06-S1	Hoody Creek, Nordegg	06	Dark grey shale with subvertical Calcite-filled tensile fractures
HC-06-S2	Hoody Creek, Nordegg	06	Brownish shale with subvertical Calcite-filled tensile fractures
HC-08-S1	Hoody Creek, Nordegg	08	Calcite-filled tensile fractures orthogonal to the bedding between boudins in carbonate-rich mudrock
HC-12-S2	Hoody Creek, Nordegg	12	Carbonate-rich mudrock with horizontal Calcite veins
HC-12-S3	Hoody Creek, Nordegg	12	Shales with horizontal Calcite veins
HC-12-S4	Hoody Creek, Nordegg	12	Calcite veins from thrust fault zone
HC-15-S1	Hoody Creek, Nordegg	15	Mirror surface with slickensides on the limb of a drag fold
W-06-S1	Wapiti Creek, Nordegg	06	Bioclastic limestone interbedded with black shales
W-06-S2	Wapiti Creek, Nordegg	06	Black shales with thin subhorizontal ca-rich interlayers

Table 3.4. List of samples collected for studying fractures in the Perdrix shale.

The field structural observations were statistically analyzed and plotted in stereonet plots and rose diagrams to determine orientation of principal stresses that acted during the different deformation phases. The orientation of bedding, axes of secondary folds, intersection lineation, cleavage and slickenlines on fault surfaces were used to infer orientation of shortening. The stereonet plots helped to illustrate different sets of fractures and analyze their structural position

with respect to mesoscopic folds and faults (Cooper, 1992). The structural data were projected on a new detailed geologic cross-section that was constructed in this study for the fieldwork area. The NE-SW cross-section is oriented at high angle to the strike of the McConnel Thrust, subparallel to the transport direction. The cross-section was built based on field observations and previously published maps (Mountjoy and Price, 1974; Douglas, 1956) and regional cross-sections (Bégin and Veilleux, 2017).

Chapter 4: RESULTS

This chapter describes the results of this study in seven sections. The first section involves the facies description from core of the Duvernay Formation carried out in seven vertical wells 1-7 (Fig. 4.6; Table 3.1). The second section includes the 3D structural model of the Kaybob area and the 3D facies models of the formation built up in 4 areas around the horizontal wells studied in this project (Fig. 4.6; Table 3.1). The third and fourth sections describe the petrophysical and mechanical properties of the mudrocks of the Duvernay Formation, respectively, based on the analysis of well-logs and core data. The fifth section contains fracture characterization in mudrocks of the Duvernay Formation based on core and thin section descriptions. The sixth section involves the analysis of natural fractures, drilling-induced fractures and borehole breakouts using FMI logs from 4 horizontal wells. Finally, the last section delineates the study of fractures in the Perdrix Formation, an outcrop analog of the Duvernay Formation.

4.1. Lithofacies of the Duvernay Formation

The Duvernay Formation in the Kaybob area is consisted of mostly mudrocks with variable amount of organic-rich matter (kerogen), clay (generally illite), silica (quartz), carbonate component (calcite, dolomite) and pyrite. Seven lithofacies were distinguished in core of the Duvernay Formation (Table 4.1). Lithofacies were defined by color, composition, grain size, sedimentary structures and mechanical properties of the mudrocks. The values of total organic carbon (TOC) and bulk density (RHOB) provided for each facies are based on core data of petrophysical testing reports in seven vertical wells (Fig. 4.6) available from AER reports (see Chapter Data and Methods).

4.1.1. F1 Relatively coarse-grained carbonate-rich organic-poor silty mudstones

Facies F1 is identified in the upper Duvernay Member. F1 is composed of light-grey mudrocks with mostly silt-size grains (calcite, quartz, dolomite) and in smaller proportion by mud-size grains (clay) (Fig. 4.1.A). The sedimentary structure is faint horizontal lamination to massive (Fig. 4.1.B). This facies is carbonate-rich, supported by the reaction with HCl. The

average TOC in mudrocks of F1 is 1.16 wt.% (range 0.76-1.48 wt.%) based on core measurements. The average bulk density (RHOB) is 2.62 gr/cm³ (range 2.56-2.66 gr/cm³).

4.1.2. F2 Planar-laminated clay-bearing organic-rich biosiliceous mudstones

Facies F2 is determined in the upper and lower Duvernay Members and rarely in thin intervals in the middle Duvernay Member. F2 consists of dark brown mudstone with subordinate thin intervals (<1 mm of thick) of silty material (quartz, calcite, dolomite grains and fossil fragments) (Fig. 4.2.A). F1 is faintly laminated, with rare thin (<1 mm) subparallel silty carbonate-rich laminae. The composition of F2 is high in organic matter, with little to no reaction with HCl (Fig. 4.2.B). The average TOC in mudrocks of F1 is 3.19 wt.% (range 2-5.25 wt.%). The average bulk density (RHOB) is 2.49 gr/cm³ (range 2.43-2.6 gr/cm³).

4.1.3. F3 Planar-laminated clay-bearing organic-rich mudstones, locally with thinly layered light-grey carbonate-rich silty interbeds

Facies F3 is described in the upper and lower Duvernay Members. It consist of dark-grey mudrocks with mud-silt grains interlaminated with light-grey silt and fine-sand grains (Fig. 4.2.C). Coarser light-grey laminae of F3 are composed of silt to fine-sand size carbonate and quartz grains, fossil fragments and in less proportion pyrite. Crystals of anhydrite are very rare. Very fine dark-grey laminae consist mostly of clay, organic matter (kerogen) and pyrite. F3 is horizontally laminated, with the very fine alternation (1-2 mm) between light carbonate-rich and dark organic-rich layers (Fig. 4.2.D). F3 is rich in carbonate composition as it reacts vigorously with HCl. Pyrite in form of lens-shaped aggregates or microlaminae (F7) is commonly found within F3. The average TOC of mudrocks in F3 is 2.71 wt.% (range 1.5-5 wt.%). The average bulk density (RHOB) is 2.53 gr/cm³ (range 2.43-2.65 gr/cm³).

4.1.4. F4 Fossiliferous bioturbated wackestones

Facies F4 is recognized in the upper Duvernay Member. F4 consists of light to medium brown and grey, massive to faintly planar-laminated and rarely wavy-laminated silty and sandy wackestones (Fig. 4.3.A). It is composed of fossil fragments (mostly Styliolinids and tentaculitid), carbonate (calcite) and quartz clastic grains and rarely pyrite lens-shaped

aggregates (Fig. 4.3.B, C and D). F4 is usually moderate to intensely bioturbated with mud and silt-infilled burrows. F4 is characterized by strong reaction to HCl. The average TOC for F4 is 2.45 wt.% (range 1.6-3.3 wt.%). The average bulk density (RHOB) is 2.56 gr/cm³ (range 2.5-2.64 gr/cm³).

4.1.5. F5 Carbonate-rich nodular mudstones

Facies F5 is described in the Middle Duvernay and in thin intervals in the Upper Duvernay. It is composed of light-grey mudstones to wackestones nodules within a medium light to dark grey argillaceous to calcareous mud matrix (Fig. 4.4. A). Mudstone nodules are composed of clay-rich to fine-sand-size detrital calcite grains and fossil fragments (Styliolinids and tentaculitid) (Fig. 4.4.B). Nodules are usually oval (2 mm - 150 mm thick in core section), and they are wrapped by beds of more ductile clay-rich mudstones. The matrix is massive to planar laminated, with beds 1 mm to 7 mm thick. F5 is commonly intensely bioturbated, with mud- and silt- infilled burrows (rarely with pyrite). F5 has high carbonate-content, supported by strong reaction to HCl. The average TOC for F5 is 0.64 wt.% (range 0.2-1 wt.%). The average bulk density (RHOB) is 2.66 gr/cm³ (range 2.6-2.69 gr/cm³).

4.1.6. F6 Clay-rich fissile mudstones

Facies F6 is identified in the Majeau Lake Formation and in thin intervals within the upper Duvernay Member. It consists of dark brown clay-rich mudrocks with discontinuous pyrite lens-shaped aggregates (<5 mm thick). F6 is fissile and horizontally laminated (Fig. 4.5.A and B). This facies is rare, and its average cumulative thickness in studied wells is less than 50 cm. F6 is high in clay, with little to no reaction to HCl. TOC and density core data is not available for F6.

4.1.7. F7 Discontinuous pyrite-rich lens-shaped aggregates and laminae

Facies F7 is recognized in the upper and lower Duvernay Member. It appears as thin intervals of 1-3 mm thick within F2, F3 and F6. It is composed of discontinuous pyrite-rich lens-shaped aggregates and laminae (2 mm - 20 mm thick) within a dark-grey clay-size organic-rich

matrix, sometimes with fossil fragments (Fig. 4.5.C and D). TOC and density core data is not available for F7.

	F1	F2	F3	F4	F5	F6	F7
Lithology	Relatively coarse-grained carbonate-rich organic-poor silty mudstones	Planar-laminated clay-bearing organic-rich biosiliceous mudstones	Planar-laminated clay-bearing carbonate-rich mudstones, locally with thinly layered light-grey carbonate-rich silty interbeds	Fossiliferous bioturbated wackestones	Carbonate-rich nodular mudstones	Clay-rich fissile mudstones	Discontinuous pyrite-rich lens-shaped aggregates and laminae
Colour	Light grey	Dark brown	Dark grey	Light brown/grey	Light grey	Dark brown	Dark grey
Bedding	Faint planar laminae, massive	Wavy, planar laminae	Wavy, planar laminae	Wavy, planar laminae	Nodular, planar laminae	Planar laminae	Discontinuous planar laminae
Grain Size	Silty mudstone	Clay-rich mudstones	Silty and clay-rich mudstone	Wackestone	Mudstone, wackestone	Clay-rich mudstone	Clay-rich mudstone
Average TOC (wt.%)	1.16 ± 0.35	3.19 ± 1.00	2.71 ± 0.96	2.45 ± 1.19	0.64 ± 0.64	X	X
Average RHOB (gr/cm³)	2.62 ± 0.04	2.49 ± 0.04	2.53 ± 0.06	2.56 ± 0.05	2.66 ± 0.03	X	X

Table 4.1. Summary characteristics of the lithofacies of the Duvernay Formation based on core description in seven vertical wells 1-7 (Table 3.1, Fig. 4.6).

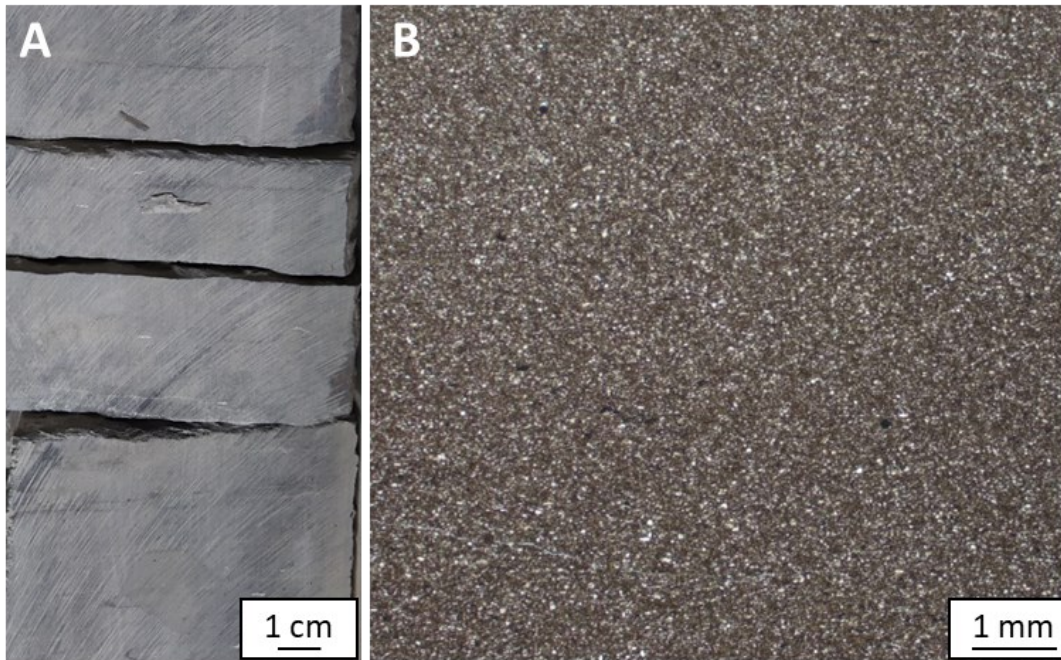


Fig. 4.1. A) Light-grey faintly laminated to massive silty mudstones, facies F1 (3260.18m, well 3). B) Thin section of a weakly laminated carbonate-rich silty mudstone (photo taken from CRC report R8955, 3526.03m, well 7). See Fig. 4.6 and Table 3.1 for the name and location of the wells.

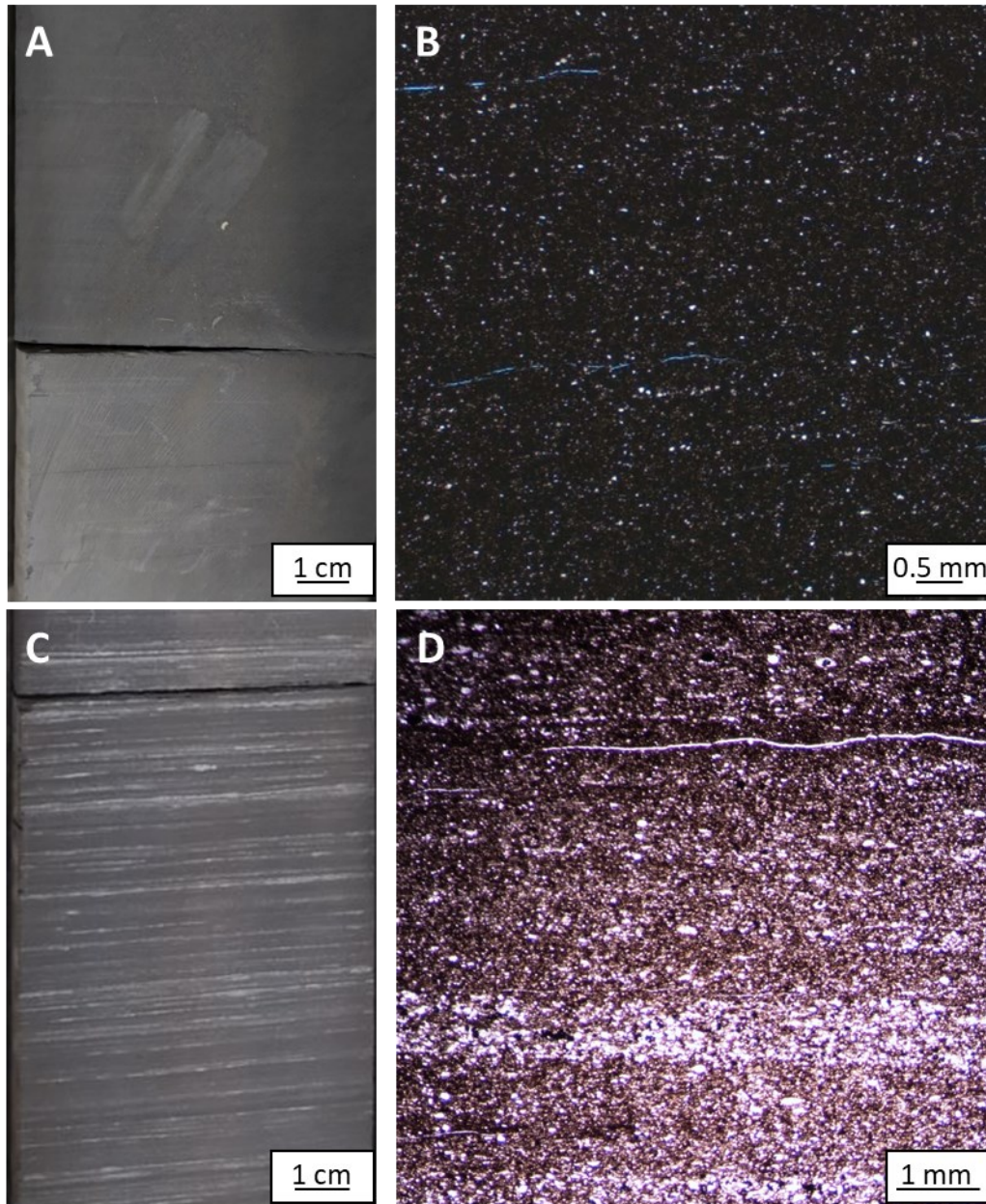


Fig. 4.2. A) Faintly planar-laminated clay-bearing mudstones of facies F2 (3279.12m, well 3). B) F2 thin section, showing faint planar-laminated structure of the organic-rich mudstone with a few bioclasts (photo of thin section is taken from CRC report R8955, 3537.75m, well 7). C) Planar laminated mudstones with thinly layered light-grey carbonate-rich silty interbeds of facies F3 (3061.18m, well 5). D) F3 thin section, displaying the alternation of organic/clay-rich and carbonate-rich interbeds (3190.93m, well 4). See Fig. 4.6 and Table 3.1 for the name and location of the wells.

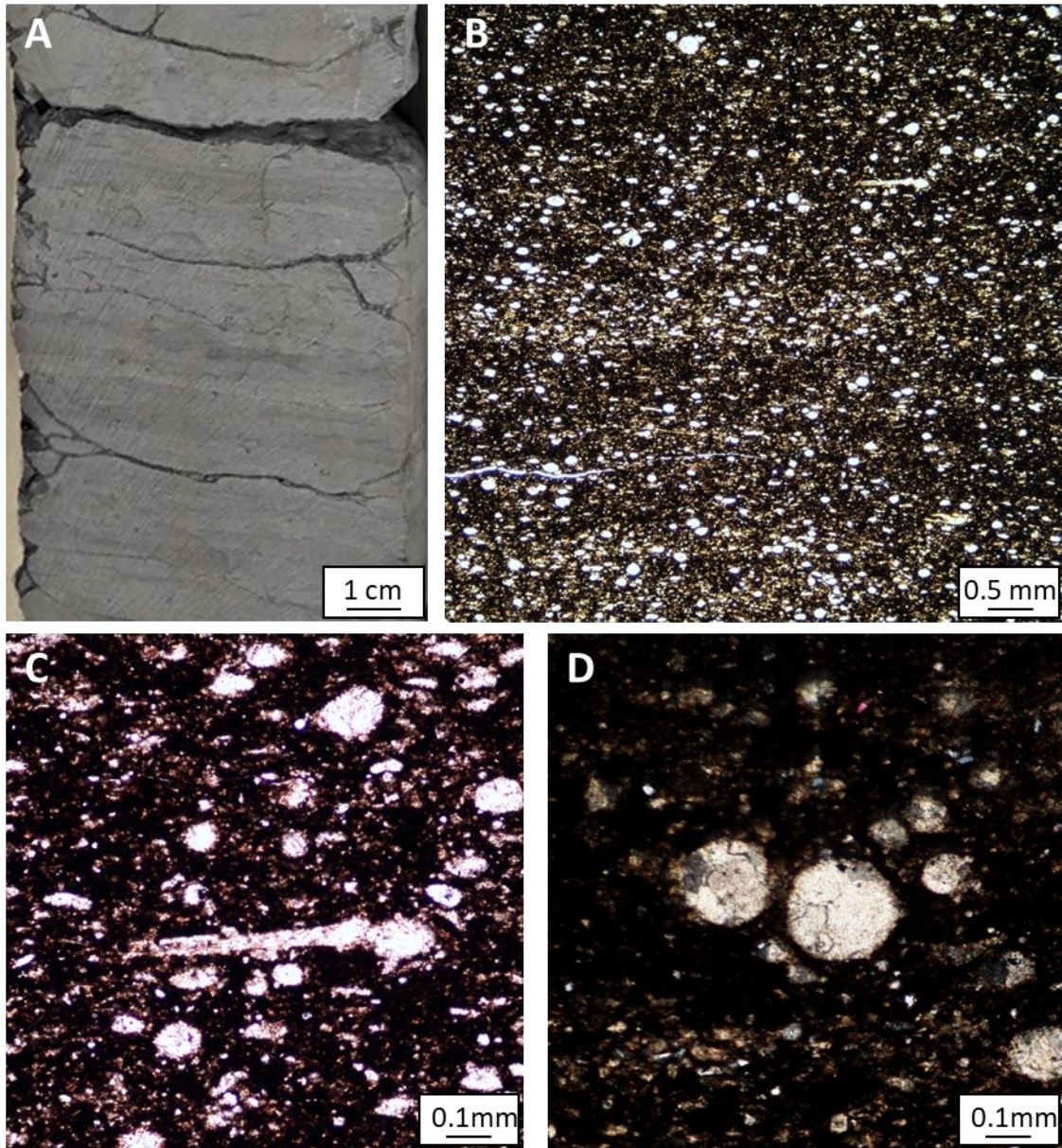


Fig. 4.3. A) Fossiliferous wackestones, facies F4 (3287.60m, well 3). B)-D) F4 thin section: B) carbonate-rich fossiliferous wackestones with Styliolinids (3528.4m, well 7). C) Close up view of Styliolinids (3528.4m, well 7). D) Close up view of a transversal section of Styliolinids (3260.24m, well 6). See Fig. 4.6 and Table 3.1 for the name and location of the wells.

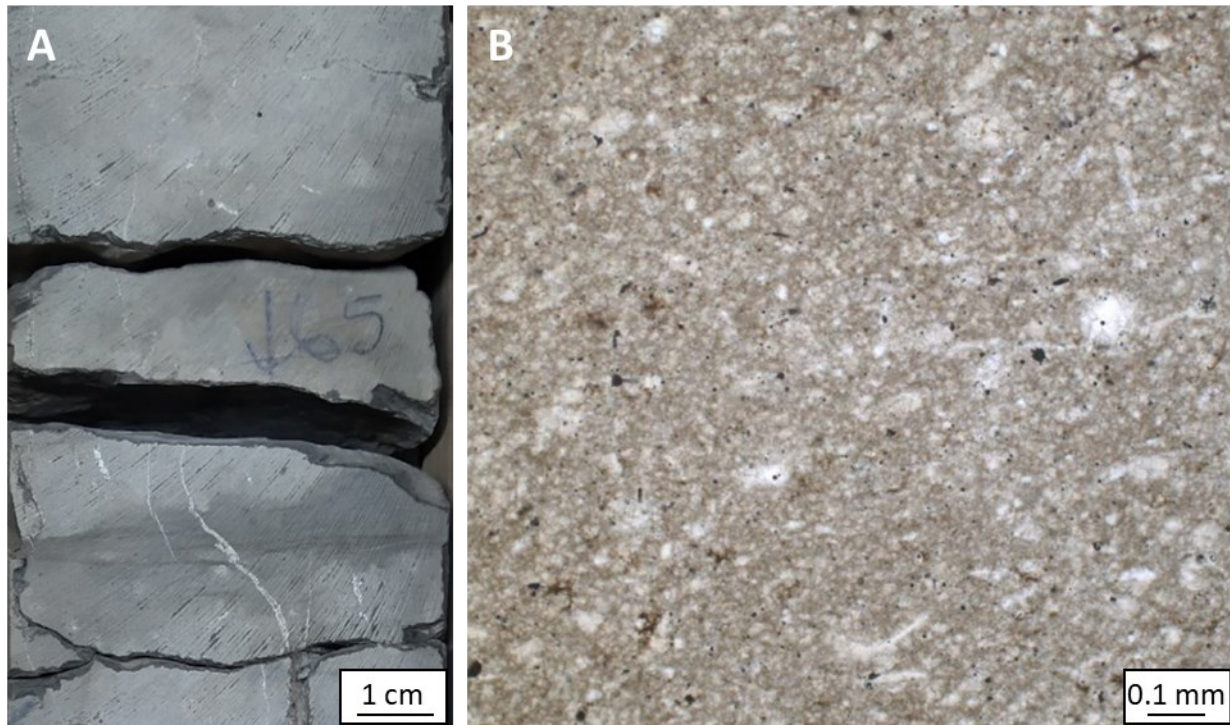


Fig. 4.4. A) Nodular mudstone, facies F5 (3304.82m, well 3). B) F5 thin section of mudstone nodule showing faint lamination to massive structure and fossils fragments (photo taken from CRC report R8955, 3541.70m, well 7). See Fig. 4.6 and Table 3.1 for the name and location of the wells.

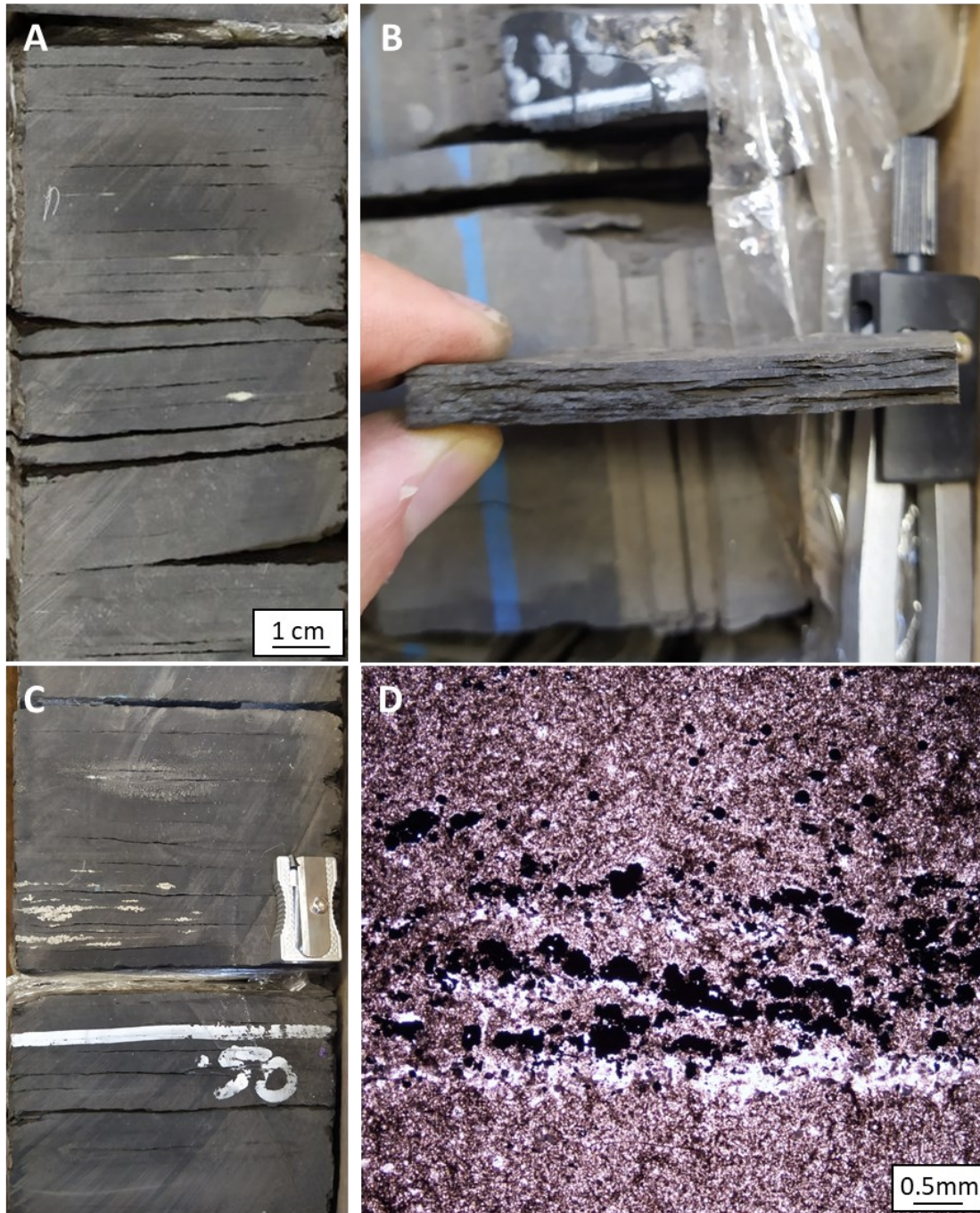


Fig. 4.5. A) Clay-rich fissile mudstones, facies F6 (3198.69m, well 4). B) F6, close up view of A) fissility in the mudstone. C) Discontinuous pyrite-rich lens-shaped aggregates and laminae, facies F7 (3203.45m, well 4). D) F7, thin section showing pyrite-rich laminae in carbonate-rich mudstone of the Perdrix Formation (sample 'W-06-S2' collected at the outcrop of the Wapiti Gap, Nordegg area, Alberta). See Fig. 4.6 and Table 3.1 for the name and location of the well and Fig. 4.64 for the outcrop location.

4.2. 3D structural and facies models of the Duvernay Formation in the Kaybob Area

4.2.1. 3D Structural model of the Duvernay Formation

The organic-rich Duvernay Formation in the Kaybob Area is limited in the south, southwest and west by the reefs of the Leduc Formation (Fig. 4.6). The elevation of the top of the Duvernay in the study area varies from 1750 meters below sea level in the NE to 2850 meters below sea level in the W, slightly dipping to the SW at $\sim 5^\circ$.

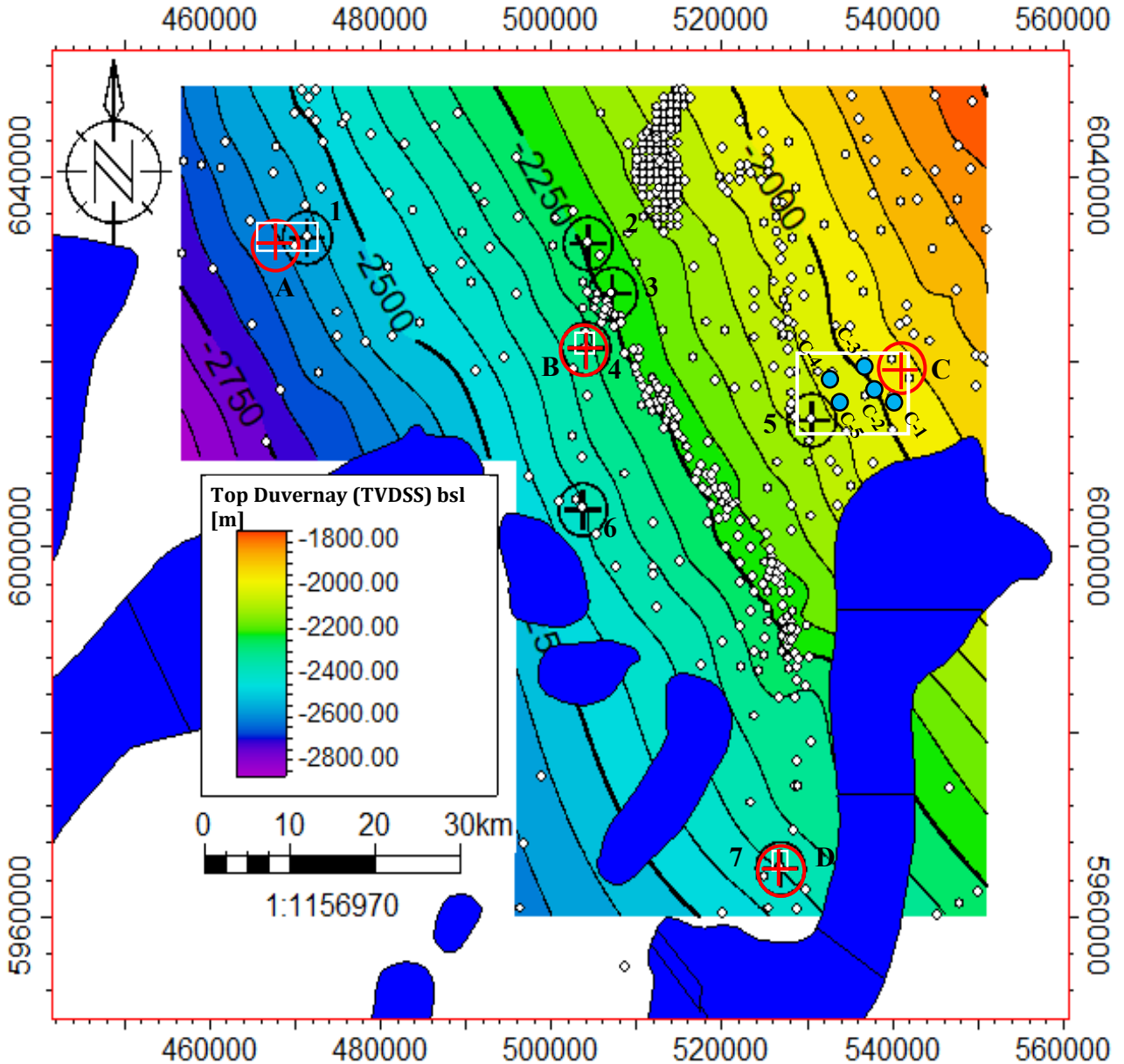


Fig. 4.6. Structural surface of the top of the Duvernay Formation (NAD 83 UTM zone 11 N). The white circles define top picks of the Duvernay Formation imported from the 3D Provincial Geological Framework Model of Alberta (2019) that were used for building the surface. Wellhead location of wells

analyzed in this study: A-D, four horizontal wells (red circles). 1-7, seven vertical wells, in which core was described (black circles). C-1 to C5, wellhead location of vertical wells (blue circles) used in 3D lithofacies and petrophysical models (white rectangles). The pairs of wells 4 and B and wells 7 and D belong to common well pads, respectively. Top picks from the studied wells were added to generate the surface. Blue polygons delineate the simplified geometry of the Leduc reefs. TVDSS, bsl, True vertical depth below sea level. See Table 3.1 for the name and location of the wells.

The carbonate-rich rocks of the Beaverhill Lake Group located below the Duvernay and Majeau Lake Formations dips towards the SW at slight angle ($\sim 5^\circ$). The depth of the Top of the Beaverhill Lake varies from 1800 meters below sea level in the NE to 2900 meters below sea level in the W (Fig. 4.7).

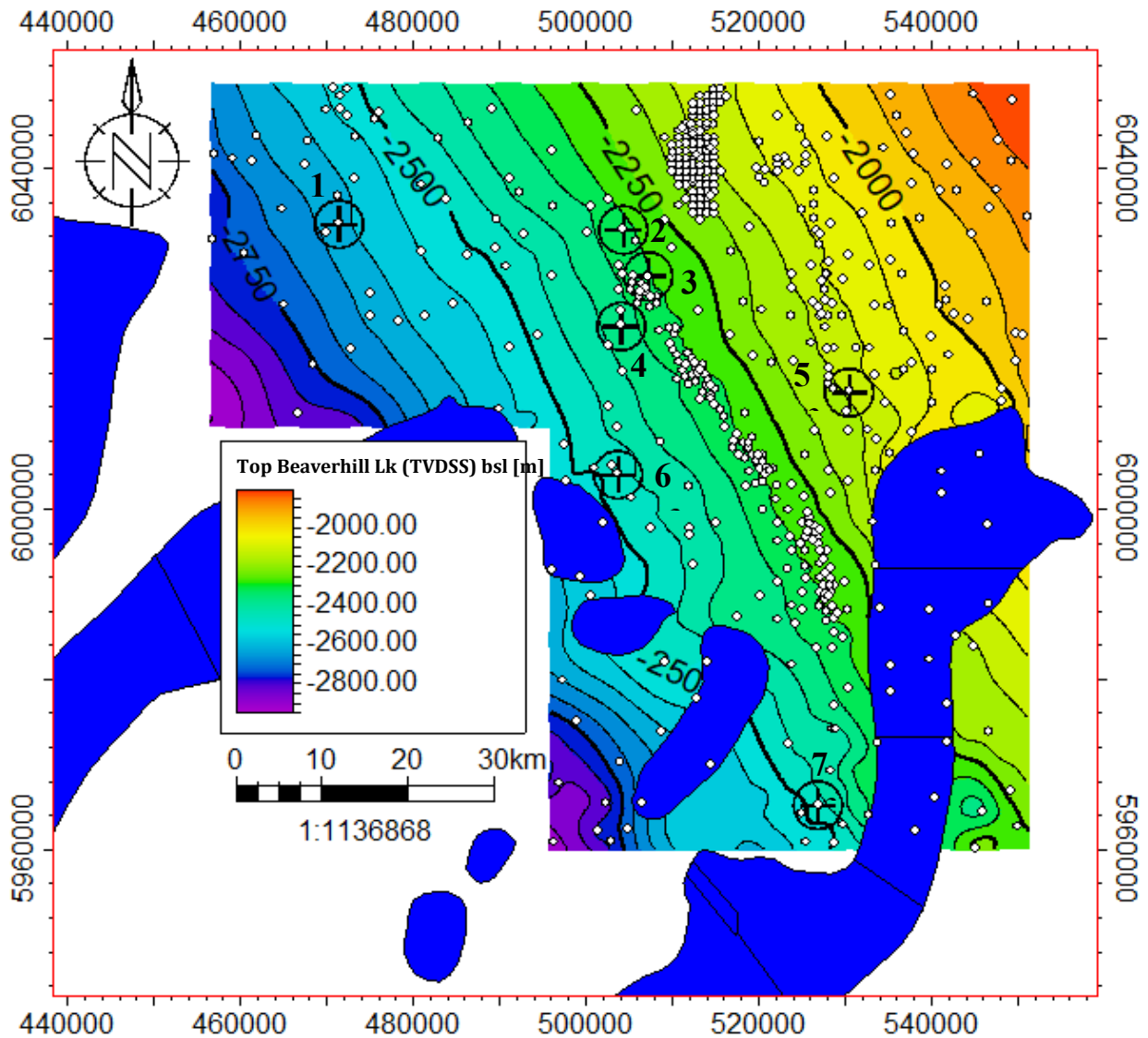


Fig. 4.7. Structural surface of the top of the Beaverhill Lake Group (NAD 83, UTM zone 11 N). The white circles define top picks of the Beaverhill Lake Group imported from the 3D Provincial Geological Framework Model of Alberta, 2019 used for building the surface. The black circles indicate the location of wellheads of the vertical wells (1-7), in which core was studied (Table 3.1); top picks from these wells were added to generate the surface. The blue polygons depict simplified geometry of the Leduc reefs. TVDSS, bsl, True vertical depth below sea level. See Table 3.1 for the name and location of the wells.

Thickness of the Duvernay and Majeau Lake Formations was estimated together as the Majeau Lake Formation is not recognized in all studied wells. The cumulative thickness of these formations is variable within the Kaybob area (Fig. 4.8). The thicker areas correspond to the center and southern parts of the basin, where thickness can reach 80 m. Thickness is reduced to the NE and NW with values lower than 45 m, and around the Leduc Reefs, which laterally replace the Duvernay and Majeau Lake Formations.

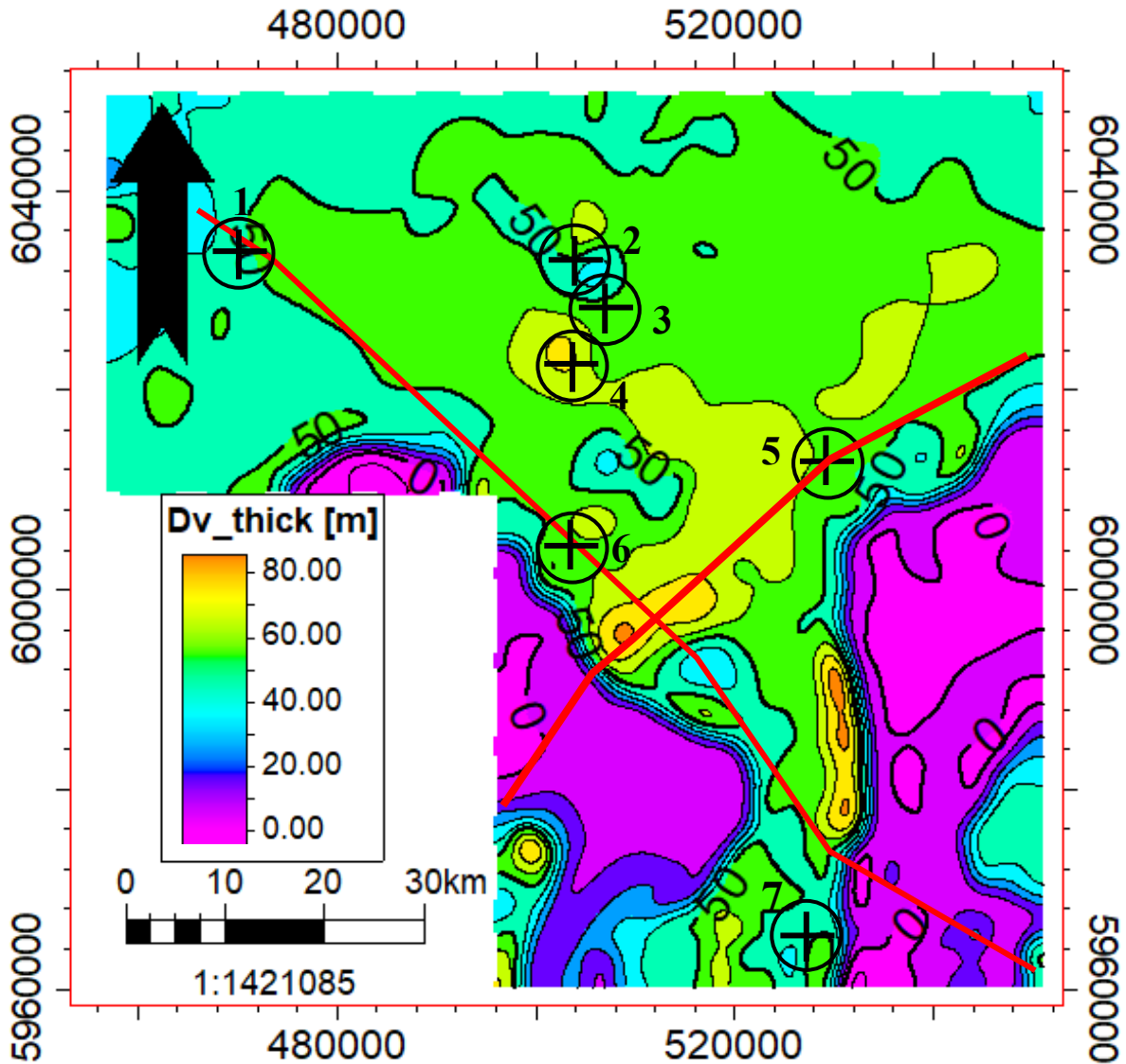


Fig. 4.8. Isopach map of Duvernay and Majeau Lake Formation. Note the increase of thickness of the Duvernay Formation towards the center of the basin and pinching out of the mudrocks around the Leduc Reefs. The red lines indicate the location of the cross-section displayed in Fig. 4.9 and Fig. 4.10. See Table 3.1 for the name and location of the wells.

Based on core description in studied seven vertical wells 1-7 (Fig. 4.6, Table 3.1), lithofacies F2 and F3 constitute of about 80% and F5 consists of around 15% of the total thickness Duvernay Formation (Fig. 4.9). The cumulative thickness of F1, F4, F6, and F7 facies consists of only 5% of the total thickness of the Duvernay Formation. The analysis of petrophysical and mechanical properties of the mudrocks of the Duvernay Formation is carried out for facies F2, F3 and F5, as they contribute 95% of the total thickness of the formation.

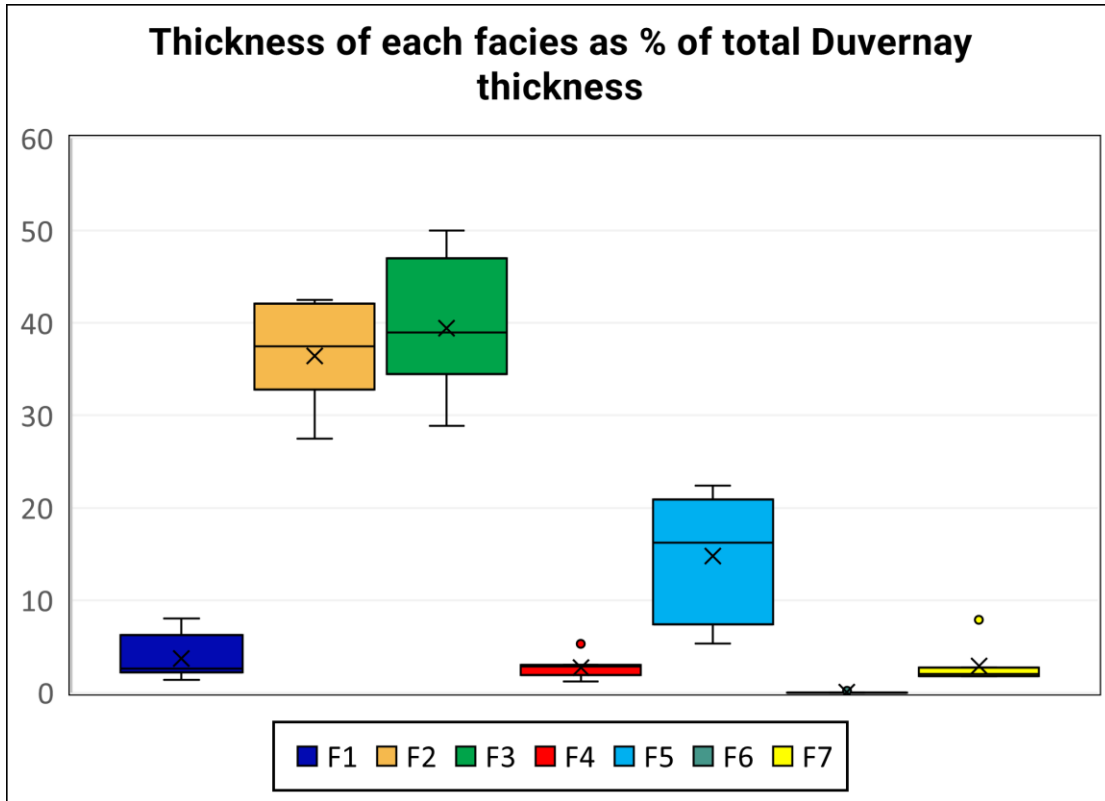


Fig. 4.9. Estimated thickness of facies F1-F7 as percent of total thickness of the Duvernay Formation based on core description in seven vertical wells 1-7 (see Table 3.1 and Fig. 4.6). Note the greater thickness of F2 and F3 compared to other facies. See Table 4.1 for the facies description.

Thickness of the Ireton Formation that overlies the Duvernay Formation varies from 150 m to 200 m across the study area, being thicker than the combined thickness of the Duvernay and Majeau Lake Formations. Thickness of the Ireton Formation increases close to the Leduc Reefs in the SW and SE, where the upper beds of the Ireton Formation overlap the reefs (Fig. 4.10 and

Fig. 4.11). Thickness of the Duvernay and Majeau Lake Formations decreases towards the NE and NW from about 80 m to < 45-50 m.

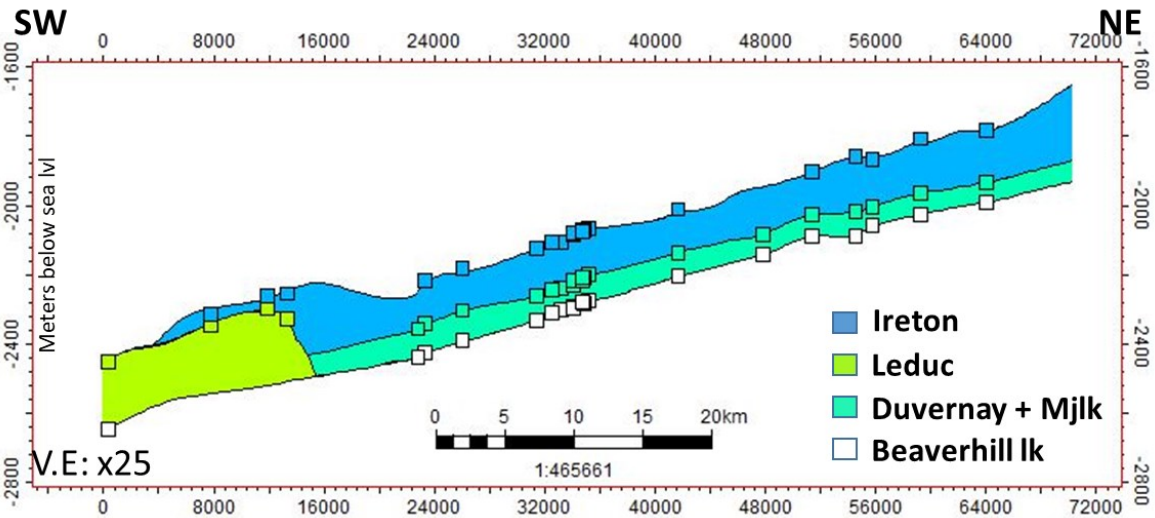


Fig. 4.10. Cross-section SW-NE of the 3D structural model, Kaybob Area. Surfaces and top picks were imported from the 3D Provincial Geological Framework Model of Alberta, 2019 <https://ags.aer.ca/publication/3d-pgf-model-v2> and modified to include the picks from the studied wells. See Fig. 4.8 for the cross-section location. Squares indicate well top picks. The Beaverhill Lake Group is below the Duvernay and Leduc Formations.

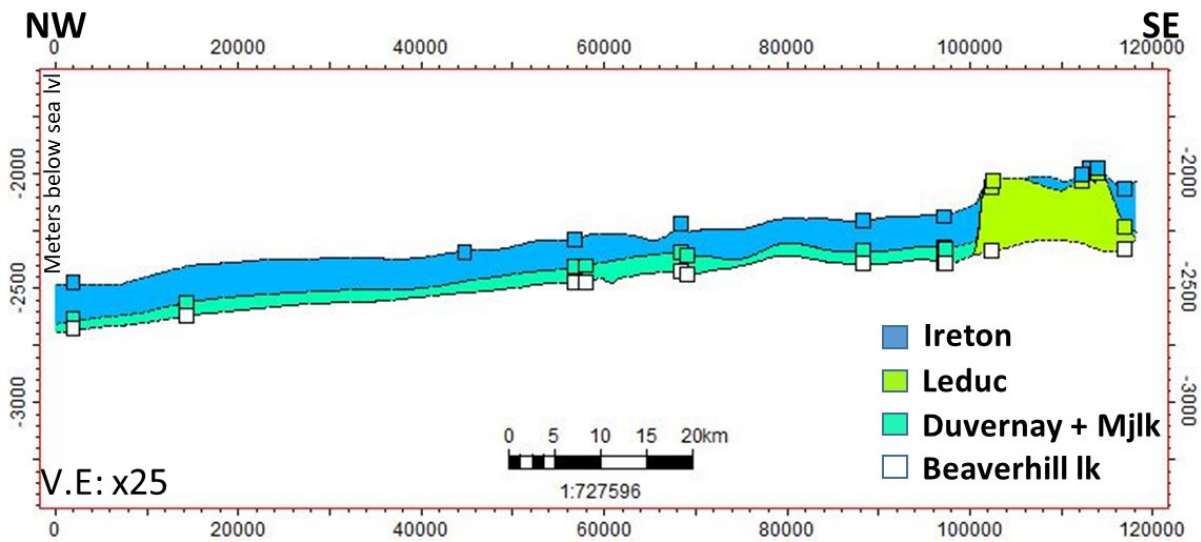


Fig. 4.11. Cross-section NW-SE of the 3D structural model, Kaybob Area. Surfaces and top picks were imported from the 3D Provincial Geological Framework Model of Alberta, 2019 <https://ags.aer.ca/publication/3d-pgf-model-v2> and modified to include the picks from the studied wells. See Fig. 4.8 for the cross-section location. Squares indicate well top picks. The Beaverhill Lake Group is below the Duvernay and Leduc Formations.

4.2.2. The 3D facies models of the Duvernay Formation

The 3D facies models of the Duvernay Formation were built around horizontal wells A, B, C and D using geostatistic methods and based on the core facies description obtained in vertical wells located at the same well pad or in the nearest (< ~5 km) position (Fig. 4.6). The lithofacies description of vertical wells was used to interpret distribution of facies of the Duvernay Formation along horizontal wells A-D and correlate the facies with fracture intensity determined from image logs in the horizontal wells (see section 4.5). It should be noted that interpreted facies distribution in 3D models have variable degree of uncertainty that increases in the areas away from vertical wells, in which facies were described from core data.

Model A (Fig. 4.12 and Fig. 4.13) is located in the northwestern area within the Kaybob area (see Fig. 4.6 to see the location of the model). According to the model, the upper Duvernay Member is mostly composed of organic-rich facies F2 and F3 with thin and localized carbonate-rich facies F1 and F5. The middle Duvernay consists of the carbonate-rich nodular mudstones of F5. The lower Duvernay contains mostly the organic-rich facies F3. The horizontal well A is targeting organic-rich facies F2 and F3 at the base of the upper Duvernay Member (Fig. 4.12 and Fig. 4.13).

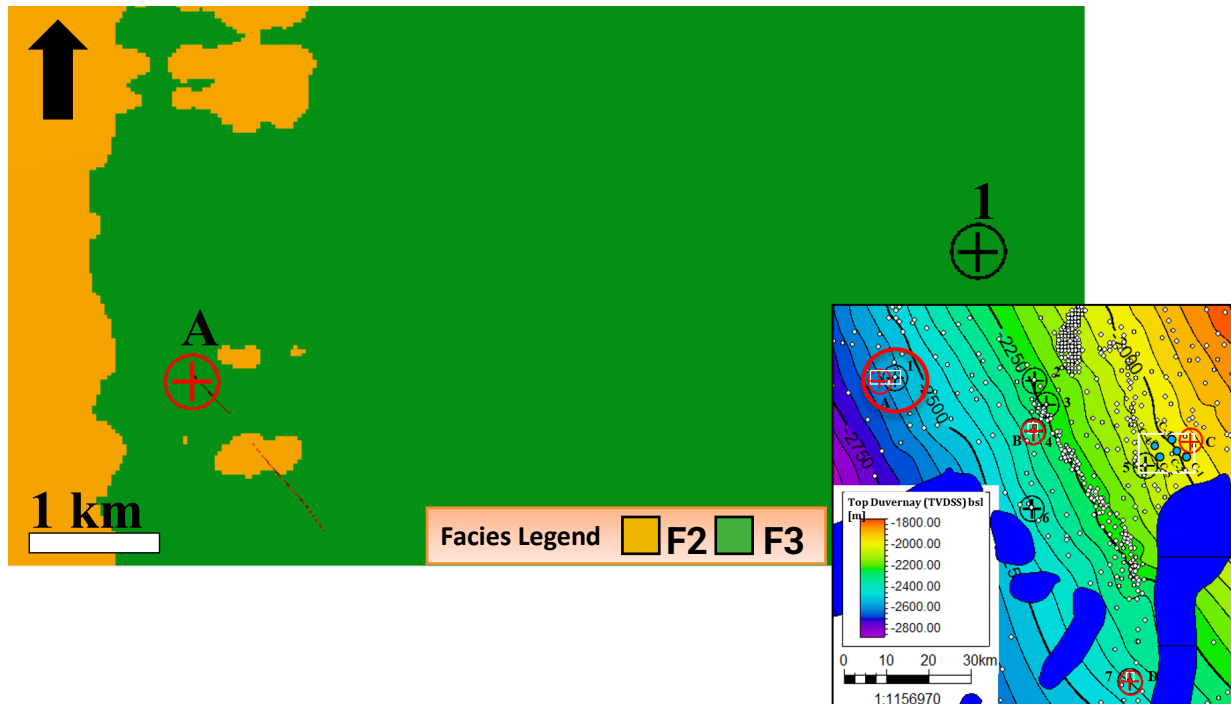


Fig. 4.12. Map of modelled facies of the Duvernay Formation in 3D model A along the horizon at the depth where the horizontal well A was landed. Red circle and line, wellhead location and trajectory of horizontal well A. Black circle, wellhead location of vertical well 1, in which core was described. The distance between well 1 and well A is 5.2 km. Table 3.1 for name of the wells within the Kaybob area. See Table 4.1 for facies description. The red circle within the inset map shows the location of wells A, 1 and model A.

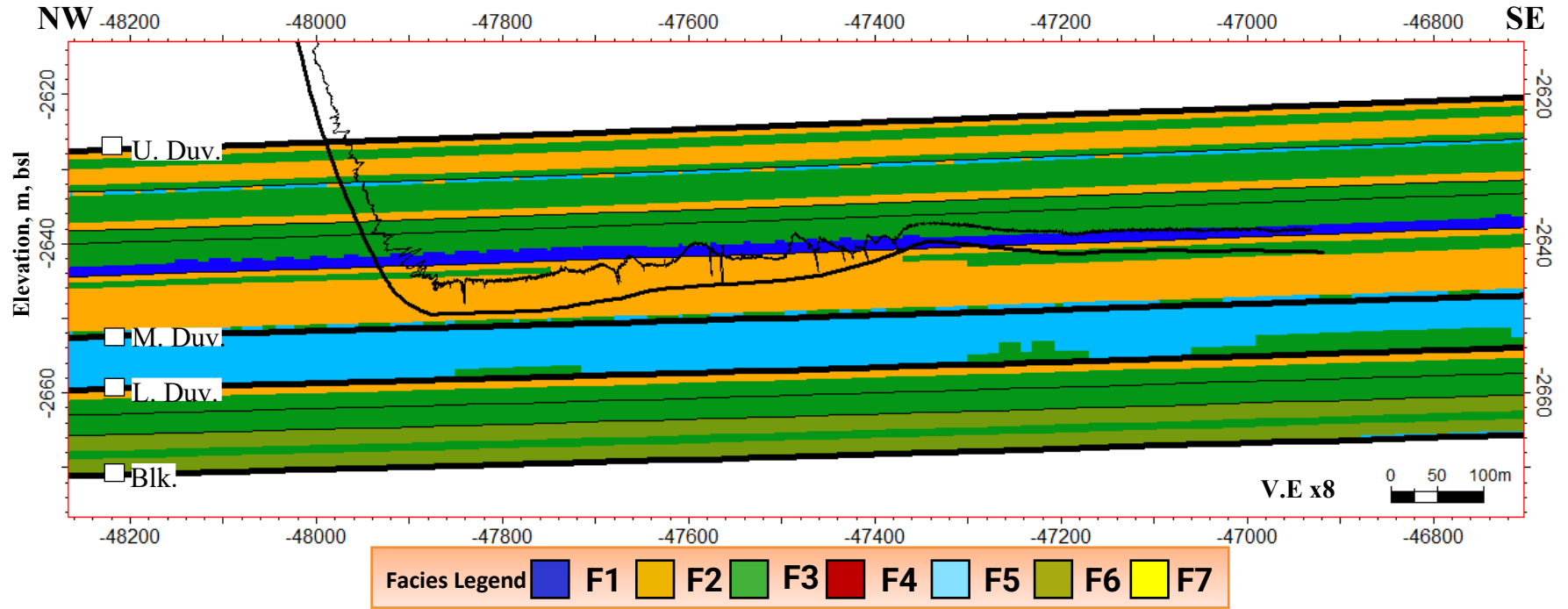


Fig. 4.13. Cross-section NW- SE along horizontal well A in 3D model A, displaying modelled facies of the Duvernay Formation. The well was landed mostly in organic-rich facies F2 and F3 of the upper Duvernay Member. Thin black line indicates GR log along well A trajectory. Formation tops: U.Duv., Upper Duvernay; M. Duv., Middle Duvernay; L.Duv., Lower Duvernay; Blk., Beaverhill Lake. See Fig. 4.6, 4.12 and Table 3.1 for location of the well, Table 4.1 for facies description.

Model B (Fig. 4.14 and Fig. 4.15) is located in the middle of Kaybob area (see Fig 4.6 for location of the model). Similarly to model A, the upper Duvernay Member is mostly composed of organic-rich facies F2 and F3 with thin and localized carbonate-rich facies F1, F4 and F5. The middle Duvernay consists of mostly the carbonate-rich nodular mudstones of F5 with relatively thin (2-3 m) layers of organic-rich facies F2 and F3. The lower Duvernay predominantly contains organic-rich facies F2 and F3. The horizontal well B is targeting organic-rich facies F2 and F3 at the base of the upper Duvernay Member (Fig. 4.14 and Fig. 4.15).

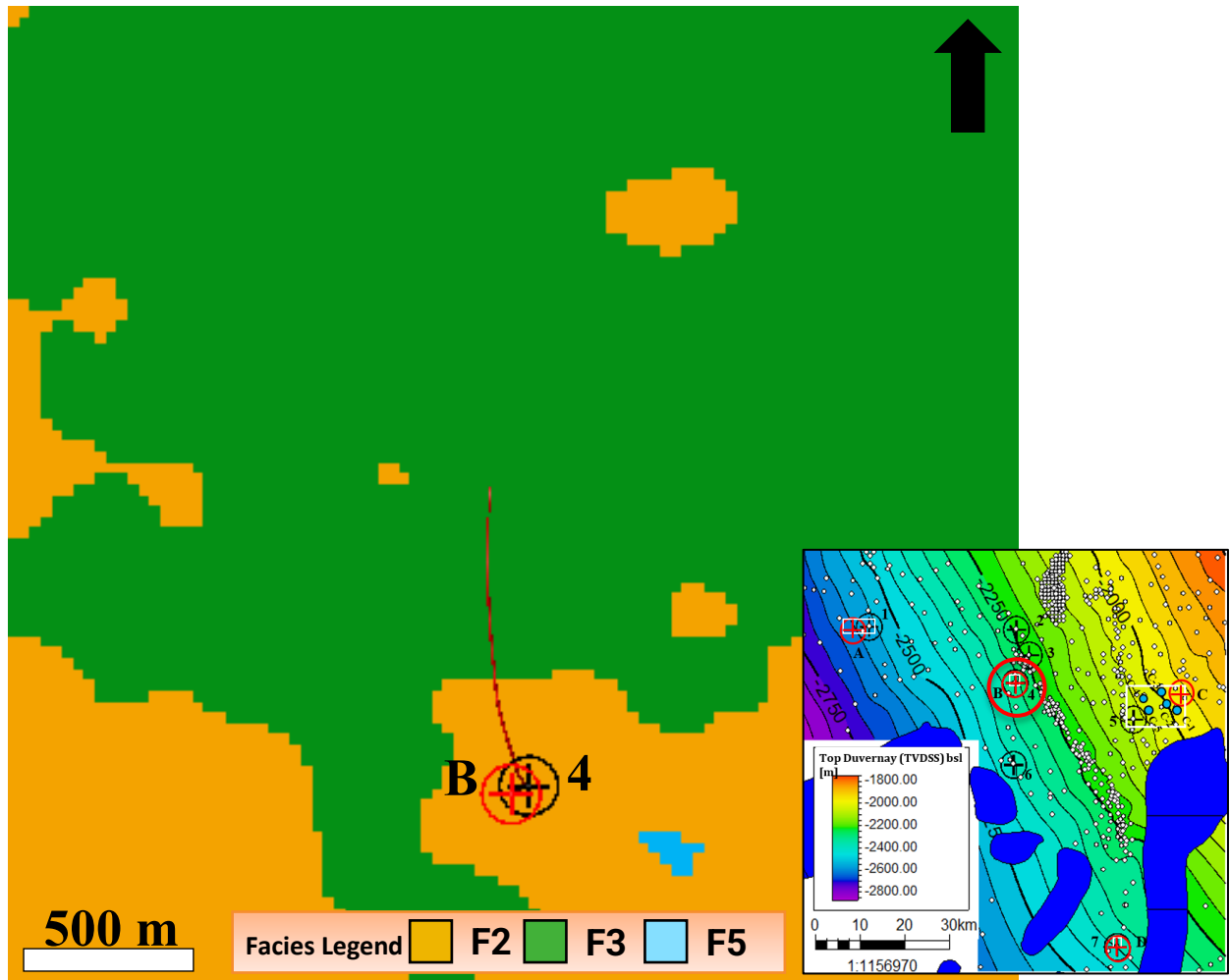


Fig. 4.14. Map of modelled facies of the Duvernay Formation in 3D model B along the horizon at the depth where the horizontal well B was landed. Red circle and line, wellhead location and trajectory of horizontal well B. Black circle, wellhead location of vertical well 4, in which core was described. See Table 3.1 name of the wells within the Kaybob area. See Table 4.1 for facies description. The red circle within the inset map shows the location of wells B, 4 and model B.

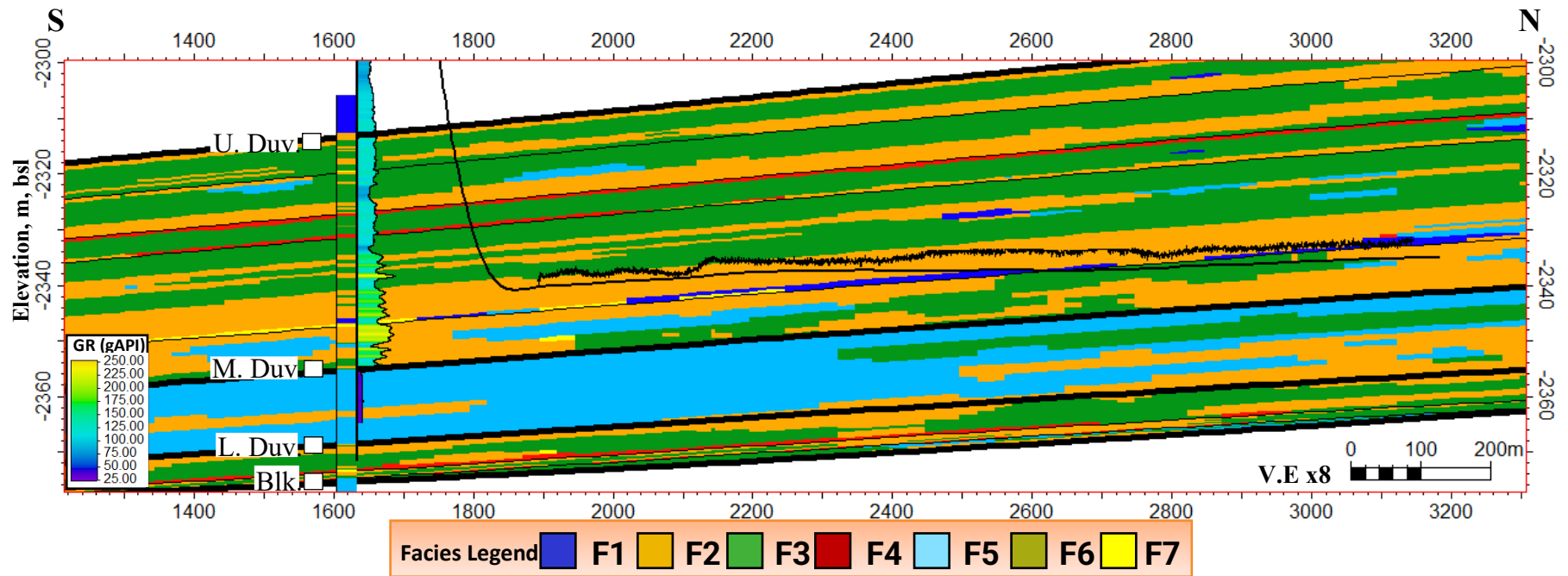


Fig. 4.15. Cross-section S-N along horizontal well B in 3D model B, displaying modelled facies of the Duvernay Formation. The well was landed mostly in organic-rich facies F2 and F3 of the upper Duvernay Member. Facies interpretation (left track) and gamma ray log (right track) are shown in vertical well 4 located in the same well pad as well B. Thin black line indicates GR log along well B trajectory. Formation tops: U.Duv., Upper Duvernay; M. Duv., Middle Duvernay; L.Duv., Lower Duvernay; Blk., Beaverhill Lake. See Fig. 4.6, 4.14 and Table 3.1 for location of the wells, Table 4.1 for facies description.

Model C (Fig. 4.16 and Fig. 4.17) is located in the eastern part of the study area (see Fig 4.6 for location of the model). It displays higher presence of carbonate-rich facies F5 to the SW, close to the Leduc Reefs. The organic-rich facies F2 and F3 dominate in the N-NW, towards the center of the basin. The upper Duvernay Member is composed of organic-rich facies F2 and F3 with intervals of carbonate-rich facies F1 and F5 that are thicker compared to Model A and B (Fig. 4.18). This may result from the closer location to the Leduc Reefs, where carbonate material is abundant. The middle Duvernay is composed mostly of the carbonate-rich nodular mudstones of F5 with discontinuous patches of F2, F3 and F5. The lower Duvernay is composed of organic-rich facies F3 with lower presence of organic-rich facies F2 and carbonate-rich facies F5. The horizontal well B and other horizontal wells drilled within the area were landed in organic-rich facies F2 and F3 at the base of the upper Duvernay Member (Fig. 4.16, 4.17, 4.18).

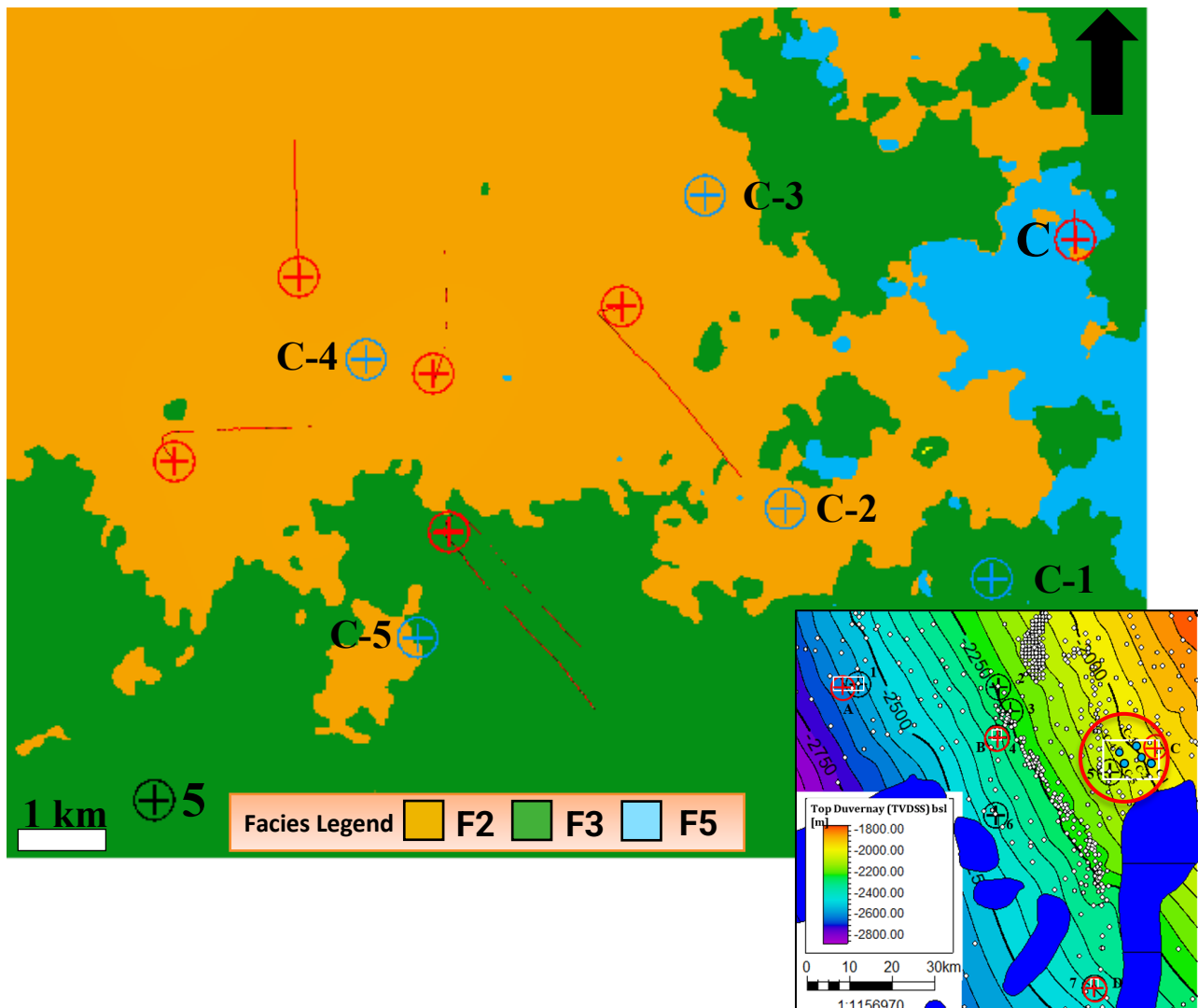


Fig. 4.16. Map showing modelled facies of the Duvernay Formation in 3D model C along the horizon at the depth where the most of the horizontal wells in the area were landed. C-1 to C-5, wellhead location of vertical wells (blue circles) used in 3D facies model C. Red circles and lines, wellhead location and trajectory of other horizontal wells drilled in the area. Black circle, wellhead location of vertical well 5, in which core was described. See Table 3.1 for name of the wells within the Kaybob area. See Table 4.1 for facies description. The red circle within the inset map shows the location of wells C, C1-C5 and model C.

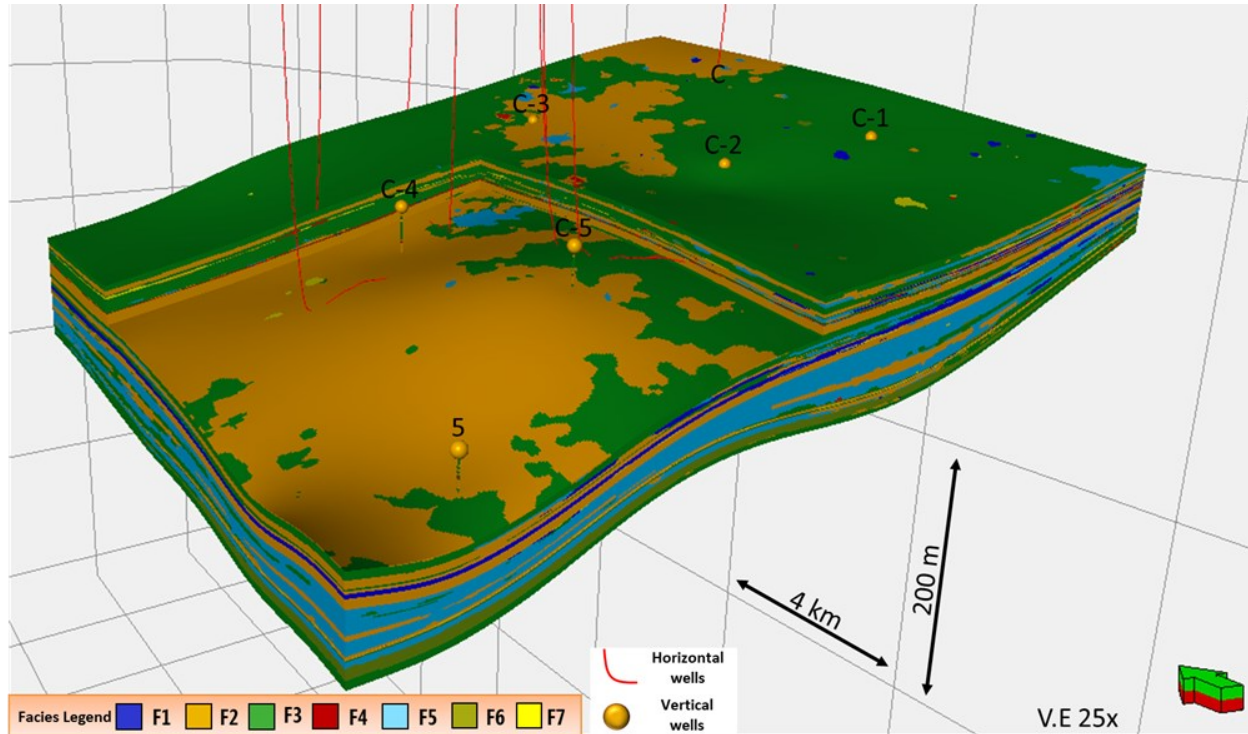


Fig. 4.17. 3D view of the Duvernay facies interpreted in model C. Facies of the Duvernay Formation interpreted in wells C-1 to C-5 based on well logs data and in well 5 based on core description are used in 3D facies model C. Labels C1-C5 and 5 indicate location of vertical wells at the top of the Duvernay Formation (yellow circles). Red lines, location and trajectory of horizontal wells drilled the area. Horizontal wells in the area are landed in organic-rich facies F2 and F3. See Fig. 4.6 and Table 3.1 for the location of the model and name of the wells within the Kaybob area. See Table 4.1 for facies description.

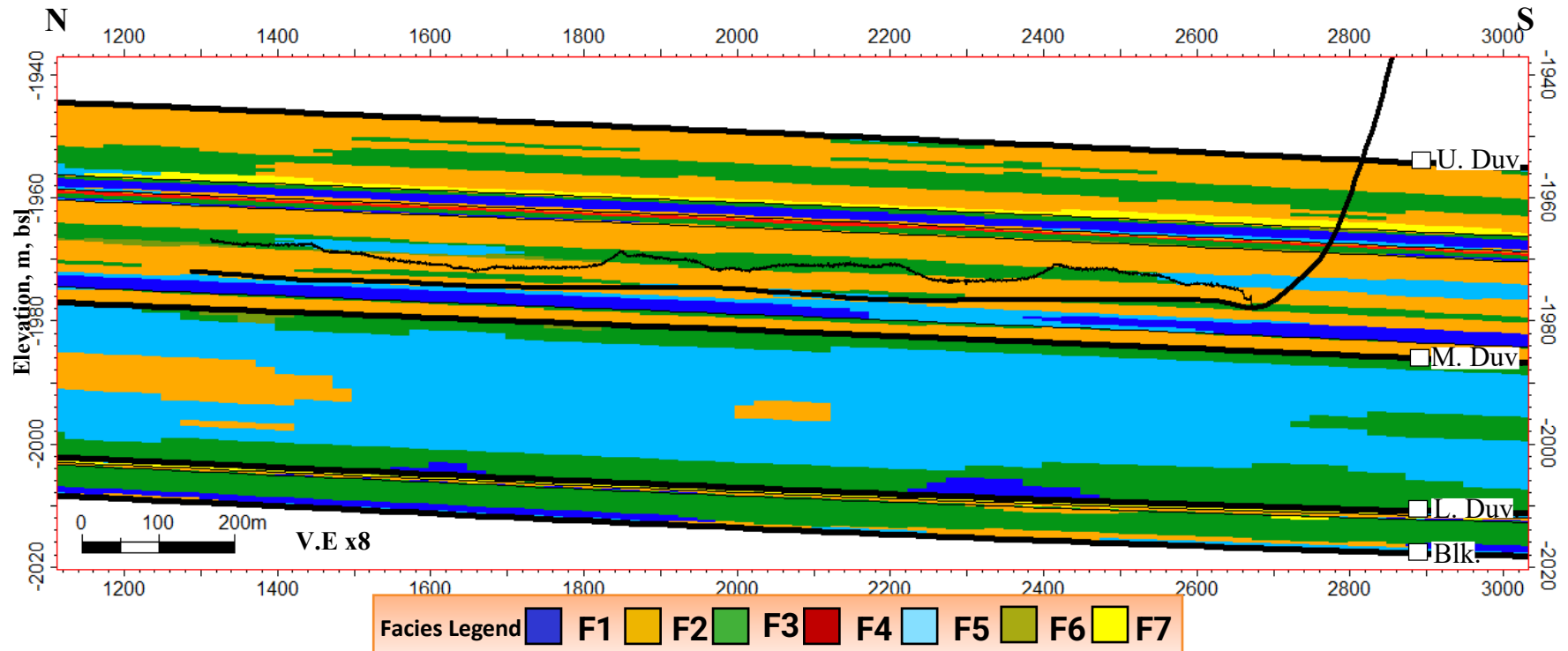


Fig. 4.18. Cross-section N-S along horizontal well C in 3D model C, displaying modelled facies of the Duvernay Formation. The well was landed mostly in organic-rich facies F2 and F3 at the base of the upper Duvernay Member. Thin black line indicates GR log along well C trajectory. Formation tops: U.Duv., Upper Duvernay; M. Duv., Middle Duvernay; L.Duv., Lower Duvernay; Blk., Beaverhill Lake. See Fig. 4.6, 4.16 and Table 3.1 for the location of the well, Table 4.1 for facies description.

Model D (Fig. 4.19) is located in the southernmost part of the Kaybob area (see Fig. 4.11 to see the location of the model), close to the Windfall Reef. The upper Duvernay Member is characterized by higher content of carbonate-rich facies F1, F4 and F5, if compared to the upper Duvernay Member in models A-C (Fig. 4.20). It may result from a higher carbonate-rich sediment supply from the carbonate reefs located close to the model. However, organic-rich facies F2 and F3 are dominant in this member. The middle Duvernay Member is composed of carbonate-rich nodular mudstones of facies F5. The lower Duvernay Member consists of organic-rich facies F2 and, in lower proportion, of facies F3. The horizontal well B is targeting organic-rich facies F2 and F3 at the base of the upper Duvernay Member, crossing sporadic carbonate sediments and nodules of facies F1 and F5 (Fig. 4.19).

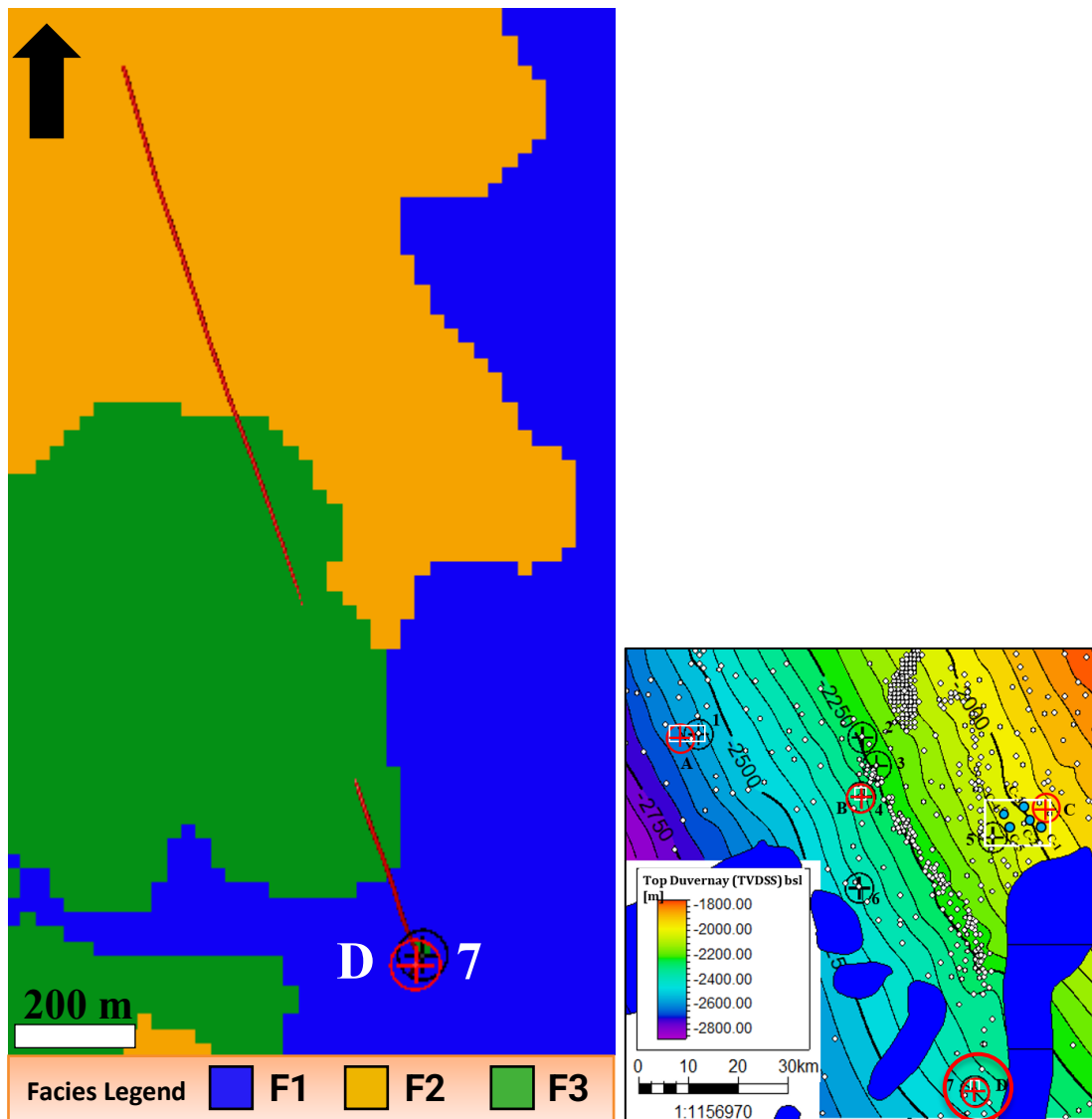


Fig. 4.19. Map showing modelled facies of the Duvernay Formation in the 3D model D along the horizon at the depth where the horizontal well D in the area was landed. Red circles and line, wellhead location of horizontal well D with its trajectory. Black circle, wellhead location of vertical well 7, in which core was described. See Table 3.1 name of the wells within the Kaybob area. See Table 4.1 for facies description. The red circle within the inset map shows the location of wells D, 7 and model D.

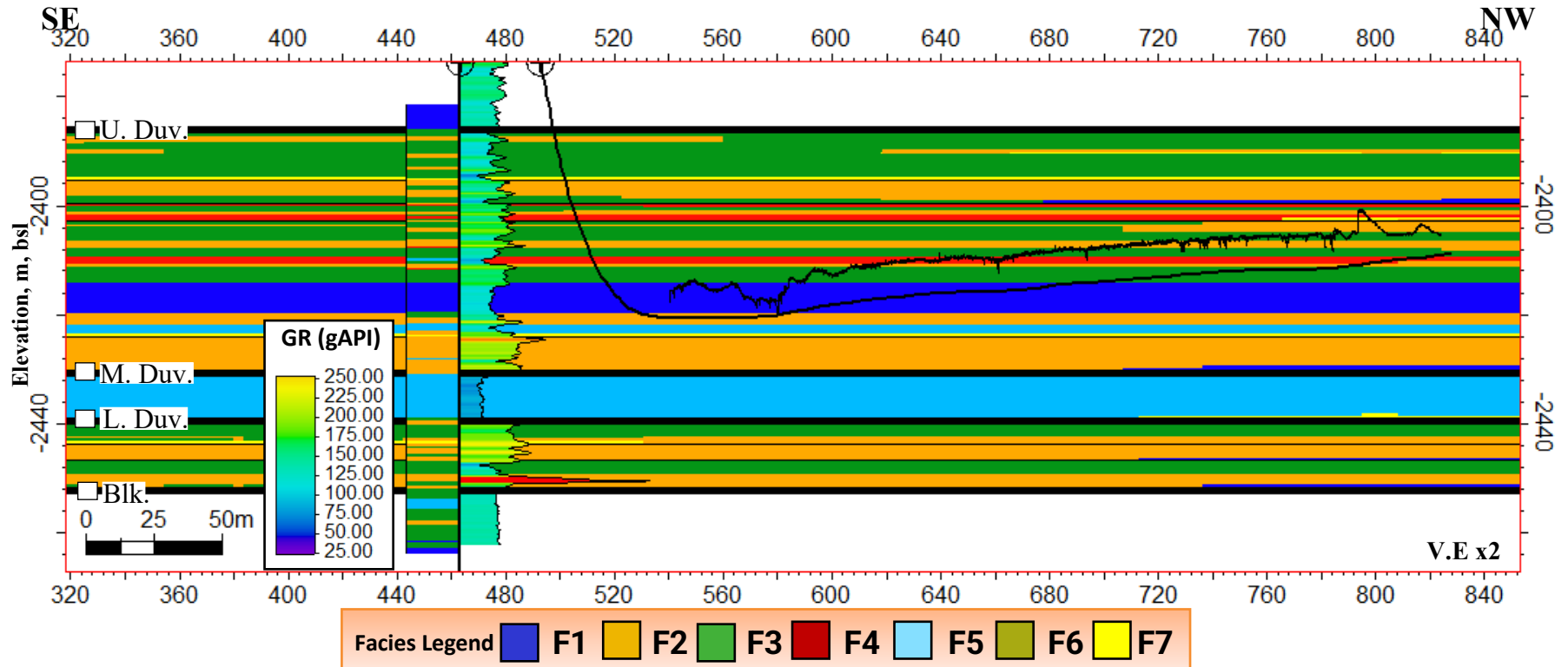


Fig. 4.20. Cross-section SE-NW along horizontal well D in 3D model D, displaying modelled facies of the Duvernay Formation. The horizontal well D was landed mostly in organic-rich facies F2 and F3. Facies interpretation (left track) and gamma ray log (right track) are shown for vertical well 7 located in the same well pad as well D (see Table 3.1, Fig. 4.6). Thin black line indicates GR log along the well trajectory. Formation tops: U.Duv., Upper Duvernay; M. Duv., Middle Duvernay; L.Duv., Lower Duvernay; Blk., Beaverhill Lake. See Fig. 4.6, 4.19 and Table 3.1 for the location of wells, Table 4.1 for facies description.

4.3. Petrophysical properties of main lithofacies of the Duvernay Formation.

Petrophysical properties analyzed in this study include total organic carbon (TOC), total porosity, permeability, and fluid saturation. Continuous profiles of TOC, total porosity and permeability were estimated and validated by petrophysical core data for six vertical wells 1, 3-7 (Table 3.1). The results for two of the seven wells are shown in log plots (Fig. 4.21 and Fig 4.22). Logs plots for the remaining wells are presented in appendix A. Petrophysical characterization is carried out for main lithofacies F2, F3 and F5 of the Duvernay Formation that compose 95% of the total thickness of the formation. The average values of petrophysical parameters and fluid saturation are estimated per well and per facies based on core testing data in six vertical wells 1, 3-7 (Table 4.2).

The average TOC is higher in F2 with a value of 3.19 wt.% (Fig. 4.23.A, Table 4.2). It is followed by F3 with an average of 2.75 wt.% (Fig. 4.24.A, Table 4.2). The carbonate-rich facies of F5 have the lowest TOC, with an average of 0.64 wt.% (Fig.4.25.A, Table 4.2). Total porosity is similar in F2 and F3, with an average of 4.87% for F2 and 4.97% for F3. F5 has the lowest porosity with an average of 1.93% (Table 4.2). Permeability is slightly higher in F2 (1.62×10^{-4} mD) than in F3 (1.11×10^{-4} mD), while in F5 is much lower (5.52×10^{-5} mD) (Table 4.2).

The average Gas Saturation (S_g) in the mudrocks of the Duvernay Formation in the Kaybob area is 57.83%, being higher in well 6 (70.38%). The average Oil Saturation (S_o) is 22.43%, being higher in well '4' (35.75%). Gas saturation is 59.41% in F2 (Fig. 4.23.B, Table 4.2), 55.84% in F3 (Fig. 4.24.B, Table 4.2) and 59.13% in F5 (Fig. 4.25.B, Table 4.2). Oil saturation is 24.21% in F2 (Fig. 4.23.C, Table 4.2), 28.20% in F3 (Fig.4.3.4.C, Table 4.2) and 21.23% in F5 (Fig. 4.25.C, Table 4.2).

	Top of Duvernay Formation (MD in m)	TOC (wt.%)	Total Porosity (%)	Permeability (mD)	Gas Saturation (%)	Oil Saturation (%)

Well 1	3425.33	3.83 ± 0.87	3.86 ± 0.60	4.36e ⁻⁶ ± 3.25e ⁻⁶	51.35 ± 2.75	32.55 ± 3.75
Well 3	3263.22	2.31 ± 1.29	4.85 ± 1.73	1e ⁻⁴ ± 9.33e ⁻⁵	50.94 ± 8.11	22.97 ± 11.46
Well 4	3191.46	2.81 ± 0.94	6.51 ± 1.64	1.3e ⁻⁴ ± 3.28e ⁻⁵	47.86 ± 9.05	35.75 ± 11.25
Well 5	3050.79	2.41 ± 1.45	3.85 ± 1.45	1.5e ⁻⁴ ± 1.55e ⁻⁴	52.07 ± 12.30	28.39 ± 9.99
Well 6	3350.54	2.80 ± 1.09	4.93 ± 1.30	7.62 e ⁻⁵ ± 6.22e ⁻⁵	72.38 ± 6.17	10.19 ± 3.07
Well 7	3499.56	2.51 ± 1.33	3.59 ± 1.24	1.6e ⁻⁴ ± 5.10e ⁻⁵	68.92 ± 10.99	22.12 ± 9.39
F2	x	3.19 ± 1.00	4.87 ± 1.43	1.62e ⁻⁴ ± 1.09e ⁻⁴	59.41 ± 11.62	24.21 ± 10.02
F3	x	2.71±	4.97 ± 1.70	1.11e ⁻⁴ ± 7.02e ⁻⁵	55.84 ± 12.81	28.20 ± 12.64
F5	x	0.64 ± 0.64	1.93 ± 1.00	5.52e ⁻⁵ ± 5.06e ⁻⁵	59.13 ± 21.33	21.23 ± 15.00

Table 4.2. Summary of petrophysical properties of mudrocks of the Duvernay Formation based on data of core petrophysical testing (AER reports) in six vertical wells 1, 3-7 (Fig. 4.6, Table 3.1) and average values estimated for lithofacies F2, F3 and F5 based on core data in all six wells (Table 4.1). The shown values correspond to average values ± standard deviation. No petrophysical core data is available for well 2 (Table 3.1).

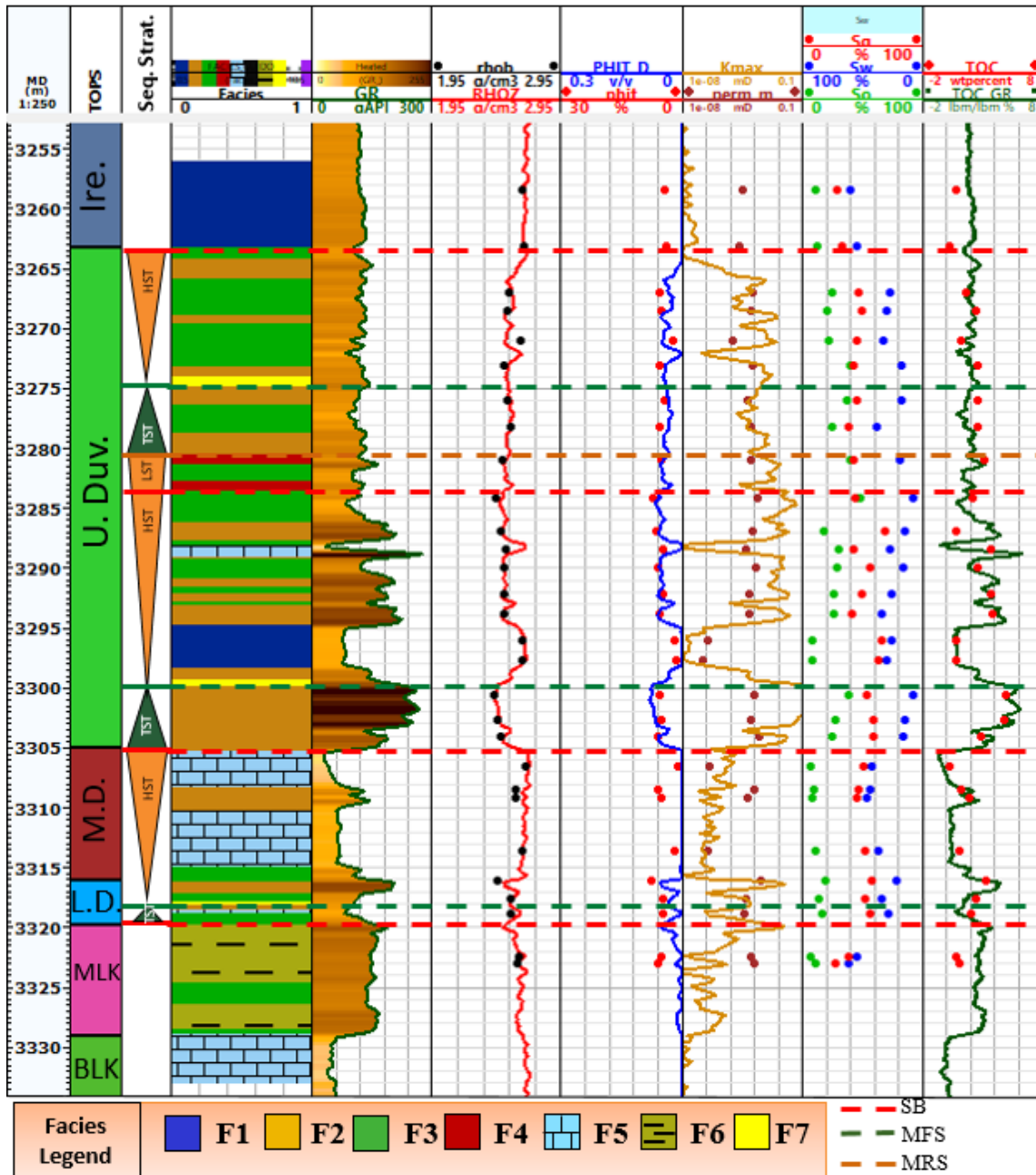


Fig. 4.21. Sequence stratigraphy boundaries, lithofacies, gamma ray (GR), bulk density (RHOB), estimated profiles of petrophysical parameters (solid lines) and XDR core testing data (dots) in well 3 (see Tables 3.1, 4.1, Fig. 4.6). PHIT, total porosity; kmax, horizontal permeability; TOC, total organic carbon; Sg, So and Sw, fluid saturation. Formation tops: U. Duv., Upper Duvernay; M.D., Middle Duvernay; L. Duv., Lower Duvernay; MLK., Majeau Lake; BLK., Beaverhill Lake. SB, sequence boundary, MFS; maximum flooding surface; MRS, maximum regressive surface.

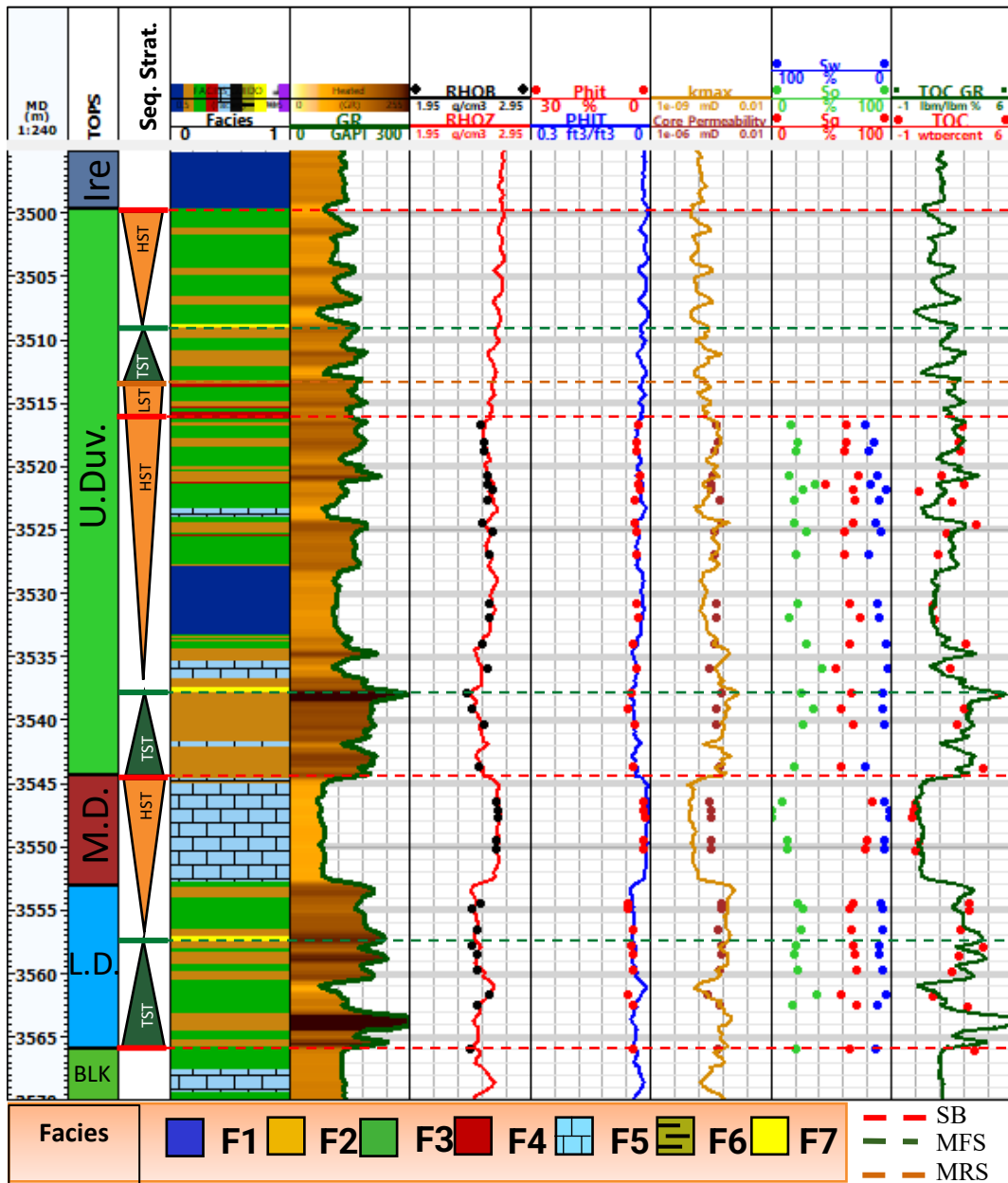


Fig. 4.22. Sequence stratigraphy boundaries, lithofacies, gamma ray (GR), bulk density (RHOB) logs, estimated profiles of petrophysical parameters (solid lines) and XDR core testing data (dots) in well 7 (see Tables 3.1, 4.1, Fig. 4.6). PHIT, total porosity; kmax, horizontal permeability; TOC, total organic carbon; Sg, So and Sw, fluid saturation. Formation tops: U. Duv., Upper Duvernay; M.D., Middle Duvernay; L. Duv., Lower Duvernay; BLK., Beaverhill Lake. SB, sequence boundary, MFS; maximum flooding surface; MRS, maximum regressive surface.

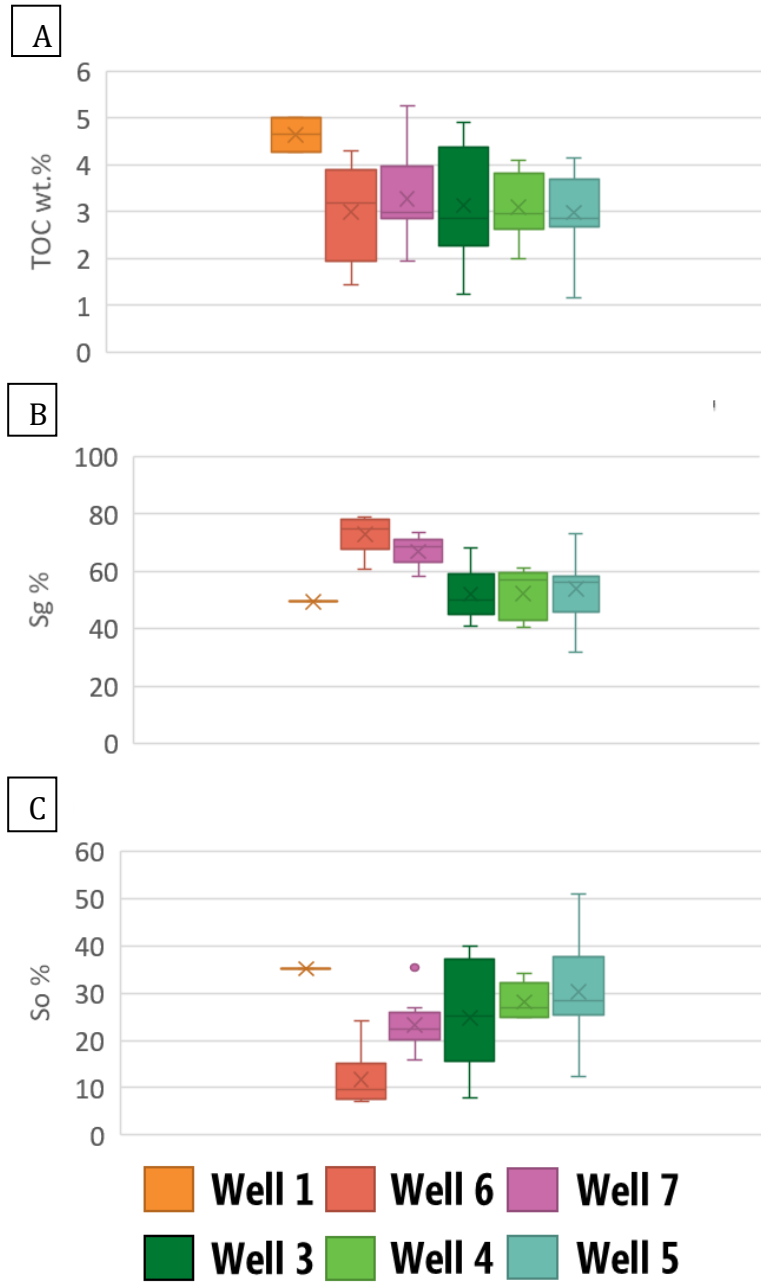


Fig. 4.23. Box plot diagrams showing petrophysical properties of facies F2 of the Duvernay mudrocks per well in six vertical wells 1, 3-7 (see Table 3.1, Fig. 4.6). A) TOC (wt.%). B) Gas saturation S_g (%). C) Oil saturation S_o (%).

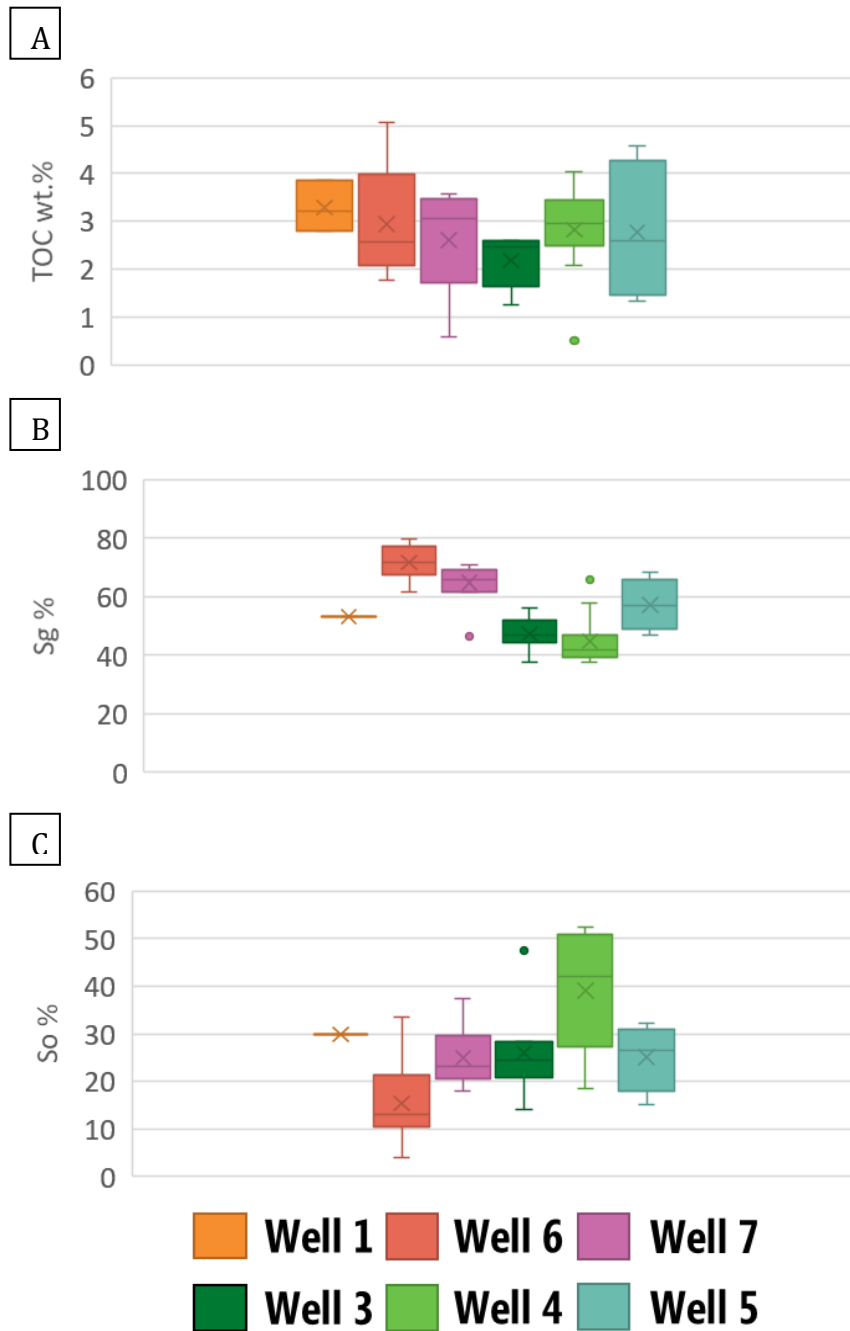


Fig. 4.24. Box plot diagrams showing petrophysical properties of facies F3 of the Duvernay mudrocks per well in six vertical wells 1, 3-7 (see Table 3.1, Fig. 4.6). A) TOC (wt.%). B) Gas saturation Sg (%). C) Oil saturation So (%).

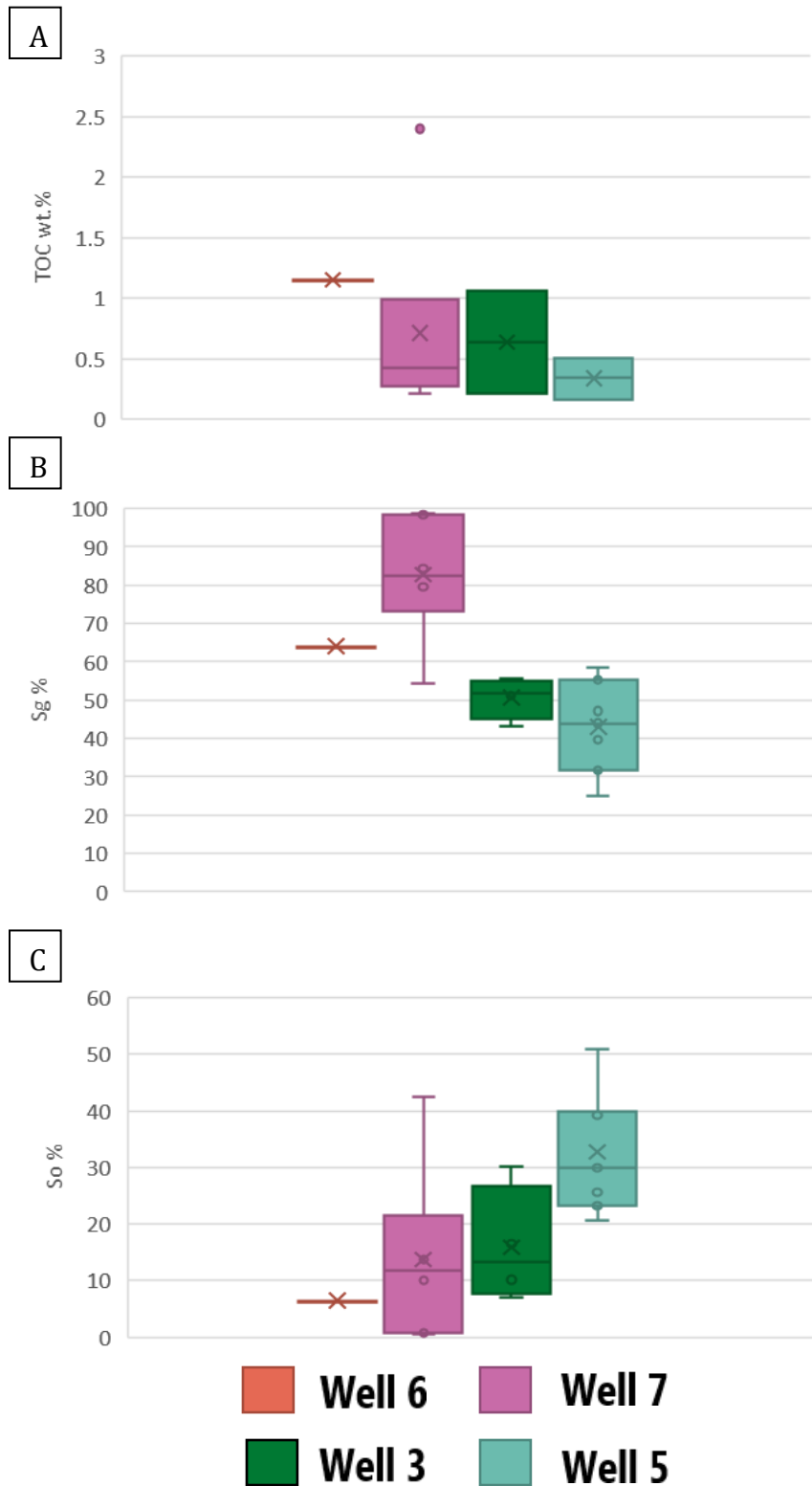


Fig. 4.25. Box plot diagrams showing petrophysical properties of Facies F5 of the Duvernay mudrocks per well in six vertical wells 1, 3-7 (see Table 3.1, Fig. 4.6). A) TOC (wt.%). B) Gas saturation Sg (%). C) Oil saturation So (%).

4.4. Mechanical properties of main lithofacies of the Duvernay Formation.

The continuous profiles of the mechanical properties of mudrocks of the Duvernay Formation are estimated in seven vertical wells 1-7 (Table 3.1, Fig. 4.6) based on log data and validated by the results of available geomechanical testing (AER reports, see Chapter Data and Methods). In this section, the resulting well log plots are shown for two vertical wells 3 and 7 (Fig. 4.27 and 4.28); the log plots for the other vertical wells are displayed in Appendix B. The range of values of selected well logs and estimated mechanical properties are summarized for facies F1-F7 (Table 4.1, 4.3).

Carbonate-rich lithofacies (F1, F4 and F5) are characterized by low gamma ray (GR) values, commonly ranging between 60 and 120 gAPI, and high density (RHOB, RHOZ) values ranging from 2.57 to 2.72 gr/cm³. Shear and compressional slowness (DTSH, DTCO) are low, with DTSH values between 95 and 110 us/ft and DTCO values between 55 and 65 us/ft. Dynamic Young's Modulus (YM) ranges from 50 GPa to 65 GPa, and static Young's Modulus varies from 39 GPa to 48 GPa. Unconfined Compressional Strength (UCS) ranges from 80 MPa to 150 MPa in these facies. Tensile Strength (TSTR) ranges from 9 MPa to 19 MPa (Fig.4.29, Table 4.4). Hardness measurements are between 550 and 720 HDL (Fig. 4.27, Fig. 4.28, Table 4.3). Based on the XRD analysis of core data, these facies have low content of illite (9 – 25 %), organic matter (0.5 – 5%) and high content of carbonate (40 - 82 %) and composed of mechanically strong rocks that are likely to deform in a brittle manner (Fig. 4.26).

Organic-rich lithofacies (F2 and F7) show high GR values (170-260 gAPI) and low density (2.5-2.55 gr/cm³). The DTSH and DTCO values are relatively high, with DTSH ranging from 120 to 135 us/ft, and DTCO ranging from 70 to 85 us/ft. The elastic and strength parameters are low, with dynamic YM varying between 30 GPa and 40 GPa, static YM ranging from 20 GPa to 35 GPa, and UCS ranging from 40 MPa to 90 MPa. TSTR ranges from 3 MPa to 8.72 MPa (Fig. 4.29, Table 4.4). Hardness values are within the range of 450-550 HDL (see Fig. 4.27, Fig. 4.28, Table 4.3). Based on the XRD analysis of core, these facies have elevated content of illite (20 – 39 %) and organic matter (5.5 – 12 %) and low content of carbonate (11 – 32 %) and are characterized by ductile behavior (Fig. 4.26).

Facies F3 is characterized by intermediate properties, if compared to the organic-rich facies (F2 and F7) and carbonate-rich facies (F1, F4, and F5). The GR and density values range from 90 to 180 gAPI and 2.54 to 2.69 gr/cm³, respectively. DTSH values range from 111 to 120 us/ft, while DTCO values are between 64 and 75 us/ft. Static YM ranges from 30 to 40 GPa, dynamic YM from 38 to 52 GPa, and UCS from 60 to 115 MPa. TSTR ranges from 6 to 11 MPa (Fig. 4.29, Table 4.4). Hardness measurements range from 500 to 700 HDL (Fig. 4.27, Fig. 4.28, Table 4.3). Based on the XRD analysis of core, these facies have intermediate content of illite (16 – 34 %), organic matter (2 – 9 %) and carbonate (20 – 55 %) and are characterized by semi-brittle to brittle behavior (Fig. 4.26).

Facies F6 is mainly present in the Majeau Lake Formation. Its mechanical properties are similar to F2 and F7 of the Duvernay Formation, being more ductile and soft compared to the intermediate (F3) and carbonate-rich (F1, F4, and F5) facies.

Facies	GR (gAPI)	RHOB (g/cm ³)	DTSH (us/ft)	DTCO (us/ft)	YMs (GPa)	YMd (GPa)	UCS (MPa)	Hardness (HDL)	Summary
F1, F4, F5	60-120	2.57-2.72	95-110	55-65	39-48	50-65	80-150	550-720	Brittle facies
F2, F6, F7	170-260	2.50-2.55	120-135	70-85	20-35	30-40	40-90	450-550	Ductile facies
F3	90-180	2.54-2.79	111-120	64-75	30-40	38-52	60-115	500-700	Intermediate facies

Table 4.3. Summary of ranges of values of selected well logs and estimated profiles of mechanical properties in lithofacies F1-F7 of mudrocks of the Duvernay Formation analyzed in seven vertical wells 1-7 (Table 3.1, Fig. 4.6). Well logs: GR, gamma ray; RHOB, bulk density; DTSH and DTCO, shear and compressional slowness, respectively. Estimated profiles: YMs and YMd, static and dynamic Young's Moduli, respectively; UCS, unconfined compressive strength. See Table 4.1 for facies description.

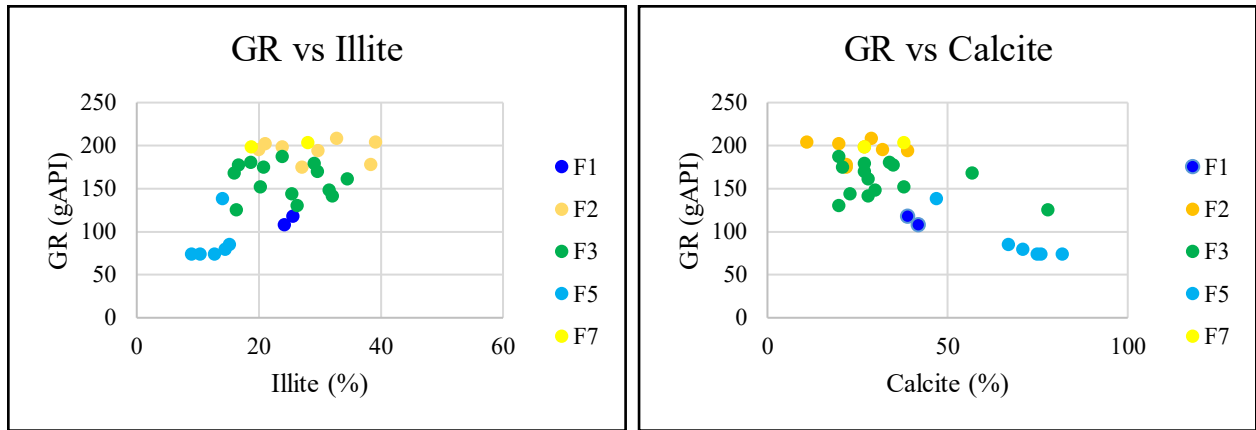


Fig. 4.26. Cross-plots of GR vs Illite (left) and GR vs Calcite (right) in facies F1-F7 of the Duvernay Formation based on XRD analysis of core in well 7. See Fig. 4.6 and Table 3.1 for the location of well 7, Table 4.1 for facies description.

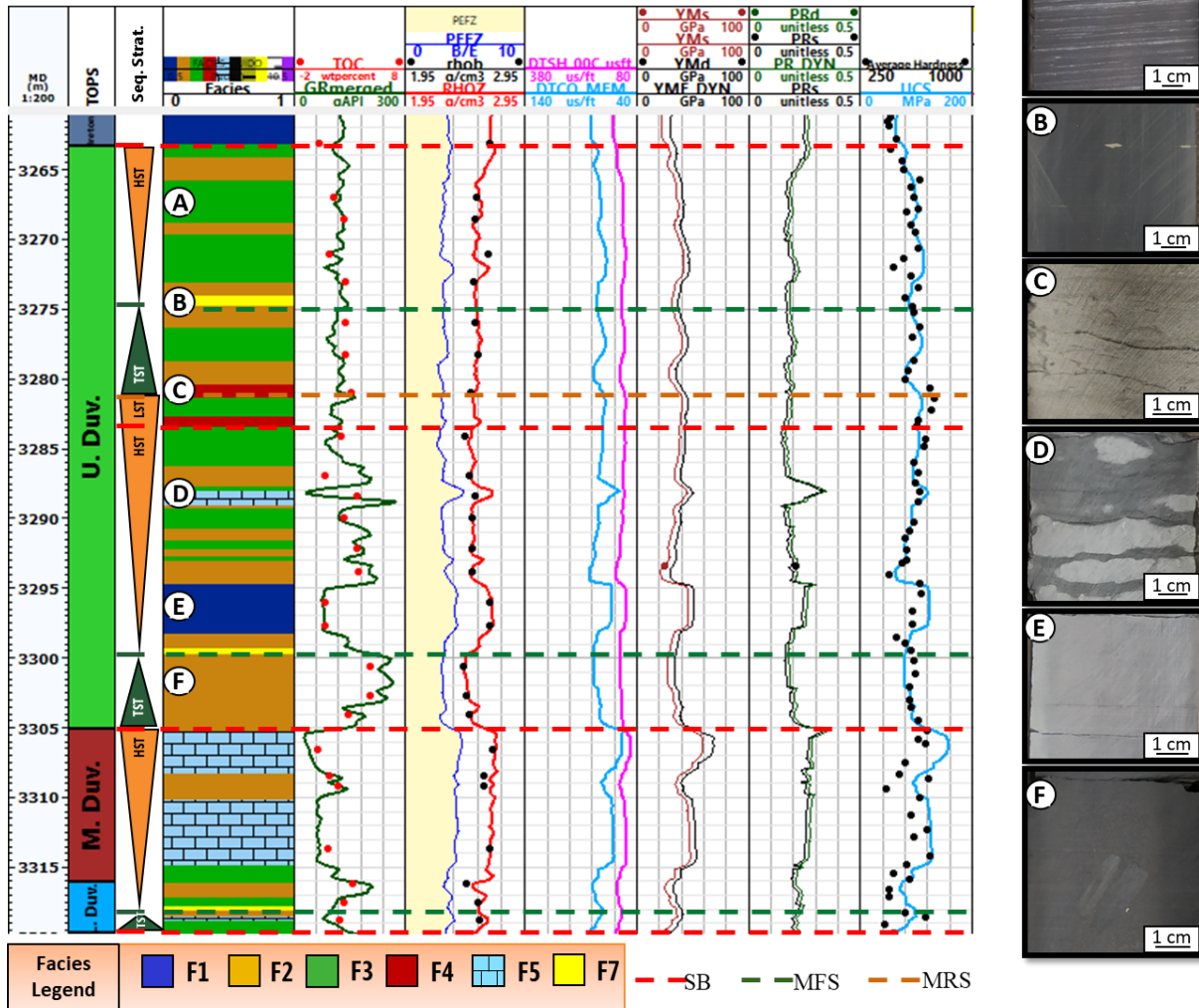


Fig. 4.27. Well 3. Lithofacies, sequence stratigraphy boundaries, well logs of Gamma Ray, Photoelectric Factor (PEF), Bulk Density (RHOB), Shear (DTSH) and Compressional (DTCO) Slowness, and estimated profiles of Young's Modulus (YM), Poisson's Ratio (PR), Unconfined Compressive Strength (UCS) and Hardness measurements in the mudrocks of the Duvernay Formation. Labels d, DYN, dynamic; s, static. On the right, photos of lithofacies: F3 (A); F7 (B); F4 (C); F5 (D); F1 (E); F2 (F).

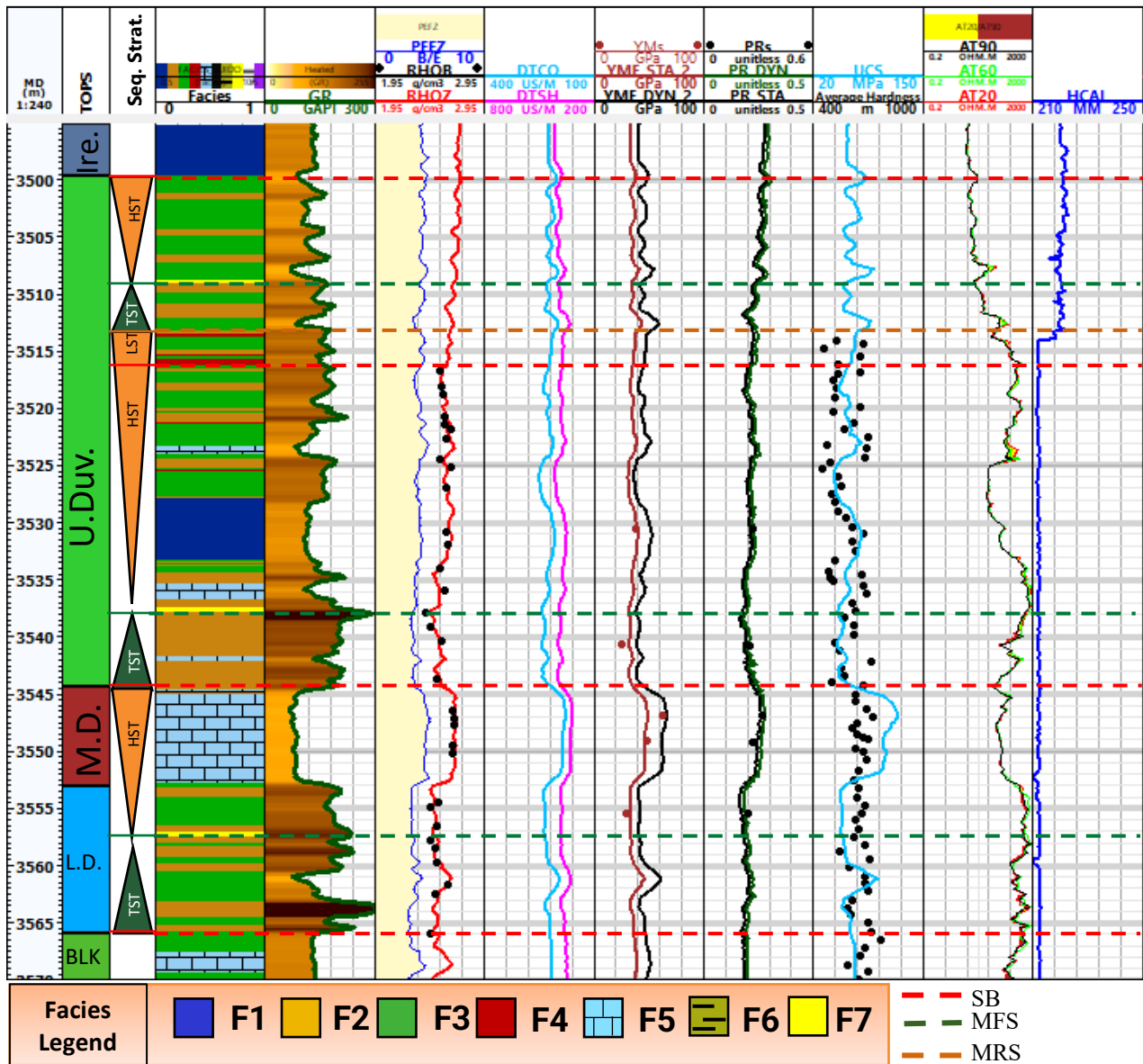


Fig. 4.28. Well 7. Lithofacies, sequence stratigraphy boundaries, well logs of Gamma Ray (GR), Photoelectric Factor (PEFZ), Bulk Density (RHOB, RHOZ), Shear and Compressional Slowness (DTSH, DTCO), Deep (AT90), Medium (AT60) and Shallow (AT20) Resistivity, Caliper (HCAL), and estimated profiles of Young’s Modulus (YM), Poisson’s Ratio (PR), Unconfined Compressional Strength (UCS), and Hardness measurements in the mudrocks of the Duvernay Formation. Labels DYN, dynamic; s, static.

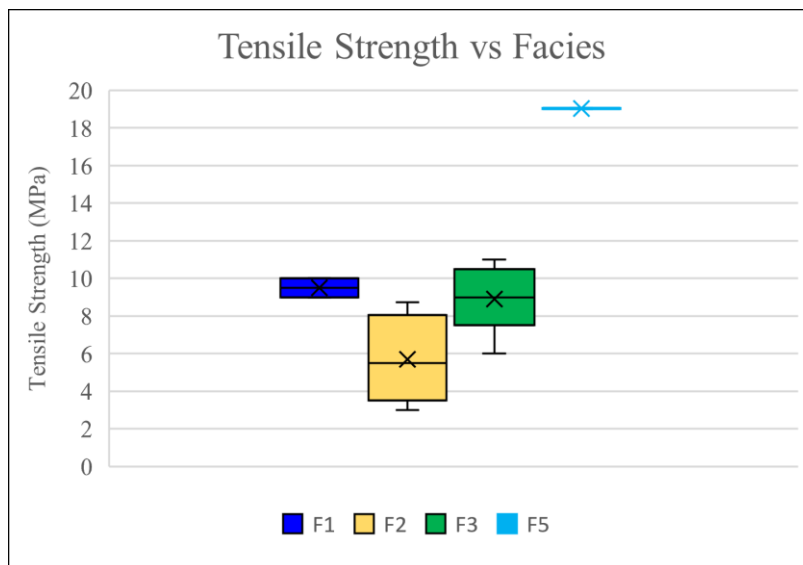


Fig. 4.29. Box-plot diagram showing the average values of Tensile Strength (TSTR) in facies F1, F2, F3 and F5 of the Duvernay Formation based on core data in wells 4, 6 and 7. See Table 3.1 and Fig 3.2 for name and location of studied vertical wells, Table 4.1 for the facies composition, Table 4.4 for TSTR values from different wells used on this figure.

Tensile Strength (MPa)	Facies	Well
10	F1	7
6	F2	7
19	F5	7
3	F2	7
6	F3	7
9	F1	4
5	F2	4
11	F3	4
9	F3	4
9	F3	4
8.03	F3	6
10.33	F3	6
8.72	F2	6

Table 4.4. Core-based Tensile Strength, Facies, and Wells used on Fig. 4.29.

4.5. Fractures in the Duvernay Formation in core of vertical wells

Natural and drilling-induced fractures were studied in core and thin sections of mudrocks of the Duvernay Formation in seven vertical wells 1-7 (Table 3.1, Fig. 4.6). Fracture intensity P10 was estimated based on core description and compared between the wells across the study area.

4.5.1. Natural fractures

Subvertical, inclined and horizontal mineralized and open natural fractures were identified in core (Fig. 4.30) and thin sections (Fig. 4.31) in mudrocks of the Duvernay Formation. The most frequent fractures in core samples are subvertical, with a typical angle to the core axis between 5° to 15° (Fig. 4.30). Most of the horizontal fractures observed in thin sections are open and clustered in organic-rich intervals only. These fractures may be related to core decompaction or drilling operations, following planes of weakness along clay-rich laminae. However, the horizontal natural fractures filled with calcite were also observed in thin sections of the core (Fig. 4.31B). Fractures are mineralized and filled with calcite with minor presence of pyrite and kerogen distinguished under the microscope (Fig. 4.31.A-B). Calcite crystals filling veins in the Duvernay Formation are commonly characterized by blocky texture (Fig. 4.31). The blocky crystal of calcite filling in fractures are either of similar grain size and composition resulting from one stage of growth (Fig. 4.31.A) or of variable size with smaller calcite crystals along fracture walls and larger crystals in fracture center of a fracture, likely formed during different growth stages (Fig. 4.31.D).

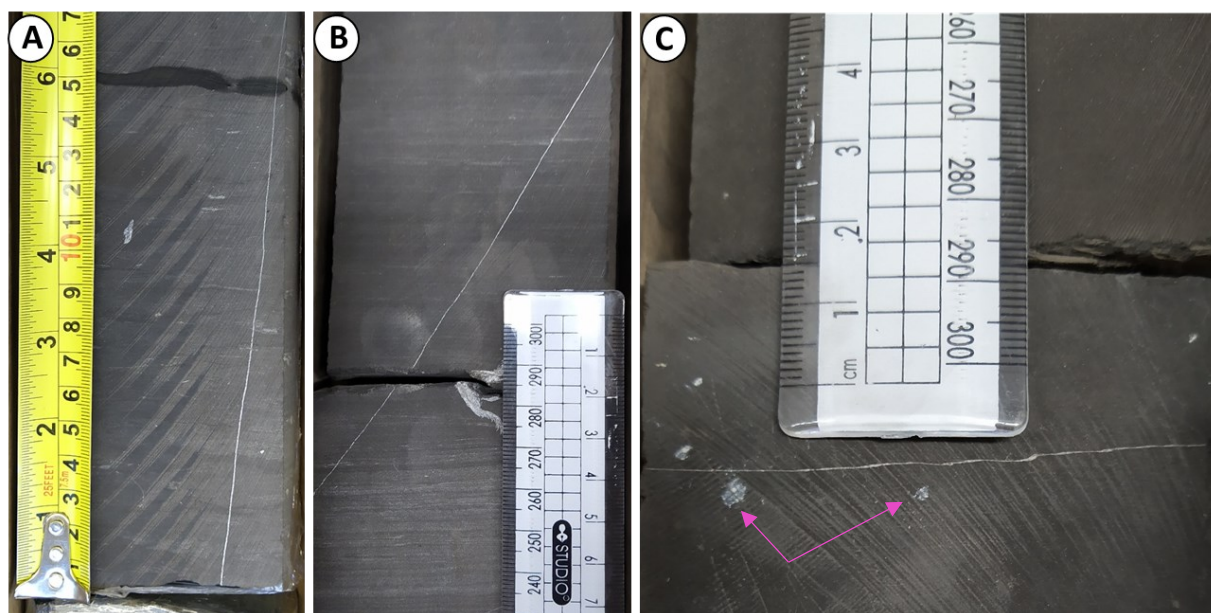


Fig. 4.30. Calcite-filled subvertical (A), inclined (B), and horizontal (C) fractures in core samples of the Duvernay Formation, well 7, depth 3522.55 for (A), well 6, depth 3360.30 m for (B), well 6, depth 3371.61 m for (C). Sparse crystals of anhydrite (pink arrows) in the mudrocks are highlighted in C. See Table 3.1 and Fig. 4.6 for the wells' name and location.

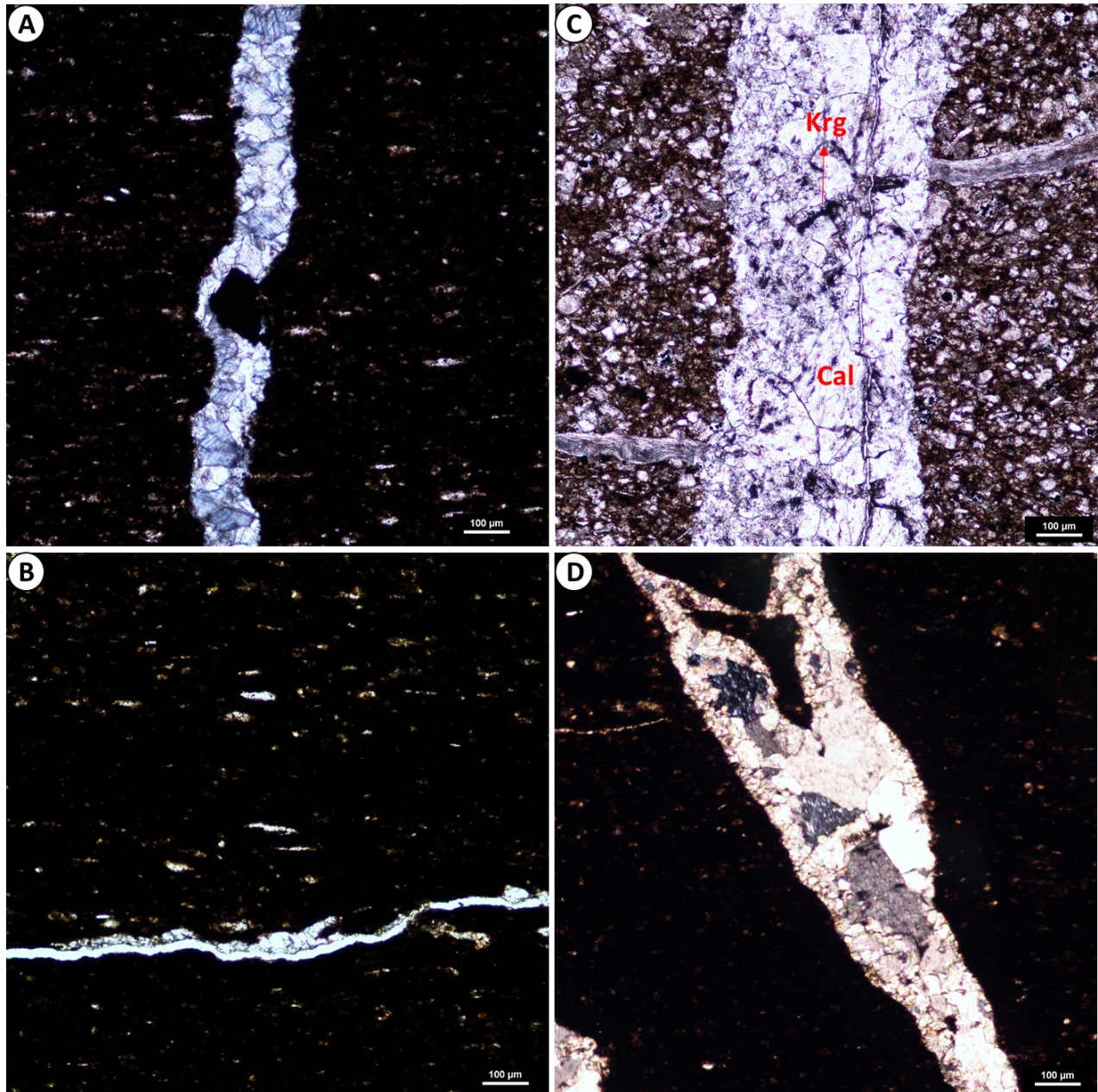


Fig. 4.31. Thin sections of fractures in the Duvernay Formation: A) Subvertical mineralized fracture with calcite and pyrite, showing blocky texture (well 1, 3435.01 m) B) Partially mineralized horizontal fracture filled with calcite (well 3, 3284.29 m). C) Subvertical mineralized fracture with crystals of calcite (10 – 100 μm) and kerogen (well 7, 3522.65 m). The fracture is crossed by a younger open subhorizontal fracture. D) Mineralized inclined fracture showing two different stages of calcite growth, one with smaller calcite crystals ($< 80 \mu\text{m}$) at the walls of the fracture, and another one with larger calcite crystals (up to 300 μm) in the center of the fracture (well 3, 3285.12 m). Bedding in A-D is subhorizontal. Parallel nicols in A-C, crossed nicols in D. See Table 3.1 and Fig. 4.6 for the wells' name and location. Abbreviations: Cal: Calcite; Krg: Kerogen.

Observed fracture height for fractures that are fully confined to the core of the Duvernay Formation is variable, ranging from 7 cm to more than 60 cm. Vertical fractures are stopped by bed boundaries between different lithofacies (Fig. 4.32.A). However, vertical fractures can also propagate across beds boundaries, when mudrocks are finely laminated with alternation of carbonate- and organic-rich laminae that are very thin of the mm scale (Fig. 4.32.B and C). This fracture behavior is more frequently observed in Facies F3. In thicker beds of carbonate-rich nodular mudstones of Facies F5, fracture height is usually higher (30 - 60 cm), although fewer fractures were detected in this facies.

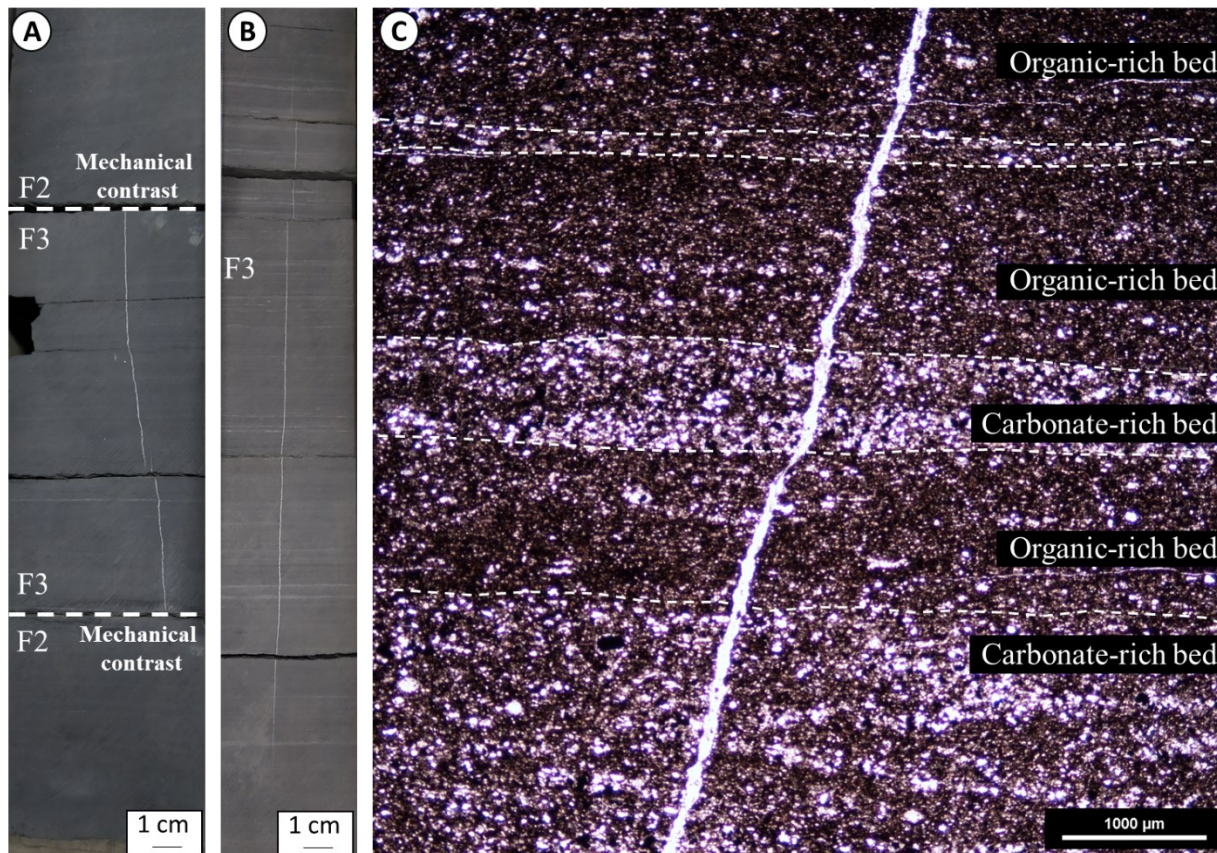


Fig. 4.32. Vertical fractures in mudrocks of the Duvernay Formation: A) Vertical calcite-filled fracture propagated in F3 and limited by rock strength contrast between facies F2 and F3 (well 3, 3280.54 m). B) Vertical calcite-filled fracture fading into the mudstones at the top and bottom tips of the fracture, facies F3 (well 3, 3282.14 m). C) Thin-section of a tensile vertical calcite-filled fracture crossing microlaminae of carbonate- and organic-rich mudrocks (well 4, 3190.93 m). Parallel nicols. See Table 3.1 and Fig. 4.6 for the wells' name and location.

The measured aperture of calcite-filled fractures in core of mudrocks of the Duvernay Formation generally ranges from <0.1 mm to 0.5 mm, with the majority between 0.1 mm and 0.2 mm (Fig. 4.33). Fractures in carbonate-rich facies F5 have larger (>0.4 mm) aperture. Fracture aperture in transtensional fractures is not always constant and changes depending on the lithology of microlaminae. Fractures are tensile with larger aperture in carbonate-rich laminae and shear with no or very small aperture in organic-rich micro-laminae (Fig 4.34).

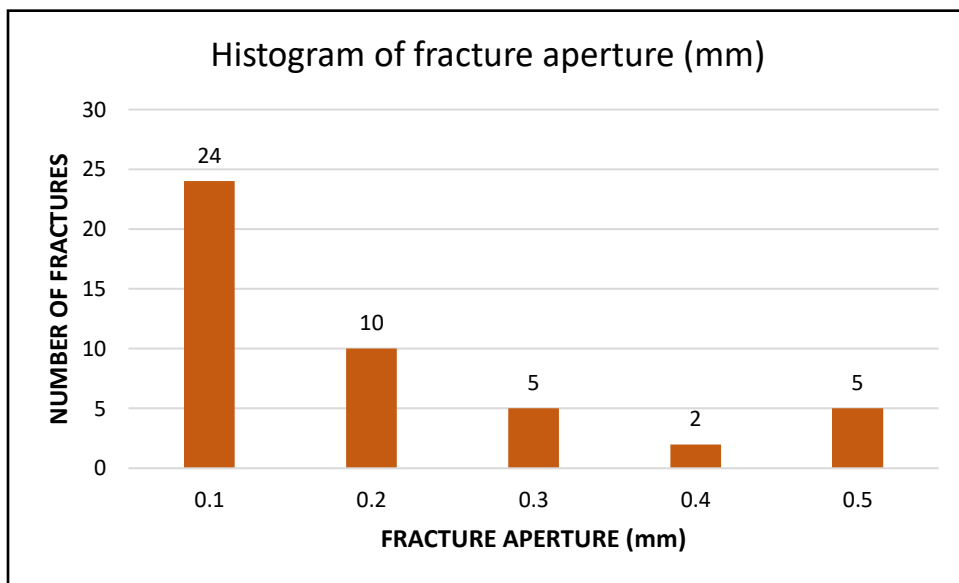


Fig. 4.33. Histogram of fracture aperture size of calcite-filled fractures in mudrocks of the Duvernay Formation. About half of measured fractures are characterized by aperture between 0.1 and 0.2 mm. Total number of samples 46.

Fractures studied in core of the Duvernay Formation are tensile (tension without vertical displacement) and transtensional, with tensile and shear segments based on the classification shown in Ferril et al., (2017). Transtensional calcite-filled fracture splays were described in core of well 3 with 20-30 cm of height and 10-30° of inclination with respect to the core axis (Fig. 4.34). These fractures start with a single short subvertical tensile fracture that splits upward in two, which in turn also split into several ones, thus forming a splay of fractures. Most of these fractures have repeating intervals of tension openings, usually in carbonate-rich laminae, and shear segments, in organic-rich laminae (Fig. 4.34, Fig. 4.35). Dilational jogs are usually seen in carbonate-rich intervals (Sibson, 2000), showing calcite filling with bigger crystal size (100 – 500 μm) as there is more space available for crystals to grow (Fig. 4.34. B, E).

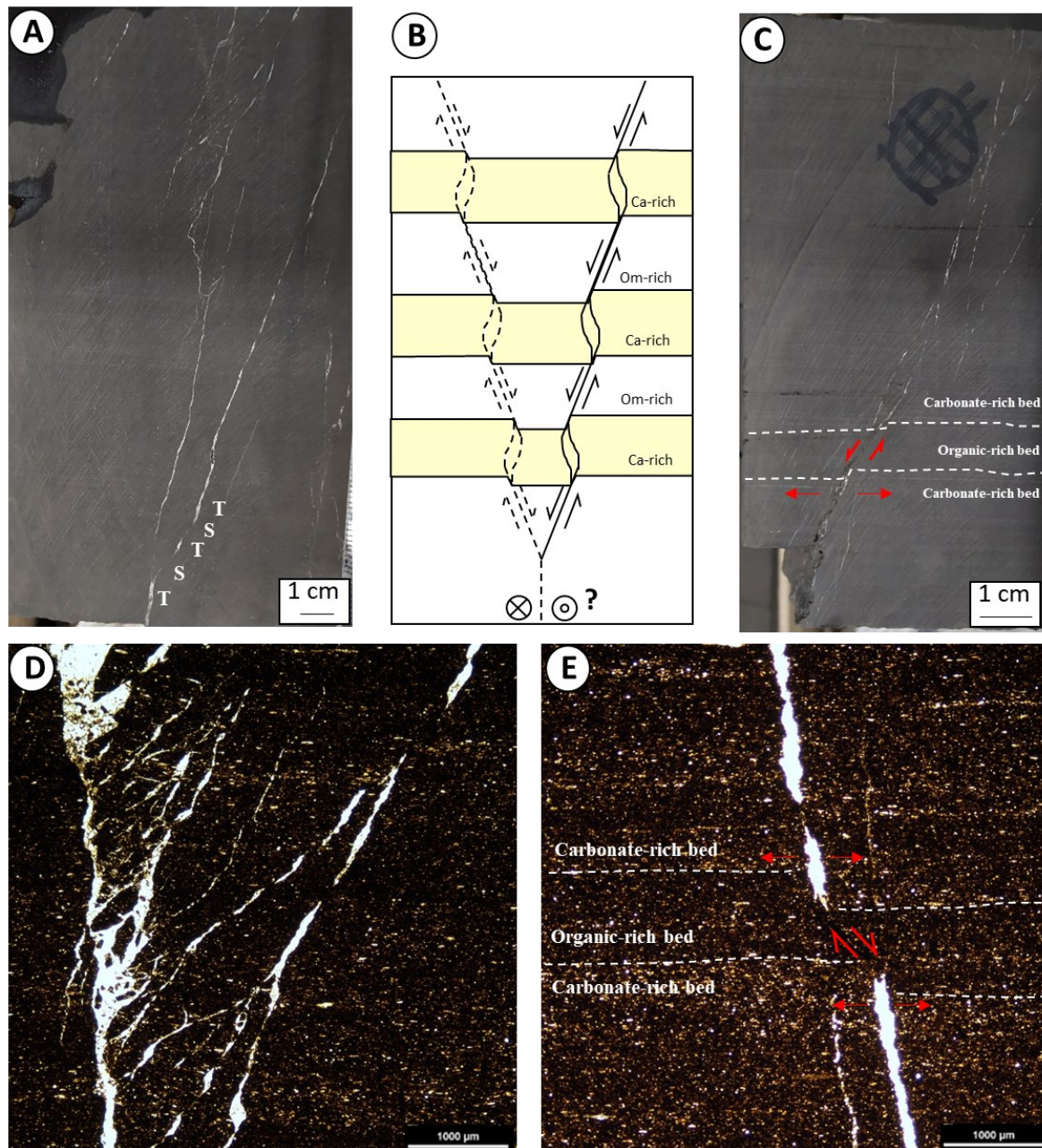


Fig. 4.34. Transtensional calcite-filled fractures in the Duvernay Formation: A) Core sample with a splay of inclined calcite-filled complex fractures characterized by repeating segments of shear (S) and tensile (T) deformation (well 3, 3285.19 m). B) Schematic representation of the influence of bed competence on deformation during fracture propagation, with tensile dilational jogs forming in carbonate-rich beds and shear deformation in ductile organic-rich beds, modified from Sibson (2000). C) Core sample with another splay of inclined calcite-filled complex fractures, showing shear deformation in organic-rich beds and tensile deformation in carbonate-rich beds (well 3, 3284.30 m). D) Thin-section of a splay of calcite-filled fractures in facies F3 (well 3, 3285.12 m). E) Thin-section of one branch of the splay of fractures in facies F3 showing shear deformation in organic-rich laminae and calcite-filled tensile deformation in

carbonate-rich laminae (well 3. 3285.12 m). Parallel nicols in B and D. See Table 3.1 and Fig. 4.6 for the wells' name and location.

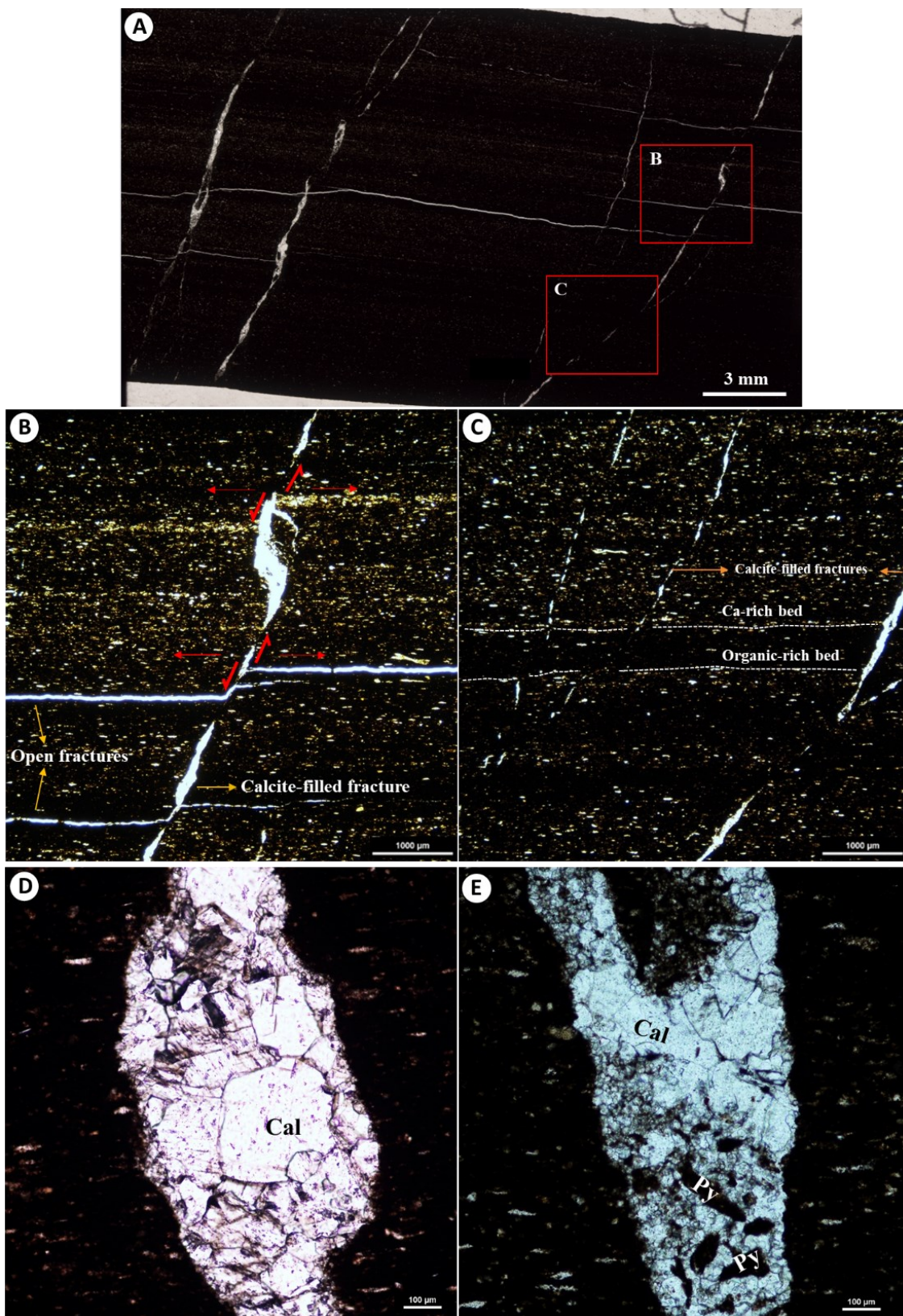


Fig. 4.35. Fractures in the Duvernay mudrocks in thin sections: A) Scanned thin section showing several branches of a transtensional complex splay of fractures. The red squares indicate the location of figures B and C. B) Calcite-filled fracture showing tension gashes in carbonate-rich beds and shear displacement in organic-rich beds. Open horizontal fractures along the bedding are displaced by high-angle transtensional fracture (well 3, 3284.29 m). C) Several sub-vertical calcite-filled fractures, showing shear deformation in organic-rich beds and tensile deformation in carbonate-rich beds (well 3, 3284.30 m). D) Calcite-filled tension gash showing blocky texture (well 3, 3284.49 m). E) Calcite and pyrite-filled tension gash showing blocky texture and different grain-size of calcite filling (well 3, 3284.29 m). Nicols parallel in B-E. See Table 3.1 and Fig. 4.6 for the wells' name and location.

Polished slip faces (PSF) with slickenside striae (Davies et al., 2013, 2014) were described in core of the Duvernay Formation in studied vertical wells (Table 3.1). PSF were detected only in well 1, in organic-rich facies F2 (Fig. 4.36.A). They are associated with pyrite-rich laminae formed parallel to slightly inclined bedding in bituminous and argillaceous mudrocks. The striae on the PSF surface indicate the direction of displacement along the PSF (Fig. 4.36.B). The shear and frictional heating along the PSF form the mirror-like faces (Fig. 4.36.B).

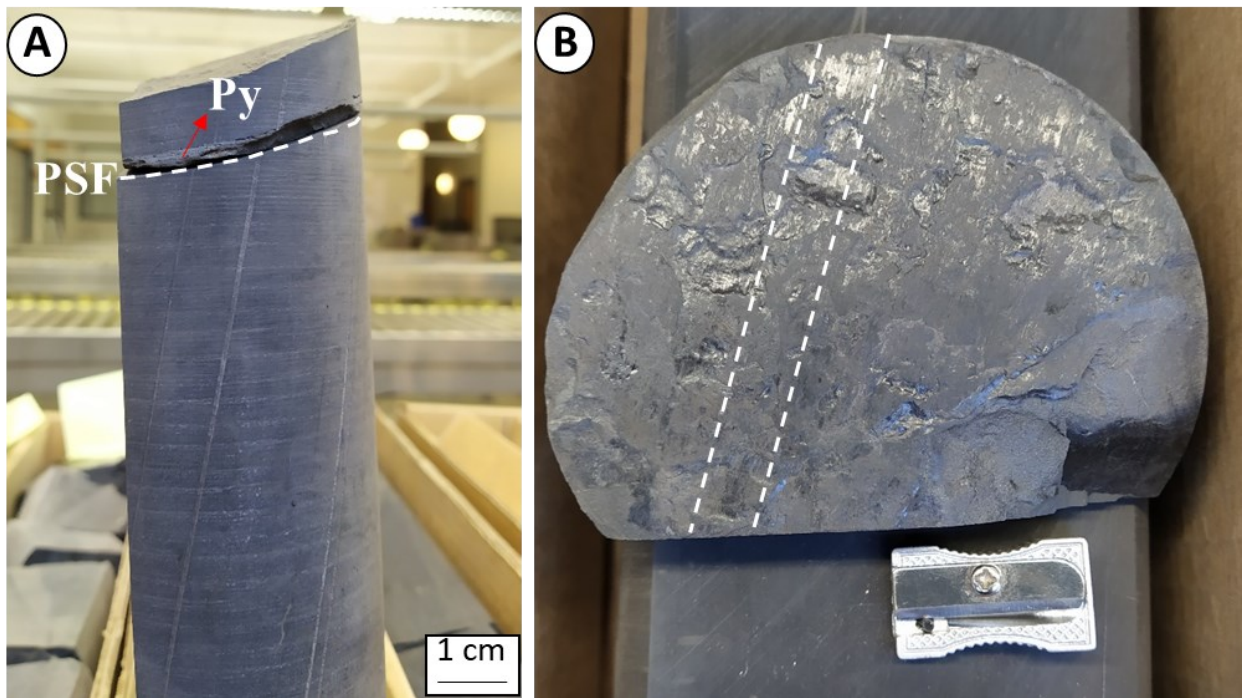


Fig. 4.36. Polished slip faces (PSF) in the mudrocks of the Duvernay Formation: A) Side-view of the core sample, showing location of PSF along pyrite-rich laminae of 3 mm thick in bituminous mudrock. B) Top

(map) view of the PSF, showing the mirror-like face with striae highlighted by white dotted lines (well 1, 3448.40 m). See Table 3.1 and Fig. 4.6 for the wells' name and location.

4.5.2. Drilling-induced fractures (DIFs)

The Drilling-induced fractures were identified in several studied vertical wells 1-7. The most common drilling-induced fractures are described as petal fractures (Fig. 4.37). The observed fractures were isolated and located at one side of the core. Surfaces of petal fractures are smooth with a concave shape with fracture dip increasing with depth (Fig. 4.37). These fractures strike for a few centimeters (5 – 10 cm), ending in the centerline of the core. Petal fractures are known to originate beneath the drilling bit while drilling resulting from the impact of the bit's weight along with the drill string. The petal fractures induced by drilling may form as a single or a pair of petal fractures located at opposite sides of the core (Kulander et al., 1990; Lorenz et al., 1990).

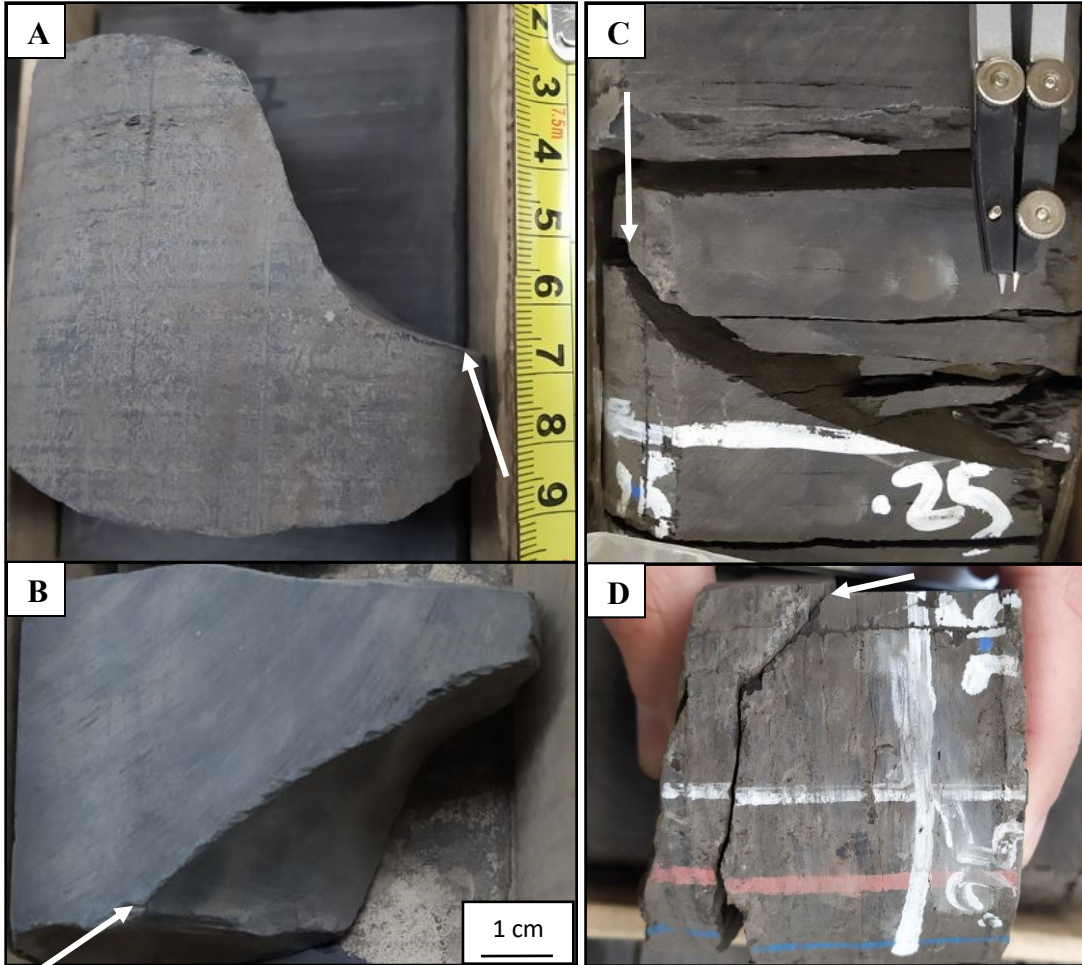


Fig. 4.37. Petal drilling-induced fractures observed in core samples of mudrocks of the Duvernay Formation in the Kaybob area: A) Well 3, 3268.42 m (side view). B) Well 3, 3268.42 m. C) Well 4, 3197.80 m. D) Well 4, 3197.80 m (side view). See Table 3.1 and Fig. 4.6 for the wells' name and location.

Irregular crack networks were observed in core of the Duvernay Formation in several vertical wells within the study area (Fig. 4.38). Most of them were described in carbonate-rich facies F1 and F5. Cracks form random networks or follow the contour of the nodules (Fig. 4.38). Usually cracks are open fractures or filled with drilling mud or rock flour from slabbing. These crack networks are typically found in fine-grained limestones and dolomites (Lorentz and Cooper, 2018). The lack of mineralization indicates that these fractures are induced, probably related to the stress concentrations during the drilling (Lorentz and Cooper, 2018).

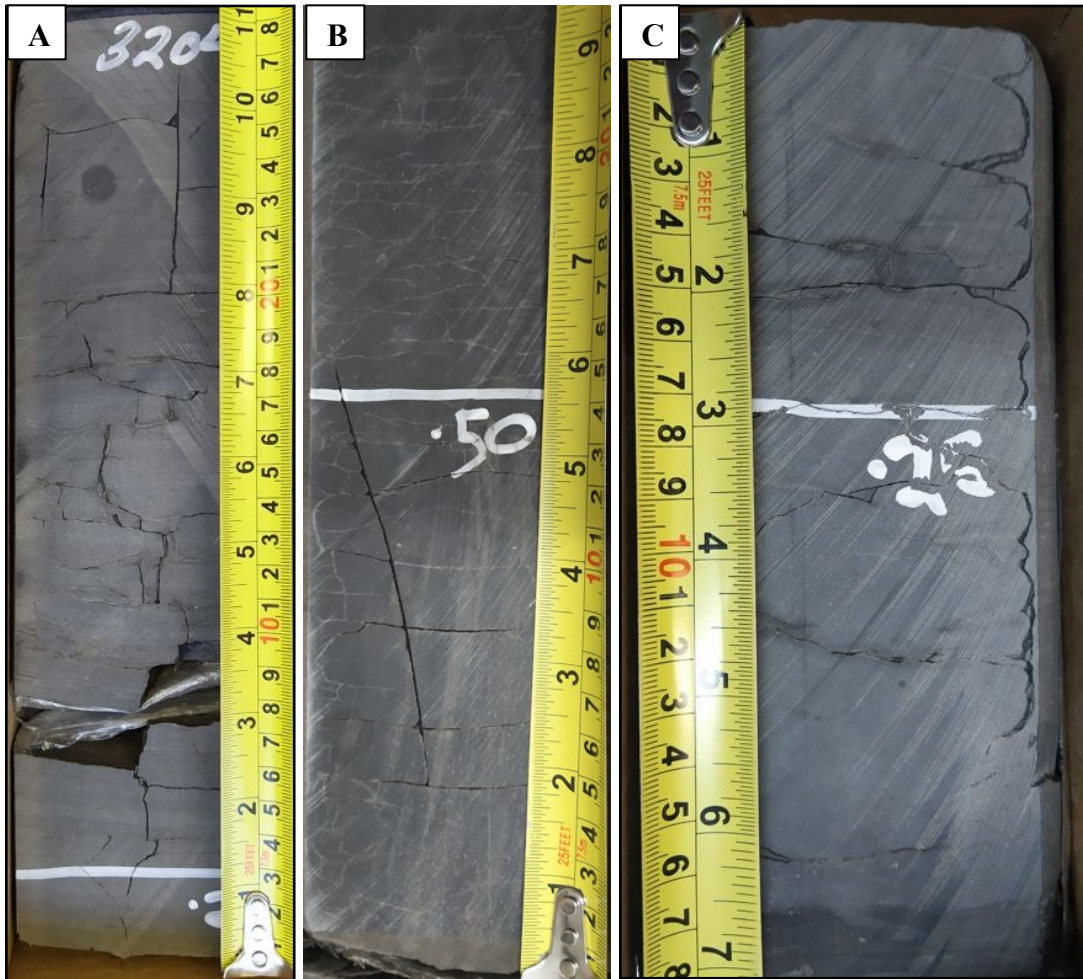


Fig. 4.38. Drilling-induced irregular crack networks observed in core samples of mudrocks of the Duvernay Formation in the Kaybob area: A) open cracks in carbonate nodules of facies F5 (well 4, 3208.65 m). B) open and rock-flour filled cracks in facies F1 (well 7, 3539.26 m). C) Open cracks replicating the shape of the carbonate nodules at the edge of the core, with several subhorizontal cracks, facies F5 (well 7, 3567.80 m). See Table 3.1 and Fig. 4.6 for the wells' name and location.

4.5.3. Fracture intensity (P10)

Vertical fracture intensity P10 was estimated for natural fractures in core of the Duvernay Formation for seven vertical wells 1-7 (Table 3.1, Fig. 4.6) and analyzed for each lithofacies (Table 4.1). The number of fractures was corrected with Terzaghi's angular correction equation (see section 3.2.1). The estimated fracture intensity P10 ranges from 0 fract/m in well 5 to 3.05 fract/m in well 7 (Fig. 4.39, Table 4.5).

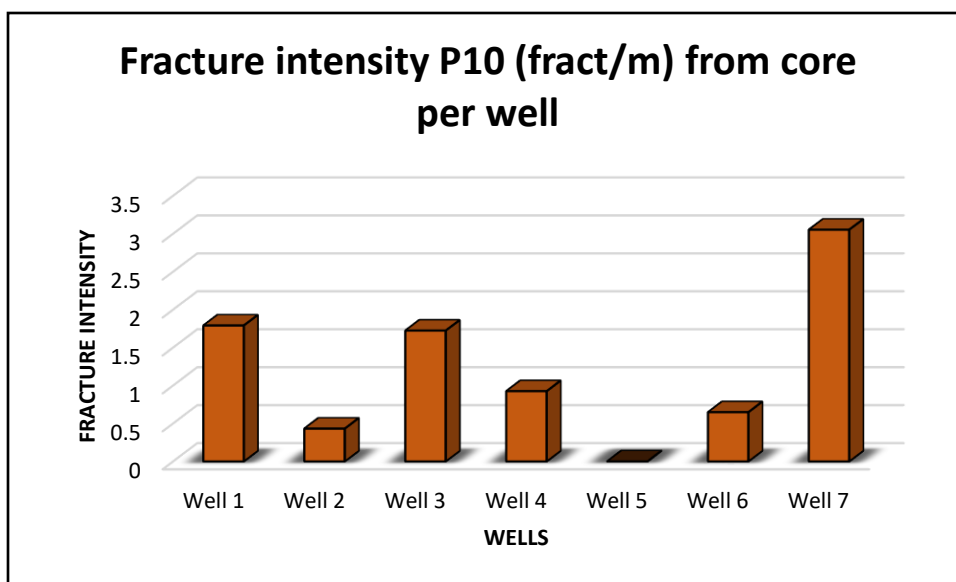


Fig. 4.39. Fracture intensity P10 (fract/m) in core of the Duvernay Formation per well after application of the Terzaghi's correction. See Table 3.1 and Fig. 4.6 for the wells' name and location.

Well	Fracture intensity P10 (fract/m)
1	1.79
2	0.43
3	1.72
4	0.93
5	0
6	0.65
7	3.05

Table 4.5. Fracture intensity P10 values (fract/m) in core of the Duvernay Formation per well after application of the Terzaghi's correction. See Table 3.1 and Fig. 4.6 for the wells' name and location.

The fracture intensity P10 that was estimated in core of the Duvernay Formation in seven wells 1-7 was extrapolated between the wells (Fig. 4.40). P10 is the highest in the W-SW reaching 3.05 fract/m in well 7, 1.79 fract/m in well 1 and 1.72 fract/m in well 3 that is located in the middle of the Kaybob area (Fig. 4.40). The lowest P10 values are estimated in the central and NE parts of the basin, varying from 0.93 fract/m in well 4 to 0 fract/m in well 5 (Fig. 4.40).

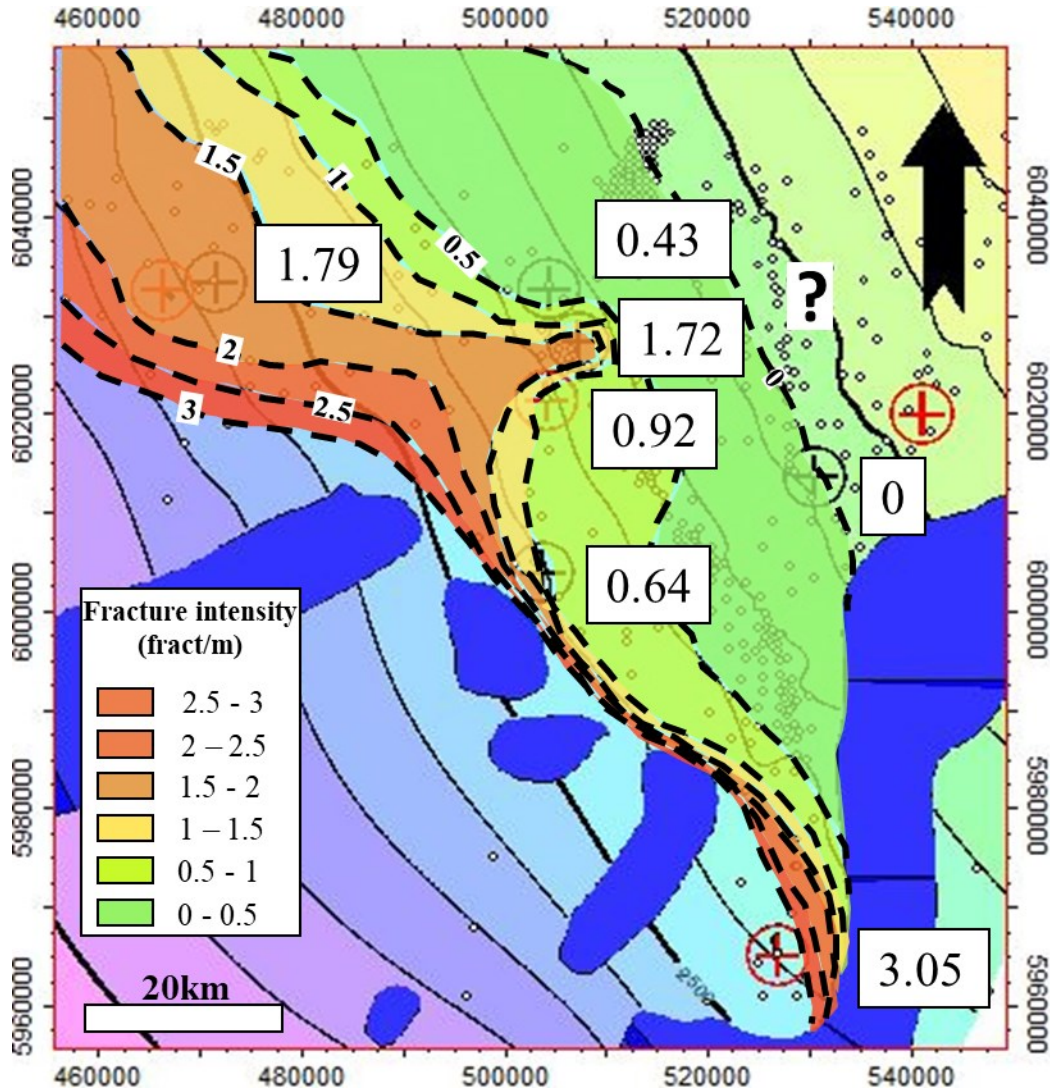


Fig. 4.40. Distribution of fracture intensity P10 in core of Duvernay Formation extrapolated between seven vertical wells 1-7. Background is the structural map (TVDSS) of the top of the Duvernay Formation. See Table 3.1 and Fig. 4.6 for the wells' name and location.

Fracture intensity P10 was estimated for each facies and normalized by facies thickness (Fig. 4.41). P10 is highest (1.58 fract/m) in organic-rich facies F3 with thin (mm scale) alternation of organic- and carbonate-rich laminations (Fig. 4.41, Table 4.6). P10 is 1.49 fract/m in facies F4, composed of fossiliferous bioturbated carbonate-rich wackestones. P10 is around 1

fract/m in carbonate- and organic-rich facies F1, F2 and F5, and 0.34 fract/m in clay-rich facies F7, and no fractures in F6 (Fig. 4.41).

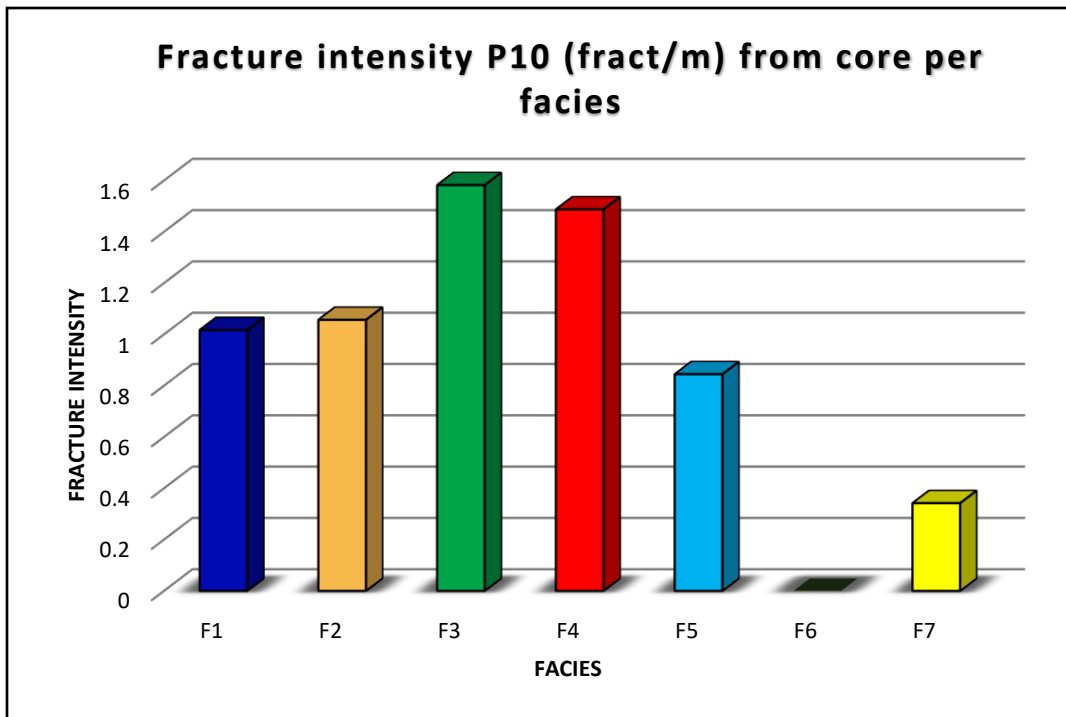


Fig. 4.41. Histogram of fracture intensity P10 (fract/m) estimated in core of the Duvernay Formation per facies after normalization by facies thickness and application of the Terzaghi's correction. See Table 4.1 for facies composition.

Facies	Fracture intensity P10 (fract/m)
F1	1.02
F2	1.06
F3	1.58
F4	1.49
F5	0.84
F6	0
F7	0.34

Table 4.6. Fracture intensity P10 (fract/m) estimated in core of the Duvernay Formation per facies after normalization by facies thickness and application of the Terzaghi's correction. See Table 4.1 for facies composition.

4.6. Fractures in horizontal wells interpreted from FMI logs

FMI image logs were studied in four horizontal wells in the Kaybob Area (Fig. 4.42). The wells are labelled from A to D. Well A is located approximately 26 km to the NW of Bigstone reef, in the NW edge of the study area. Well B is found at ~17 km to the NE of Bigstone reef, in the center of the basin. Well C is located at 11 km to the N of Windfall reef, close to the eastern boundary of the study area. Well D is positioned in the south of the study area, at 8.6 km to the W of the Windfall reef. The lateral sections of horizontal wells are oriented N144°E for well A; N03°E for well B; N01°E for well C; and D N343°E for well D. The diameter of production casing of horizontal sections is 114.3 mm (4.5 in) for wells A, B, and D, and 139.7 mm (5.5 in) for well C. The horizontal sections of wells B, C, and D are approximately 1.3 km long, and about 1.05 km for well A. As shown below (Fig. 4.53, 4.56, 4.57, and 4.61), all four horizontal wells were landed within the upper Duvernay Member, mostly crossing organic-rich facies F2 and F3. Locally, wells are intersecting carbonate-rich facies F1 and F5.

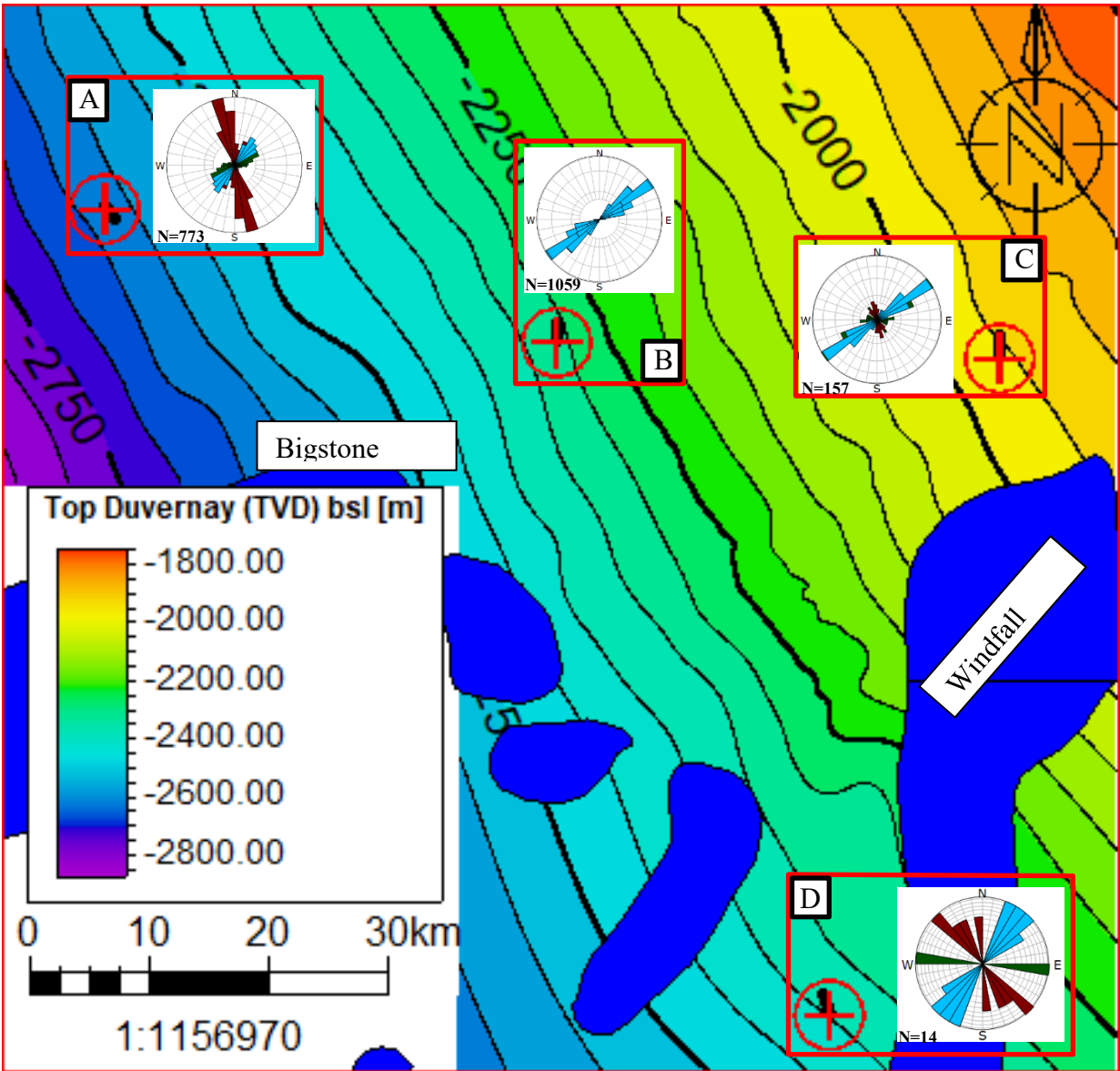


Fig. 4.42. Depth structural map of the top of the Duvernay Formation (bsl). Location of four horizontal wells, in which FMI image logs were studied, is shown. The blue polygons depict simplified geometry of the Leduc Reefs. Rose diagrams show the strike of each set of fractures per well and the total number of fractures per well (N). See Table 4.1 for the number of fractures per set and per well.

4.6.1. Orientation of natural fractures

Natural fractures interpreted in horizontal wells include resistive, continuous and discontinuous conductive fractures.

4.6.1.1. Well A N144°E

Three sets of natural fractures of different orientation were identified in well A (Fig. 4.43. and Fig. 4.44, Table 4.7). The natural fractures are mostly subvertical and abundant (N=773) in this well. The mean fracture plane of Set 1 has a strike NE-SW (N40°E/85°); for Set 2, it is oriented NW-SE (N168°E/85°); and for Set 3, it is oriented NE-SW (N72°E/83°). The number of fractures per set is different, being 165 for Set 1; 526 for Set 2; and 82 for Set 3 (Table 4.7). The bedding of the Upper Duvernay Formation is subhorizontal. The mean bedding plane has a strike of NW-SE (N175°E) and dips at 06° to the SW (Fig. 4.44). Based on the description of the core in the neighboring vertical well, bed thickness varies widely, ranging from 30 cm in carbonate-rich facies to thinly laminated beds with laminae thickness the scale of millimeters, resulting from the alternating micro-layers of dark grey organic-rich and light-grey carbonate-rich laminae. Carbonate nodules are rare and randomly distributed in horizontal section of the well.

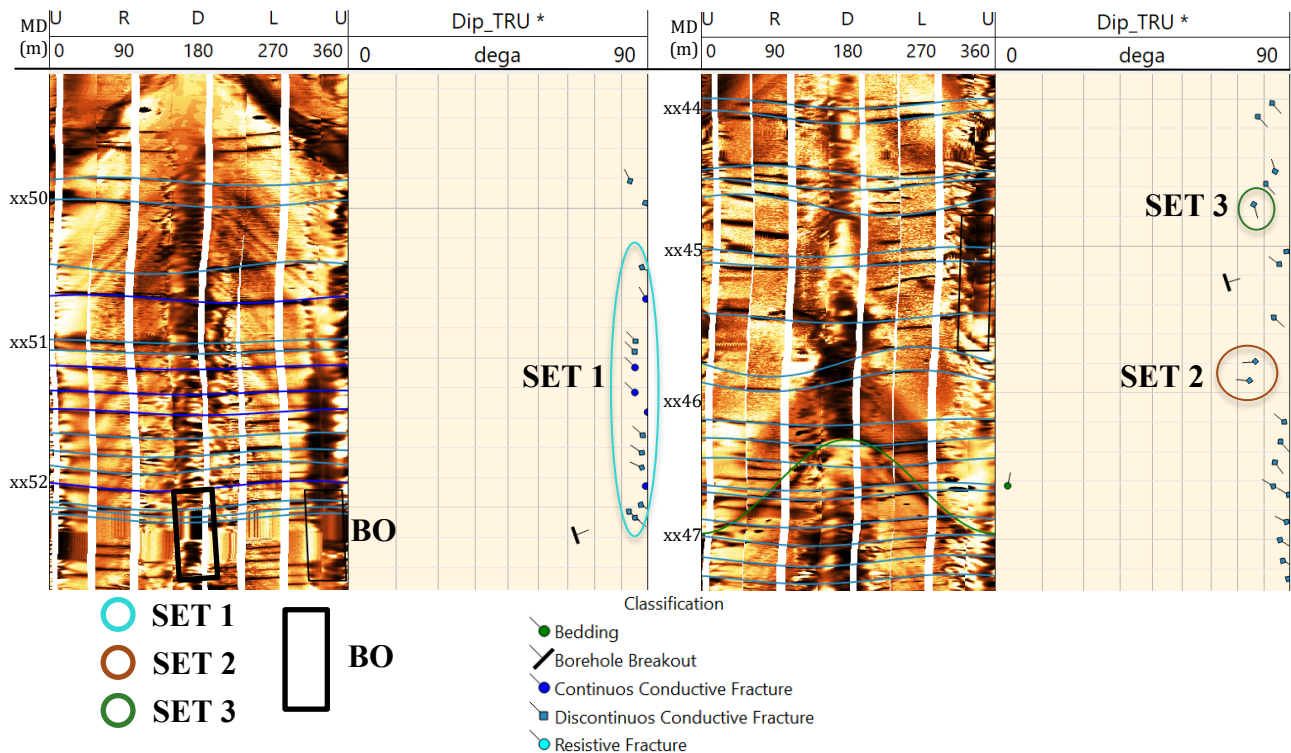


Fig. 4.43. Example of interpreted FMI log in well A. Three sets of subvertical natural fractures of variable orientation are marked by circles of different colors. Borehole breakout (BO) is shown by black polygons. Most of the fractures represented as sinusoids that cross the borehole entirely. See Fig. 4.42 for well location.

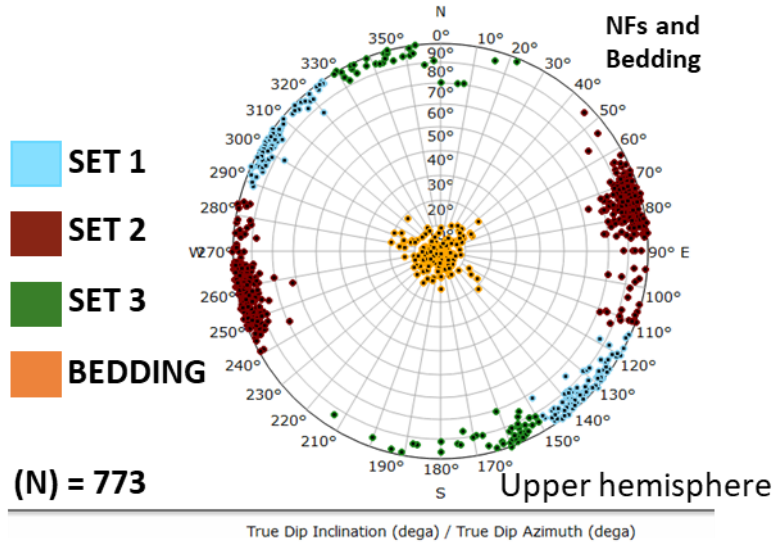


Fig. 4.44. Stereographic equal area projection of three sets of natural fractures (NF) and bedding picked in well A plotted as poles to planes (true dip azimuth and true dip angle, upper hemisphere). See Fig. 4.42 for well location.

	Bedding	BO	DIFs	Set 1	Set 2	Set 3
Well A	NW-SE	NW-SE	-	NE-SW	NW-SE	NE-SW
	N175°E/06°SW	N141°E/81°		N40°E/85°	N168°E/85°	N72°E/85°
				N = 165	N = 526	N = 82
Well B	N-S	-	NE-SW	NE-SW	-	-
	N179°E/05°W		N55°E/86°	N53°E/87°		
				N = 1059		
Well C	N-S	-	NE-SW	NE-SW	NW-SE	W-E
	N178°E/05°W		N53°E/77°	N55°E/81°	N161°E/71°	N93°E/70°
				N = 118	N = 19	N = 20
Well D	NW-SE	NW-SE	-	NE-SW	NW-SE	W-E
	N158°E/06°SW	N340°W/87°		N38°E/85°	N134°E/81°	N90°E/79°
				N = 7	N = 5	N = 2

Table 4.7. Orientation (strike azimuth and dip angle) of bedding, Borehole Breakouts (BO), Drilling-induced fractures (DIFs) and sets of natural fractures (Set 1 to 3) for each horizontal well. Number of fractures per set and per well are shown.

4.6.1.2. Well B N03°E

Well B is characterized by the presence of the highest number of fractures (N=1059) compared to other three wells. Natural fractures of one set were identified (Fig. 4.45 and Fig. 4.46, Table 4.7), oriented NE-SW (N53°E/87°), which is close to the orientation of fractures of set 1 in well A. The mean bedding plane is oriented N-S (N179°E) and dips at 5° to the S (Fig. 4.46). The lithofacies interpreted in core of vertical well 4 from the same well pad reveals that well B was positioned within organic-rich facies F2 and F3. The bed thickness in these facies varies from 1 cm to ~5 cm with mm-thick laminations. The carbonate nodules are rare in the horizontal well B.

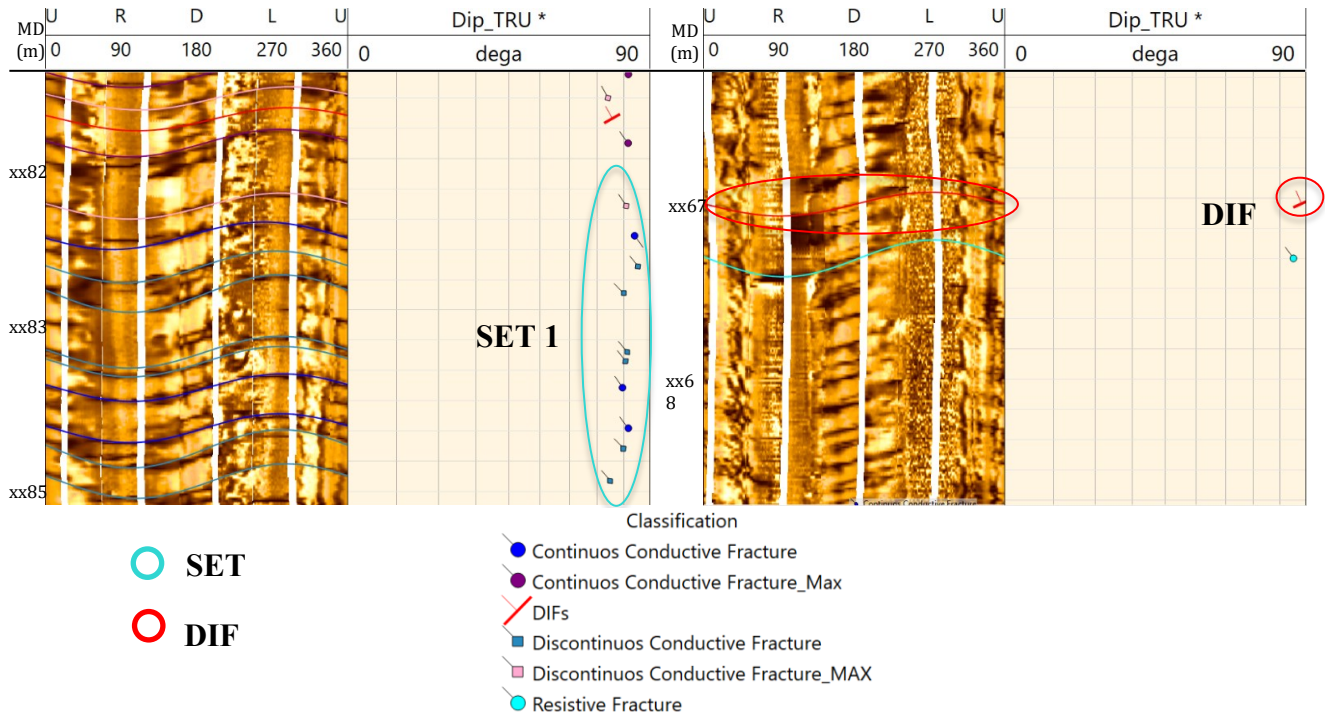


Fig. 4.45. Example of interpreted FMI log in well B. Set 1 of the NE-SW-striking subvertical natural fractures is marked with oval of blue color. Drilling-induced fractures (DIF) are outlined by red circle. See Fig. 4.42 for well location.

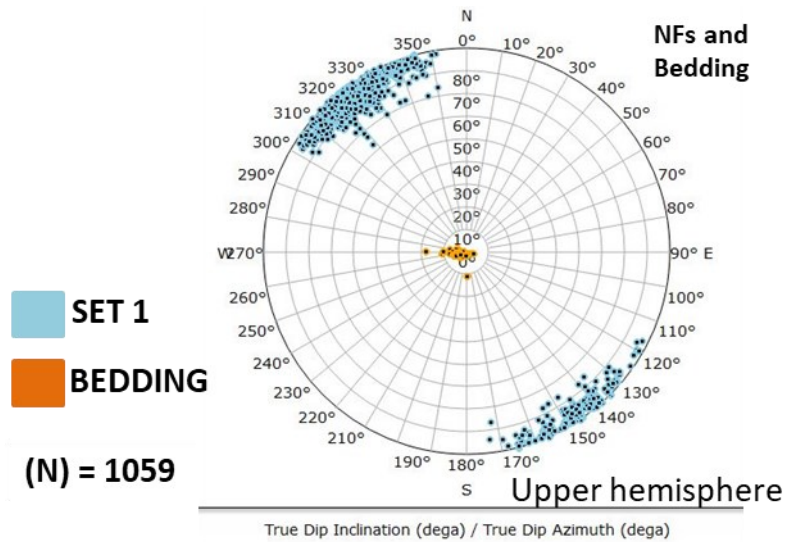


Fig. 4.46. Stereographic equal area projection of set 1 of natural fractures and bedding picked in well B and plotted as poles to planes (true dip azimuth and true dip angle, upper hemisphere). See Fig. 4.42 for well location.

4.6.1.3. Well C N01°E

Well C is characterized by lower number of fractures ($N=157$), compared with wells A and B. Three sets of subvertical fractures were distinguished (Fig. 4.47 and Fig. 4.48, Table 4.7). Set 1 is oriented NE-SW ($N55^{\circ}E/81^{\circ}$); Set 2 is NW-SE ($N161^{\circ}E/71^{\circ}$); Set 3 is W-E ($N93^{\circ}E/70^{\circ}$). The number of fractures per set is different, being 118 for Set 1; 19 for Set 2; and 20 for Set 3 (Table 4.7) Bedding is subhorizontal and oriented almost N-S ($N178^{\circ}E$), dipping at 05° to the S. Although the image log quality in this well is relatively poor, small carbonate nodules of a few centimeters large were detected.

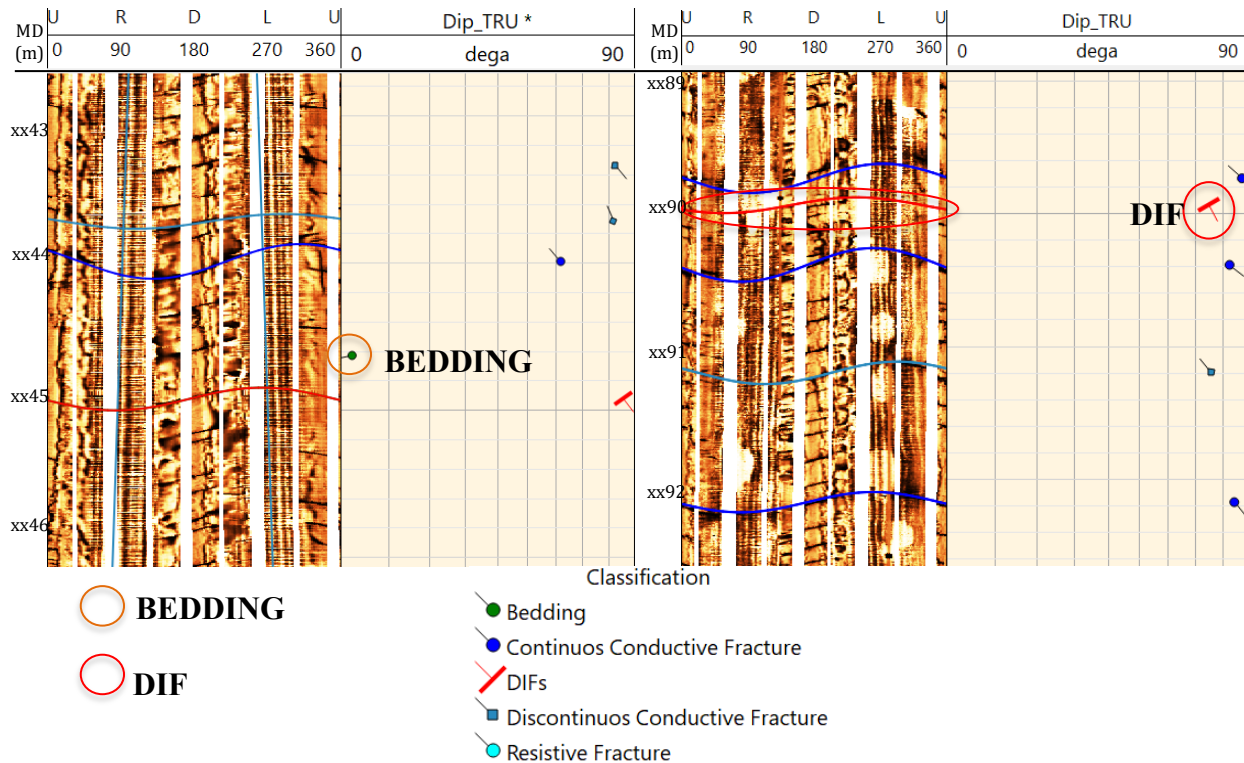


Fig. 4.47. Example of interpreted FMI log in well C. See Fig. 4.42 for well location.

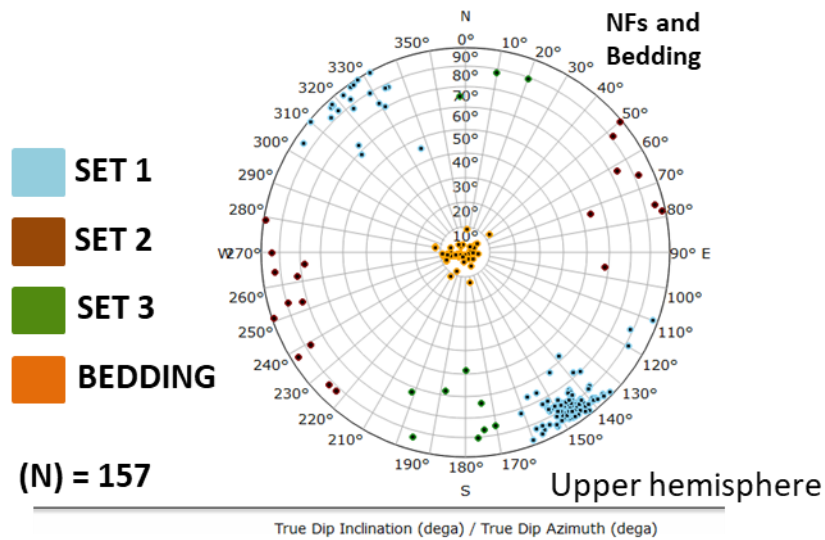


Fig. 4.48. Stereographic equal area projection of three sets of natural fractures and bedding picked in well C plotted as poles to planes (true dip azimuth and true dip angle, upper hemisphere). See Fig. 4.42 for well location.

4.6.1.4. Well D N343°E

A few fractures were picked in well D (N=14), where six of them are present in the carbonate nodule (Fig. 4.49). The quality of the image log is quite poor in the well, which explains the low number of detected fractures. Three sets of subvertical fractures were interpreted (Fig. 4.50, Table 4.7). Set 1 is oriented NE-SW (N38°E/85°); Set 2 is NW-SE (N134°E/81°); Set 3 is W-E (N90°E/79°). From the 14 fractures picked in this well, 7 are included in Set 1, 5 in Set 2 and 2 in Set 3 (Table 4.7). Bedding is oriented NE-SW (N158°E) and dips at 06° to the SW. The lithofacies interpreted in core of vertical well 7 of the same well pad reveals that carbonate-rich facies F1 and F5 with abundant carbonate nodules are located close to the heel of well D (Fig. 4.61), while organic-rich facies F2 and F3 dominate in the middle of the horizontal section and at the toe of the well. The size of carbonate nodules varies from a few centimeters to more than ~10 cm, the borehole diameter.

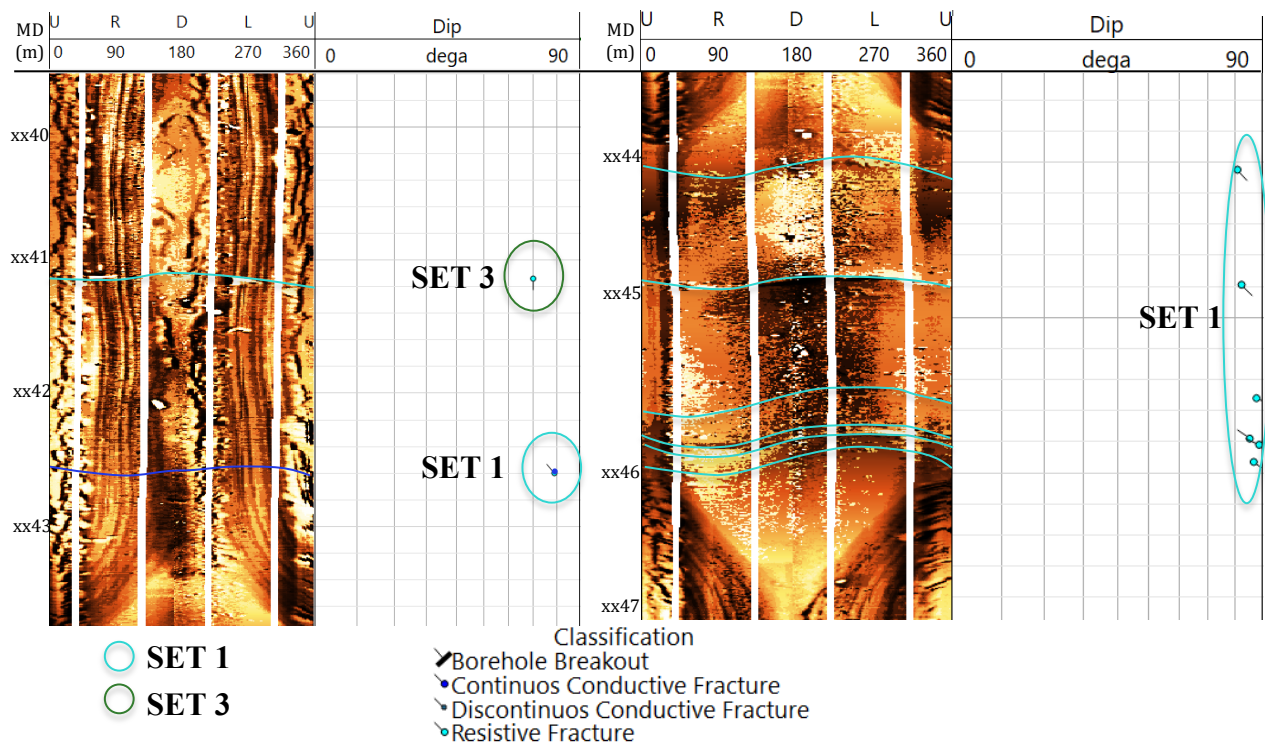


Fig. 4.49. Example of interpreted FMI log in well D. Set 1 and 2 of subvertical natural fractures are marked with blue and green circles. See Fig. 4.42 for well location.

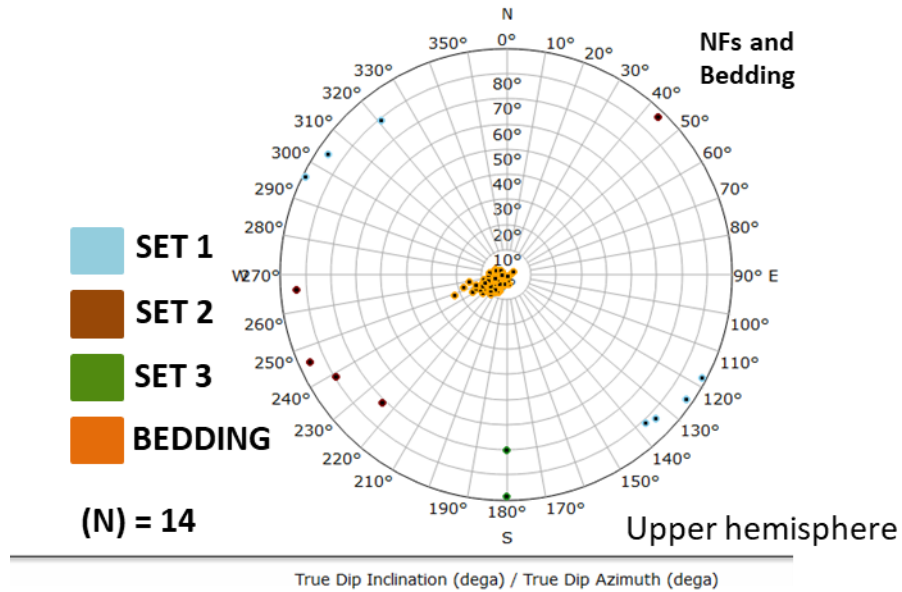


Fig. 4.50. Stereographic equal area projection of three sets of natural fractures and bedding picked in well D plotted as poles to planes (true dip azimuth and true dip angle, upper hemisphere). This well shows the lower number of fractures (N=14). See Fig. 4.42 for well location.

4.6.1.5. Orientation of resistive and conductive natural fractures

Resistive (mineralized) and conductive (open) natural fractures were distinguished in the four horizontal wells (Fig. 4.51, Table 4.8). Conductive fractures in FMI logs are represented by sinusoids of dark color, while resistive fractures are light in color. In general, conductive fractures are more abundant than resistive fractures in studied wells. Well B has the highest number of conductive fractures (N=1039), while well A has the highest number of resistive fractures (N=138). Both types of fractures have similar orientation in wells A, B and C. The low number of fractures in well D (7 conductive and 7 resistive) does not allow interpretation of statistically significant sets of fractures. Fractures in all wells are mostly subvertical with just a few inclined fractures detected in well C.

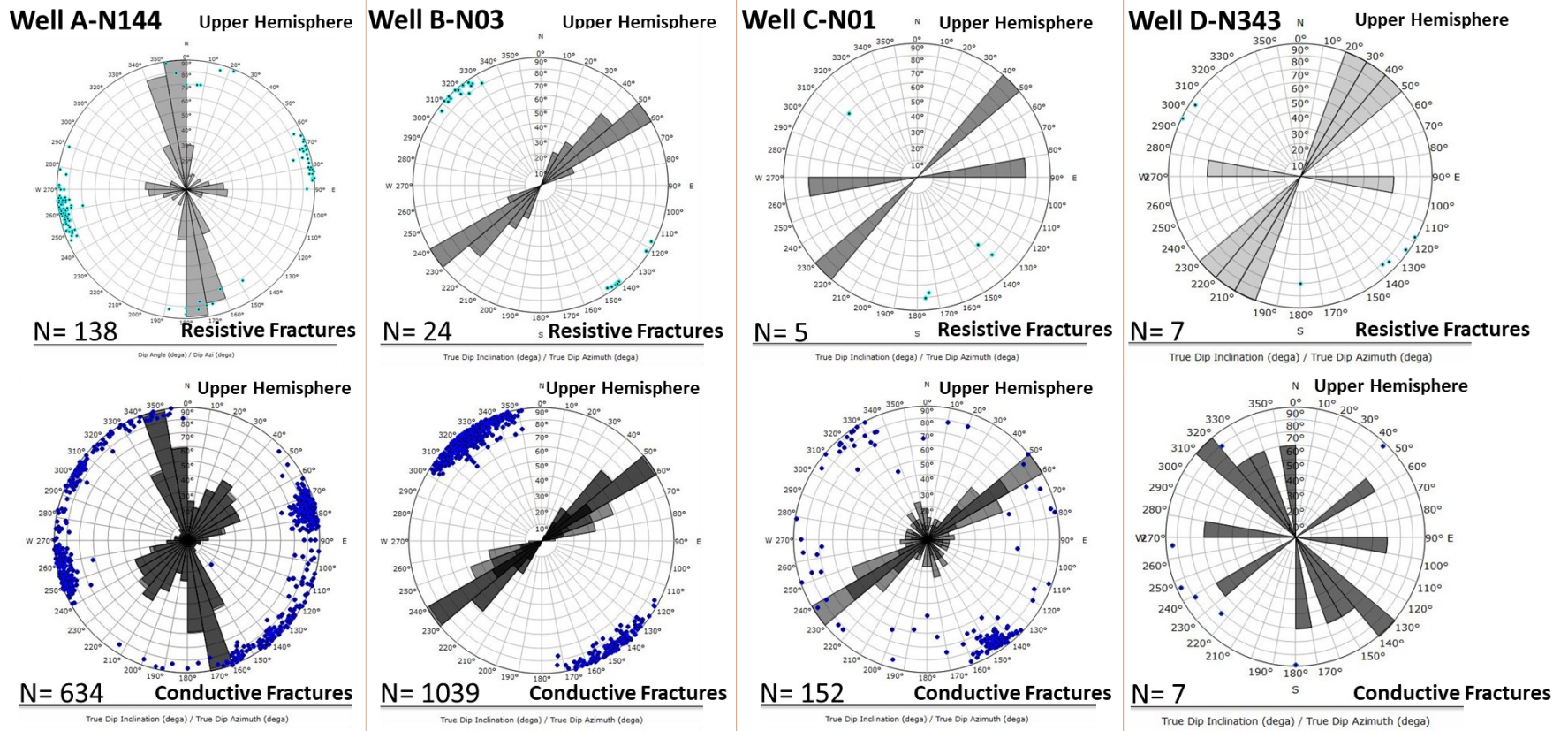


Fig. 4.51. Rose diagrams and stereographic equal area projection (upper hemisphere) showing poles to planes of natural fractures (true dip angle, true dip azimuth) and strike of resistive (upper row) and conductive (lower row) fractures for each horizontal well.

	Resistive fractures			Conductive fractures		
	Set 1	Set 2	Set 3	Set 1	Set 2	Set 3
Well A	N39°E	N170°E	N89°E	N40°E	N168°E	N72°E
Well B	N51°E	-	-	N55°E	-	-
Well C	N46°E	-	N85°E	N55°E	N161°E	N96°E
Well D	N36°E	-	N90°E	N51°E	N150°E	N90°E

Table 4.8. Strike of resistive and conductive fractures per set in four horizontal wells.

4.6.1.6. Summary of orientation of natural fractures

From the analysis of FMI logs in 4 horizontal wells, three sets of subvertical natural fractures were interpreted (Fig. 4.52). Fractures of Set 1 are more abundant (N=1350) and oriented NE-SW (N53°E/85°), subparallel to the regional S_{Hmax} . Fractures of Set 1 are dominant in well B (N=1059), well C (N=118) and well D (N=7) (Fig. 4.42). Fractures of Set 2 (N=550) have a strike of NW-SE (N165°E/85°), being oriented at high angle (112°) to the S_{Hmax} . Fractures of Set 2 are dominant in well A, with N=526 (Fig. 4.42). Set 3 has the lowest number of fractures (N=103), which are oriented NE-SW (N74°E/82°), at low angle (21°) to the regional S_{Hmax} .

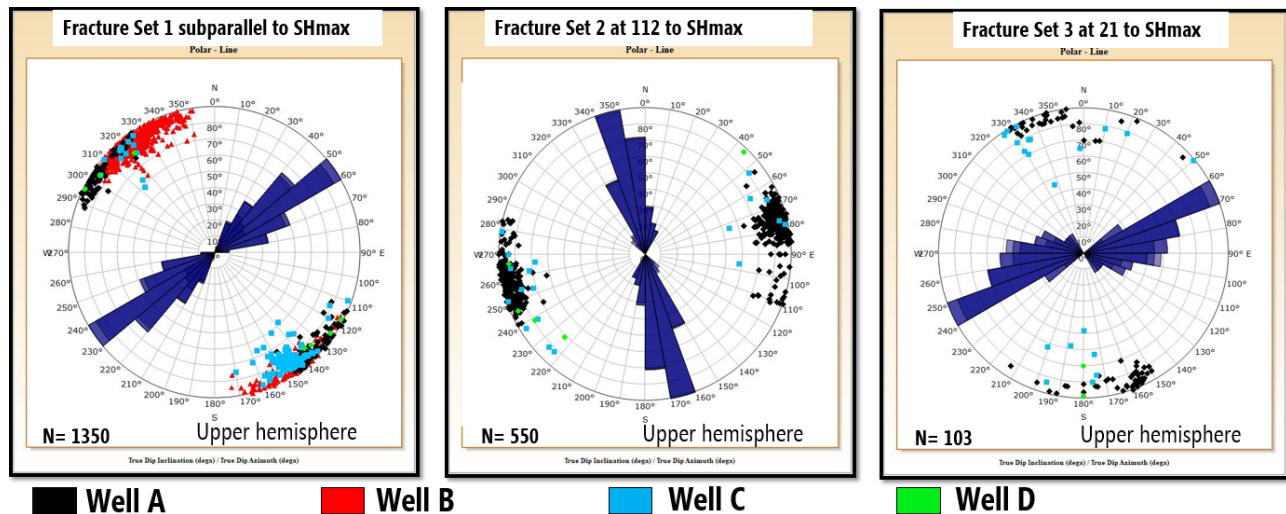


Fig. 4.52. Rose diagrams and stereographic equal area projection (upper hemisphere) showing poles to planes of natural fractures (true dip angle, true dip azimuth) and strike of three main sets of natural fractures determined in four horizontal wells A-D from image log analysis. See Fig. 4.42 for well location.

4.6.2. Fracture distribution and intensity P10, P32

Fracture distribution and intensity are described for each well and correlated with recorded GR and rate of penetration logs, lithofacies interpreted from neighboring vertical wells, and well trajectory curvature. Fracture intensity P10 and P32 is estimated with a step and window size of 0.5 m as described in Methods. The Terzaghi's correction was applied during the image log interpretation.

4.6.2.1. Well A N144°E

Well A was landed in the upper Duvernay Member (Fig. 4.53). Open fractures are abundant (N=634), detected along the entire wellbore trajectory with an exception for the intervals of organic-rich facies with $GR > 200$ gAPI, in which only a few fractures were picked. Open fractures are usually discontinuous, crossing the borehole partially. Resistive fractures are lower in number (N=138) and clustered in three segments of 50-75 m long in facies with $150 < GR < 200$ gAPI with relatively higher carbonate content (Fig. 4.53).

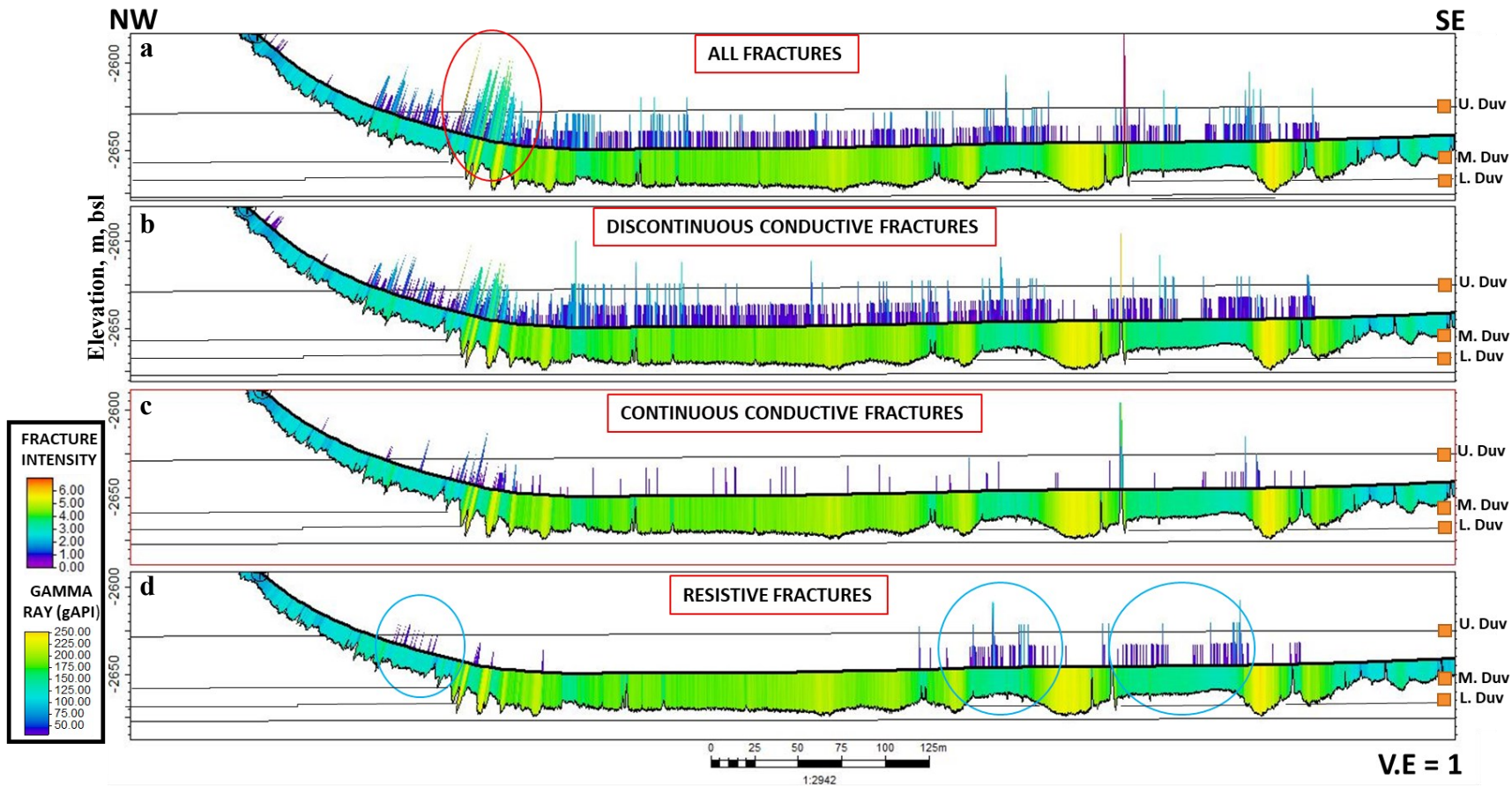


Fig. 4.53. Cross-section along well A. Surfaces of the tops of the Upper (U.Duv), Middle (M. Duv) and Lower Duvernay (L. Duv) Members are modeled based on the well tops in neighboring vertical wells. The GR log and histograms of fracture intensity P10 are shown along well A trajectory. P10 is shown for all fractures (a) and by fracture type (b-d): discontinuous conductive (b), continuous conductive (c), and resistive (d). Red circle highlights the interval of maximum curvature of the borehole trajectory, close to the heel of the well. Blue circles depict location of resistive fractures clustered in intervals of carbonate-rich facies with low GR ($150 < GR < 200$ gAPI).

The mean fracture intensity in well A is 2.84 ± 2.49 fractures/m (P10) and 2.86 ± 3.48 m²/m³ (P32). Both conductive and resistive fractures are frequent in facies F3 with intermediate to relatively elevated carbonate content and $\sim 150 < GR < 200$ gAPI. The fracture intensity in F3 is about 2.9 ± 3.29 up to 15 fractures/meter (P10) and 2.96 ± 2.12 to 10 m²/m³ (P32) (Table 4.9). In contrast, intervals of organic-rich facies with $GR > 200$ gAPI (Facies F2) are characterized by a decrease in fracture intensity to 0.96 ± 2.32 fractures/m (P10) or 0.96 ± 1.26 m²/m³ (P32) (Table 4.9). Resistive fractures are mainly clustered in carbonate-rich intervals F3 with $150 < GR < 200$ gAPI and rate of penetration of 8-10 m/h (Figs 4.53, 4.54) that is lower than in organic-rich facies F2 (12-16 m/h).

In the interval of maximum curvature at the heel of the well (Figs 4.53, 4.54), fracture intensity is high, reaching values of 13 fractures/m (P10) (mean 5.02 ± 3.4 fractures/m) and 10.5 m²/m³ (P32) (mean 5.21 ± 2.93 m²/m³). Most of the fractures picked in this interval are discontinuous conductive fractures (open fractures). An overestimation of natural fracture intensity might be expected because some of drilling-induced fractures might merge with natural fractures of the same orientation.

	GR (gAPI)	Mean P10 (frac/m)	Mean P32 (m ² /m ³)	Facies	Total P10 (frac/m) per well	Total P32 (m ² /m ³) per well
Well A	150<GR<200	2.9 ± 3.29	2.96 ± 2.12	F3	2.84 ± 2.49	2.86 ± 3.48
	>200	0.96 ± 2.32	0.96 ± 1.26	F2		
Well B	150<GR<200	4.43 ± 2.6	4.55 ± 1.98	F3	1.37 ± 2.45	1.37 ± 2.16
	>200	0.53 ± 1.76	0.51 ± 1.44	F2		
Well C	150<GR<200	0.62 ± 1.33	0.64 ± 1.02	F3	0.37 ± 1.11	0.37 ± 0.83
	~125 (middle section of the hz well)	0.26 ± 1.01	0.26 ± 0.66	F1-F3		
Well D	<75	0.143	-	F5	0.07 ± 0.1	-
	100<GR<150	0.007	-	F2-F3		

Table 4.9. Mean fracture intensity P10 and P32 estimated in each horizontal well in total and for intervals with different values of GR log. See Table 4.1 and text for the facies definition.

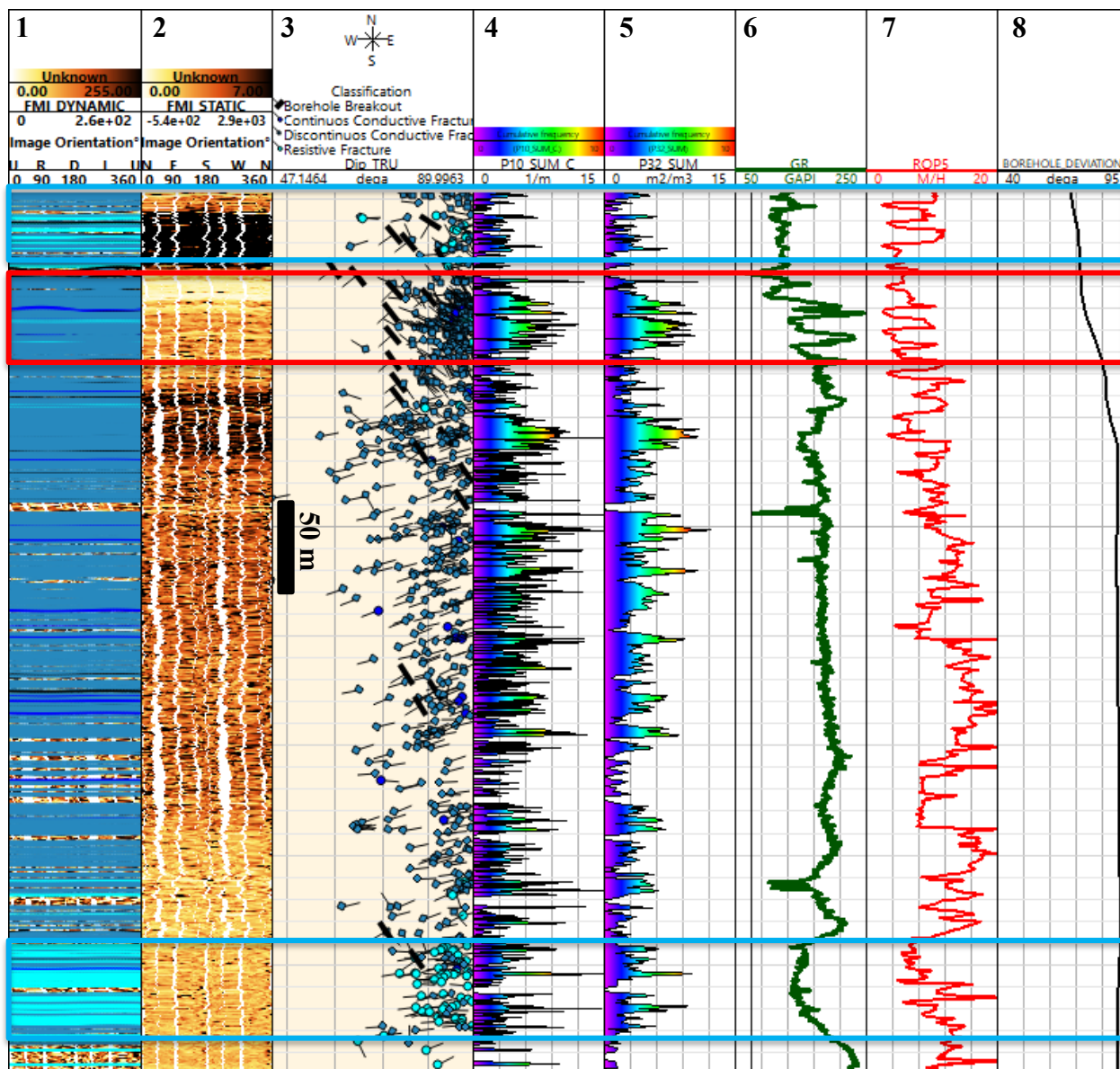


Fig. 4.54. Log plot for well A showing interpreted dynamic (track 1) and static (track 2) FMI logs, orientation of interpreted structures (track 3), fracture intensity P10 (track 4) and P32 (track 5), GR log (track 6), Rate of Penetration (ROPS) log (track 7), and borehole deviation (track 8). The blue rectangles define segments with dominant resistive fractures (mineralized), low GR and ROPS. The red rectangle depicts an interval of the maximum curvature of the borehole trajectory with dominant conductive fractures (open).

The NE-SW-striking fractures of set 1 (subparallel to the regional S_{Hmax}) were mostly picked in the interval of maximum curvature of the borehole (Fig. 4.55). Most of these fractures are discontinuous conductive fractures (N=153) with subordinate number of continuous conductive (7) and resistive (2) fractures. Some fractures of set 1 may represent drilling-induced fractures that have similar NE-SW orientation as described below.

The NW-SE-striking fractures of set 2 (oriented at high angle to S_{Hmax}) are present through the entire horizontal section of the well (Fig. 4.55), with higher number of fractures (N=528) compared to set 1 (N=162) and set 3 (N=83). Similarly to set 1, most of these fractures are discontinuous conductive (N=393), while only 14 are continuous and 121 are resistive. While open fractures are homogeneously distributed through the entire horizontal section (Fig. 4.53b-c), resistive fractures are clustered in carbonate-rich intervals (Fig. 4.53-d).

The NE-SW fractures of set 3 (oriented at low angle to S_{Hmax}) are more abundant close to the heel of the well, with fewer fractures picked in the horizontal section (Fig. 4.55). Most of these fractures are discontinuous conductive (N=63) while only 4 are continuous and 16 resistive. Similarly to set 1 and 2, resistive fractures are present in carbonate-rich segments, while open fractures are mostly close to the heel of the well, with just a few present in the horizontal section of the well.

	Set	P10 (fractures/m)
Well A	Set 1	0.49 ± 1.94
	Set 2	1.81 ± 2.80
	Set 3	0.54 ± 2.61
Well B	Set 1	1.37 ± 2.45
Well C	Set 1	0.21 ± 1.76
	Set 2	0.08 ± 0.77
	Set 3	0.08 ± 1.01
Well D	Set 1	0.05 ± 1.40
	Set 2	0.02 ± 0.43
	Set 3	0.002 ± 0.07

Table 4.10. Mean P10 values for each set of fractures per horizontal well.

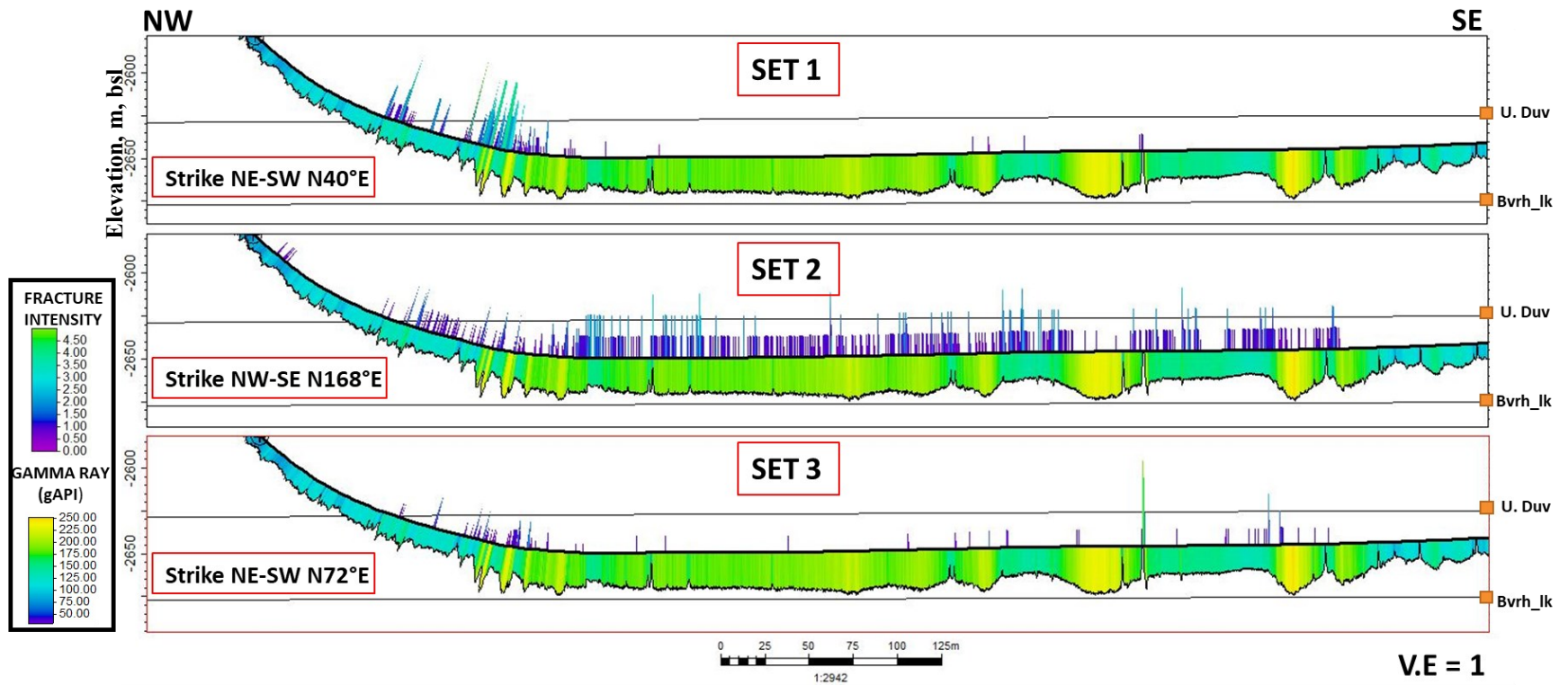


Fig. 4.55. Cross-section along well A. Surfaces of the tops of the upper Duvernay Member (U.Duv) and Beaverhill Lake Group (Bvrhl_lk) are modeled based on the well tops in vertical wells. The GR log and histograms of fracture intensity P10 are shown along the well trajectory. P10 is shown for three sets of natural fractures of different orientation (Table 4.10).

4.6.2.2. Well B N03°E

Well B was landed in the upper Duvernay Member (Fig. 4.56). Open fractures are abundant (N=1039), detected mostly in the first ~200 m of the lateral section of the well. However, most of the open fractures are discontinuous conductive (N=855), with only 184 continuous conductive fractures. Resistive fractures are random in well B (N=24), widespread throughout the horizontal section of the well. According to interpretation of lithofacies in core of vertical well 4 from the same pad, well D is mostly drilled in organic-rich facies F2 and F3 (Fig. 4.56). The middle section of the horizontal well is located in interval of the organic-rich facies with GR > 225 gAPI, and it is characterized by the lowest number of fractures. All natural fractures interpreted in well B belong to set 1 oriented subparallel to the regional S_{Hmax} (Table 4.7).

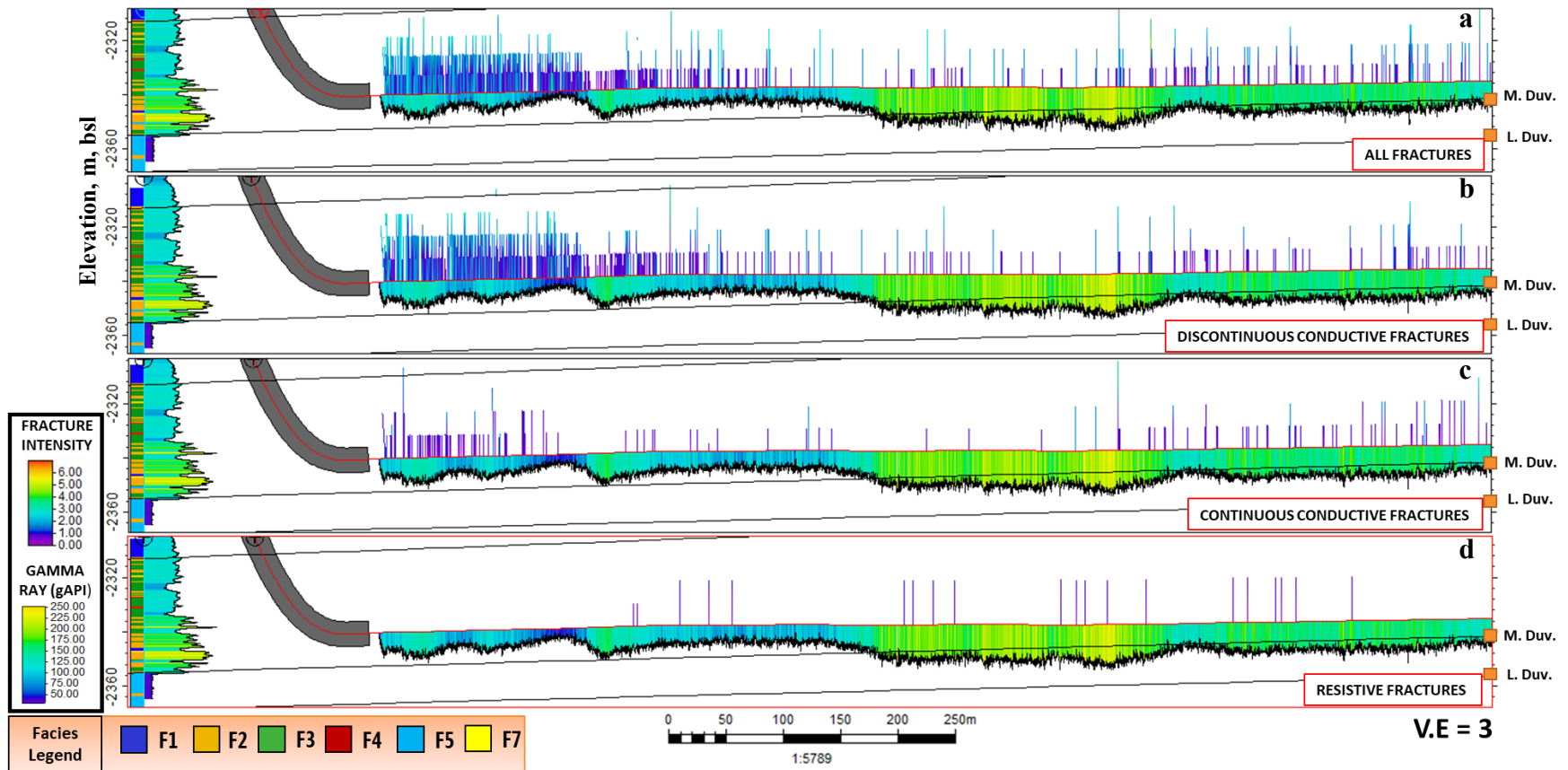


Fig. 4.56. Cross-section along well B. Surfaces of the tops of the Middle Duvernay (M. Duv.) and Lower Duvernay (L. Duv.) Members are modeled based on the well tops in vertical well 4. The GR log and histograms of fracture intensity P10 are shown along well B trajectory. P10 is shown for all fractures (a) and by fracture type (b-d): discontinuous conductive (b), continuous conductive (c), and resistive (d). The GR log and core-based interpreted facies in vertical well 4 of the same well pad are shown.

The mean fracture intensity in well B is 1.37 ± 2.45 fractures/m (P10) and 1.37 ± 2.16 m^2/m^3 (P32). Mean fracture intensity P10 is 4.43 ± 2.6 fractures/m and P32 is 4.55 ± 1.98 m^2/m^3 in the interval of relatively high carbonate-rich facies (F3) with GR of 150-200 gAPI that is located in the first ~200 meters of the lateral section of the well (Fig. 4.57, Table 4.9). In organic-rich and more ductile facies (F2) with GR > 200 gAPI, fracture intensity is lower (mean P10: 0.53 ± 1.44 fractures/m; P32: 0.53 ± 1.77 m^2/m^3) (Table 4.9).

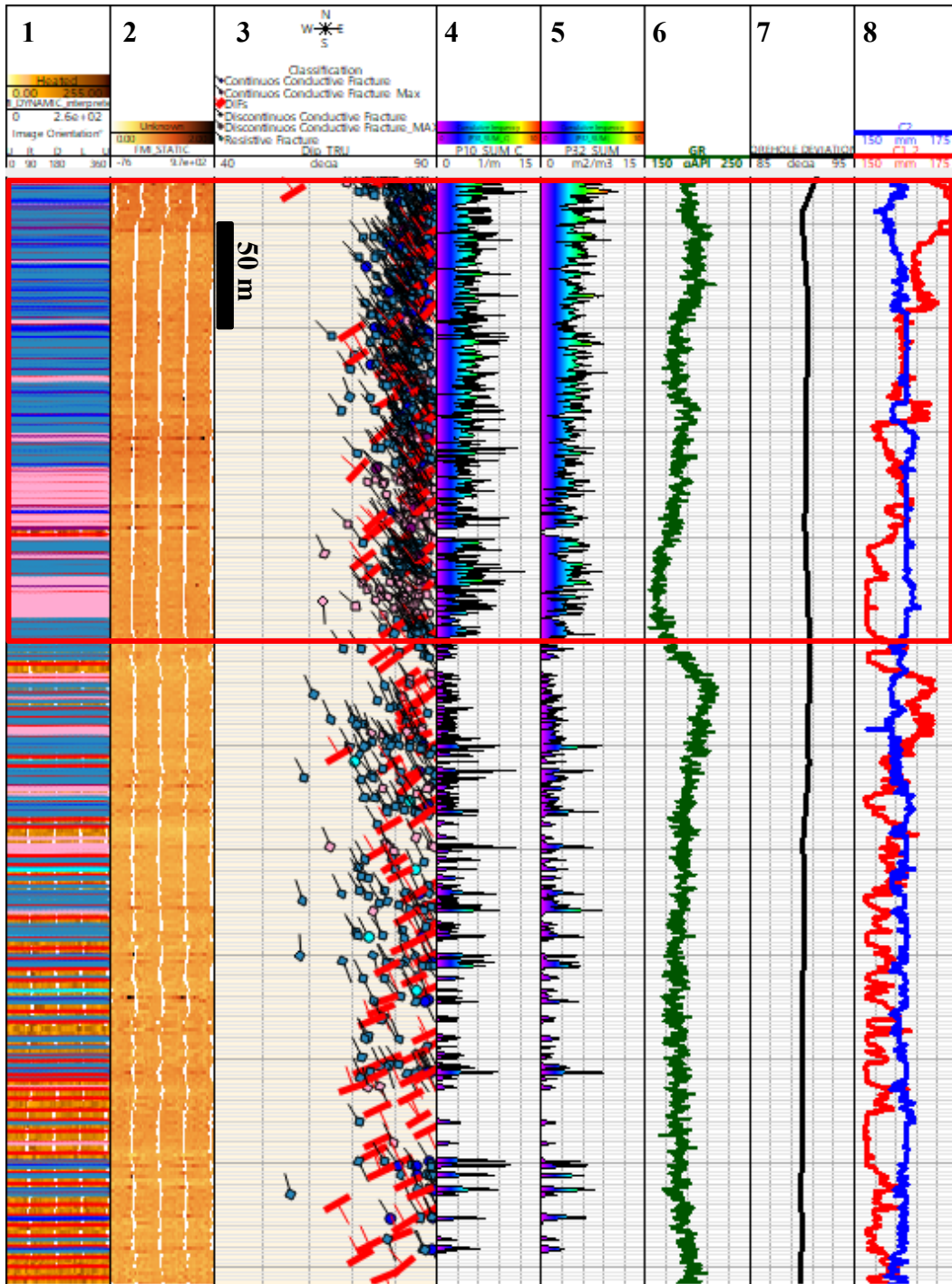


Fig. 4.57. Log plot for well B showing interpreted dynamic (track 1) and static (track 2) FMI logs, orientation of interpreted structures (track 3), fracture intensity P10 (track 4) and P32 (track 5), GR log (track 6), borehole deviation (track 7) and calipers (track 8). The purple and pink sinusoids displayed in track 1 correspond to discontinuous and continuous conductive fractures. The red rectangle corresponds to a segment with dominant conductive fractures (open) in carbonate rich facies (GR < 200 gAPI).

4.6.2.3. Well C N01°E

Well C was landed in the upper Duvernay Member (Fig. 4.58). Open fractures are relatively more abundant (N=152) in intervals with GR < 200 gAPI, that is lower compared to the number of fractures interpreted in wells A and B. Although natural fractures are present through the horizontal section of the well, they are more common in the ~250 m of the lateral section close to the heel of the well. Resistive fractures are interpreted in the intervals with GR < 170 gAPI, close to the toe of the well. Overall, resistive fractures are less numerous (N=5) in well C than in wells A (N=138) and B (N=24).

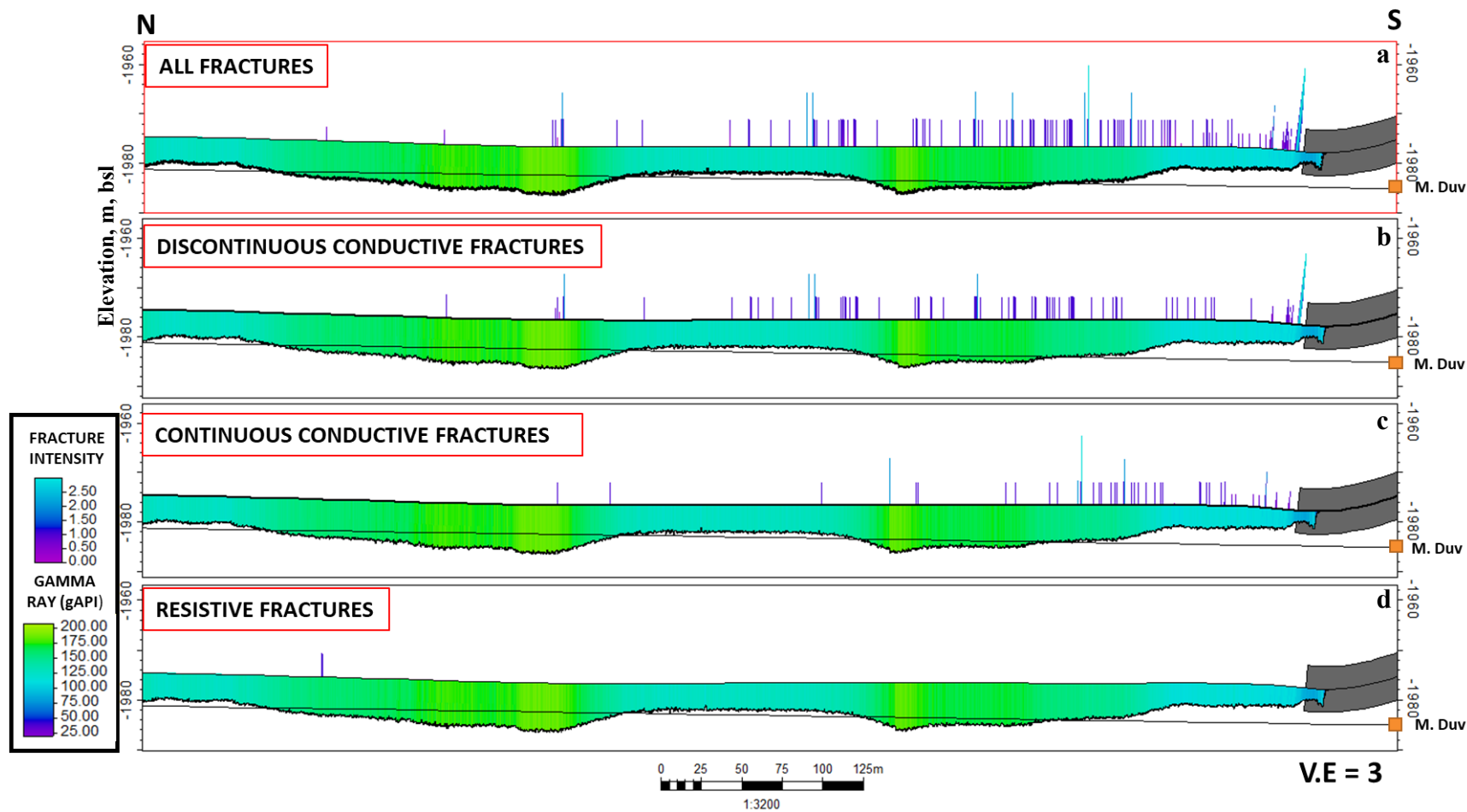


Fig. 4.58. Cross-section along well C. Surface of the top of the middle Duvernay Member (M. Duv.) is modeled based on the well tops in neighboring vertical wells. The GR log and histograms of fracture intensity P10 are shown along well C trajectory. P10 is shown for all fractures (a) and by fracture type (b-d): discontinuous conductive (b), continuous conductive (c), and resistive (d).

The mean fracture intensity interpreted in well C is 0.37 ± 1.11 fractures/m (P10) and 0.37 ± 0.83 m²/m³ (P32) that is lower compared with well A and B (Fig. 4.59, Table 4.9). Fracture intensity P10 (track 3) and P32 (track 4) is higher in relatively high carbonate-rich facies (F3) with GR < 200 gAPI and lower resistivity. P10 values in this interval ranges from <1 to 8 fractures/m (average 0.62 ± 1.33 fractures/m), and P32 from <1 to 9 m²/m³ (average 0.64 ± 1.02 m²/m³) (Table 4.9). In the middle section of the lateral section of the well, where facies (F1) are likely stiffer (GR ~125 gAPI), a few natural fractures were interpreted (Fig. 4.59). The average P10 and P32 for this middle section of the well is 0.26 ± 1.04 fractures/m and 0.26 ± 0.66 m²/m³ (Table 4.9).

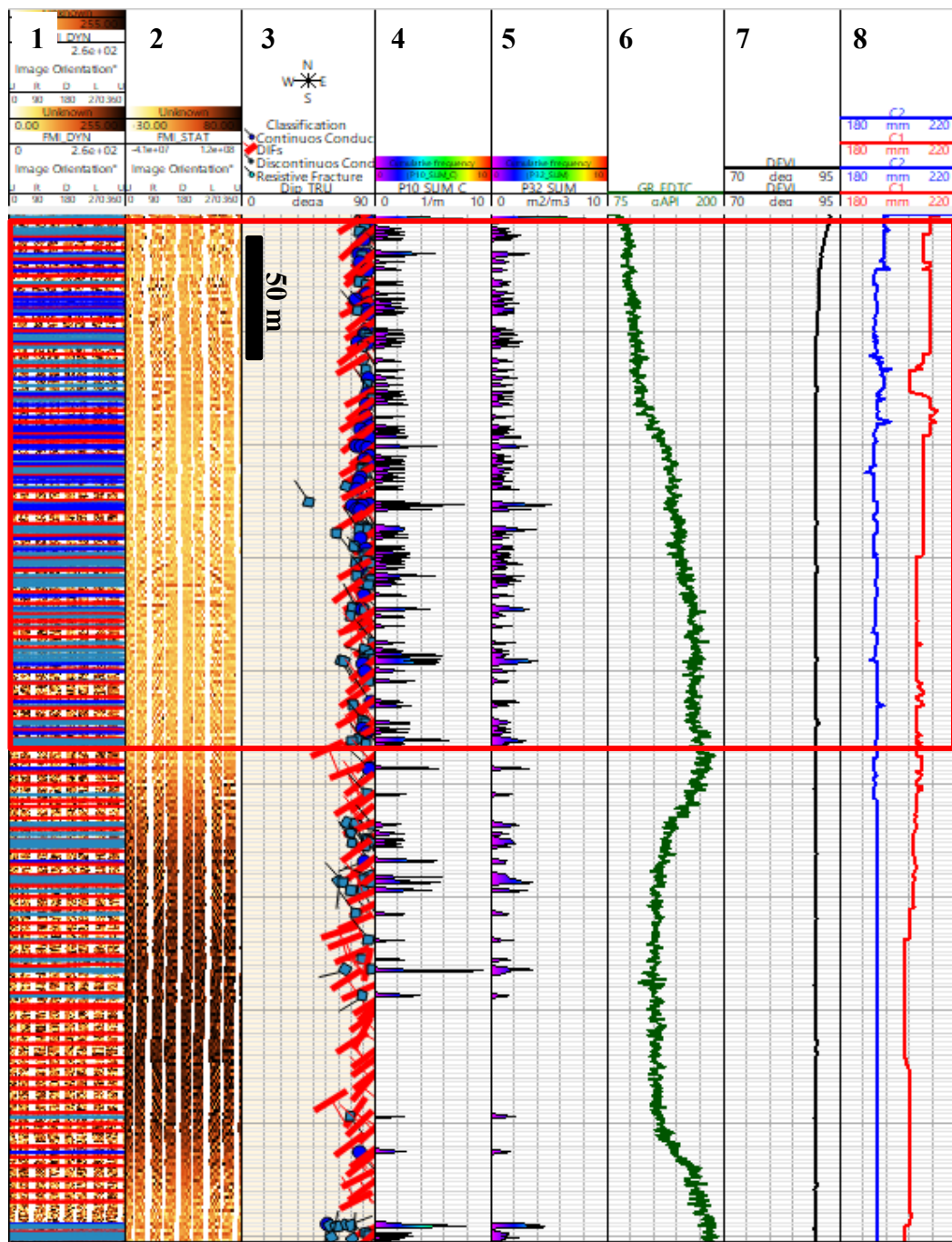


Fig. 4.59. Log plot for well C showing interpreted dynamic (track 1) and static (track 2) FMI logs, orientation of interpreted structures (track 3), fracture intensity P10 (track 4) and P32 (track 5), GR log (track 6), borehole deviation (track 7), and calipers (track 8). The red rectangle shows a segment with dominant conductive fractures (open) of lower resistivity.

The NE-SW-striking natural fractures of set 1 (subparallel to the regional S_{Hmax}) in well C are more abundant (N=126) than fractures of set 2 (N=20) and 3 (N=11). Fractures of set 1 are likely more abundant in intermediate to carbonate rich facies (F1-F3) and tend to be located in the intervals close to the heel of the well (Fig. 4.60). Discontinuous conductive fractures are higher in number (N=73) than continuous (N=50) and resistive fractures (N=3). The NW-SE-striking fractures of set 2 (at high angle to S_{Hmax}) are present in the intermediate interval of horizontal section with low to intermediate GR < 200 gAPI. All fractures of set 2 are conductive (open), including 16 discontinuous and 4 continuous fractures. The NE-SW-striking fractures of set 3 at relative low angle to S_{Hmax} are random and mostly located close to the heel of the well. Discontinuous conductive fractures of set 3 are slightly greater in number (N=7) than continuous conductive fractures (N=2) and resistive fractures (N=2).

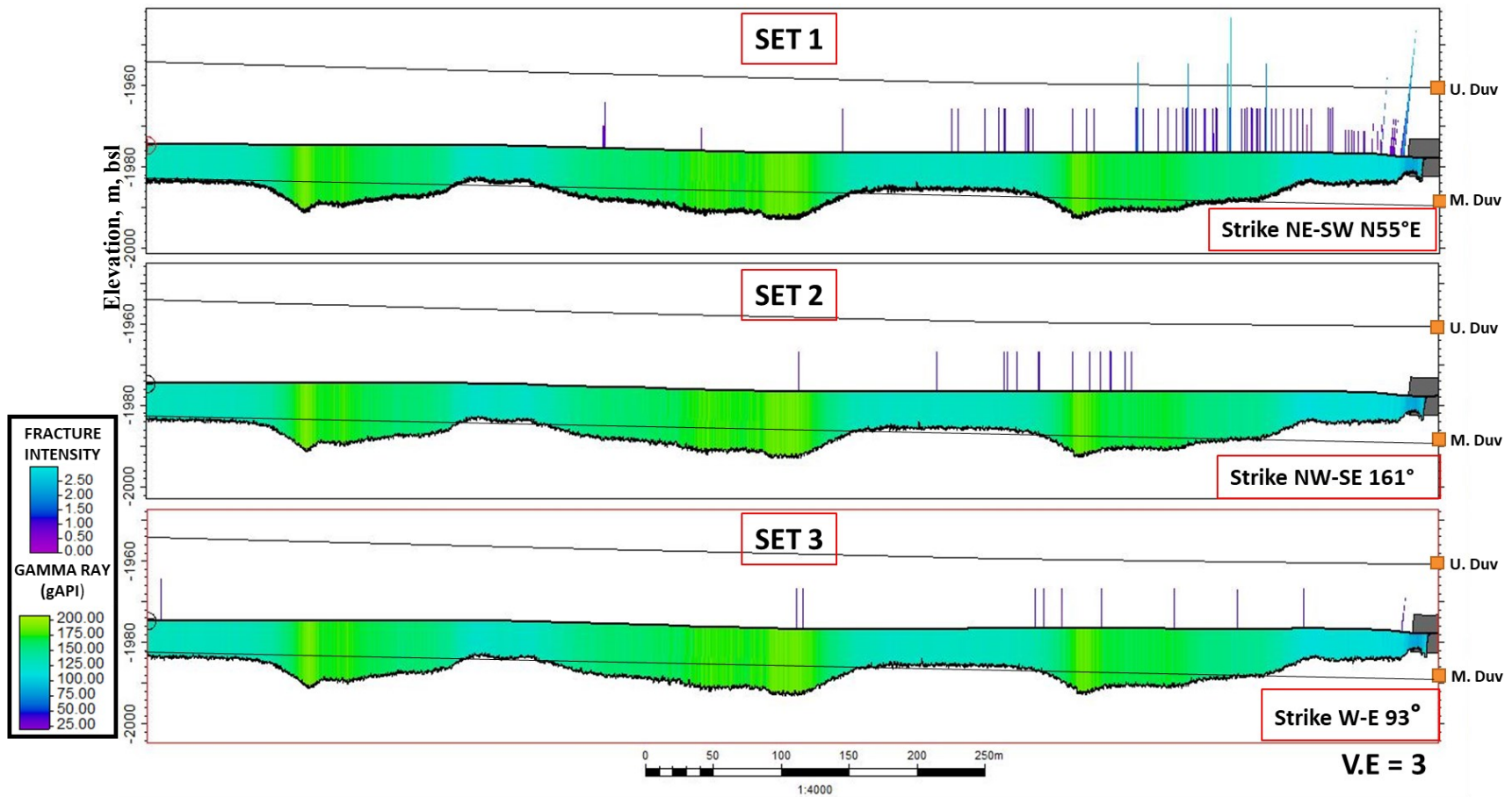


Fig. 4.60. Cross-section along well C. Surfaces of the tops of the Upper Duvernay (U. Duv.) and Middle Duvernay (M. Duv.) are modeled based on the well tops in vertical wells. GR log and histograms of fracture intensity P10 are shown along the well C trajectory. P10 is shown for determined three sets of fractures of different orientation (Table 4.10).

4.6.2.4. Well D N343°E

Well D was landed in the upper Duvernay Member. The number of interpreted fractures in well D is low (N=14) with fracture intensity close to zero in most of the horizontal section of the well (Fig. 4.61). The well is penetrating organic-rich facies F2 and F3 and carbonate-rich facies F1 and F5, interpreted in core of the vertical well 7 located at the same well pad.

The mean fracture intensity in Well D is 0.07 ± 0.1 fractures/m (P10) (Table 4.9). Most of the resistive fractures of set 1 oriented NE-SW (subparallel to the regional S_{Hmax}) in well D are clustered in a carbonate-rich nodule (Facies F5) with $GR < 75$ gAPI (Fig. 4.49, Table 4.9), located close to the heel of the well (Fig. 4.61). The NW-SE-striking fractures of set 2 (N=5) in well D are discontinuous conductive, oriented at high angle to the S_{Hmax} and located in the middle interval and at the toe of the well. The NE-SW fractures of set 3 oriented at low angle to S_{Hmax} are rare (N=2), with one resistive fracture picked in the carbonate nodule (Fig. 4.49) and one discontinuous conductive fracture in the toe of the well (Fig. 4.61).

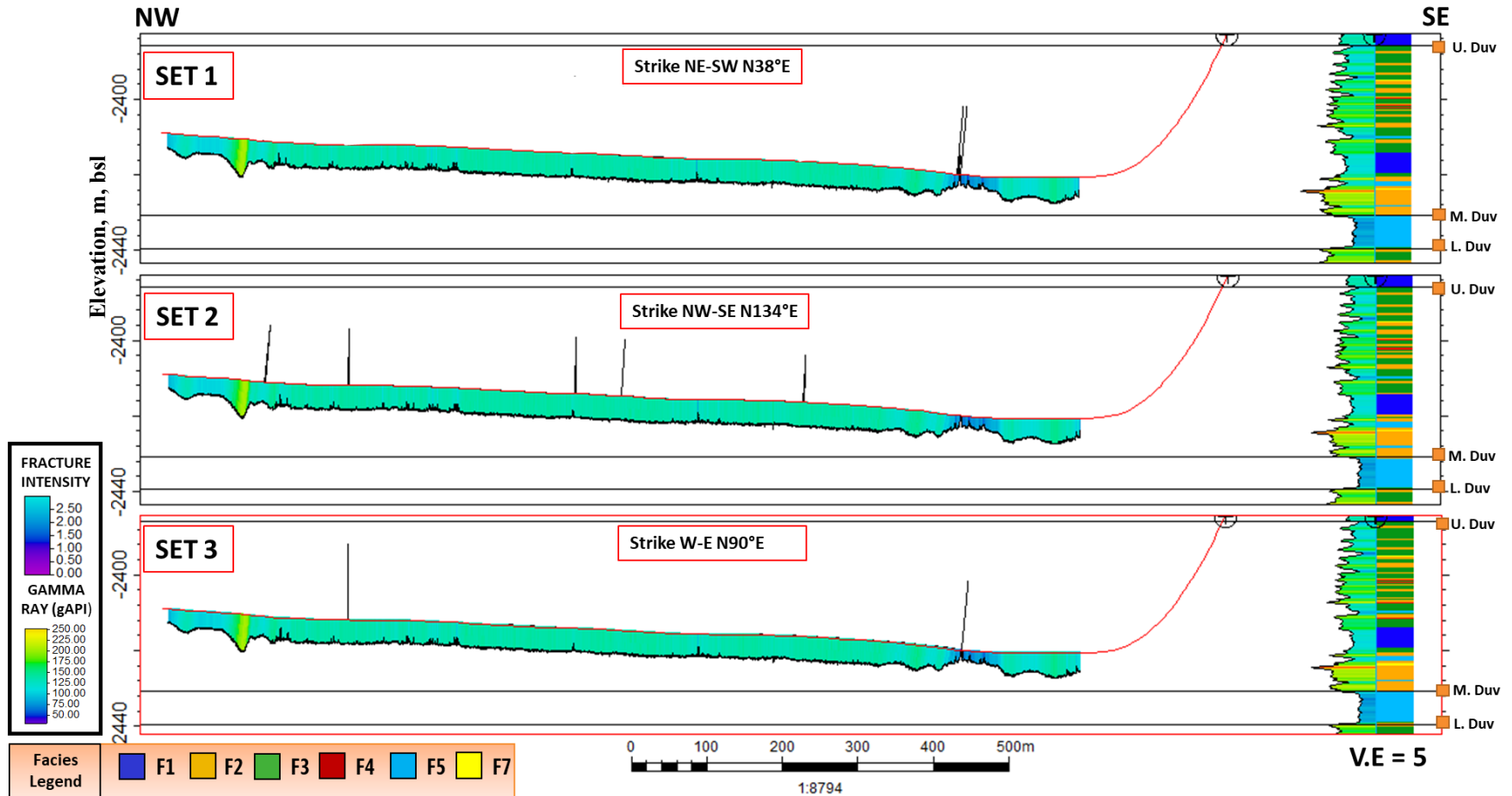


Fig. 4.61. Cross-section along well D. Surfaces of the tops of the Upper Duvernay (U. Duv.), Middle Duvernay (M. Duv.) and Lower Duvernay (L. Duv.) members are modeled based on the well tops in vertical well 7 from the same well pad. The GR log and histograms of fracture intensity P10 are shown along well D trajectory. P10 is shown for determined three sets of fractures of different orientation (Table 4.10). The GR and facies interpreted for vertical well '7' are shown on the right.

4.6.3. Drilling-induced fractures and borehole breakouts orientation

Drilling-induced fractures (DIFs) were interpreted in horizontal wells B and C. The interpreted DIFs are subvertical and oriented NE-SW: $N55^{\circ}E \pm 2^{\circ}/86^{\circ}$ in well B and $N53^{\circ}E \pm 2^{\circ}/77^{\circ}$ in well C (Fig. 4.62, Table 4.7). The DIFs form in a borehole during drilling operations in the direction parallel to the remote maximum principal stress σ_1 and perpendicular the remote minimum principal stress σ_3 that act around the borehole. As wells B and C are horizontal and DIFs are subvertical and strike NE-SW, it can be concluded that σ_1 corresponds to regional S_{Hmax} orientation, which therefore in the analyzed wells consists of $N53^{\circ}E$ - $N55^{\circ}E$.

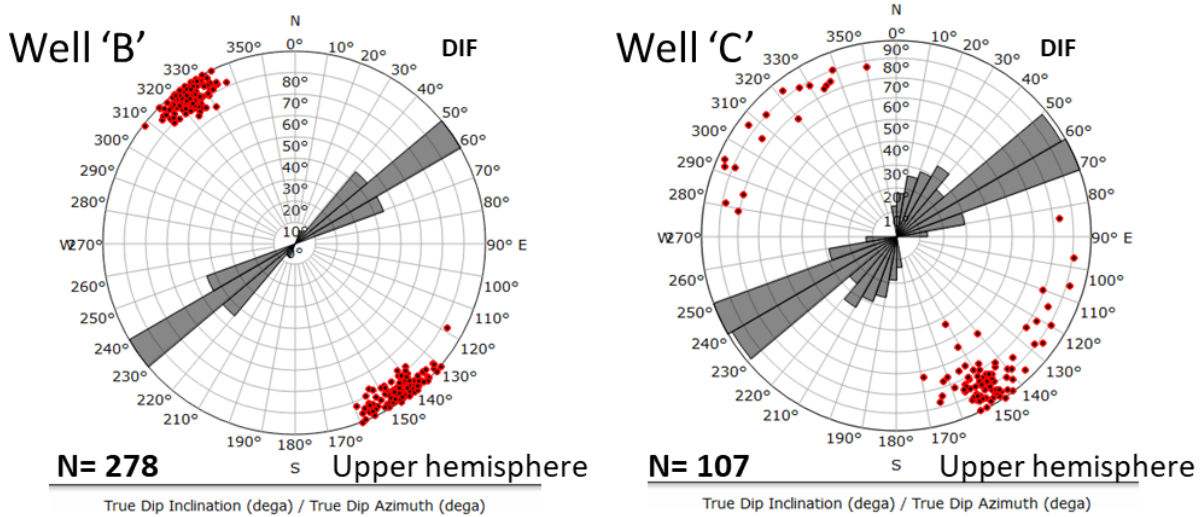


Fig. 4.62. Rose diagrams and stereographic equal area projection (upper hemisphere) showing poles to planes (true dip angle, true dip azimuth) and strike of drilling-induced fractures in horizontal wells B and C. The red dots shows true dip azimuth and true dip angle, and the grey histograms show the strike of the fractures. See Fig. 4.42 for well location.

Borehole breakouts were interpreted in wells A and D (Fig. 4.63). Borehole breakouts are located at the top and bottom of the horizontal wells (Fig 4.43) and oriented NW-SE $N141^{\circ}E/81^{\circ}$ (S_{Hmax} $N51^{\circ}E$) in Well A and $N340^{\circ}W/87^{\circ}$ (S_{Hmax} $N70^{\circ}E$) in Well D (Table 4.7). Orientation of S_{Hmax} from borehole breakouts in well A (Fig. 4.63) is consistent with orientation of drilling induced fractures in wells B and C (Figs. 4.62). There is likely a local stress rotation in the Duvernay mudrocks in well D (Fig. 4.63) that is located close to the Windfall reef.

Borehole breakouts form in a borehole during drilling operations to be parallel to remote minimum principal stress σ_3 and orthogonal to the remote maximum principal stress σ_1 acting around the borehole (Fig. 4.62). As breakouts are located at the top and bottom of the horizontal wells, σ_3 is vertical, and σ_1 is horizontal. It can be therefore concluded that σ_3 corresponds to vertical stress S_v and σ_1 - to regional S_{Hmax} , and that the vertical stress ($S_v = \sigma_3$) is lower than the $S_{Hmax} = \sigma_1$ (Fig. 4.62).

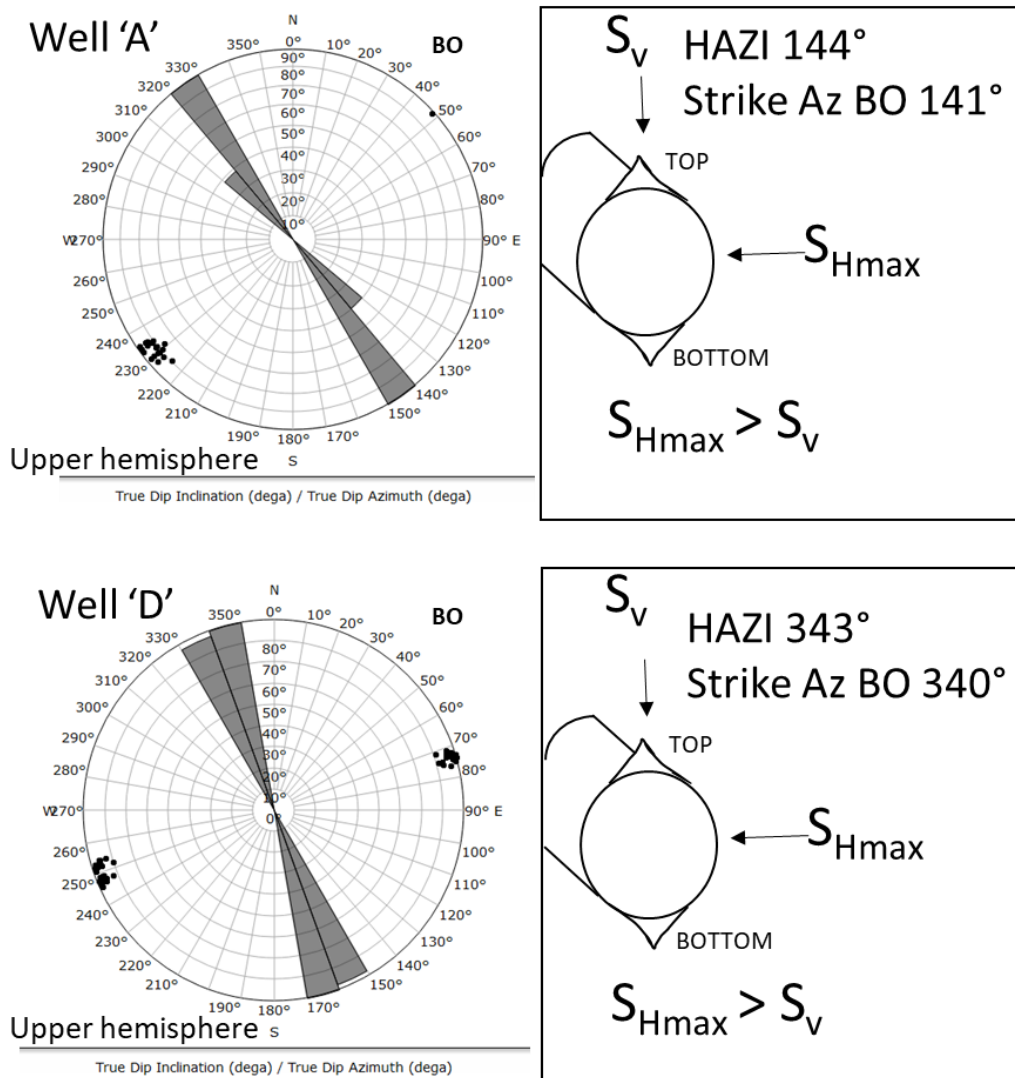


Fig. 4.63. Rose diagrams, stereographic equal area projection (upper hemisphere) and interpretation schemes of orientation of borehole breakouts (BO) in horizontal wells A and D. True dip angle and true dip azimuth of fractures are shown in black dots; strike is displayed in grey histograms. HAZI, borehole azimuth. See Fig. 4.42 for well location.

4.7. Composition, structural elements and fractures in the Perdrix Formation

In this project, we studied outcrops of the Perdrix Formation exposed in the Front Ranges (Hoodoo Creek) and Foothills (Wapiti Gap) of the Rocky Mountains, in the vicinity of the North Saskatchewan River valley, Nordegg area, Alberta (Fig. 2.25). This area is recognized as a transverse lithofacies boundary in the paleogeography of the Upper Devonian (Frasnian) deposits (Workum and Hedinger, 1992; Spratt et al., 2004). The off-reef shales of the Mount Hawk, Perdrix, and Flume Formations form organic-rich facies of the Cline Channel that are exposed in the Front Ranges in the area of the present-day North Saskatchewan River. These organic-rich facies change laterally into the carbonate-rich facies of hydrocarbon-bearing dolostones of the Southesk and Cairn Formations (Leduc and Nisku reefs) to the north and south of the Cline Channel and eastward in the Foothills (Workum and Hedinger, 1992; Spratt et al., 2004).

The Hoodoo Creek outcrop is located in the Front Ranges, 33 km to the south-west of Nordegg (Fig. 4.64). The Perdrix Formation is exposed in a tectonic slice between the McConnell and Sulphur Mountain Thrusts. The tectonic slice of the Hoodoo Creek is composed of Upper Devonian shale and carbonate rocks overlying the faulted dolomites of the Cambrian Ghost River Formation. This tectonic slice is thrust to the NE over the tectonic slices, which are composed mostly of Cambrian carbonate and, to less extent, Devonian rocks and limited in the NE by the McConnell Thrust that delineates the Front Ranges. Cambrian and Devonian rocks displaced by the McConnell Thrust are thrust over Lower Cretaceous deposits of the Luscar Group and Mountain Park Formation of the Foothills. To the SW, Mississippian and Triassic carbonate and shaly rocks of the Banff, Livingstone, Mount Head Formations, and Spray River Group thrust over the Hoodoo Creek tectonic slice. The Perdrix Formation in the Hoodoo Creek is composed of black organic-rich shales (Fig. 4.65.A) that are exposed in the northeastern limb of an inclined regional syncline whose fold axial plane dips to the southwest (Fig. 4.64). Strike azimuth and dip angle of mean bedding plane of the Perdrix Formation in the Hoodoo Creek is N 126°/53° (Fig. 4.65. B). The syncline limb in the Hoodoo Creek is cut by the NE-verging thrust and NW-SE subvertical dextral strike-slip fault, as discussed below.

The Wapiti Gap outcrop of the Perdrix Formation is located in the hanging wall of the Bighorn Thrust in the Foothills, 22 km to the north-west of Nordegg (Fig. 4.64). Cambrian,

Devonian and Mississippian sedimentary rocks are thrust over Upper Cretaceous clastic deposits along the Big Horn Thrust. The Perdrix Formation in the Wapiti Gap is mostly composed of carbonate-rich fossiliferous limestone locally interbedded with pyrite-bearing organic-rich shales (Fig. 4.65.C-D).

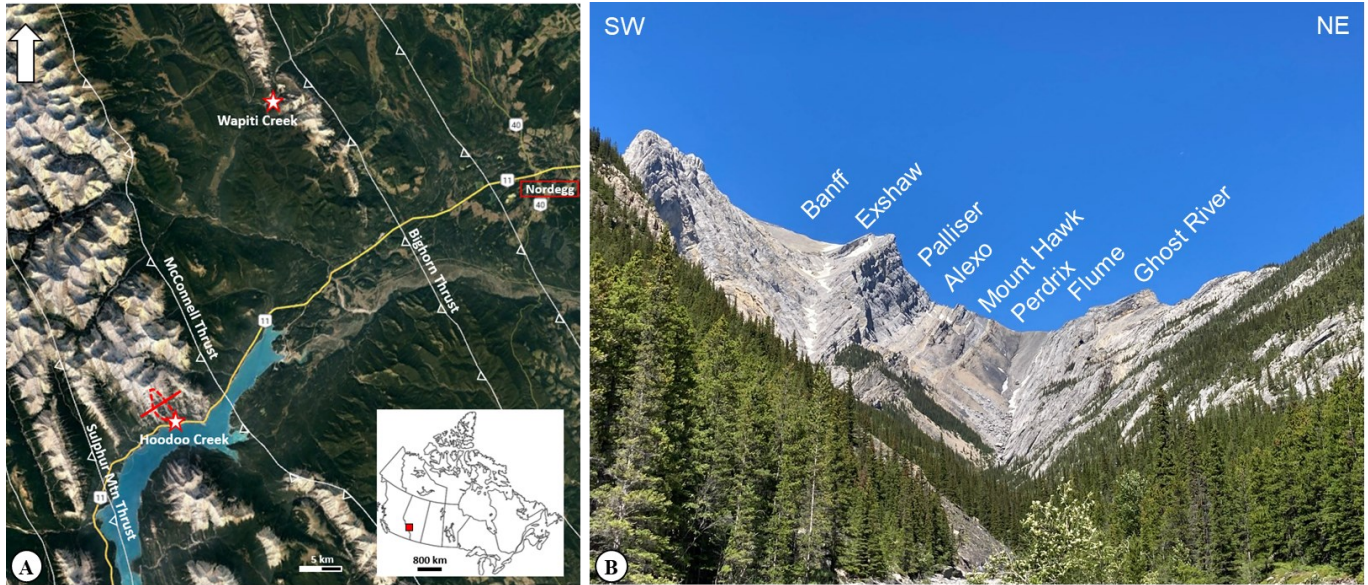


Fig. 4.64. A) Google Earth map of Front Ranges and Foothills in the Nordegg area with projected main thrust faults (white lines), after the AER dataset (Hamilton et al., 1999), with location of the Hoodoo Creek ($52^{\circ}16'20.59''$ N, $116^{\circ}27' 21.23''$ W) and Wapiti Gap ($52^{\circ}29'10.99''$ N, $116^{\circ}24'29.59''$ W) outcrops (red stars). The red line indicates the location of the cross-section B. B) photo of the outcrop across the Hoodoo Creek.

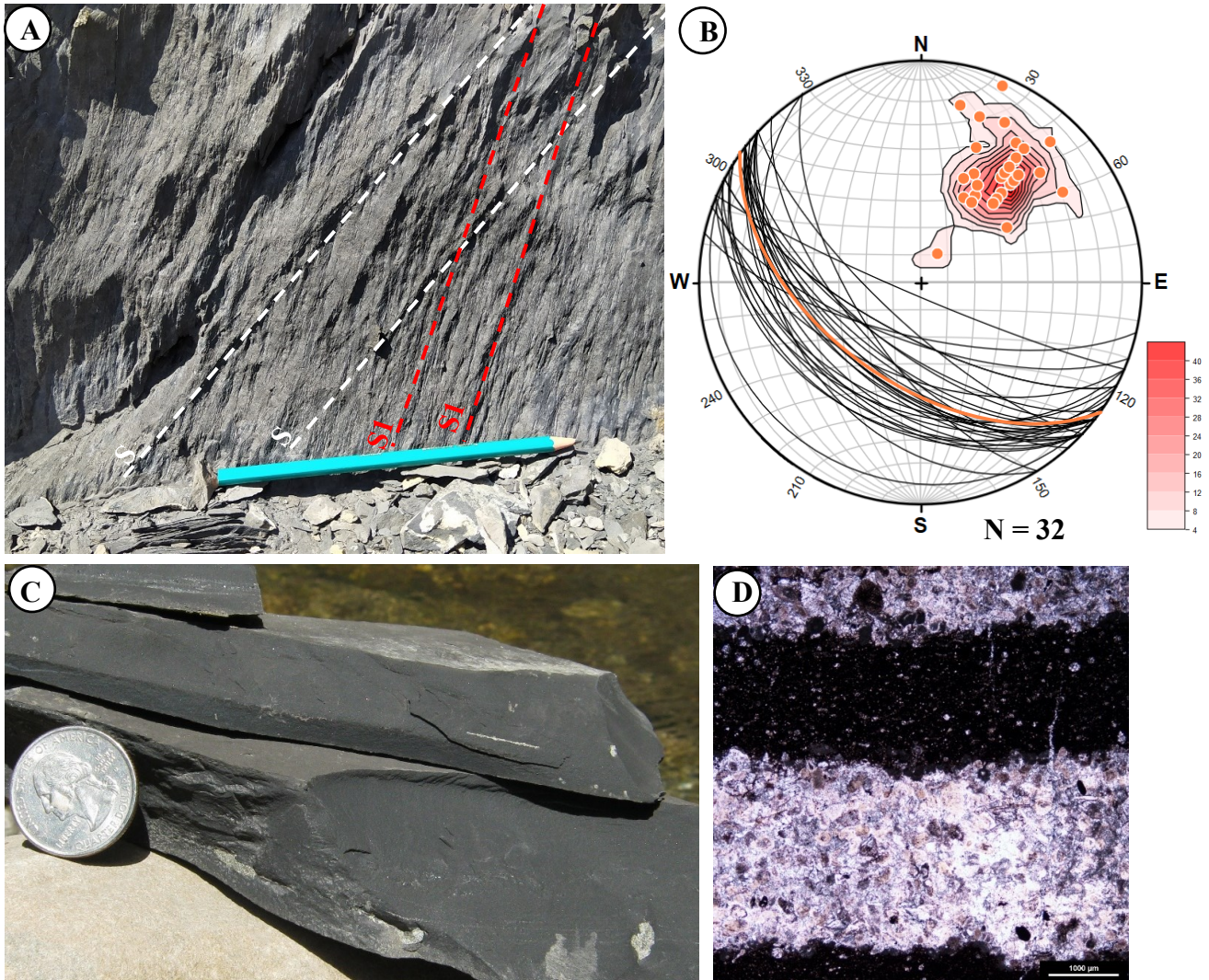


Fig. 4.65. Organic-rich shales of the Perdrix Formation, Hoodoo Creek (A-B) and Wapiti Gap (C-D). A) Outcrop photo, bedding planes (S0) are highlighted by white dashed lines. The red-dashed lines indicate cleavage (S1). B) Stereographic equal area projection of bedding of the Perdrix Formation in the Hoodoo Creek, plotted as planes (black lines, strike and dip angle) and poles to planes (orange dots, dip azimuth and dip angle, lower hemisphere). The orange line depicts the azimuth of strike and dip angle of mean bedding plane determined from high-density pole to plane location. Red color contours indicate density of pole to planes. C) Outcrop photo of organic-rich shale of the Perdrix Formation in the Wapiti Gap (W-04-S1), D) Thin section of interbedded organic-rich shale and limestone (W-06-S1). Calcite-filled tensile fractures in carbonate-rich beds that stop in the shale beds.

The cleavage planes (S1) in the Perdrix Formation of the Hoodoo Creek are subvertical dipping to the SW, azimuth of strike and dip angle of mean cleavage plane is N 121°/77° (Fig. 4.66.B), parallel to the axial plane of the mesoscopic fold. The intersection lineation measured between bedding and cleavage planes (Fig. 4.66.A) is subhorizontal and plunges to the NW and SE at low angles (Fig. 4.66.C). The mean trend azimuth and plunge of intersection lineation determined from stereogram as an intersection between mean bedding and mean cleavage planes is N 301°/08° (Fig. 4.66) that is close to the orientation of the measured linear elements and parallel to the mesoscopic fold axis.

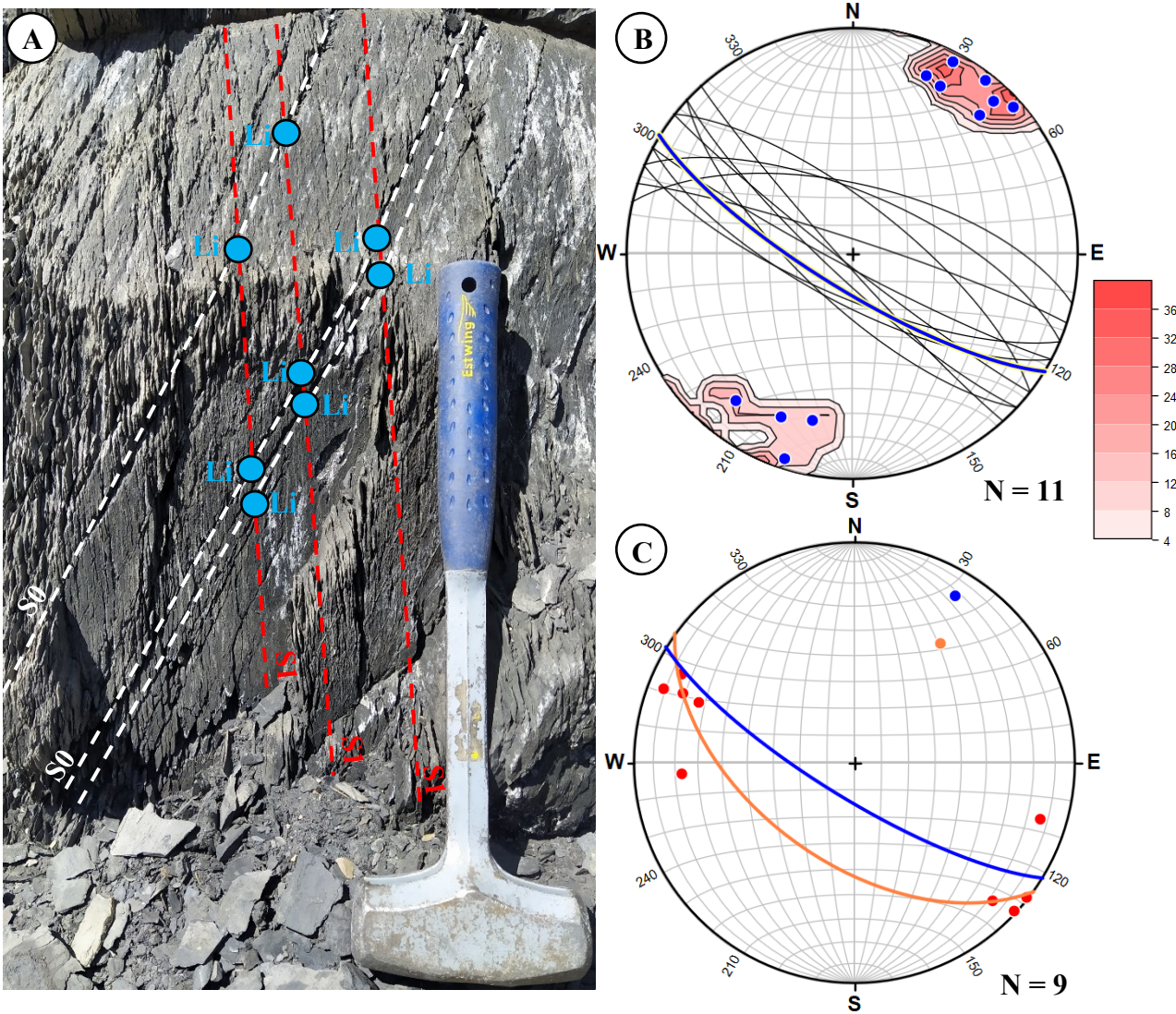


Fig. 4.66. Structural elements in the organic-rich shales of the Perdrix Formation, Hoodoo Creek: A) Bedding (S0 white-dashed lines), subvertical cleavage (S1 red-dashed lines) and intersection lineation (Li blue dots). B) Stereographic equal area projection of cleavage plotted as planes (black lines, strike azimuth and dip angle) and poles to planes (blue dots, dip azimuth and dip angle, lower hemisphere). The blue line is the mean strike azimuth and dip angle of the cleavage. Density contours for the poles to planes S1 are highlighted by red color. C) Stereographic equal area projection of mean plane and pole of bedding (orange line and dot) and cleavage (blue line and dot), and trend azimuth and plunge of intersection lineation (red dots), lower hemisphere.

Natural fractures in the organic-rich facies of the Duvernay Formation are open (Fig. 4.67) or mineralized, filled with calcite (Fig. 4.68.B).

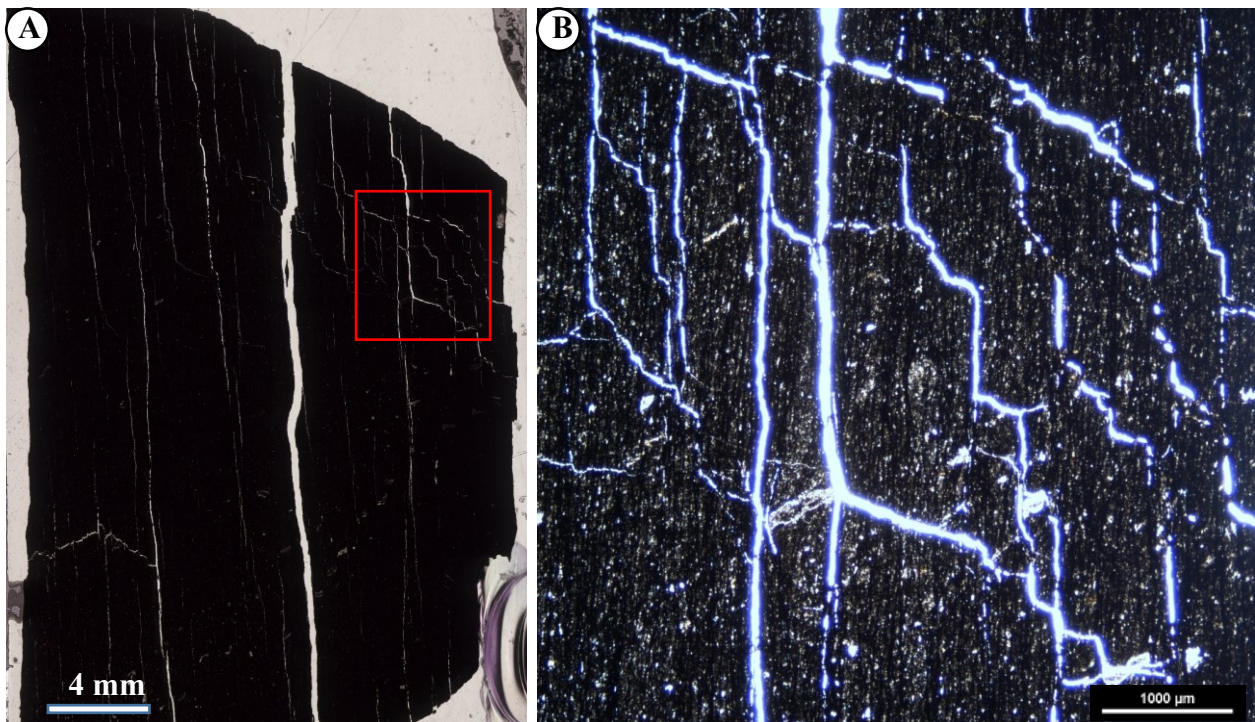


Fig. 4.67. A) Scanned thin section of organic-rich shale of the Perdrix Formation (HC-01-S1) with strong subvertical cleavage and a network of open fractures. B) Thin-section of vertical cleavage (HC-01-S1). Open subhorizontal fractures are connected with subvertical fractures, creating a lattice pattern. Some of these fractures are partially mineralized and filled with blocky crystals of calcite.

A thrust fault zone is oriented N124°/53° in the Hoodoo Creek. The high-density subhorizontal calcite-filled fractures developed in the Perdrix shales above the main thrust zone (Fig. 4.68). Subhorizontal veins are orthogonal to the subvertical cleavage S1 (Fig. 4.68.B), the both are consistent with subhorizontal maximum compressive stress. Later subvertical fractures that cut through subhorizontal veins were developed under the settings of subvertical maximum compressive stress (Fig. 4.68.B).

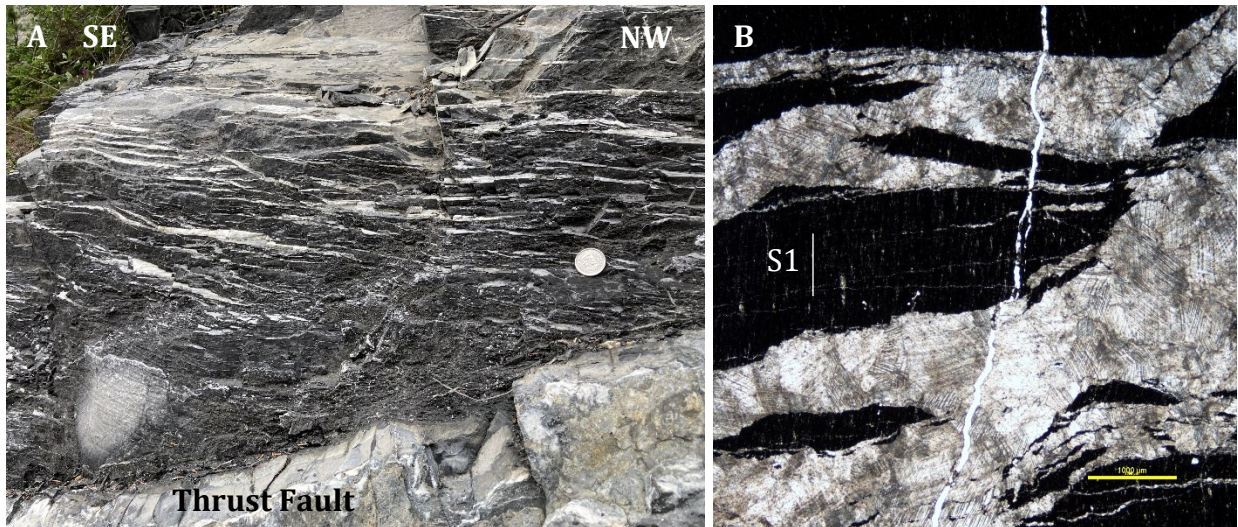


Fig. 4.68. High-density subhorizontal calcite-filled fractures in the Perdrix organic-rich shales above the thrust fault zone: outcrop photo, frontal view (A) and thin section, sample HC-12-S2 (B). Thick calcite and quartz veins developed along the thrust fault zone. Subhorizontal veins are orthogonal to the subvertical cleavage S1. Late subvertical fractures cut through subhorizontal veins.

The dextral subvertical strike-slip fault zone was recognized in the Hoodoo Creek (Fig. 4.69). The mean strike and dip angle of the strike-slip faults is N128°/87°. The shear zone along the fault is about 0.8 m-1.5 m wide. Sigmoidal schistosity S2 in shales, drag folds, carbonate-filled lenses, mirrors planes and fractures are present within the shear zone (Fig. 4.69). Drag folds form in incompetent beds between competent beds as minor asymmetric folds and can be used to determine the direction of relative movement of beds in the limbs of a major fold. Fractures within the shear zone are filled with calcite, showing complex distribution. The orientation of drag folds is variable, the fold axes are plotted close to the planes of the schistosity S2 (Fig. 4.69). Slickenlines and mirror planes occur in the deformed Perdrix shales on the limbs of the drag folds in the dextral strike-slip shear zone in the Hoodoo Creek (Fig. 4.70).

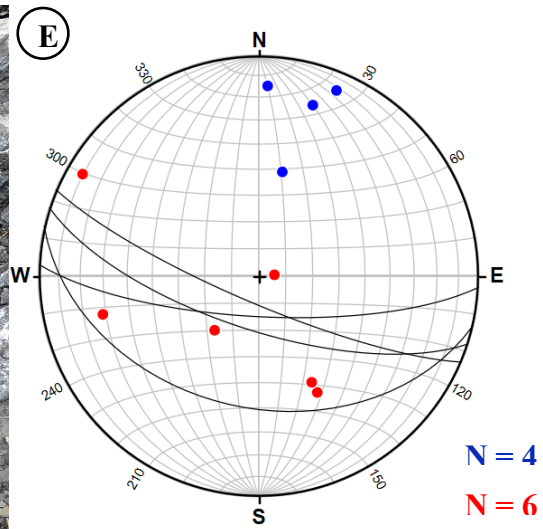
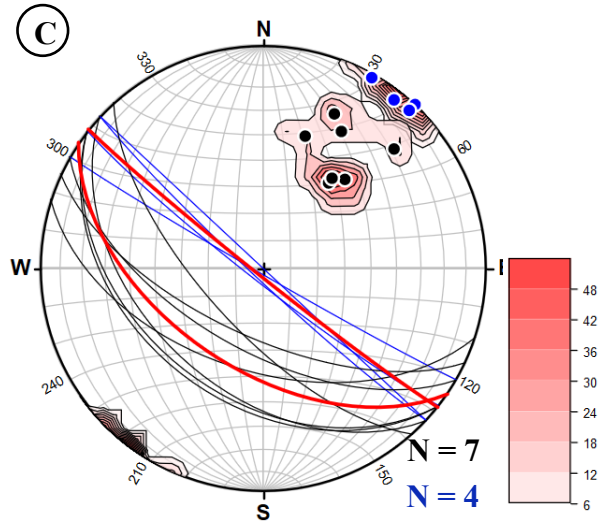
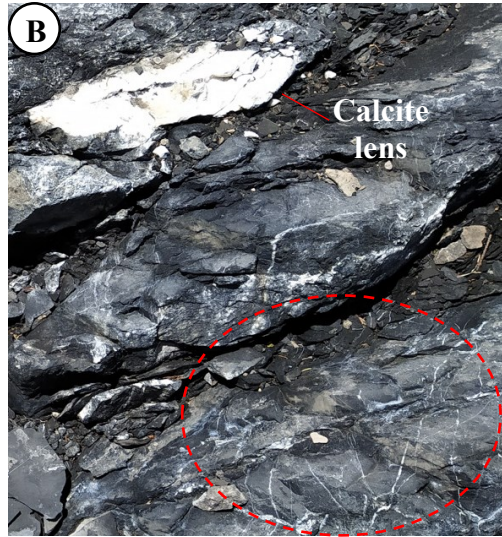
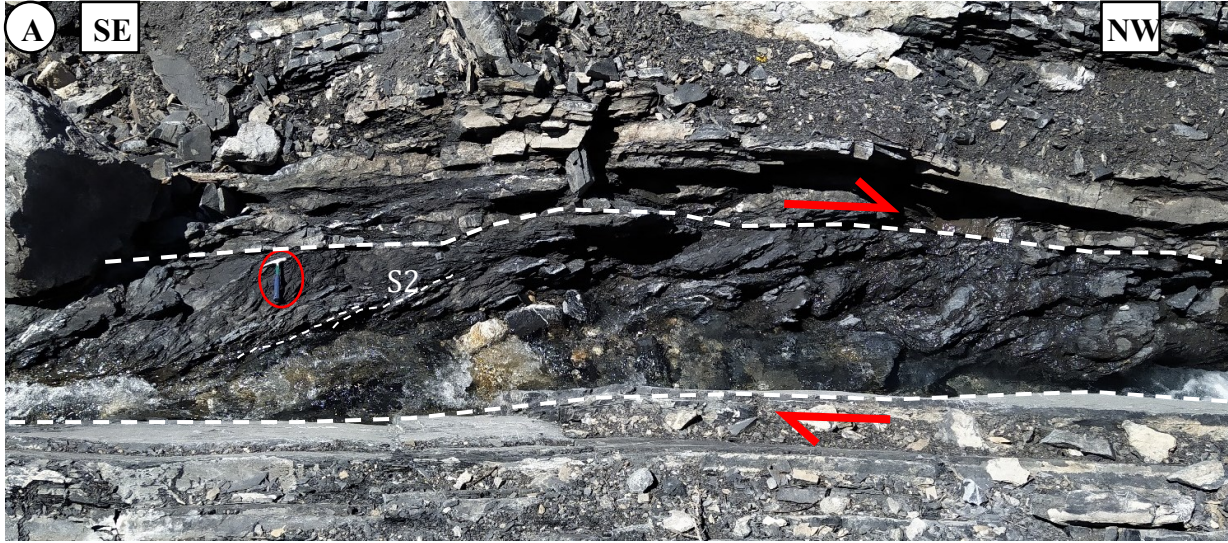


Fig. 4.69. Deformation elements in the Perdrix shales along the dextral strike-slip fault, the Hoodoo Creek: A) Shear zone along the subvertical dextral strike-slip fault, map view. The organic-rich shales of the Perdrix Formation display sigmoidal schistosity S2 consistent with the dextral displacement along the shear zone. B) Calcite lens and calcite-filled fractures (red circle) in the shear zone. C) Stereographic equal area projection planes (lines) and poles to planes (dots) of mapped thrusts (black) and strike-slip faults (blue), lower hemisphere. The red lines indicate the mean strike azimuth and dip angle of the thrusts and strike-slip faults. Contours are built in poles to planes, with red colors indicating higher intensity of pole to planes. D) Drag folds within the shear zone. E) Stereographic equal area projection of trend and plunge of axes of drag folds (red dots) and strike (black lines) with poles to planes of schistosity S2 (blue dots) in the dextral strike-slip shear zone, lower hemisphere.

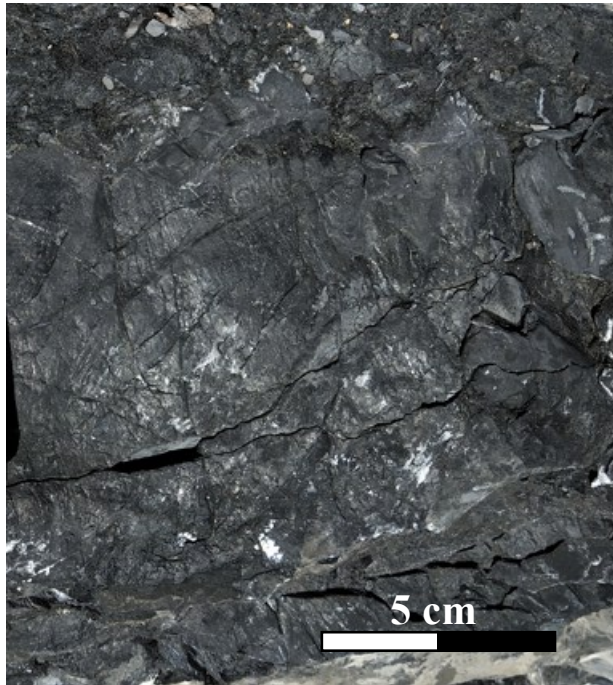


Fig. 4.70. Slickenlines and mirror planes developed in drag folds in the deformed organic-rich shales of the Perdrix Formation within the dextral strike-slip shear zone, Hoodoo Creek.

Open and calcite-filled fractures are present in the Perdrix Formation in the Hoodoo Creek and Wapiti Gap. Open fractures sometimes have distinct plumose patterns on the joint surfaces (Fig. 4.71.A). Each mudrock layer has its own plumose structure, indicating independent fracturing for each layer, similar to other siltstones and shales (Helgeson and Aydin, 1991). Several sets of calcite-filled tensile fractures were determined, oriented parallel, oblique and orthogonal to the subvertical cleavage (S1) (Fig. 4.71.B). Locally, slickenlines were

observed in calcite filling in low-angle veins (Fig. 4.71.C) orthogonal to the subvertical cleavage S1 indicating updip shear displacement to the SE (trend azimuth and plunge N293°/23°). Kerogen and pyrite are present in calcite-filled tensile fractures (Fig. 4.72).

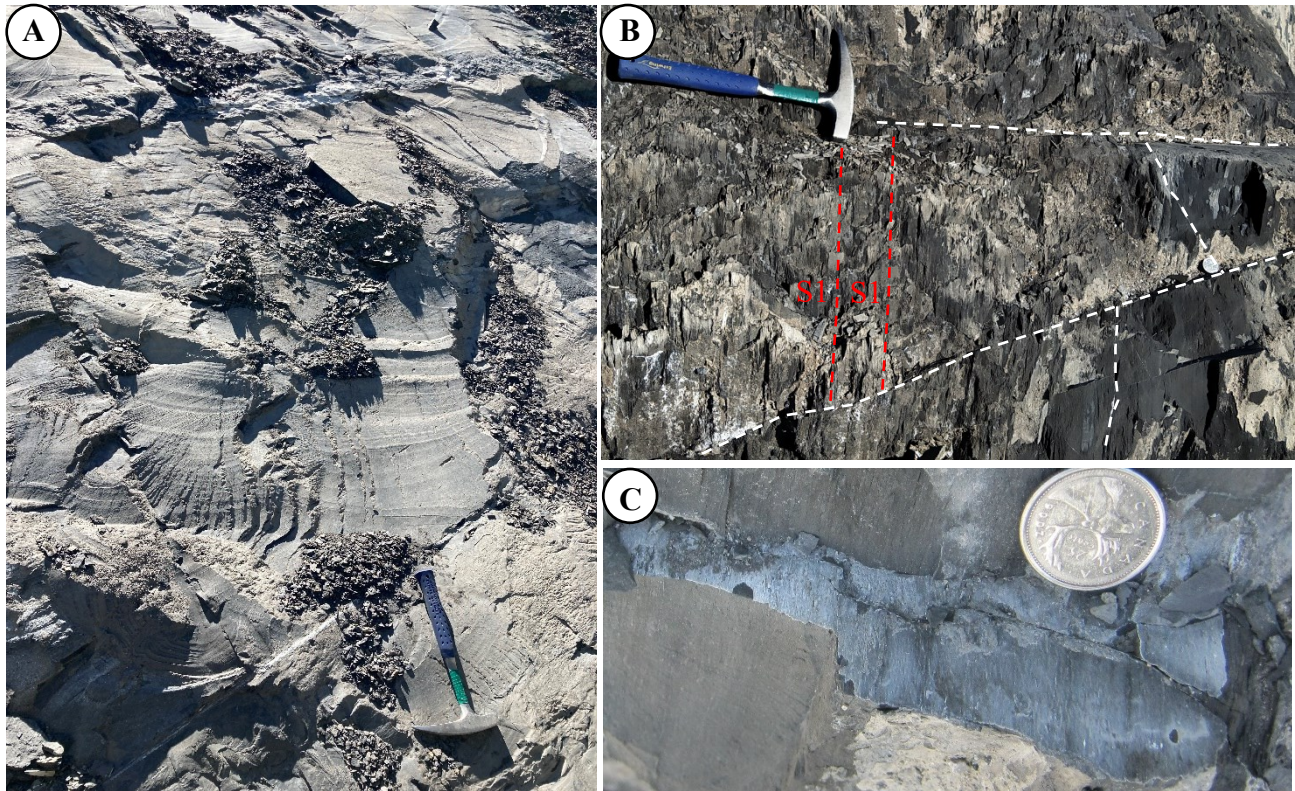


Fig. 4.71. Open subvertical NNW-SSE fractures (joints) with plumose structure (A) and calcite-filled fractures (B-C) in organic-rich shales of the Perdrix Formation, Hoodoo Creek. Low-angle calcite-filled fractures are orthogonal to the subvertical cleavage S1 and characterized by slickenlines (C) indicating updip shear slip to the SE. The white-dashed lines (B) highlight the fractures.

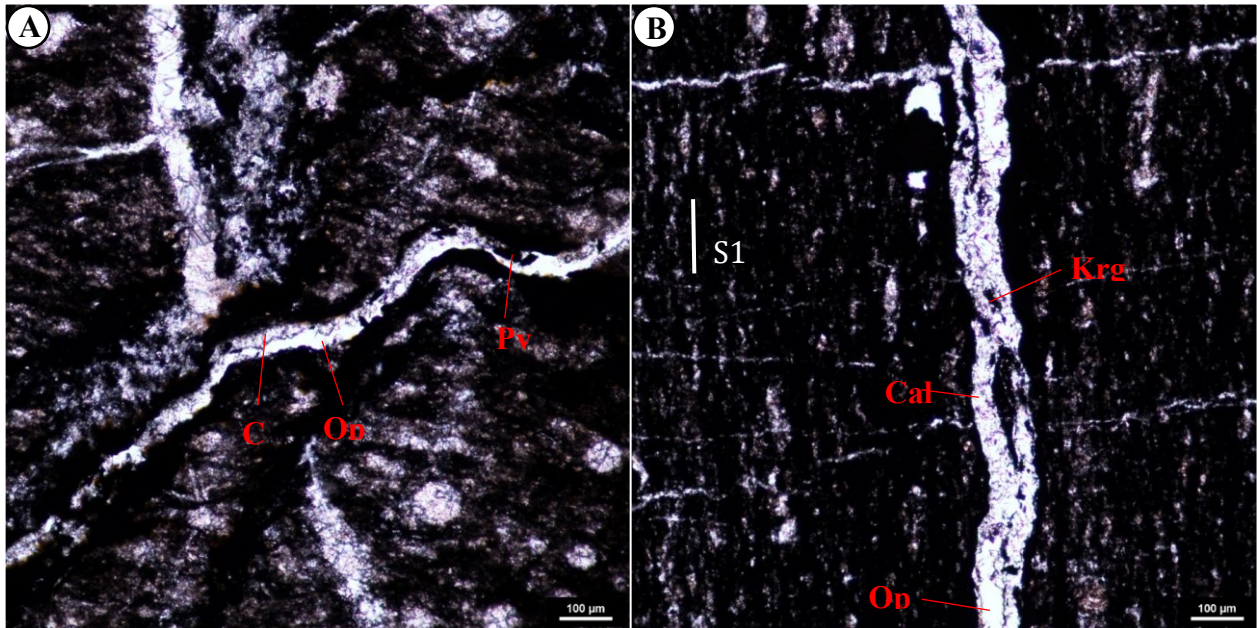


Fig. 4.72. Tensile calcite-filled fractures in organic-rich shales of the Perdrix Formation, Hoodoo Creek, thin sections, nicols parallel: A) oblique fracture partially filled with blocky calcite and pyrite. B) horizontal and subvertical fractures orthogonal and parallel to subvertical cleavage S1, respectively. Subvertical fracture is partially filled with calcite and kerogen. Abbreviations: Cal = Calcite, Py = Pyrite, Krg = Kerogen.

In the units of the Perdrix Formation composed of interbedded carbonate-rich mudstones and organic-rich shales, the stiffer carbonate-rich mudrocks experienced boudinage during the folding. Tensile calcite-filled fractures form between the boudins in the extended carbonate-rich beds as the are folded (Fig. 4.73. A-B). Tensile and transtensional calcite-filled fractures in organic-rich shales form conjugate sets of semi-brittle left- and right-lateral shear zones oriented at about 30° between them (Fig. 4.74).

Fracture height in mudrocks of the Perdrix Formation is variable, ranging from < 10 cm to < 3 m. Fracture height is generally larger in thicker carbonate-rich beds and shorter in organic-rich shales. Although fractures are normally bed-bounded (Fig. 4.73. A-B, D), some fractures propagate across the bed boundaries (Fig. 4.73. C-D). Fracture aperture vary from 0.1 mm to 10 cm. Tensile fractures with large aperture occur between boundins in extended carbonate-rich mudstone beds (Fig. 4.73).

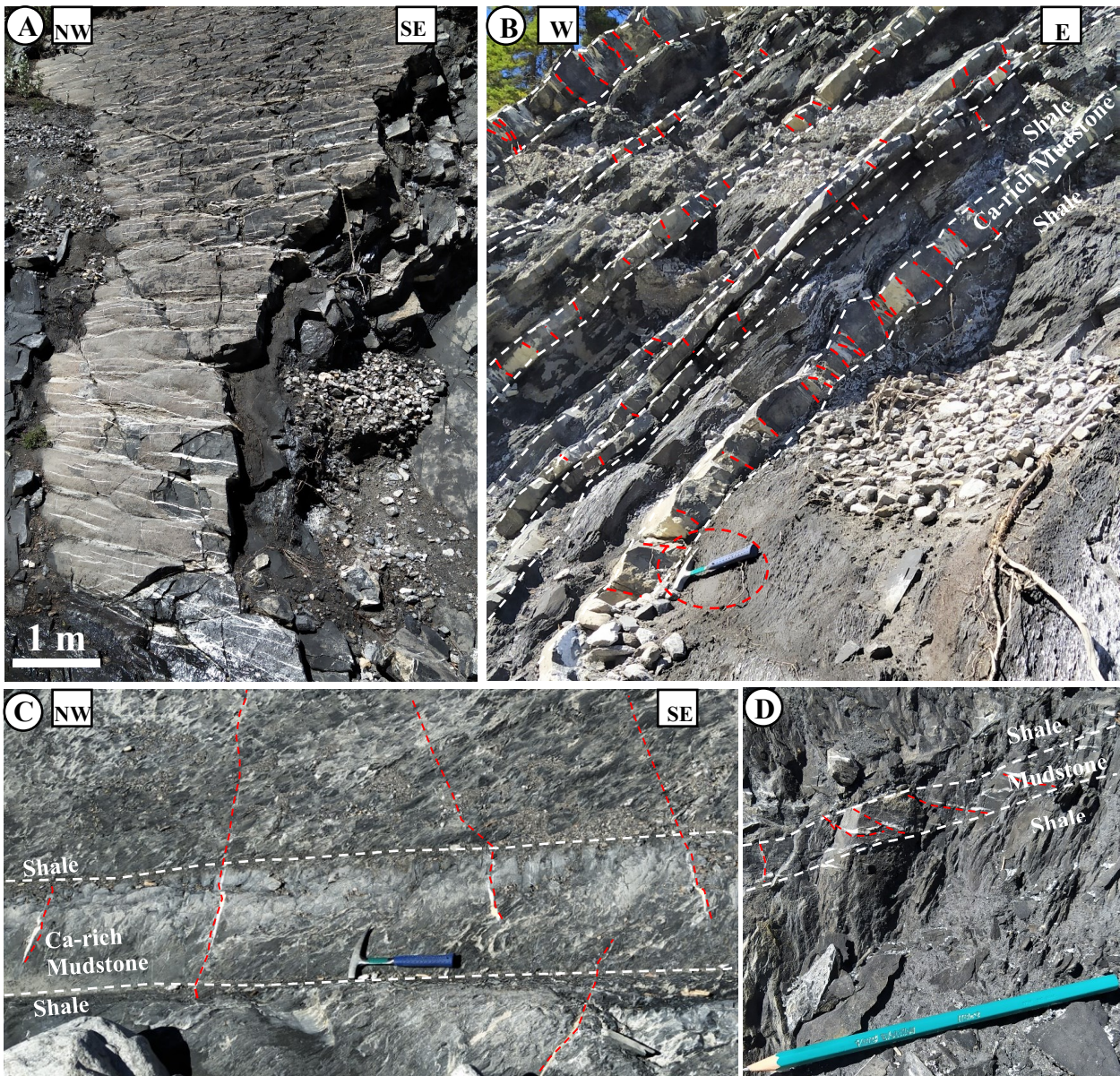


Fig. 4.73. Tensile calcite-filled fractures in the mudrocks of the Perdrix Formation, Hoodoo Creek: A-B). Top (A) and side (B) view of carbonate-rich and organic-rich mudstones. The carbonate-rich beds experienced boudinage with calcite veins formed between boudins. C) Calcite-filled fractures with height > 50 cm crossing bed boundary between carbonate-rich mudstones and organic-rich shales. The calcite-filled veins start in the carbonate-rich mudrocks, where they have larger aperture, and propagate into the shales across the bed boundary. D) subhorizontal tension gashes (calcite-filled fractures) with height < 5 cm propagated within the mudstone bed.

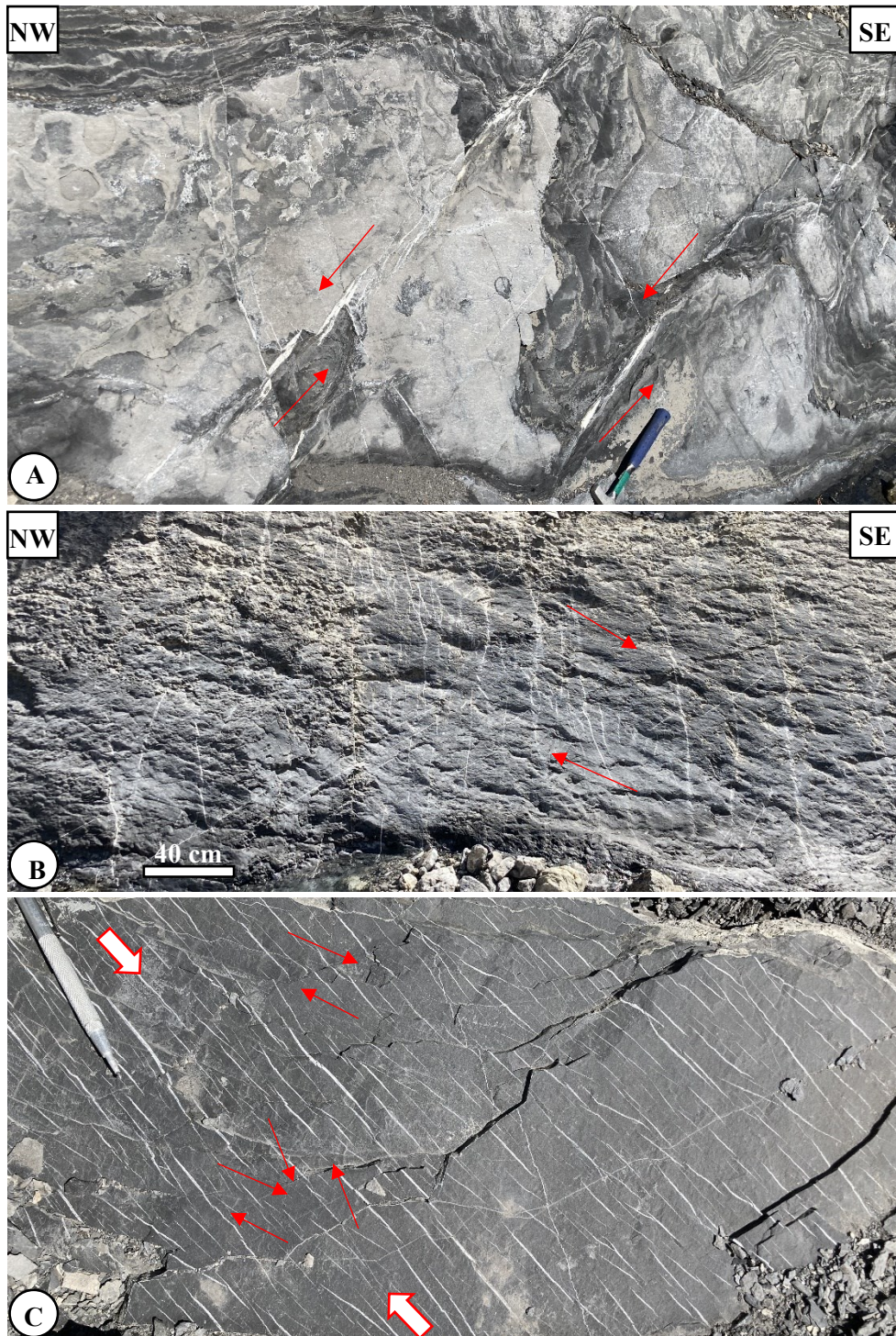


Fig. 4.74. Conjugate tensile calcite-filled fractures in organic-rich shales of the Perdrix Formation, Hoodoo Creek. Conjugate sets of fractures form left-lateral (A) and right-lateral (B) semi-brittle shear zones are highlighted by red arrows. (C) Slab of organic-rich shales detached from the outcrop. The axis (white arrows) bisecting the acute angle between the conjugate tensile fractures is oriented in the outcrop NW-SE, trend and plunge $N128^{\circ}/05^{\circ}$.

Extensional shear fractures in mudrocks of the Perdrix Formation in the Hoodoo Creek exhibit normal displacements of 1-2 mm, crossing the beds or flattening along the detachment in organic-rich shale interbeds (Fig. 4.75). The extensional shear fractures postdate and displace the horizontal calcite-filled fractures and predate formation of subvertical tensile fractures that cut through the shear fractures. In other samples, the younger transtensional fracture with a shear component of displacement displaces the older tensile fracture, splits and propagates along the wall of the older fracture (Fig. 4.76. A-B).



Fig. 4.75. Horizontal, vertical tensile and extensional shear fractures in thinly interbedded carbonate-rich mudrocks and organic-rich shales of the Perdrix Formation, Hoodoo Creek, thin sections, nicols parallel (HC-03-S1): Extensional shear fracture (red-dashed line) cut through the beds with ~1 mm of normal displacement. The shear fracture postdates (displaces) horizontal tensile fractures (blue arrows), and it predates (is crossed by) subvertical tensile fractures (green arrow).

Pressure shadows filled up with fibrous calcite grow around the well-shaped cubic pyrite crystals of 0.1 to 0.5 mm size (Fig. 4.76. C-D). The pressure shadows grow parallel to cleavage S1 and the low compressive stress, perpendicular to the main compressive stress. Subhorizontal calcite-filled tensile fractures are oriented perpendicular and at low angle to the subvertical cleavage S1. The dissolution along the cleavage planes results in apparent shift of segments of the orthogonal veins (Fig. 4.76. C). Fibrous calcite in pressure shadows overgrows the horizontal veins (Fig. 4.76.D).

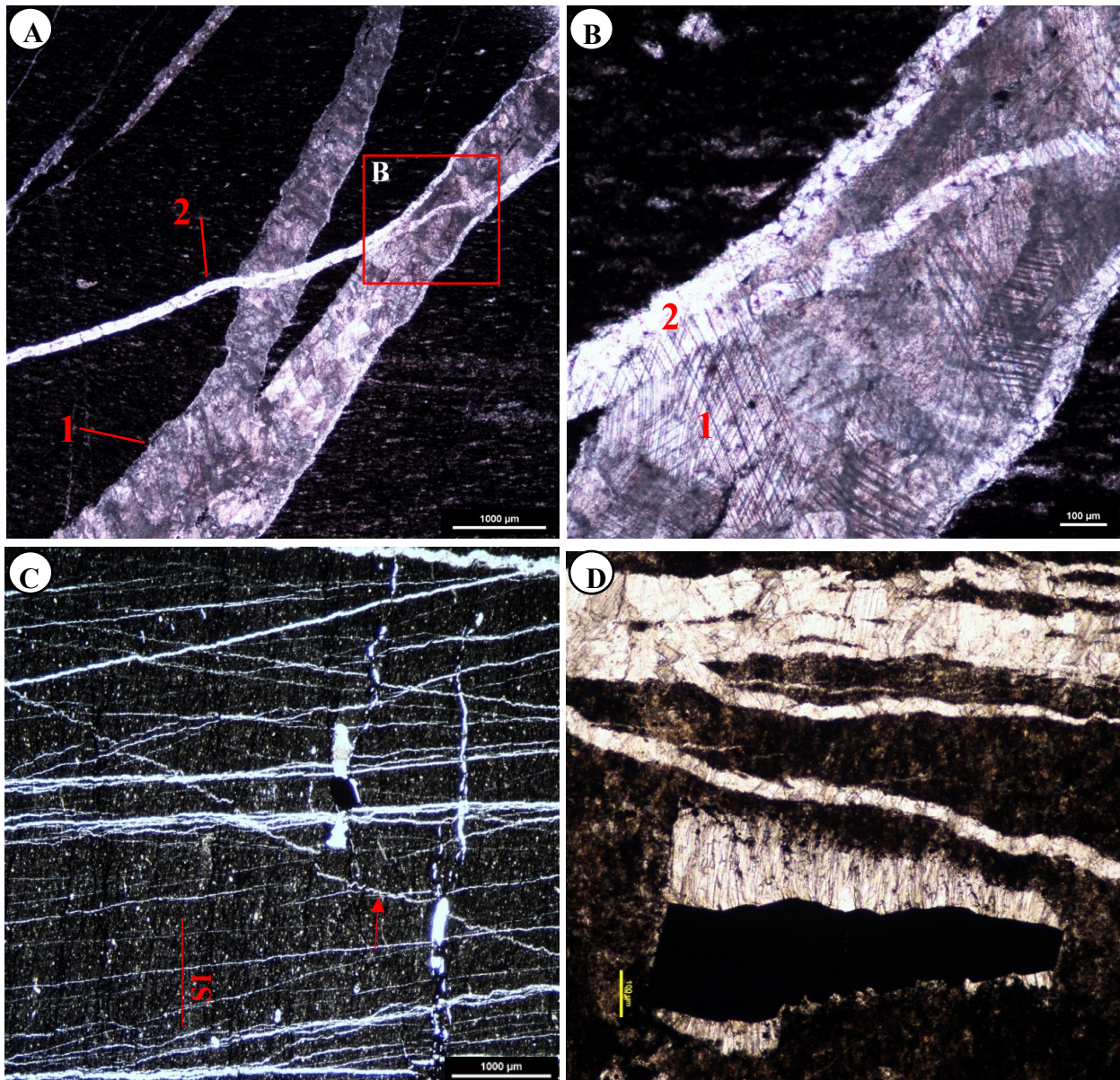


Fig. 4.76. Several generations of calcite-filled fractures, cleavage and pressure shadows around pyrite in thin sections of the Perdrix shales, the Hoodoo Creek, nicols parallel: A) Cross-cutting relationship of

calcite-filled fractures. The younger transtensional fracture with a shear component of displacement (2) displaces the older tensile fracture (1), splits and propagates along the wall of the older fracture (1), sample HC-12-S4. B) Detail of thin section A. C) Subhorizontal calcite-filled tensile fractures oriented perpendicular and at low angle to subvertical cleavage (S1= red line). The dissolution along the cleavage planes results in apparent shift of segments of the orthogonal veins highlighted by the red arrow, sample HC-06-S1. D) Subvertical pressure shadows filled with fibrous calcite around the pyrite crystal, growing parallel to subvertical cleavage S1, in the direction orthogonal to the main compressive stress.

Subhorizontal stylolites, generated by pressure dissolution, were described outcrops and in thin-sections in the Perdrix mudrocks of the Hoodoo Creek area (Fig. 4.77). The observed stylolites are similar to previously recognized rectangular and peak types of stylolites (Koehn et al., 2016). The spacing between different stylolites ranges from 1 to 2 cm. Subvertical orientation of stylolites teeth indicate the subvertical orientation of the main compressive stress.

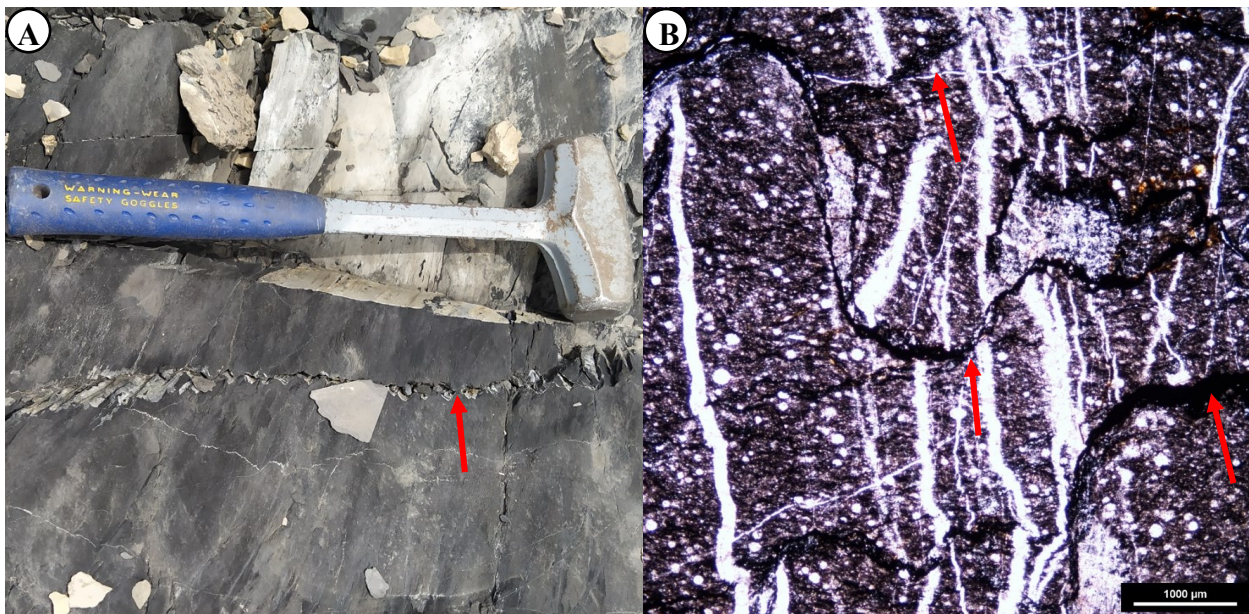


Fig. 4.77. Outcrop photo (A) and thin section, sample HC-08-S1 (B) of subhorizontal stylolites in fossiliferous carbonate-rich mudstone and wackstone of the Perdrix Formation, Hoodoo Creek. Dissolution along the stylolites results in an apparent shift of subvertical calcite-filled veins. The red arrows point out the stylolites.

Three sets of fractures were identified in the Perdrix Formation of the Hoodoo Creek area (Set 1, Set 2, and Set 3) based on a total of 57 measurements (Fig. 4.78). Transtensional right-lateral fractures of Set 1 (N = 11) are oriented NE – SW dipping to the SE, with mean strike azimuth and dip angle of N 28°/74°. Open tensile fractures with plumose structure of Set 2 (N = 29) are oriented NNW-SSE dipping to the E, with mean strike azimuth and dip angle of N 356°/62°. Transtensional left-lateral fractures of Set 3 (N = 17) is oriented ENE-WSW, dipping to the N, with mean strike azimuth and dip angle of N 267°/54°. The angle between conjugate transtensional fractures of sets 1 and 3 is about 60°.

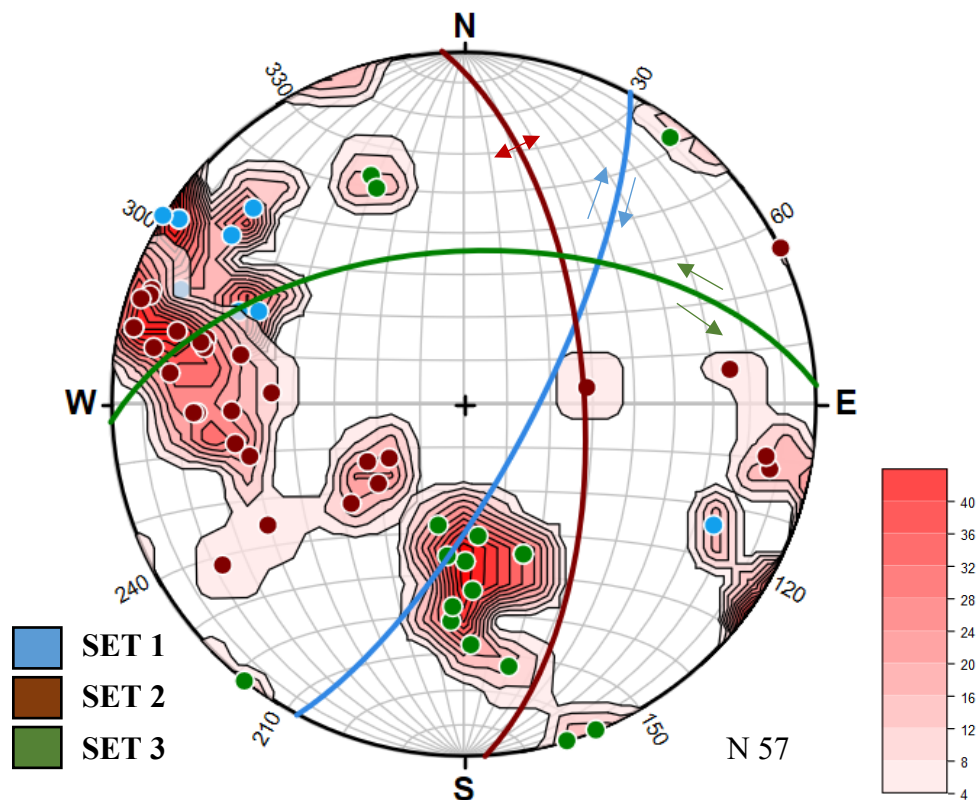


Fig. 4.78. Orientation of calcite-filled and open tensile fractures of set 2 and conjugate transtensional semibrittle fracture sets 1 and 3 in organic-rich shales of the Perdrix Formation, Hoodoo Creek. Mean strike azimuth and dip angle of three sets of fractures (lines) and poles to planes (dots) are plotted on stereographic equal area projection, lower hemisphere. Density contours of poles to planes are highlighted by red color. No bedding rotation is applied.

Based on the outcrop and thin sections observations, there are three groups of paragenetically-linked structural elements in the Perdrix Formation, Hoodoo Creek.

Group 1 comprises structural elements resulting from SW-NE shortening. The SW-dipping bedding of the Perdrix Formation intersects with the NW-SE subvertical cleavage (S1) dipping at $\sim 80^\circ$ to the SW. The intersection lineation (L1) between bedding and cleavage S1 is subhorizontal and oriented NW-SE. The fibrous calcite filling in subvertical pressure shadows around pyrite are parallel to cleavage S1 and likely formed at the time of regional folding and cleavage development during the shortening. The SW-dipping thrust fault zone filled with calcite and quartz indicates NE direction of transport. The sub-horizontal and low-angle tensile fractures filled with calcite occur in the hanging wall of the thrust and are likely formed during the thrusting and the SW-NE shortening, before the onset of cleavage, as these fractures display an apparent “shift” caused by dissolution along the subvertical cleavage planes. The tensile bedding-perpendicular calcite-filled fractures were likely formed between the boudins in more competent carbonate-rich beds during the folding. The conjugate tensile and transtensional calcite-filled fractures forming left- and right-lateral semi-brittle shear zones of sets 1 and 3 likely developed with other elements of group 1.

Group 2 involves structural elements formed during dextral strike-slip deformation likely under the N-S shortening: the NW-SE subvertical dextral semi-brittle strike-slip shear zone, sigmoidal schistosity S2, drag folds, calcite lenses.

Group 3 includes structural elements formed during the extension. It involves inclined normal shear fractures; post-dating subvertical tensile fractures filled with calcite; subhorizontal stylolites with subvertical orientation of stylolite teeth; NNW-SSE open subvertical fractures with plumose structure of set 2. All elements indicate vertical orientation of the main compressive stress.

Conjugate semibrittle transtensional fractures of sets 1 and 3 (Fig. 4.78), subhorizontal to low angle tensile and shear calcite-filled fractures (Fig. 4.71) and bedding-orthogonal tensile fractures between boudins in the mudrocks of the Perdrix Formation could have been formed during the SW-NE shortening, folding and burial. Open tensile fractures of set 2 (Fig. 4.78) may correspond to the phase of extension during uplift and erosion.

Fracture intensity (P10) and (P21) in the mudrocks of the Perdrix Formation was estimated in two outcrops of the Hoodoo Creek area using the Terzaghi's correction method for P10 and circular scanline method for P21. The circular scanline method is based on the number of intersections within a circle and the radius of the circle (Mauldon et al., 2001):

$$F(P21) = n/4r$$

where:

F : Fracture intensity P21

n : number of fractures intersecting the circle

r : radius of the circle

At the first outcrop, P10 is 8.48 (fract/m) for scanline A and 5.32 (fract/m) for scanline B (Fig. 4.79). The radius for the circle on the first outcrop is 0.34 m, with 11 intersections for circle A and 10 intersections for circle B. P21 is 8.09 (m/m^2) in circle A, and 7.35 (m/m^2) in circle B.

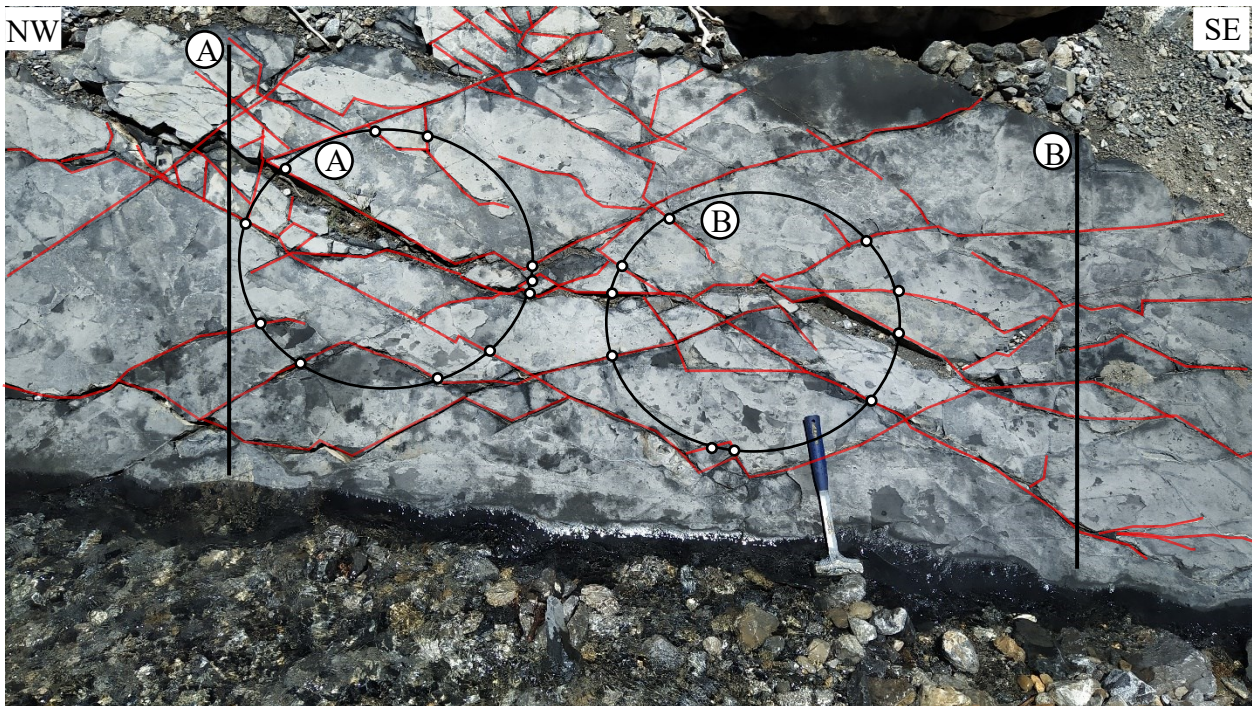


Fig. 4.79. The map view of the top of carbonate-rich mudstone bed of the Perdrix Formation, Hoodoo Creek. The red lines highlight mapped open fractures. The black lines and circles A and B indicate the scanlines used for the estimation of fracture intensity P10 and P21, respectively. The small white circles are plotted at the intersections of fractures with the circular scanline.

At the second outcrop, fracture intensity P10 is 4.76 (fract/m) for scanline A and 5.12 (fract/m) for scanline B. The radius for circles A and B is 0.43 m, with 6 intersections in circle A and 7 in circle B. The calculated fracture intensity (P21) is 3.45 m/m^2 for circle A and 4.02 m/m^2 for circle B (Fig. 4.80).

The average fracture intensity P10 and P21 for the first outcrop is 6.90 (fract/m) and $7.72 \text{ (m/m}^2)$ respectively, and 4.94 (fract/m) and $3.73 \text{ (m/m}^2)$ for the second outcrop. The first outcrop is characterized by fracture intensity P10 30 % (P10) and 48 % (P21) higher than in the second outcrop. The first outcrop mostly consists of open fractures while the fractures mapped in the second outcrop are calcite-filled fractures. The higher fracture intensity in the first outcrop could be related to formation of fractures during different phases of deformation, or to differences in rock composition and orientation of fractures and scanlines between the outcrops.

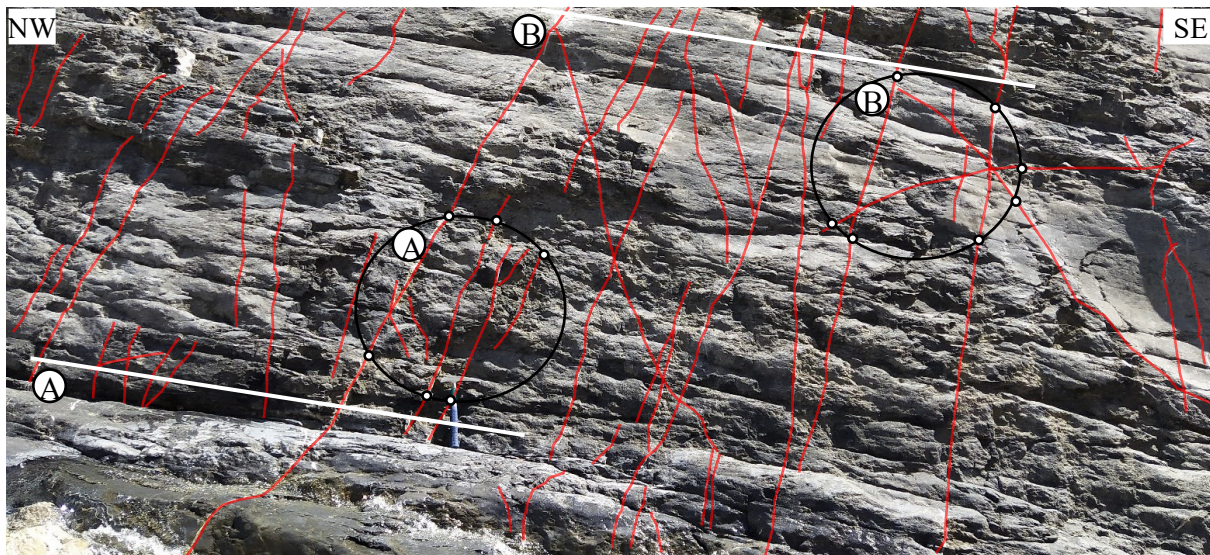


Fig. 4.80. The map view of the top of carbonate-rich mudstone bed of the Perdrix Formation, Hoodoo Creek. The red lines highlight mapped calcite filled fractures. The black lines and circles A and B indicate the scanlines used for the estimation of fracture intensity P10 and P21. The small white circles are plotted at the intersections of fractures with the circular scanline.

Chapter 5: DISCUSSION

5.1. Relationship between lithofacies, mechanical properties and rock composition

The mechanical properties of rocks, deformation domain, strain localization, stress concentration and anisotropy, and pore pressure can influence where and how natural fractures would initiate and propagate vertically and laterally (Long et al., 2019; Liao et al., 2020; Zhou et al., 2022). Rock units with stiffer mechanical properties may be more prone to fracture initiation (Yang et al., 2018; Wust et al., 2020; Fu et al., 2022). Understanding these parameters helps in predicting distribution and intensity of natural fractures in the subsurface.

The three main lithofacies (F2, F3 and F5) that compose about 95% of the Duvernay Formation (Table 4.1) are characterized by significant variability in mechanical properties, in particular in stiffness (static Young Modulus) and compressional (UCS) and tensile strength. Based on the analysis of core and log data in seven vertical wells (Fig. 5.1.A), static Young's Modulus increases from organic-rich biosiliceous mudstones of facies F2 (average of 27 GPa) to organic-rich silty interbedded mudstones of facies F3 (average of 35 GPa) and to carbonate-rich nodular mudstones of facies F5 (average of 44 GPa). Similar trend is observed for bulk density, Unconfined Compressional Strength and hardness (Fig. 5.1.B-D). Density of mudrocks of facies F5 is higher (average of 2.64 g/cm³) than F3 (average 2.60 g/cm³) and F2, the latter being characterized by lower density of 2.52 g/cm³. The Unconfined Compressional Strength is notably lower in F2, with an average of 65 MPa, in contrast to F3 and F5, which have average values of 86 MPa and 115 MPa, respectively. Average hardness varies from 500 in F2, to 600 in F3, to 630 in F5 (Fig. 5.1.D). The average tensile strength varies from 5.7 MPa in facies F2 to 8.9 MPa in facies F3, up to 19 MPa in facies F5 (Fig. 4.29, Table 4.4).

The differences in mechanical properties of the analyzed three main lithofacies of the Duvernay Formation can be correlated with the variation in mineral composition of the mudrocks (Fig. 5.2), similar to the results of previous studies (Dong et al., 2018; Venieri et al., 2019). Mineral composition of the Duvernay mudrocks available in the XRD core tests in well 7 has strong correlation with log-based estimated elastic and strength parameters (Fig. 5.2). Content of calcite is in positive correlation with static Young's Modulus and Unconfined Compressional Strength (Fig. 5.2) and tensile strength (Fig. 4.29). This suggests that an increased content of carbonate material enhances the stiffness and strength of the mudrocks.

Another component that enhances the strength of mudrocks of the Duvernay Formation is biogenic silica supplied by microfossils of radiolarians, sponges and diatoms (Dong et al., 2018). The Total Organic Carbon (TOC) and illite content (Fig. 5.2) are characterized by negative correlation with Young's Modulus and Unconfined Compressional Strength, indicating that facies with higher TOC and illite content are associated with lower rock stiffness and compressional strength. Tensile strength is lower in organic-rich facies F2 and F3 with high TOC values than in carbonate-rich facies F5 (Fig. 4.29, Table 4.4). The correlation coefficient of static Young's Modulus and UCS vs mineral composition from XRD core analysis is lower for the illite content than for calcite and TOC content (Fig. 5.2).

Summarizing, the organic-rich biosiliceous mudstones of facies F2 are characterized by higher content of illite (20 – 39 %) and organic matter TOC (5.5 – 12 %) and lower content of calcite (11 – 32 %) and more ductile behavior, if compared to facies F3. The organic-rich thinly laminated organic- and carbonate-rich mudstones of facies F3 are intermediate in content of illite (16 – 34 %), organic matter TOC (2 – 9 %), and calcite (20 – 55 %), stiffness and strength compared to facies F2 and F5. Mechanical properties of facies F2 and F3 determine the behavior of the upper and lower Duvernay Member, in which they represent the dominant facies. The carbonate-rich nodular mudstones of facies F5 of the middle Duvernay Member are characterized by the highest content of calcite (40 – 82 %), illite (9 – 25 %) and organic matter (0.5 – 5 %) and highest stiffness, compressional and tensile strength compared to facies F2 and F3. Facies F5 behaves as a stiff and strong unit, similar to the results of the previous studies (Soltanzadeth et al., 2015; MacKay et al., 2018).

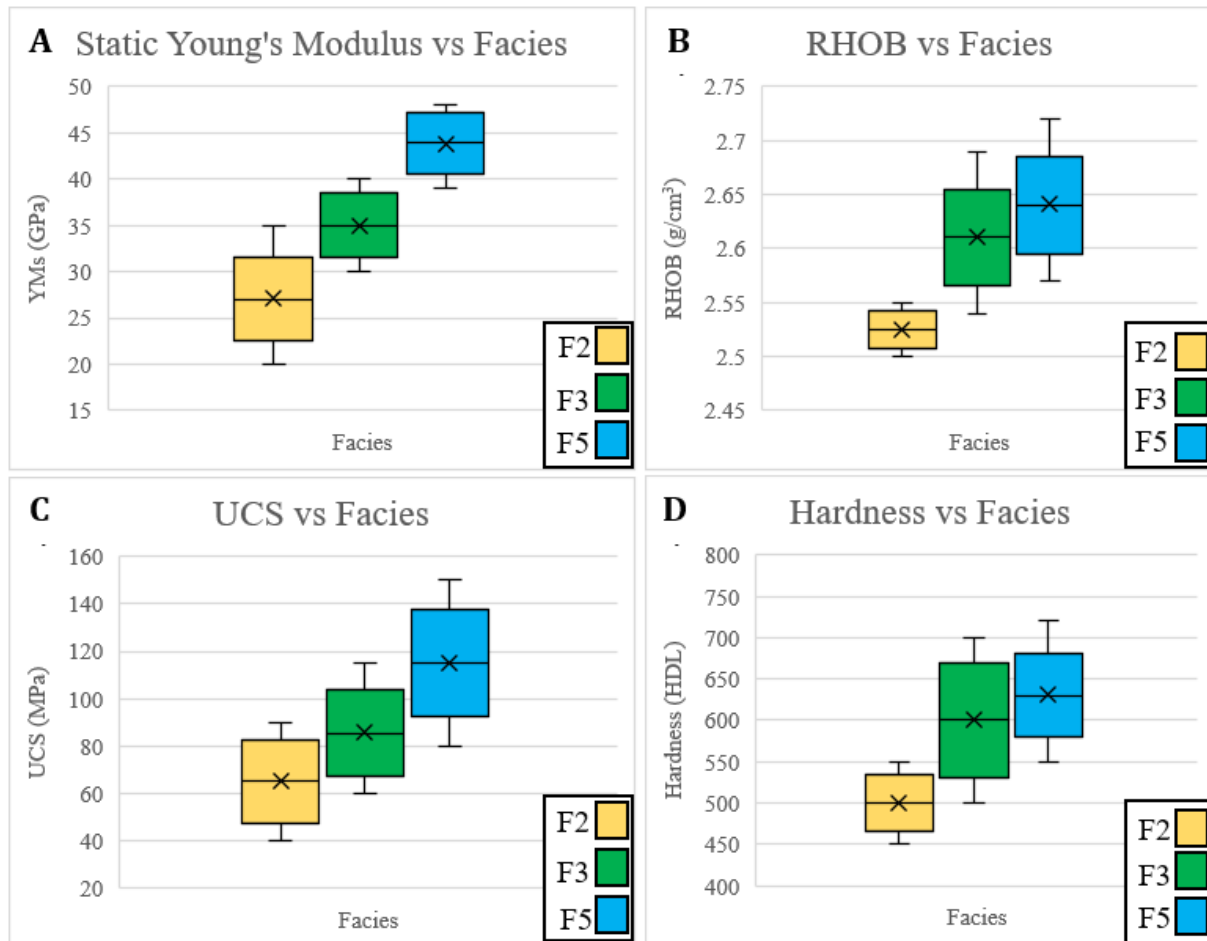


Fig. 5.1. Box-plot diagram of average values of static Young's Modulus (A), bulk density, RHOB (B), Unconfined Compressional Strength, UCS (C), and Hardness (D) in three main lithofacies F2, F3, F5 of the Duvernay Formation based on core and log data in seven vertical wells 1-7. See Table 3.1 and Fig. 3.2 for name and location of studied seven vertical wells, Table 4.1 for the facies composition.

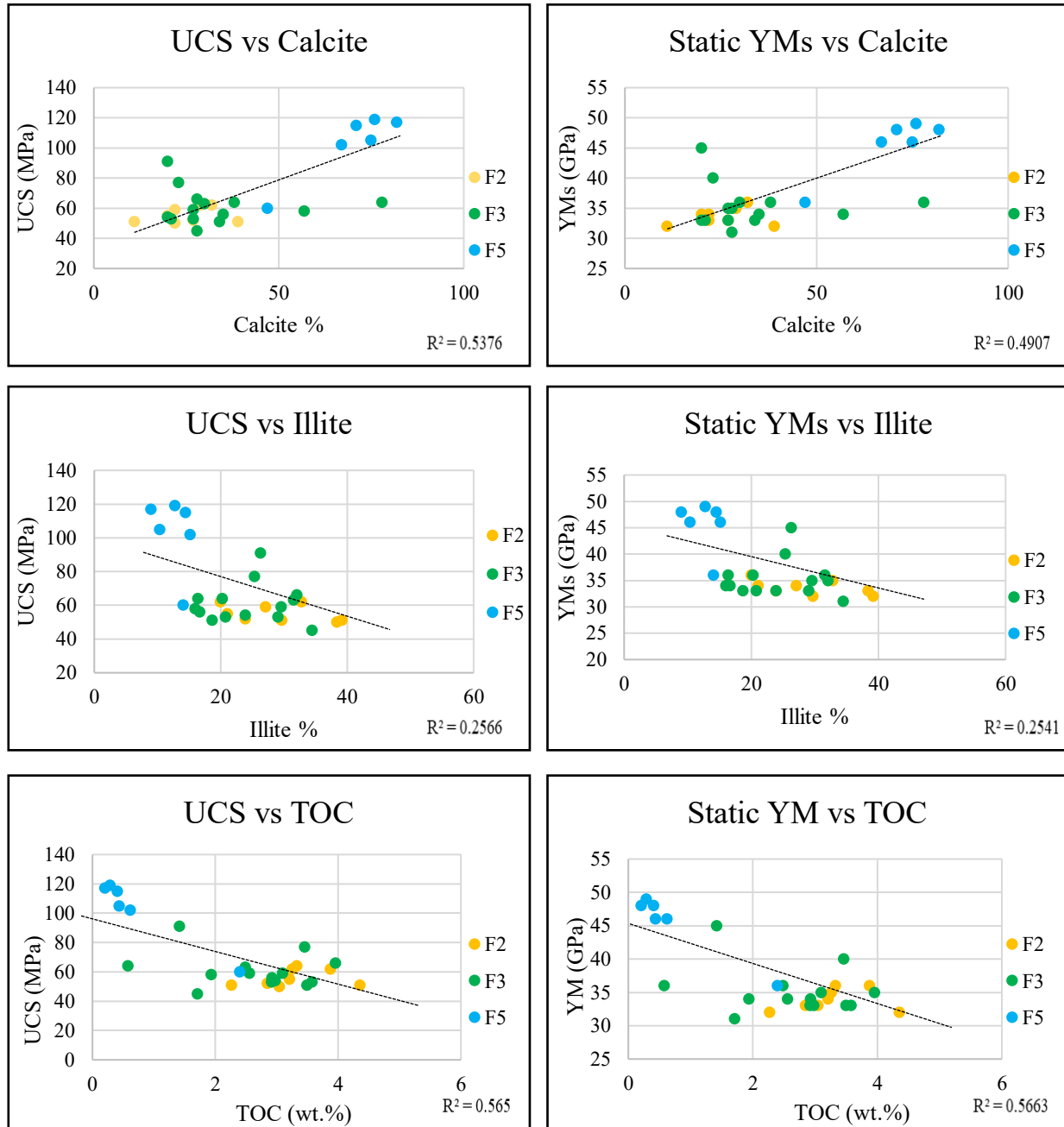


Fig. 5.2. Cross-plots of log-based estimated Unconfined Compressive Strength (UCS) (MPa) and static Young's Modulus (GPa) vs core-based mineral composition of mudrocks of the Duvernay Formation for three main lithofacies F2, F3 and F5 in well 7. The mineral content of Calcite (%), Illite (%), and Total Organic Carbon (TOC) (wt.%) is obtained from the XRD core data of the Duvernay Formation in well 7. See Table 4.1 for lithofacies definition. See Table 3.1 and Fig. 3.2 for well's name and location.

5.2. Controlling factors for fracture development

Lithofacies, mineral composition and mechanical properties of mudrocks of the Duvernay Formation contribute to building contrasting properties between mechanical stratigraphic units in the formation. Thickness of facies and contrasts in mechanical properties control the height and spacing of natural fractures. Typically, tensile vertical fractures orthogonal to bedding are stopped at the boundaries of distinct lithofacies F2, F3 and F5 with strong difference in mechanical properties (Fig. 4.32.A). In thinly bedded mudrocks of facies F3 composed of alternation of microlaminae of organic- and carbonate-rich mudrocks, fractures can propagate vertically up to about 60 cm until fading out (Fig. 4.32.B and C). The stiffness and compressional and tensile strength of facies F3 are higher than in facies F2 and less than in facies F5 (Tables 4.3-4.4, Figs 4.29, 5.1, 5.2). In more ductile organic-rich mudrocks of facies F2, vertical tensile fractures are shorter (3-5 cm), while in stronger and stiffer carbonate-rich nodular mudrocks of facies F5 vertical tensile fractures can grow up to 2 m.

It was shown that taller fractures are generally characterized by wider spacing, following the relationship determined by Michaelis and Menten non-linear equation (Michaelis and Menten, 1913). Fracture spacing in mudrocks of main lithofacies F2, F3 and F5 of the Duvernay Formation can be evaluated by comparing fracture analysis in seven vertical and four horizontal wells. Bed thickness, linear intensity (P10) (Table 4.6) and height of vertical fractures orthogonal to the bedding based on core description in vertical wells are compared to fracture intensity and spacing of vertical fractures analyzed in FMI logs in horizontal wells (Table 4.9). Linear fracture intensity is corrected with the Terzaghi's correction. Based on core data (Table 4.6), linear intensity (P10) of vertical fractures in thinly (0.5-1 cm) bedded mudrocks of facies F3 is 1.58 fract/m that is almost 1.5-2 higher than in organic-rich mudrocks (5 – 40 cm thick) of facies F2 (1.05 fract/m) and in thick (30 - 70 cm) beds of facies F5 (0.84 fract/m). Similarly, fracture intensity P10 and P32 is higher in mudrocks of facies F3 than in facies F2 and F5 as interpreted from image logs in the Duvernay Formation in horizontal wells (Table 4.9). Mean fracture intensity P10 and P32 varies from 2.90 fract/m and 2.96 m²/m³ in well A to 4.43 fract/m to 4.45 m²/m³ in well B, respectively. Mean fracture intensity P10 and P32 in mudrocks of facies F2 ranges from 0.53 ± 1.44 fract/m and 0.53 ± 1.77 m²/m³ in well B to 0.96 ± 2.32 fract/m and 0.96 ± 1.26 m²/m³ in well A. Mean fracture intensity P10 in facies F5 is 0.143 fract/m. The higher linear fracture intensity in mudrocks of facies F3 reflects more narrow spacing in F3 than in facies F5 and F2. Fracture spacing varies from 20-30 cm in facies F3 in wells A and B (Figs

4.43, 4.64) to about 0.5 m – 0.7 m in organic rich mudstone of facies F2 and about 1 m in carbonate-rich mudrocks of facies F5 (Figs 4.47, 4.49). Lower fracture intensity and larger fracture spacing in facies F2 and F5, if compared to facies F3, can be related to more ductile mechanical properties of facies F2, which are not favorable for fracture propagation, and higher thickness of beds in facies F5.

According to fracture-height classification (Fig. 5.3), vertical fractures orthogonal to bedding can be perfect bed-bounded, top-bounded, hierarchical and unbounded (Hooker et al., 2013; Gale et al., 2014; Galvis Portilla, 2022). Fractures orthogonal to bedding studied in the Duvernay and Perdrix Formations are either perfect bed-bounded (Figs 4.32.A, 4.73.B and D) or hierarchical, crossing bed boundaries (Fig. 4.73.C), and less frequently unbounded (Fig. 4.32.B and C). Similar fracture behavior was observed in the Upper Devonian New Albany shale in the Illinois Basin, where some fractures are arrested by bed boundaries, while others fractures cross bed boundaries between beds of different composition (Gale et al., 2014).

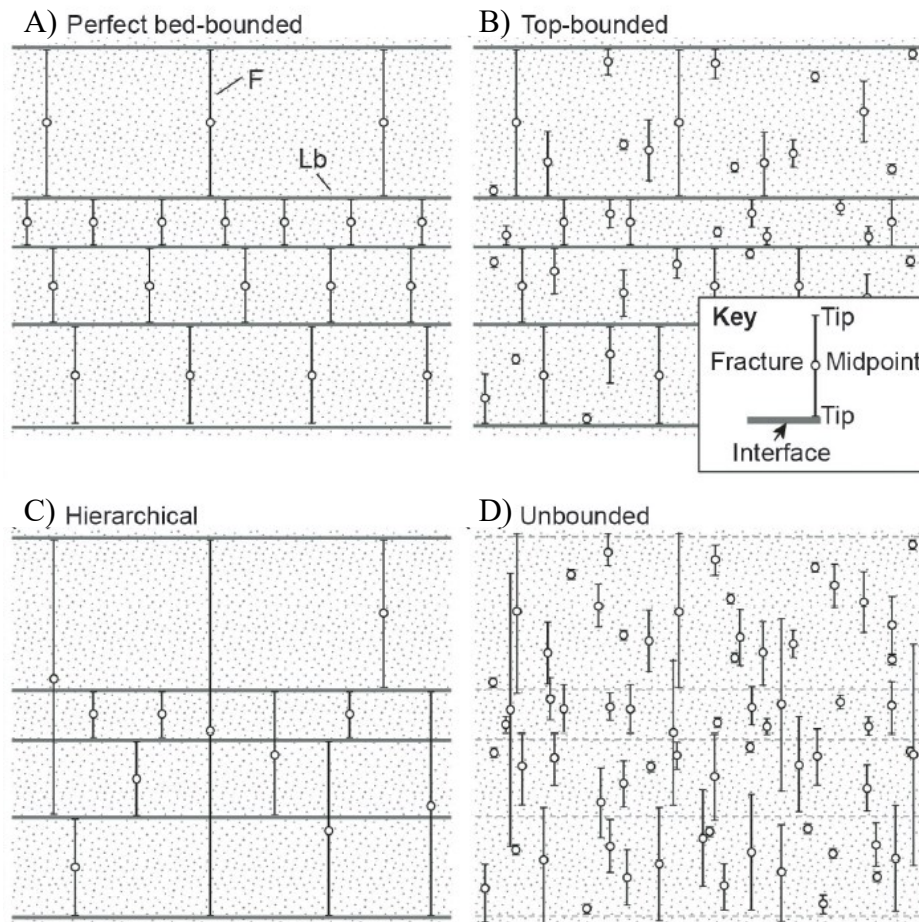


Fig. 5.3. Fracture height classification, after Gale et al., (2014); Hooker et al., (2013). A) Perfect bed-bounded fractures. B) Top-bounded fractures. C) Hierarchical fractures. D) Unbounded fractures.

5.3. Relationship between fracture intensity, thermal maturity, fluid pressure, and burial depth of the Duvernay Formation in the Kaybob area of the West Shale Basin

The linear fracture intensity in core of the Duvernay Formation in seven vertical wells across the Kaybob area increases from the northeast to the west and southwest (Fig. 4.40). This trend likely aligns with the increase in burial depth (Fig. 2.14), fluid pressure (Fig. 2.17) and thermal maturity of organic matter (Fig. 2.15) in mudrocks of the Duvernay Formation (Rokosh et al., 2012; Lyster et al., 2017; Yeates et al., 2022). Higher fracture intensity in well B compared to well A (Table 4.9, Fig. 4.6) may be correlated with high overpressure in the central part of the Kaybob area (Fig. 2.17).

Indeed, an increase of burial depth of organic-rich shales results in thermal maturation of organic matter, fluid expansion and expulsion of hydrocarbons that contribute to a fluid pressure buildup. That represents one of four main mechanisms that generate overpressure: undercompaction, fluid expansion, lateral transfer and tectonic loading (Bowers, 2002). An overpressure may form as a result of undercompaction of shales during fast burial, when low permeability prevents pore fluid from escaping as rapidly as pore space tries to compact. Fluid expansion mechanisms such as heating, hydrocarbon maturation, and the expulsion/expansion of intergranular water during clay diagenesis can result in an overpressure in shales (Bowers, 1995). Here, overpressure results from the rock matrix constraining the pore fluid as the fluid tries to increase in volume. Transformation of smectite into illite during clay diagenesis is another fluid-expansion mechanism that can cause overpressure (Lahann, 2002; Lahann and Swarbrick, 2011). Lateral transfer mechanism involves fluid transport and pressure increase that occur along a dipping sand enclosed in shale (Yardley and Swarbrick, 2000). Tectonic loading implies the mechanism when trapped pore fluid is squeezed by tectonically driven lateral stresses inducing overpressure (Yassir and Addis, 2002). Fluid expansion and tectonic loading are capable of generating high overpressure (Bowers, 2002; Swarbrick et al., 2002; Yassir and Addis, 2002).

The hydrocarbon generation and associated overpressure have previously been suggested as possible factors contributing to fracture growth in organic-rich shales (Spencer, 1987; Ozkaya, 1988; Marquez and Montjoy, 1996; Berg and Gangi, 1999; Ma et al., 2017). Burial and high

overpressure in the organic-rich mudrocks of the Upper Devonian Duvernay Formation (Lyster et al., 2017; Shen et al., 2019) might have contributed to initiation and propagation of natural fractures during burial of the shales.

The burial and basin fluid flow in the Alberta Basin occurred during several main deformation phases (Fig. 2.16). The early (shallow) burial phase (0 - 1500 m) is related to the Antler tectonic phase from the Late Devonian to the Mississippian (Green and Mountjoy, 2005). Temperatures of 45°C to 75°C for pervasive dolomitization would have been reached during the late Devonian to Jurassic, at burial depths of about 700 m to 1500 m. The intermediate phase (~ 1500 – 2500 m) is associated with the Columbian orogeny from the Late Jurassic to Early Cretaceous. The later (deep) burial phase (> 2500 m) occurred during the Laramide Orogeny from the Late Cretaceous to Paleocene (Fig. 2.16). The maximum burial in the Alberta Basin occurred at about 60 Ma based on the results of Apatite fission track analysis for Cretaceous, Paleozoic and Precambrian borehole samples along two major transects through the Western Canada Sedimentary Basin (Issler et al., 1999). The Wabamun Group of the West Shale Basin was buried down up to about 5200 m - 5500 m and temperature of 175°C during the Laramide orogeny (Green and Mounjoy, 2005; Stacey et al., 2020). The Duvernay Formation in the center of the West Shale Basin reached the oil window (60°C - 150°C) at about 70-80 Ma ago and the gas window (120°C - 150°C) at about 50 Ma ago based on the basin modeling (Creaney et al., 1994; Wang et al., 2018). In the eastern Foothills, the amount of subsidence was even higher (Fig. 2.16) than in the West Shale Basin, reaching up to 9 km during the Laramide Orogeny (Price, 1994; Stacey et al., 2020).

Two main different stages of fracturing have occurred in carbonate rocks of the Leduc, Swan Hills Formation and Wabamun Group during different burial phases (Green and Mountjoy, 2005; Stacey et al., 2020). According to Green and Montjoy (2005), the first phase of fracturing occurred after early replacive dolomitization (Type I) and stylolitization and before massive replacement dolomitization (Type II). That is supported by observations that dolomite of Type II overgrows or replaces early mosaic calcite, columnar cements and possible early fracture filling cements indicating a post early-calcite cementation timing. The second phase of fracturing occurred after saddle dolomite cementation and before hydrothermal dissolution. It is supported by the observations that saddle dolomite commonly lines secondary solution pores (vugs and

molds) and fractures in massive dolostones. Saddle dolomite generally is most prevalent in areas that have undergone extensive Type II subsurface dolomitization, dissolution, fracturing and brecciation. Pyrobitumen commonly postdates the saddle dolomite phases, shown by the lining of saddle dolomite by black isotropic material. The first stage of fracturing is related to the early relatively shallow (1000 m – 1500 m) burial during the Antler orogeny (Late Devonian-Mississippian). The second stage of fracturing is associated with intermediate (1500 m – 2500 m) and deep (> 2500 m) burial during the Columbian and/or Laramide orogeny (Green and Mountjoy, 2005; Stacey et al., 2020). Oxygen isotope thermometry and Sr isotopes suggests that Type II dolomite may have formed at temperatures ranging from about 45° to 75°C (Green and Montjoy, 2005). Burial depths, at which temperatures of 45° to 75 ° C would be attained, assuming a geothermal gradient of 30°C/km and surface temperature of 25°C, would be at about 700 m to 1500 m depth. These depths would have been reached in the latest Devonian through Jurassic time and correspond to the first phase of fracturing (Green and Montjoy, 2005). In the West Shale Basin, the Th of saddle dolomite ranges from 125 to 190°C (Swan Hills Formation), 127 to 195°C (Leduc Formation) and 133 to 174°C (Wabamun Group) (Stacey et al., 2020). Based on the burial history curves of Green and Mountjoy (2005), the Swan Hills Formation, Leduc Formation and Wabamun Group in the West Shale Basin have maximum burial depths of 5525m (ca. 180°C), 5,450 m (175°C) and 5,525 m (170°C) respectively. The integral geothermal gradient in the study area is estimated 20-30C/km (Atlas, 1994, Chapter 30).

Based on the discussed above results of the previous studies of burial and fracture generation in the Upper Devonian carbonate rocks of the West Shale Basin, in might be suggested that natural fractures studied in the Duvernay Formation might also have been formed during the Antler and Laramide orogeny. If thermal maturity, fluid expansion and hydrocarbon generation are the main cause of high overpressure and fracture generation in the Duvernay Formation, it is likely that fracturing in the organic-rich mudstones occurred mostly during the Laramide orogeny. However, fracturing in mudrocks of the Duvernay Formation during the Antler orogeny cannot be excluded. Additionally, some natural fractures could have formed during the uplift and erosion occurred after the maximal burial during the Laramide orogeny, at around 48 Ma as reconstructed from the analysis of the vitrinite reflectance data (Kalkreuth and McMechan 1988; Woodland and Bell 1989; Issler et al. 1999). The amount of erosion is estimated from approximately 500-900 m in the east to around 1400 m to 3000 m in the west of

the Alberta basin (Magara, 1978; Nurkowski, 1984; Woodland and Bell, 1989; Kalkreuth and McMechan, 1988, 1996).

The present-day maximum horizontal stress is oriented NE-SW (Fig. 2.19) and stress regime is mostly strike-slip in the Alberta Basin (McLellan, 1989; Bell and Grasby, 2012; Cui et al., 2013; Reiter et al., 2014; Shen et al., 2019; Lundstern and Zoback, 2020). The present-day stress orientation might have been preserved since the Laramide orogeny, which was characterized by the NE-SW/ E-W shortening, as the main thrust sheets in the eastern margin of the Canadian Rockies are oriented NW-SE/N-S (Dahlstrom, 1970; Jones and Workum, 1978; Spratt et al., 2004). The NW-SE thrusts in the Front Ranges were formed during the Campanian – Maastrichtian (79 – 68 Ma) and Paleocene (64 – 55 Ma), and in the Foothills, east of the McConnell Thrust, during the Eocene (54-51 Ma) (Pana, 2021). Additionally, right-lateral displacement for more than 450 km of along the Northern Rocky Mountain Trench is reconstructed during the Late Cretaceous and Early Paleocene (Roderick, 1967; Price, 1994). The dextral strike-slip reactivation of older normal faults and brittle dextral strike-slip faults cutting the Eocene extensional shear zones were recognized in the Front Ranges (Finley, 2020). Fracturing occurred in the Duvernay Formation during the Laramide orogeny can therefore be analyzed with respect to present-day stress field.

5.4. Orientation of natural fractures in the Duvernay Formation and present-day horizontal stresses

Three sets of natural fractures were interpreted in the Duvernay Formation from image logs in four horizontal wells (Fig. 4.42). Fractures of set 1 (N=1350) are oriented NE-SW strike N53°E/85°. As interpreted from the FMI images in four horizontal wells, these fractures are tensile and can be classified as opening-mode I fractures (Rice, 1968). Fractures of set 1 are sub-parallel to the present-day maximum horizontal stress $S_{Hmax} = \sigma_1$ that is oriented in the Kaybob Area N45°E±5° (Bell and Bachu, 2003; Bell and Grasby, 2012; Reiter et al., 2014; Shen et al., 2019) and formed perpendicular to the minimum principal stress $S_{hmin} = \sigma_3$. Fractures of set 2 (N=550) are oriented NW-SE strike N165°E/85°, at a high angle to fractures of set 1 and S_{Hmax} . Fractures of set 2 are determined mostly (526 fractures) in well A, with fewer (24) fractures in wells C and D. Tensile fractures of sets 1 and 2 could have been formed as a system of orthogonal fractures (vertical joints). Fractures of set 3 (N=103) are oriented NE-SW strike

N74°E/82°, at a low (20°) angle to SHmax that likely corresponds to transtensional settings (Fig. 5.4). Fractures with tensile and shear behavior form at a low angle (~16°) to maximum compressive principal stress σ_1 (Fig. 5.4) under specific conditions, when confining pressure ranges from 3 to 5 times of tensile strength (Suppe, 1985), also known as extensional shear Griffith criterion (Sibson, 2000).

Fractures can form during both burial and uplift and erosion (Twiss and Moores, 1992; Davies and Raynolds, 1996). During the burial deeper than 3 km, fluid pressure in shales may increase either as a result of undercompaction and/or hydrocarbon generation. When fluid pressure becomes higher than minimum compressive stress, tensile fractures will form. During the uplift and erosion, as vertical stress decreases, the total horizontal stresses decrease too, according to Hook's law to accommodate the Poisson's effect of elastic material and thermal contraction of the rock associated with temperature decrease. If fluid pressure in shales remain high, horizontal effective stresses may become negative (tensile), and vertical joints orthogonal to the horizontal stresses would form as a system of orthogonal joints. Orthogonal vertical joints are a common feature in flat-lying sedimentary rocks.

Transtensional fractures of set 3 are described in core of multilayered mudrocks of facies F3 composed of thinly (few mm scale) bedded alternation of carbonate- and organic-rich laminae (Figs 4.34, Fig. 4.35). These fractures are characterized by alternation of segments of tensile opening in carbonate-rich layers and shear segments in organic-rich layers, and they form fracture splays, similar to the negative flower structure. The alternation of dilational jogs in permeable layers and shear segments in impermeable layers along an extensional/transtensional fracture or a fault is a well-known effect of the influence of competence (tensile strength) layering on brittle failure mode under an extensional regime (Sibson, 2000). Difference in mechanical properties of multilayered sandstone-shale units can result in time-dependent fracturing of these lithologies, when tensile fractures develop first in sandstone beds and then propagate into shale beds (Twiss and Moores, 1992). Such mechanism can likely be applied to the multilayered units composed of alternation of carbonate- and organic-rich shale layers. Because carbonate-rich layers have higher competence than organic-rich shale layers, the carbonate-rich layers can support larger differential stress than shales. The minimum horizontal stress is thus lower in the carbonate-rich layers than in shales, and smaller fluid pressure is

required to cause tensile fracturing in carbonate layers than in shales. Therefore, as fluid pressure increases during the burial, tensile fractures form first in the carbonate-rich layers and do not extend into the shales. When fluid pressure in organic-rich shales increases sufficiently to cause hydrofracture, fractures would cross the lithological contacts into the shales.

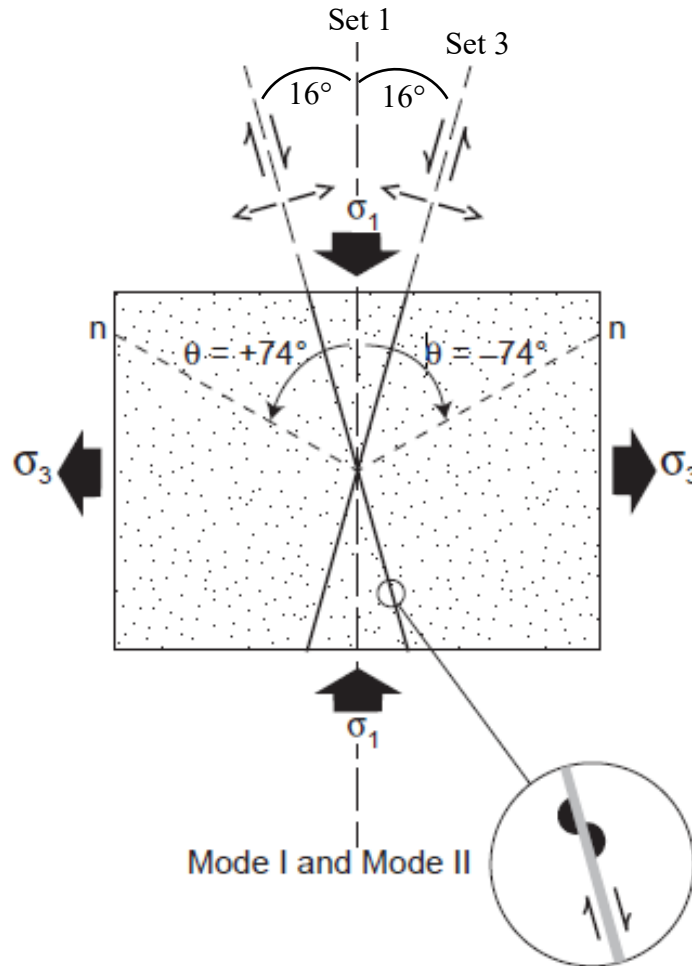


Fig. 5.4. Conjugate fractures formed under transitional tensile behavior conditions, modified from (Davies and Reynolds, 1996).

Fractures of set 3 may be critically stressed fractures, prone to reactivation under minor stress or pore pressure variations, given their orientation at a small angle to the regional SHmax (Fothergill et al., 2014). Understanding the presence of critically stressed fractures is vital, as they have the potential to enhance hydrocarbon production from the Duvernay Formation (Fox and Soltanzadeh, 2015).

5.5. Natural fractures in the Duvernay and Perdrix Formations and phases of deformation

Structural elements described in the Perdrix Formation in the Front Ranges (Hoodoo Creek) form three groups that developed under the settings of (1) thrusting (SW-NE shortening), (2) dextral strike-slip semi-brittle deformation (N-S shortening?), and (3) extension during uplift and erosion (see section 4.7 of chapter Results). Natural fractures described in the Duvernay Formation might be associated with some of these groups.

Fractures of group 1 of the Perdrix Formation were formed under the settings of the SW-NE shortening, NE-vergent thrusting, folding, and burial. Some of these fractures are horizontal and low-angle tensile and shear fractures filled with calcite (Fig. 4.67, 4.68, 4.71, 4.76). Other fractures of group 1 are NE-SE and ENE-WSW conjugate tensile and transtensional high-angle calcite-filled fractures that form left- and right-lateral semi-brittle shear zones of sets 1 and 3 (Fig. 4.73, 4.74, 4.78), and bedding-orthogonal tensile fractures located between boudins in carbonate-rich mudrocks (Fig. 4.73). The fibrous calcite in subvertical pressure shadows around pyrite is parallel to cleavage S1 (Fig. 4.76) and formed under the SW-NE shortening. The polished slip faces (Fig. 4.36), horizontal calcite-filled fractures (Figs 4.31.B, 4.35.B) and tensile subvertical fractures (Figs 4.32, 4.34) of set 1 and 3 (Figs 4.42, 4.52) in the Duvernay Formation can be associated with structural elements of group 1 in the Perdrix Formation, which formed under the settings of the SW-NE shortening and burial during the Laramide orogeny. During the orogeny, the Upper Devonian carbonate rocks of the Wabamun Group in the West Shale Basin were buried down to about 5200 m and temperature of 175°C (Green and Mountjoy, 2005; Stacey et al., 2020).

Fractures within group 3 of the Perdrix Formation were formed under the settings of extension during uplift and erosion. The fractures of group 3 include inclined normal shear fractures (Fig. 4.75) and subvertical tensile fractures filled with calcite (Figs 4.67, 4.68, 4.72, 4.75) that cut through the horizontal fractures of group 1. The subhorizontal stylolites with a subvertical orientation of stylolite teeth (Fig. 4.77) and NNW-SSE open subvertical fractures with a plumose structure of set 2 (Fig 4.78) also belong to group 3. The subvertical NW-SE tensile fractures of set 2 (Figs 4.42, 4.52) and transtensional fractures splays filled with calcite

described in well 3 (Fig. 4.34) in the Duvernay Formation could have been formed either as a set of vertical joints during uplift and erosion (Wright et al., 1994) or post-Eocene strike-slip deformation (Finley, 2020) postdating the Laramide orogeny.

The NW-SE subvertical dextral strike-slip shear zone of group 2 that deforms the Perdrix Formation in Hoodoo Creek may have formed under N-S shortening. This fault can be correlated with the post-Eocene NW-SE dextral strike-slip faults in the Front Ranges of the southeastern BC that were reactivated along older normal faults or formed as brittle dextral strike-slip faults cutting the Eocene extensional shear zones (Ristau et al., 2007; Finley, 2020).

5.6. Fracture intensity and spacing of extensional fractures in the Duvernay Formation and its analogs

Fracture intensity in organic-rich shales (Table 5.1) analogous to the Duvernay Formation have previously been described in the United States (Ault, 1989; Comer et al., 2006; Engelder et al., 2009; Gale et al., 2014). The Upper Devonian Woodford Formation is one of the main source rocks of oil and gas in the Permian Basin (Comer, 1991). Fractures have been studied in the FMI logs in two vertical wells in the Woodford Formation (Coyle, 2011). According to this study, fracture intensity P10 varies among different wells, ranging from 0.23 fract/m to 1.23 fract/m. Fracture intensity P32 in the Woodford Formation is about 2.08 m²/m³ estimated in a core of a subvertical well (Gale et al., 2014). The Mississippian Barnett shale in the Permian Basin is characterized by fracture intensity of P32 ranging from 0.35 m²/m³ to 4.01 m²/m³ as estimated in core of four vertical wells (Gale, et al., 2014). In the Middle Devonian Marcellus shale in the Appalachian Basin, fracture intensity P32 is 1.66 m²/m³ based on the analysis of 3 combined cores (Gale et a., 2014). The Upper Devonian New Albany shales are characterized by fracture intensity P32 ranging from 0.33 m²/m³ and 1.34 m²/m³ based on the study of core in two vertical wells. The estimated fracture intensity in the Upper Devonian and Mississippian shales is comparable with the fracture intensity observed in the Duvernay Formation estimated in core of seven vertical wells and image logs in horizontal wells (Table 5.1). In the Duvernay Formation, P10 ranges from 0 to 3.05 fract/m in core of vertical wells; P10 varies from <0.1 to 2.84 fract/m and P32 ranges from 0.37 to 2.86 m²/m³ horizontal wells.

Finding an appropriate outcrop analog of a subsurface formation can be a challenge (Ukar et al., 2020). The measured fracture intensity (P10) of the outcrops from the Perdrix

Formation ranges from 4.94 fract/m to 6.90 fract/m that is almost twice higher than fracture intensity P10 estimated in core and from image logs of the Duvernay Formation (Table 5.1). Mudrocks of the Perdrix Formation in the Front Ranges underwent more intense deformation than the mudrocks of the Duvernay Formation in the subsurface of the Alberta Basin. Burial, folding and faulting likely resulted in intense fracturing in the Perdrix Formation, similar to the development of natural fracture system in the Cardium sandstone in the Foothills of west-central Alberta (Jamison, 2016). Uplift and decompaction could also have contributed to fracture development in the Perdrix Formation (Narr and Currie, 1982; English, 2012). As a result, using outcrops as analogs to compare fracture intensity might be challenging, as one should define fracture sets generated by different phases of deformation. Fracture orientation in outcrops should be corrected for bedding tilting. Fracture orientation in outcrops and the subsurface may vary as it was determined for the Upper Devonian New Albany shale in the Illinois Basin (Gale and Laubach, 2009; Fidler, 2011). This variation might be related to different burial histories and/or local changes in the stress field. In the deeper part of the Illinois Basin, gas was generated in the Upper Devonian organic-rich shale, while the same mudrocks exposed in the outcrops were not buried deep enough for gas generation (Gale et al., 2014). Hence, fractures in the subsurface may be associated with gas generation, while fractures in outcrops may be attributed to an uplift (Gale et al., 2014).

Careful consideration should be given when comparing fractures in outcrops and in subsurface. However, outcrop observation may provide direct observation of lateral and vertical changes in lithofacies and fracture orientation and distribution over a larger area and within a significant stratigraphic interval, whereas core in a vertical well or image log in a horizontal well allows us to make observations in a limited range of an area and depth interval.

Unit	Age	Basin	Data	Source	P10 (fract/m)	P32 (m ² /m ³)
Woodford	Upper Devonian	Permian	Core and image logs	Coyle, 2011; Gale et al., 2014	0.23 to 1.23	2.08
Barnett	Mississippian	Permian	Core	Gale et al., 2014	x	0.35 to 4.01

Marcellus	Middle Devonian	Appalachian	Core	Gale et al., 2014	x	1.66
New Albany	Upper Devonian	Illinois	Core	Gale et al., 2014	x	0.33 to 1.34
Duvernay	Upper Devonian	Alberta (Kaybob area)	Image logs	Section 4.6, this project.	<0.1 to 2.84	0.37 to 2.86
Duvernay	Upper Devonian	Alberta (Kaybob area)	Core	Section 4.5, this project	0 to 3.05	
Perdrix	Upper Devonian	Front Ranges	Outcrops	Section 4.7, this project	4.94 to 6.90	x

Table 5.1. Comparison of fracture intensity P10 (fract/m) and P32 (m^2/m^3) estimated from core and image logs in mudrocks of the Duvernay and Perdrix Formations and their analogs in the United States. See text for the source reference papers.

5.7. Suggested future work

The characterization of natural fractures in mudrocks of the Duvernay Formation obtained in this study provide information on fracture orientation, length, height and aperture in different lithofacies. This information may help to constrain the parameters used in generation of Discrete Fracture Network and hydraulic fracture modelling used for optimizing the hydraulic fracturing operations.

Further studies of fluid inclusions in calcite-filled fractures and U-Pb dating of calcite-filled fractures in the mudrocks and faults of the Duvernay and Perdrix Formations would help to constrain P-T conditions and timing of fracture development in the Upper Devonian organic-rich mudrocks, similar to other areas (Luczaj and Goldstein, 2000; Mottram et al., 2020; Gasparini et al., 2021).

Chapter 6: CONCLUSIONS

The comprehensive characterization of natural fractures in the Upper Devonian Duvernay Formation was conducted in the Kaybob area of the Western Canada Sedimentary Basin. This analysis was based on the detailed description and examination of approximately 418 meters of core, core tests, and well logs from seven vertical wells, along with about 4.4 kilometers of image logs from four horizontal wells. Additionally, 3D structural and facies modeling were employed to interpret the lateral distribution of lithofacies. The study also involved structural analysis of fractures, folds, and faults in the Upper Devonian Perdrix Formation, which serves as an outcrop analog of the Duvernay Formation in the Front Ranges and Foothills of the Canadian Rockies.

The parameters of natural fractures, including height, length, aperture, and orientation, alongside fracture intensity, were integrated with the analysis of lithofacies, mechanical properties, and structural settings of the mudrocks. The obtained results were discussed in the context of the geochemistry, thermal maturity, fluid pressure of the Duvernay Formation, burial history of the Devonian carbonate rocks, tectonic evolution, and present-day stress field in the Alberta Basin.

Based on the study, the following conclusions are drawn:

- Natural fractures in the Duvernay Formation are predominantly calcite-filled and subvertical, with occasional open and subhorizontal fractures. Vertical tensile fractures form an orthogonal network, with the primary set oriented SW-NE parallel to SH_{max} , and a secondary set oriented NW-SE parallel to Sh_{min} . Less frequent subvertical ENE-WSW transtensional fractures of oblique set 3 are oriented at approximately 20° to SH_{max} .
- Fracture intensity in mudrocks of the Upper Devonian Duvernay Formation varies in different lithofacies. The highest fracture intensity is observed in thinly bedded mudrocks of facies F3. This facies is characterized by alternating microlaminae of organic- and carbonate-rich mudrocks, intermediate stiffness and compressive and tensile strength compared to other facies.

- The natural fractures in the Duvernay Formation may have formed during the burial phases of the Antler (Late Devonian-Mississippian) and/or Laramide (Late Cretaceous to Paleocene) orogeny. Additionally, some fractures could have formed during the uplift and erosion in the Alberta Basin around 48 Ma.
- Analysis of drilling-induced fractures and borehole breakouts indicates a present-day strike-slip tectonic regime ($S_{Hmax} > S_v > S_{Hmin}$) in the Kaybob area, consistent with previous results and mechanisms of induced earthquakes. S_{Hmax} in analyzed wells A-C is oriented $N53^\circ-55^\circ$ with local rotation to $N70^\circ$ in well D, close to the Windfall reef.
- Natural fractures in the Upper Devonian Perdrix Formation of the Front Ranges are filled with calcite or open; horizontal, orthogonal to the bedding and vertical. They formed under the settings of SW-NE shortening during the Laramide orogeny, post-Eocene dextral strike-slip faulting, and late W-E extension during uplift and erosion. Fracture intensity in the Perdrix Formation is higher than in the Duvernay Formation due to more complex deformation.
- The study provides insights into the association of structural elements and phases of fracturing in the Duvernay and Perdrix Formations during different tectonic events.

In conclusion, the results obtained in this study provide new information on natural fractures in the Duvernay Formation, that can be used in fracture modeling, and have practical implications for enhancing exploration, drilling, and production practices in the source rock reservoir of the Alberta Basin. Recommendations for further studies, such as fluid inclusion analysis and U-Pb dating, are proposed to refine the understanding of P-T conditions and the timing of fracture development in the Upper Devonian organic-rich mudrocks in the Alberta Basin and the Front Ranges of the Canadian Rocky Mountains.

References

- Aadnøy, B.S. & Bell, J.S. (1998). Classification of Drilling-Induced Fractures and Their Relationship to in-Situ Stress Directions. *The Log Analyst*, 39, 27-42.
- Alabert, F. (1987). Stochastic imaging of spatial distributions using hard and soft information (Master's thesis). Stanford University, Stanford, CA.
- Allan, J. & Creaney, S. (1991). Oil families of the Western Canada Basin. *Bulletin of Canadian Petroleum Geology*, v. 39, p. 107-122.
- Ameen, M.S., MacPherson, K., Al-Marhoon, M.I., & Rahim Z. (2012). Diverse fracture properties and their impact on performance in conventional and tight-gas reservoirs, Saudi Arabia: the Unayzah, South Haradh case study Unayzah conventional and tight-gas fractures. *AAPG Bulletin* 96(3):459–492. <https://doi.org/10.1306/06011110148>
- Amthor, J. E., Mountjoy, E. W., & Machel, H. G. (1993). Subsurface dolomites in Upper Devonian Leduc Formation buildups, central part of Rimbey-Meadowbrook reef trend, Alberta, Canada. *Bulletin of Canadian Petroleum Geology*, 41(2), 164–185.
- Anderson, E.M. (1951). The dynamics of faulting and dike formation with application to Britain. Oliver and Boyd, 2nd Edition, Edinburgh, 133-147.
- Andrichuk, J.M. & Wonfor, J.S. (1954). Late Devonian geologic history in Stettler area, Alberta, Canada *Bulletin of American Association of Petroleum Geologists*, v. 38, p. 2500-2536.
- Andrichuk, J. M. (1958). Cooking lake and Duvernay (late devonian) sedimentation in Edmonton area of central Alberta, Canada. *AAPG Bulletin*, 42. <https://doi.org/10.1306/0bda5bb5-16bd-11d7-8645000102c1865d>
- Andrichuk, J. M. (1961). Stratigraphic evidence for tectonic and current control of Upper Devonian reef sedimentation, Duhamel Area, Alberta, Canada (Vol. 45, Issue 5). http://pubs.geoscienceworld.org/aapgbull/article-pdf/45/5/612/4687960/aapg_1961_0045_0005_0612.pdf
- Aoudia, K., Miskimins, J. L., Harris, N. B., & Cheryl A. M. (2010). Statistical Analysis of the Effects of Mineralogy On Rock Mechanical Properties of the Woodford Shale And the Associated Impacts For Hydraulic Fracture Treatment Design. Paper presented at the 44th U.S. Rock Mechanics Symposium and 5th U.S.-Canada Rock Mechanics Symposium, Salt Lake City, Utah, June 2010.

- Atkinson, L.A., Pawley, S.M., Andriashek, L.D., Hartman, G.M.D., Utting, D.J. & Atkinson, N. (2020): Sediment thickness of Alberta, version 2; Alberta Energy Regulator / Alberta Geological Survey, AER/AGS Map 611, scale 1:1 000 000.
- Aulbach, S., Griffin, W., Pearson, N. O'Reilly, S., Kivi, K., & Doyle, B. (2004). Mantle formation and evolution, Slave Craton: Constraints from HSE abundances and Re-Os isotope systematics of sulfide inclusions in mantle xenocrysts. *Chemical Geology*. 208. 61-88. 10.1016/j.chemgeo.2004.04.006.
- Babcock, E. A. (1978). Measurement of subsurface fractures from dipmeter logs. *American Association of Petroleum Geologists Bulletin*, v. 62, p. 111-1126.
- Barclay, J.E., Krause, F.F., Campbell, R.I. & Utting, J. (1990). Dynamic casting and growth faulting: Dawson Creek Graben Complex, Carboniferous-Permian Peace River Embayment, Western Canada. *Bulletin of Canadian Petroleum Geology*, v. 38A, p. 115-145.
- Barrett, K., (2014). The role of differential chemical compaction in the formation of the Gold Creek Collapse Structure, West Central Alberta. *Bulletin of Canadian Petroleum Geology*, 62(3), 132-156.
- Bahat, D., & Engelder, T. (1984). Surface Morphology of Joints of the Appalachian Plateau, New York and Pennsylvania, *Tectonophysics*, 104, 299-313.
- Bégin, N. & Veilleux, B. (2017). Effects of sedimentary facies on structural styles in the Canadian Rocky Mountain Fold and Thrust Belt: 2017 Meeting of the GSA Rocky Mountain Section: GSA Field Guide 48, p. 1-46. 10.1130/2017.0048(01).
- Bell, J. S., & Bachu, S. (2003). In situ stress magnitude and orientation estimates for Cretaceous coal-bearing strata beneath the plains area of central and southern Alberta. In *Bulletin of Canadian Petroleum Geology (Vol. 51, Issue 1)*.
<http://pubs.geoscienceworld.org/cspg/bcpg/article-pdf/51/1/1/3312160/1.pdf>
- Bell, J. S., & Grasby, S. E. (2012). The stress regime of the Western Canadian Sedimentary Basin. *Geofluids*, 12(2), 150–165. <https://doi.org/10.1111/j.1468-8123.2011.00349.x>
- Belyea, H.R. (1964). Upper Devonian, Part II - Woodbend, Winterburn and Wabamun Groups. In: Geological History of Western Canada. R.G. McCrossan and R.P. Glaister (eds.). Calgary, *Alberta Society of Petroleum Geologists*, p. 66-68.

- Berg, C. R. (2019), Methods for Estimating Fracture Abundance and Size From Borehole Observations, *Society of Petroleum Engineers*, preprint for the Reservoir Characterization Journal. <https://doi.org/10.2118/195583-PA>.
- Berg, C. R. (2021), The Theory for Estimating Fracture Density and Size from Borehole Data, ResearchGate.net, <http://dx.doi.org/10.13140/RG.2.2.29439.89769>.
- Berg, R. R., and A. F. Gangi, 1999, Primary migration by oilgeneration microfracturing in low-permeability source rocks: Application to the Austin Chalk, Texas: *AAPG Bulletin*, v. 83, p. 727–756.
- Blakey, R. (2013). North American paleogeographic maps. Paleogeography Library, Colorado Plateau Geosystems, Inc. Accessible online at <<http://www.cpgeosystems.com/nam.html>>(accessed 7 July 2013).
- Bond, G.C. & Kominz, M.A. (1991). Disentangling Middle Paleozoic sea level and tectonic events in cratonic margins and cratonic basins of North America. *Journal of Geophysical Research*, v. 96, p. 6619–6639
- Bons, P. D., Elburg, M. A., & Gomez-Rivas, E. (2012). A review of the formation of tectonic veins and their microstructures. *Journal of Structural Geology*, 43, 33–62. <https://doi.org/10.1016/j.jsg.2012.07.005>
- Bowers, G. L. (1995). Pore pressure estimation from velocity data: Accounting for overpressure mechanisms besides undercompaction. *SPE Drilling & Completion*, 10(02), 89–95. <https://doi.org/10.2118/27488-pa>
- Bowers, G. L. (2002). Detecting high overpressure. *The Leading Edge*, 21(2), 174–177. <https://doi.org/10.1190/1.1452608>
- Bratton, T., Canh, D.V., Que, N., Van Duc, N.V., Gillespie, P., Hunt, D., Li, B., Marcinew, R., Ray, S., Montaron, B., & Nelson, R. (2006). The nature of naturally fractured reservoirs. *Oilfield Rev* 18(2):4–23
- Budai, J. M., Martini, A. M., Walter, L. M., & Ku, T. C. W. (2002). Fracture-fill calcite as a record of microbial methanogenesis and fluid migration: A case study from the devonian Antrim shale, Michigan basin. *Geofluids* 2 (3), 163–183. doi:10.1046/j.1468-8123.2002.00036.x
- Burwash, R. A., McGregor, C. R. & Wilson, J. A. (1994). Precambrian basement beneath the Western Canada Sedimentary Basin. In G. D. Mossop and I. Shetsen (eds.), *Geological*

- Atlas of the Western Canada Sedimentary Basin, Published Jointly by the *Canadian Society of Petroleum Geologists* and the Alberta Research Council, Chapter 5, p. 49-56.
- Butler, R. W. H., Bond, C. E., Cooper, M. A., & Watkins, H. (2018). Interpreting structural geometry in fold-thrust belts: Why style matters. *Journal of Structural Geology*, *114*, 251–273. <https://doi.org/10.1016/j.jsg.2018.06.019>
- Campbell, G. (1946). New Albany shale. *Geological Society of America Bulletin*, *57* (9), 829–908.
- Chacko, T., De, K.S., Creaser, R.A., & Muehlenbachs, K. (2000). Tectonic setting of the Taltson magmatic zone at 1.9–2.0 Ga: a granitoid-based perspective: *Canadian Journal of Earth Sciences*, *37*, 1597–1609.
- Chaney, P. E. (1950). Abnormal pressure and lost circulation: *World Oil*, v. 130, p. 122–126.
- Chatterjee, S., & Mukherjee, S. (2023). Review on drilling-induced fractures in drill cores. *Marine and Petroleum Geology*, *151*, 106089. <https://doi.org/10.1016/j.marpetgeo.2022.106089>
- Chow, N., Wendte, J., & Stasiuk, L.D. (1995). Productivity versus preservation controls on two organic-rich carbonate facies in the Devonian of Alberta: sedimentological and organic petrological evidence. *Bulletin of Canadian Petroleum Geology* *43*, 433–460. <https://doi.org/10.35767/gscpgbull.43.4.433>.
- Covey, M.C., Vrolijk, P., & Pevear, D.R. (1994). Direct dating of fault movement in the Rocky Mountain front ranges of southern Alberta. *Geol. Soc. Am. Abstr. Programs*. 26. A467.
- Cooper, M. (1992). The analysis of fracture systems in subsurface thrust structures from the foothills of the Canadian Rockies. *Thrust Tectonics*, 391–405. https://doi.org/10.1007/978-94-011-3066-0_35
- Corlett, H., Schultz, R., Branscombe, P., Hauck, T., Haug, K., MacCormack, K., & Shipman, T. (2018). Subsurface faults inferred from reflection seismic, earthquakes, and sedimentological relationships: Implications for induced seismicity in Alberta, Canada. *Marine and Petroleum Geology*, *93*, 135–144. <https://doi.org/10.1016/j.marpetgeo.2018.03.008>
- Corrigan, D., Hajnal, Z., Németh, B. & Lucas, S.B. (2005). Tectonic framework of a Paleoproterozoic arc-continent to continent-continent collisional zone, Trans-Hudson

- Orogen, from geological and seismic reflection studies; *Canadian Journal of Earth Sciences*, v. 42, p. 421–434.
- Cox, J. W. (1970). The high resolution dipmeter reveals dip-related borehole and formation characteristics. Paper presented at 11th Annual Logging Symposium of the Society of Professional Well Log Analysts, Los Angeles, May 3-6, 1970.
- Coyle, P. (2011). Petrophysical analysis of natural fractures: Comparison to the rock mechanical properties and the potential effects on hydrocarbon formation, West Texas. Integrated Petroleum Geoscience (IPG) report, Department of Earth and Atmospheric Sciences, University of Alberta, AB, Canada.
- Creaney, S., Allan, J., Cole, K. S., Fowler, M. G., Brooks, P. W., Osadetz, K. G., & Riediger, C. L. (1994). Petroleum generation and migration in the Western Canada Sedimentary Basin. *Geological Atlas of the Western Canada Sedimentary Basin*, 31, 455–468.
- Cui, A., Brezovski, R., & Glover, K. (2013). Controls of Anisotropic In-situ Stress and Permeability in Optimization of Wells and Hydraulic Fractures for Unconventional Reservoirs: Examples from the Western Canada Sedimentary Basin. Paper presented at the 47th U.S. Rock Mechanics/Geomechanics Symposium, San Francisco, California.
- Currie, C. (2021). Wild Card - Natural Fractures in the Devonian Duvernay Formation, Western Canada Sedimentary Basin. CSPG Structural Division. Calgary Alberta.
- Currie, J. B., & Nwachukwu, S. O. (1974). Evidence on incipient fracture porosity in reservoir rocks at depth. *Bulletin of Canadian Petroleum Geology*, 22(1), 42-58.
- Cutright, B. (2011). The Transformation of Tight Shale Gas Reservoirs to Geothermal Energy Product. Washington, D.C; United States. Dept. of Energy. Office of Energy Efficiency and Renewable Energy.
- Dahlstrom, C.D. (1970). Structural geology in the eastern margin of the Canadian Rocky Mountains. *Bulletin of Canadian Petroleum Geology*, 18, 332-406.
- Davies, G. R., Hume, D., Fox, A., Haysom, S., Nevokshonoff, G., & Reinmiller, R. (2014). Core-Based Structural Fabrics in Mudstones of the WCSB: 'PSF' and Cleavage. In SPE/AAPG/SEG Unconventional Resources Technology Conference (pp. URTEC-1923429). URTEC.
- Davis, G.H. & Reynolds, S. (1996). *Structural Geology of Rocks and Regions*. Wiley.

- Dix, G. R. (1990). Stages of platform development in the Upper Devonian (Frasnian) Leduc Formation, Peace River Arch, Alberta. *Bulletin of Canadian Petroleum Geology*, 38(1), 66-92.
- Dong, T., Harris, N. B., Knapp, L. J., McMillan, J. M., & Bish, D. L. (2018). The effect of thermal maturity on geomechanical properties in shale reservoirs: An example from the Upper Devonian Duvernay Formation, Western Canada Sedimentary Basin. *Marine and Petroleum Geology*, 97, 137–153. <https://doi.org/10.1016/j.marpetgeo.2018.07.007>
- Douglas, R.J.W. (1956). Preliminary map 55-34, scale 1:63 360, Nordegg, Alberta; *Geological Survey of Canada*, Sheet 83 C-B.
- Douglas J. C. & Stockmal, G. S. (2011). The Alberta foreland basin: relationship between stratigraphy and Cordilleran terrane-accretion events. *Canadian Journal of Earth Sciences*. 26(10): 1964-1975.
- Duggan, J. P., Mountjoy, E. W., & Stasiuk, L. D. (2001). Fault-controlled dolomitization at Swan Hills Simonette oil field (Devonian), deep basin west-central Alberta, Canada. *Sedimentology*, 48(2), 301–323. <https://doi.org/10.1046/j.1365-3091.2001.00364.x>
- Dunn, L. A., Schmidt, G., Hammermaster, K., Brown, M., Bernard, R., Wen, E., Befus, R., & Gardiner, S. (2012). The Duvernay Formation (Devonian): Sedimentology and Reservoir Characterization of a Shale Gas/Liquids play in Alberta, Canada. *Canadian Society of Petroleum Geologists Annual Core Convention program with abstracts*, May 2012.
- Dunn, L. A., & Humenjuk, J. A. (2014). Fifty Shades Darker: Integrating Sedimentology, Sequence Stratigraphy, Chemostratigraphy and Geophysics to Identify Sweet Spots the Liquids-Rich Duvernay Shale Play, Kaybob Alberta. In FOCUS-Adapt.
- Durney, D. (1973). Incremental strains measured by syntectonic crystal growths. Gravity and tectonics, 67–96.
- Eaton, D. W., & Mahani, A. B. (2015). Focal mechanisms of some inferred induced earthquakes in Alberta, Canada. *Seismological Research Letters*, 86(4), 1078–1085. <https://doi.org/10.1785/0220150066>
- Eaton, D.W. & Schultz, R. (2018). Increased likelihood of induced seismicity in highly overpressured shale formations, *Geophys. J. Int.*, 214, 751–757, Oxford University Press.
- Eaton, D. W., Igonin, N., Poulin, A., Weir, R., Zhang, H., Pellegrino, S., & Rodriguez, G. (2018). Induced seismicity characterization during hydraulic-fracture monitoring with a

- shallow-wellbore geophone array and broadband sensors. *Seismological Research Letters*, 89(5), 1641–1651. <https://doi.org/10.1785/0220180055>
- Eliyahu, M., Emmanuel, S., Day-Stirrat, R. J., & Macaulay, C. I. (2015). Mechanical properties of organic matter in shales mapped at the nanometer scale. *Marine and Petroleum Geology*, 59, 294-304.
- Emmanuel, S., Eliyahu, M., Day-Stirrat, R. J., Hofmann, R., & Macaulay, C. I. (2016). Impact of thermal maturation on nano-scale elastic properties of organic matter in shales. *Marine and Petroleum Geology*, 70, 175-184.
- Engelder, T. (1985). Loading paths to joint propagation during a tectonic cycle: An example from the Appalachian Plateau, U.S.A. *Journal of Structural Geology*, 7(3–4), 459–476. [https://doi.org/10.1016/0191-8141\(85\)90049-5](https://doi.org/10.1016/0191-8141(85)90049-5)
- Engelder, T. (2004). Tectonic implications drawn from differences in the surface morphology on two joint sets in the Appalachian Valley and Ridge, Virginia. *Geology*, 32(5), 413. <https://doi.org/10.1130/g20216.1>
- Engelder, T., & Gross, M. R. (1993). Curving cross joints and the lithospheric stress field in eastern North America. *Geology*, 21(9), 817.
- English, J. M. & Johnston, S. T. (2004). The Laramide Orogeny: What Were the Driving Forces?, *International Geology Review*, 46:9, 833-838, DOI: 10.2747/0020-6814.46.9.833
- English J. M. (2012). Thermomechanical origin of regional fracture systems: *AAPG Bulletin*, v. 96, no. 9, p. 1597–1625, doi: <https://doi.org/10.1306/01021211018>.
- Faskhoodi, M., Damani, A., Kanneganti, K., Zaluski, W., Ibelegbu, C., Qiuguo, L., Xu, C., Mukisa, H., Ali Lahmar, H., Andjelkovic, D., Perez Michi, O., Zhmodik, A., Rivero, J. A., & Ameuri, R. (2020). Unlocking unconventional reservoir for optimum production through integrated multi-disciplinary approach - A case study. Paper presented at the SPE Europec, Virtual, December 2020. doi: <https://doi.org/10.2118/200531-MS>
- Ferri, F., Hickin, A.S. & Huntley, D.H. (2011): Besa River Formation, western Liard Basin, British Columbia (NTS 094N): geochemistry and regional correlations; in *Geoscience Reports 2011*, British Columbia Ministry of Energy and Mines, pages 1–18.
- Ferrill, D. A., McGinnis, R. N., Morris, A. P., Smart, K. J., Sickmann, Z. T., Bentz, M., & Evans, M. A. (2014). Control of mechanical stratigraphy on bed-restricted jointing and normal faulting: Eagle Ford Formation, south-central Texas. *AAPG Bulletin*, 98(11), 2477-2506.

- Ferrill, D. A., Morris, A. P., McGinnis, R. N., Smart, K. J., Wigginton, S. S., & Hill, N. J. (2017). Mechanical stratigraphy and normal faulting. *Journal of Structural Geology*, *94*, 275–302. <https://doi.org/10.1016/j.jsg.2016.11.010>
- Ferrill, D. A., Smart, K. J., Evans, M. A., Cawood, A. J., Morris, A. P., Lehrmann, D. J., & McGinnis, R. N. (2022). Contractional fold amplification through bed-parallel gypsum vein (“beef”) formation. *Journal of Structural Geology*, *156*, 104532. <https://doi.org/10.1016/j.jsg.2022.104532>
- Finley, T. (2020). Fault-Hosted Geothermal Systems in Southeastern British Columbia, University of Alberta.
- Fjaer, E. (2019). Relations between static and dynamic moduli of sedimentary rocks. *Geophysical Prospecting*, *67(1)*, 128–139. <https://doi.org/10.1111/1365-2478.12711>
- Fothergill, P., Boskovic, D., Schoellkopf, N., Murphy, P., & Mukati, M. A. (2014). Regional modelling of the late devonian duvernay formation, western Alberta, Canada. *Society of Petroleum Engineers - SPE/AAPG/SEG Unconventional Resources Technology Conference*. <https://doi.org/10.15530/urtec-2014-1923935>
- Fox A. D., & Soltanzadeh, M. (2015). A Regional Geomechanical Study of the Duvernay Formation in Alberta, Canada. GeoConvention 2015, Calgary, AB, Canada.
- Fu, X., Gong, L., Su, X., Liu, B., Gao, S., Yang, J., & Qin, X. (2022). Characteristics and Controlling Factors of Natural Fractures in Continental Tight-Oil Shale Reservoir. *Minerals*, *12(12)*, 1616. <https://doi.org/10.3390/min12121616>
- Gabrielse, H. & Yorath, C. J. (1989). DNAG #4. The Cordilleran Orogen in Canada. *Geoscience Canada*, *16(2)*, 67–83.
- Gale, J.F.W., Laubach, S.E. Olson, J.E., Eichhubl, P. & Fall, A. (2014). Natural fractures in shale: A review and new observations. *AAPG Bulletin*, v. 98, no. 11, p. 2165-2216.
- Galvis Portilla, H. A. (2022). Sedimentology, stratigraphy, and reservoir characterization of the late Devonian Duvernay Formation of the East Shale Basin: an integrated outcrop and subsurface study (Doctoral thesis, University of Calgary, Calgary, Canada). Retrieved from <https://prism.ucalgary.ca>.
- Gasparrini, M., Lacombe, O., Rohais, S., Belkacemi, M., & Euzen, T. (2021). Natural mineralized fractures from the Montney-Doig unconventional reservoirs (Western Canada

- sedimentary basin): Timing and controlling factors. *Marine and Petroleum Geology*, 124, 104826. <https://doi.org/10.1016/j.marpetgeo.2020.104826>
- Gibbs, A. D. (1984). Structural evolution of extensional basin margins. *Journal of the Geological Society*, 141(4), 609–620. <https://doi.org/10.1144/gsjgs.141.4.0609>
- Glover, P.W., & Bormann, P. (2007). The characterization of trough and planar cross-bedding from borehole image logs. *Journal of Applied Geophysics*, 62, 178-191.
- Green, D. G. & Mountjoy, E. (2005). Fault and conduit controlled burial dolomitization of the Devonian west-central Alberta Deep Basin. *Bulletin of Canadian Petroleum Geology*, 53(2), 101–129. <https://doi.org/10.2113/53.2.101>
- Haimson B.C., & Song I. (1993). A laboratory study of borehole breakouts in Cordova Cream: a case of shear failure mechanism. *Int. J. Rock Mech. Min. Sci.*, 30:7, 1047-1056.
- Hajnal, Z., Lewry, J., White, D., Ashton, K., Clowes, R., Stauffer, M., Gyorfi, I. & Takacs, E. (2005). The Sask Craton and Hearne Province margin: seismic reflection studies in the western Trans-Hudson Orogen; *Canadian Journal of Earth Sciences*, v. 42, p. 403–419.
- Hamilton, W. N., Langerberg, C. W., Price, M. C. & Chao, D. K., comp., (1999). Geological map of Alberta, Alberta Energy and Utilities Board, EUB/AGS Map 236, scale 1:1000000.
- Haq, B. U., & Schutter, S. R. (2008). A Chronology of Paleozoic Sea-Level Changes. www.sciencemag.org
- Harris, N. B., McMillan, J. M., Knapp, L. J., & Mastalerz, M. (2018). Organic matter accumulation in the Upper Devonian Duvernay Formation, Western Canada Sedimentary Basin, from sequence stratigraphic analysis and geochemical proxies. *Sedimentary Geology*, 376, 185–203. <https://doi.org/10.1016/j.sedgeo.2018.09.004>
- Hart, B. S., Marfurt, K. J., Varban, B. L., & Plint, A. G. (2007). Blind thrusts and fault-related folds in the Upper Cretaceous Alberta Group, Deep Basin, west-central Alberta: Implications for fractured reservoirs. *Bulletin of Canadian Petroleum Geology*, 55(2), 125–137. <https://doi.org/10.2113/gscpgbull.55.2.125>
- Hayes, B. J. R., Christopher, J. E., Rosenthal, L., Los, G., McKercher, B., Minken, D., & Smith, D. G. (1994). Cretaceous Mannville Group of the western Canada sedimentary basin. *Geological Atlas of the Western Canada sedimentary basin*, 4, 317-334.

- Hazra, B., Vishal, V., Sethi, C., & Chandra, D. (2022). Impact of supercritical CO₂ on shale reservoirs and its implication for CO₂ sequestration. *Energy & Fuels*, 36(17), 9882–9903. <https://doi.org/10.1021/acs.energyfuels.2c01894>
- Hedberg, H. D. (1974). Relation of methane generation to undercompacted shales, shale diapirs, and mud volcanics: *AAPG Bulletin*, v. 58, p. 661–673
- Heidbach, O., Tingay, M., Barth, A., Reinecker, J., Kurfeß, D., & Müller, B. (2010). Global crustal stress pattern based on the World Stress Map database release 2008. *Tectonophysics*, 482(1-4), 3-15. <https://doi.org/10.1016/j.tecto.2009.07.023>
- Helgeson, D. E. & Aydin, A. (1991). Characteristics of joint propagation across layer interfaces in sedimentary rocks. *Journal of Structural Geology*, 13(8), 897–911. [https://doi.org/10.1016/0191-8141\(91\)90085-w](https://doi.org/10.1016/0191-8141(91)90085-w)
- Hooker, J. N., Cartwright, J., Stephenson, B., Silver, C. R. P., Dickson, A. J., & Hsieh, Y.-T. (2017). Fluid evolution in fracturing black shales, Appalachian Basin. *AAPG Bulletin*, 101(08), 1203–1238. <https://doi.org/10.1306/10031616030>
- Hope, J., Eaton, D., & Ross, G. (1999). Lithoprobe seismic transect of the Alberta Basin: Compilation and overview. *Bulletin of Canadian Petroleum Geology*. 47.
- Hopkins, J.C. (1972). Petrography and distribution and diagenesis of foreslope and basin sediments. Miette and Ancient Wall carbonate complexes, (Devonian), Alberta. [Ph.D. Thesis]; McGill University, Montreal, Canada, 234-p
- Huang, Q., & Angelier, J. (1989). Fracture spacing and its relation to bed thickness. *Geological Magazine*, 126(4), 355-362. doi:10.1017/S0016756800006555
- Hyman, J. D., Jiménez-Martínez, J., Viswanathan, H. S., Carey, J. W., Porter, M. L., Rougier, E., Karra, S., Kang, Q., Frash, L., Chen, L., Lei, Z., O'Malley, D., & Makedonska, N. (2016). Understanding hydraulic fracturing: A multi-scale problem. *Philosophical Transactions of the Royal Society A: Mathematical, Physical and Engineering Sciences*, 374(2078), 20150426. <https://doi.org/10.1098/rsta.2015.0426>
- Issler, D.R., Beaumont, C., Willett, S.D., Donelick, R.A. & Grist, A.M. (1999). Paleotemperature history of two transects across the Western Canada Sedimentary Basin: constraints from apatite fission track analysis, *Bull. Can. Pet. Geol.*, 47, 475–486.
- Jaeger, J. C. & Cook, N. G. W. (1976). Fundamentals of rock mechanics. 2nd ed. London: Chapman and Hall, 585p.

- Jamison, W. R. (2016). Fracture system evolution within the Cardium Sandstone, central Alberta foothills folds. *AAPG Bulletin*, 100(07), 1099–1134. <https://doi.org/10.1306/03011515082>
- Johnson, J. G., & Klapper, G. (1985). Devonian eustatic fluctuations in Euramerica. <http://pubs.geoscienceworld.org/gsa/gsabulletin/article-pdf/96/5/567/3419349/i0016-7606-96-5-567.pdf>
- Jones, P. B., & Workum, R. H. (1978). Geological Guide to the central foothills and Rocky Mountains of Alberta; *Canadian Society of Petroleum Geologists*, 61p.
- Kalkreuth, W., & McMechan, M. (1988). Burial history and thermal maturity, Rocky Mountain Front Ranges, Foothills, and Foreland, east-central British Columbia and adjacent Alberta, Canada, *Am. Assoc. Pet. Geol. Bull.*, 72, 1395–1410.
- Kalkreuth, W., & McMechan, M. (1996): Coal rank and burial history of Cretaceous–Tertiary strata in the Grande Cache and Hinton areas, Alberta, Canada: implications for fossil fuel exploration; *Canadian Journal of Earth Sciences*, v. 33, p. 938–957, doi:10.1139/e96-071
- Kao, H., Hyndman, R., Jiang, Y., Visser, R., Smith, B., Babaie Mahani, A., Leonard, L., Ghofrani, H., & He, J. (2018). Induced seismicity in Western Canada linked to tectonic strain rate: Implications for regional seismic hazard. *Geophysical Research Letters*, 45(20). <https://doi.org/10.1029/2018gl079288>
- Khoshbakht, F., Azizzadeh, M., Memarian, H., Nourozi, G.H., & Moallemi, S.A. (2012a) Comparison of electrical image log with core in a fractured carbonate reservoir. *J Pet Sci Eng* 86:289–296.
- Kienan, M., Salvage, R., & Eaton, D., (2021). Investigating sources of induced seismicity in west-central Alberta. GACMAC 2021, London, Ontario.
- Knapp, L. J. (2016). Controls on organic-rich mudstone deposition: the Devonian Duvernay Formation, Alberta, Canada.
- Knapp, L. J., McMillan, J. M., & Harris, N. B. (2017). A depositional model for organic-rich Duvernay Formation mudstones. *Sedimentary Geology*, 347, 160-182.
- Knapp, L. J., Harris, N. B., & McMillan, J. M. (2019). A sequence stratigraphic model for the organic-rich Upper Devonian Duvernay Formation, Alberta, Canada. *Sedimentary Geology*, 387, 152–181. <https://doi.org/10.1016/j.sedgeo.2019.04.008>
- Konstantinovskaya, E., & Bahramiyarahmadi, A. (2020). Fracture systems in the Perdrix Formation and Devonian carbonates, Roche Miette, Jasper National Park: evidences of

- thrust-related deformation and implications for fluid migration. Geoconvention 2020, Virtual Event.
- Konstantinovskaya, E., Li, Q., Zhmodik, A., Ibelegbu, C., Schultz, R., & Shipman, T. (2021). Lateral fluid propagation and strike slip fault reactivation related to hydraulic fracturing and induced seismicity in the Duvernay Formation, Fox Creek area, Alberta. *Geophysical Journal International*, 227(1), 518–543. <https://doi.org/10.1093/gji/ggab234>
- Kosari, E., Kadkhodaie, A., Bahroudi, A., Chehrazi, A., & Talebian, M. (2017) An integrated approach to study the impact of fractures distribution on the Ilam-Sarvak carbonate reservoirs: a case study from the Strait of Hormuz, the Persian Gulf. *J. Petrol. Sci. Eng.* 152:104–115
- Kulander, B. R., Dean, S. L., & Ward, B. J. (1990). Fractured Core Analysis: Interpretation, Logging, and Use of Natural and Induced Fractures in Core. <https://doi.org/10.1306/mth8516>
- Kuypers, M. M., Pancost, R. D., Nijenhuis, I. A., & Sinninghe Damsté, J. S. (2002). Enhanced productivity led to increased organic carbon burial in the euxinic North Atlantic basin during the late Cenomanian oceanic anoxic event. *Paleoceanography*, 17(4), 3-1.
- Labani, M. M., & Rezaee, R. (2015). The importance of geochemical parameters and shale composition on rock mechanical properties of gas shale reservoirs: A case study from the Kockatea Shale and Carynginia Formation from the Perth Basin, Western Australia. *Rock Mechanics and Rock Engineering*, 48(3), 1249-1257.
- Ladeira, F. L., & Price, N. J. (1981). Relationship between fracture spacing and bed thickness. *Journal of Structural Geology*, 3(2), 179–183. [https://doi.org/10.1016/0191-8141\(81\)90013-4](https://doi.org/10.1016/0191-8141(81)90013-4)
- Laflamme, A. K. (1990). Replacement dolomitization in the Upper Devonian Leduc and Swan Hills Formations, Caroline area, Alberta, Canada, (master's thesis), McGill University, Montreal, Canada.
- Lahann, R. (2002). Impact of smectite diagenesis on compaction modeling and compaction equilibrium. A.R. Huffman, G.L. Bowers (Eds.), *Pressure Regimes in Sedimentary Basins and Their Prediction*, AAPG, Tulsa (2002), pp. 61-72

- Lahann, R. W., & Swarbrick, R. E. (2011). Overpressure generation by load transfer following shale framework weakening due to smectite diagenesis. *Geofluids*, *11*(4), 362–375.
<https://doi.org/10.1111/j.1468-8123.2011.00350.x>
- Lai, J., Wang, G., Fan, Z., Wang, Z., Chen, J., Zhou, Z., Wang, S., & Xiao, C. (2017). Fracture detection in oil-based drilling mud using a combination of borehole image and sonic logs. *Mar. Pet. Geol.* *84*:195–214.
- Langenberg, C.W. & Erdmer, P. (1992). Field guide to the structural geology of the Nordegg area, Alberta; Alberta Research Council, ARC/AGS Open File Report 1992-23, 15 p
- Langenberg, C. W., Beaton, A., & Berhane, H., (2002). Regional evaluation of the coalbed methane potential of the foothills/mountains of Alberta, 2d ed.: Energy and Utility Board/Alberta Geological Survey Earth Science Report 2002-05 , 90 p.
- Lash, G., Loewy, S., & Engelder, T., (2004). Preferential jointing of Upper Devonian black shale, Appalachian Plateau, U.S.A.: evidence supporting hydrocarbon generation as a joint-driving mechanism, in Rogers, C. M., and Engelder, T. (eds.). The initiation, propagation, and arrest of joints and other fractures: Geological Society Special Publication 231, London, pp. 129151.
- Lash, G. G., & Blood, D. R. (2006). The Upper Devonian Rhinestreet black shale of western New York state—Evolution of a hydrocarbon system. In New York State Geological Association, 78th Annual Meeting Guidebook, University of Buffalo, 223–289.
- Leckie, D. A. & Smith, D. G. (1992). Regional setting, evolution, and depositional cycles of the western Canada foreland basin. *Foreland Basins and Fold Belts*.
<https://doi.org/10.1306/m55563c2>
- Lemieux, S. (1999). Seismic Reflection Expression and Tectonic Significance of Late Cretaceous Extensional Faulting of the Western Canada Sedimentary Basin in Southern Alberta. *Bulletin of Canadian Petroleum Geology*, *47*, 375-390.
- Li, Y., & Schmitt, D. R. (1998). Drilling-induced core fractures and in situ stress. *Journal of Geophysical Research: Solid Earth*, *103*(B3), 5225–5239.
<https://doi.org/10.1029/97jb02333>
- Li, T., Gu, Y. J., Wang, J., Wang, R., Yusifbayov, J., Canales, M. R., & Shipman, T. (2021). Earthquakes induced by wastewater disposal near Musreau Lake, Alberta, 2018–2020. *Seismological Research Letters*, *93*(2A), 727–738. <https://doi.org/10.1785/0220210139>

- Li, Q., Konstantinovskaya, E., Zhmodik, A., & Ibelegbu, C. (2023). Interaction of natural and hydraulic fractures: The impact on reservoir pressure buildup and risk of shear fault reactivation in the Upper Devonian Duvernay Formation, Fox Creek, Alberta. *Geomechanics and Geophysics for Geo-Energy and Geo-Resources*, 9(1). <https://doi.org/10.1007/s40948-023-00537-z>
- Liao, Z., Wu, M., Chen, X., & Zou, H. (2020). Fracture mechanical properties of carbonate and evaporite caprocks in Sichuan Basin, China with implications for reservoir seal integrity. *Marine and Petroleum Geology*, 119, 104468. <https://doi.org/10.1016/j.marpetgeo.2020.104468>
- Long, J. J., Jones, R. R., Oxlade, D. M., Daniels, S. E., & Gilment, S. R. (2019). Multiscale fracture length analysis in carbonate reservoir units, Kurdistan, ne iraq. *Petroleum Geoscience*, 25(4), 429–442. <https://doi.org/10.1144/petgeo2018-168>
- Lorenz, J.C., Finley, S.J., & Warpinski, N.R. (1990). Significance of coring-induced fractures in Mesaverde core, northwestern Colorado: American Association of Petroleum Geologists Bulletin, 74, 1017–1029.
- Lorenz, J. C., & Cooper, S. P. (2018a). Atlas of natural and induced fractures in Core. Wiley Blackwell.
- Luczaj, J. A. & Goldstein, R. H. (2000). Diagenesis of the lower Permian Krider Member, southwest Kansas: fluid inclusion, UPb, and fission-track evidence for reflux dolomitization during latest Permian time. *J. Sed. Res.* 70, 762-773.
- Lund Snee, J.E., & Zoback, M.D. (2018). State of stress in the Permian Basin, Texas and New Mexico: implications for induced seismicity. *Lead. Edge* 37 (2), 127–134.
- Lund Snee, J.E. & Zoback, M.D. (2020). Multiscale variations of the crustal stress field throughout North America, *Nat. Commun.*, 11, 1–9, Springer US.
- Luo, X. & Vasseur, G., (1996). Geopressuring mechanism of organic matter cracking: numerical modeling, *AAPG Bull.*, 80(6), 856–873.
- Lyster, S., Corlett, H.J. & Berhane, H. (2017). Hydrocarbon resource potential of the Duvernay Formation in Alberta – update, Alberta Energy Regul./Alberta Geol. Surv. Open File Rep., 2017-02. Retrieved from http://ags.aer.ca/OFR_2017_02.html

- Lyu, W., Zeng, L., Liu, Z., Liu, G., & Zu, K. (2016). Fracture responses of conventional logs in tight-oil sandstones: a case study of the upper triassic Yanchang formation in southwest Ordos Basin, China. *AAPG Bull* 100(9):1399–1417. <https://doi.org/10.1306/04041615129>
- Ma, C., Elsworth, D., Dong, C., Lin, C., Luan, G., Chen, B., Liu, X., Muhammad, J. M., Muhammad, A. Z., Shen, Z., & Tian, F. (2017). Controls of hydrocarbon generation on the development of expulsion fractures in organic-rich shale: Based on the Paleogene Shahejie Formation in the Jiyang Depression, Bohai Bay Basin, East China. *Marine and Petroleum Geology*, 86, 1406–1416. <https://doi.org/10.1016/j.marpetgeo.2017.07.035>
- MacKay, M. K., Eaton, D. W., Pedersen, P. K., & Clarkson, C. R. (2018). Integration of outcrop, subsurface, and microseismic interpretation for rock-mass characterization: An example from the Duvernay Formation, Western Canada. *Interpretation*, 6(4), T919–T936. <https://doi.org/10.1190/INT-2017-0156.1>
- Mackenzie, W.S. & Mountjoy, E.W. (1973). Stratigraphy of the southern part of the Devonian ancient wall carbonate complex, Jasper National Park, Alberta; *Geological Survey of Canada*, Paper 72-20, 121 p.
- Magara, K. (1978) *Compaction and Fluid Migration: Practical Petroleum Geology*. Elsevier Scientific Publication.
- Markou, N., & Papanastasiou, P. (2018). Petroleum geomechanics modelling in the Eastern Mediterranean basin: Analysis and application of fault stress mechanics. *Oil & Gas Science and Technology*. 73. 57. [10.2516/ogst/2018034](https://doi.org/10.2516/ogst/2018034).
- Marquez, X. M., and E. W. Mountjoy, (1996). Microcracks due to overpressures caused by thermal cracking in well-sealed Upper Devonian reservoirs, deep Alberta basin: *AAPG Bulletin*, v. 80, p. 570–588.
- Mauldon, M., Dunne, W. M., & Rohrbaugh, M. B. (2001). Circular scanlines and circular windows: New tools for characterizing the geometry of Fracture Traces. *Journal of Structural Geology*, 23(2–3), 247–258. [https://doi.org/10.1016/s0191-8141\(00\)00094-8](https://doi.org/10.1016/s0191-8141(00)00094-8).
- Mazdarani, A., Kadkhodaie, A., & Wood, D.A. (2023). Natural fractures characterization by integration of FMI logs, well logs and core data: a case study from the Sarvak Formation (Iran). *J Petrol Explor Prod Technol* 13, 1247–1263. <https://doi.org/10.1007/s13202-023-01611-8>

- Mba, K., & Prasad, M. (2010). Mineralogy and its contribution to anisotropy and kerogen stiffness variations with maturity in the Bakken Shales. In SEG International Exposition and Annual Meeting (pp. SEG-2010). SEG.
- McCrossan, R. G. (1961). Resistivity mapping and Petrophysical Study of Upper Devonian Inter-reef calcareous shales of central Alberta, Canada. *AAPG Bulletin*, 45. <https://doi.org/10.1306/bc74366b-16be-11d7-8645000102c1865d>
- McLaren, D.J., (1955). Devonian formations in the Alberta Rocky Mountains between Bow and Athabasca rivers; *Geological Survey of Canada*, Bulletin 35.
- McLean, D., & Mountjoy, E. (1993). Upper devonian buildup-margin and slope development in the southern Canadian Rocky Mountains. *Geological Society of America Bulletin*, 105(10), 1263–1283. [https://doi.org/10.1130/00167606\(1993\)105<1263:udbmas>2.3.co;2](https://doi.org/10.1130/00167606(1993)105<1263:udbmas>2.3.co;2).
- McLellan, P. (1989). In - Situ Stress Magnitudes from Hydraulic Fracturing Treatment Records: A Feasibility Study. <https://doi.org/10.4095/130531>
- Michaelis, L., & Menten, M. L. (1913). Die kinetik der invertinwirkung. *Biochem. z*, 49(333-369), 352.
- Milad B., & Slatt R. (2018) Impact of lithofacies variations and structural changes on natural fracture distributions. Interpretation. <https://doi.org/10.1190/int-2017-0138.1>
- Monger, J., & Price (2002). The Canadian Cordillera: Geology and tectonic evolution, *CSEG Recorder* 27, no. 2, 17–36.
- Morris, A., Ferrill, D. A., & Brent Henderson, D. B. (1996). Slip-tendency analysis and fault reactivation. *Geology*, 24(3), 275. [https://doi.org/10.1130/0091-7613\(1996\)024<275:staafr>2.3.co;2](https://doi.org/10.1130/0091-7613(1996)024<275:staafr>2.3.co;2)
- Mottram, C. M., Kellett, D. A., Barresi, T., Zwingmann, H., Friend, M., Todd, A., & Percival, J. B. (2020). Syncing fault rock clocks: Direct comparison of U-Pb carbonate and k-ar illite fault dating methods. *Geology*, 48(12), 1179–1183. <https://doi.org/10.1130/g47778.1>
- Mountjoy, E.W. & Price, R.A. (1974). Geology, Whiterabbit Creek (west half), west of fifth meridian, Alberta; *Geological Survey of Canada*, “A” Series Map 1389A, scale 1:50 000.
- Mountjoy, E. W., & Halim-Dihardja, M. K. (1991). Multiple phase fracture and fault-controlled burial dolomitization, Upper Devonian Wabamun Group, Alberta. *Journal of Sedimentary Research*, 61(4), 590–612. <https://doi.org/10.1306/D426776C-2B26-11D7-8648000102C1865D>

- Murray, G. H., (1968). Quantitative fracture study—Sanish pool, McKenzie County, North Dakota: *AAPG Bulletin*, v. 52, p. 57–65.
- Narr, W., & Suppe, J. (1991). Joint spacing in Sedimentary Rocks. *Journal of Structural Geology*, 13(9), 1037–1048. [https://doi.org/10.1016/0191-8141\(91\)90055-n](https://doi.org/10.1016/0191-8141(91)90055-n)
- Narr, W., & Currie, J. B. (1982). Origin of fracture porosity—example from Altamont field, Utah. *AAPG Bulletin*, 66(9), 1231-1247.
- Narr, W. (1996). Estimating Average Fracture Spacing in Subsurface Rock. *AAPG Bull.* 80 (10): 1565–1586. <https://doi.org/10.1306/64EDA0B4-1724-11D7-8645000102C1865D>.
- Nelson R. A. (2001) Geologic analysis of naturally fractured reservoirs. Gulf Professional Publishing, Houston, 332 p.
- Nelson, J.L., Paradis. S., Christensen, J., & Gabites, J. (2002). Canadian cordilleran Mississippi Valley-type deposits: a case for Devonian-Mississippian backarc hydrothermal origin. *Economic Geology*, 93, 184-200.
- Nelson, R. A. (2020). Static Conceptual Fracture Modeling: Preparing for Simulation and Development. John Wiley & Sons Ltd. 183 p.
- Nesteroff, W. D., & VI, F. (1973). 23. Petrography and mineralogy of sapropels. In Initial Reports of the Deep Sea Drilling Project: A Project Planned by and Carried Out with the Advice of the Joint Oceanographic Institutions for Deep Earth Sampling (Vol. 13, p. 713).
- Nie, X., Zou, C., Pan, L., Huang, Z., & Liu, D. (2013). Fracture analysis and determination of in-situ stress direction from resistivity and acoustic image logs and core data in the Wenchuan earthquake fault scientific drilling borehole-2(50–1370 m). *Tectonophysics* 593:161–171. <https://doi.org/10.1016/j.tecto.2013.03.005>
- Nurkowski, J.R. (1984). Coal quality, coal rank variation and its relation to reconstructed overburden, Upper Cretaceous and Tertiary plains coals, Alberta, Canada. *American Association of Petroleum Geologists, Bulletin*, v. 68, p. 285-295
- Oldale, H. S., Munday, R. J., & Ma, K. (1994). Devonian Beaverhill Lake Group of the western Canada sedimentary basin. In Geological Atlas of the Western Canada Sedimentary Basin (Vol. 4). Calgary, AB: Canadian Society of Petroleum Geologists and Alberta Research Council.
- Oliver, T.A., & Cowper, N.W. (1965). Depositional Environments of Ireton Formation, Central Alberta. *AAPG Bulletin*, 49, 1410-1425.

- Ozkaya, I., (1988). A simple analysis of oil-induced fracturing in sedimentary rocks: *Marine and Petroleum Geology*, v. 5,no. 3, p. 293–297, doi:10.1016/0264-8172(88)90008-6.
- Pana, D., Waters, J., & Grobe, M. (2001). GIS compilation of structural elements in northern Alberta. Alberta Geological Survey. Earth Sciences Report, 1, 53.
- Pana, D.I., & Elgr, R. (2013). Geology of the Alberta Rocky Mountains and Foothills: Energy Resources Conservation Board, ERCB/AGS Map 560, scale 1:500,000, 1 sheet.
- Pana, D. (2021). $^{40}\text{Ar}/^{39}\text{Ar}$ dating of phyllonite in the southern Rocky Mountain Trench and adjacent Rocky Mountains unravels kinematic links between the Omineca and Foreland belts of the southern Canadian Cordillera: *The Journal of Geology*, v. 129, p. 255–281, <https://doi.org/10.1086/715243>.
- Pana, D.I., Elgr, R., Waters, E.J., Warren, J.E., Weiss, J.A., Lopez, G.P. & Pawlowicz, J.G. (2021): Structural elements in the Alberta Plains; Alberta Energy Regulator / Alberta Geological Survey, AER/AGS Open File Report 2021-01, 33 p.
- Parrish, J.T., & Curtis, R.L. (1982). Atmospheric circulation, upwelling, and organic-rich rocks in the Mesozoic and Cenozoic eras. *Palaeogeography, Palaeoclimatology, Palaeoecology*, 40, 31-66.
- Parrish, J. T., Droser, M. L., & Bottjer, D. J. (2001). A Triassic upwelling zone: the Shublik formation, Arctic Alaska, USA. *Journal of Sedimentary Research*, 71(2), 272-285.
- Passchier, C. W., & Trouw, R. A. (2005). *J: Microtectonics*. Springer-Verlag Berlin Heidelberg. 372 p.
- Peacock, D. C. P., Nixon, C. W., Rotevatn, A., Sanderson, D. J., & Zuluaga, L. F. (2016). Glossary of fault and other Fracture Networks. *Journal of Structural Geology*, 92, 12–29. <https://doi.org/10.1016/j.jsg.2016.09.008>
- Pedersen, T., & Calvert, S. (1990). Anoxia vs. productivity: what controls the formation of organic- carbon-rich sediments and sedimentary rocks? *American Association of Petroleum Geologists Bulletin*. 74. 454-466. 10.1306/0C9B232B-1710-11D7-8645000102C1865D.
- Philipp, S. L., Afşar, F., & Gudmundsson, A. (2013). Effects of mechanical layering on hydrofracture emplacement and fluid transport in reservoirs. *Frontiers in Earth Science*, 1, 4.
- Plumb, R.A. (1994). Influence of composition and texture on the failure properties of clastic rocks, Paper presented at the Rock Mechanics in Petroleum Engineering, Delft,

- Netherlands, August 1994. Paper Number: SPE-28022-MS, doi:10.2118/28022-MS, pp. 13–20.
- Pollock, C. A. (2011). Reference section for the Majeau Lake Formation. *Canadian Journal of Earth Sciences*. 4(5): 873-876. <https://doi.org/10.1139/e67-060>
- Preston, A., Garner, G., & Beavis, K. (2016). Duvernay Reserves and Resources Report: A Comprehensive Analysis of Alberta's Foremost Liquids-Rich Shale Resource. Edmonton, Alberta.
- Price, R. A., & Mountjoy, E. W. (1970). Geologic structure of the Canadian Rocky Mountains between Bow and Athabasca Rivers—A progress report: Geological Association of Canada Special Paper 6.
- Price, R. A. (1973). Large-scale gravitational flow of supracrustal rocks, southern Canadian Rockies. In: Gravity and Tectonics. K. A. De Jong and R. Scholten (eds.). New York, Wiley and Sons, p. 491-502.
- Price, R.A. (1994). Cordilleran Tectonics and the Evolution of the Western Canada Sedimentary Basin. In: Geological Atlas of the Western Canada Sedimentary Basin (Chapter 2). Canadian Society of Petroleum Geologists.
- Prioul, R., Jocker, J. (2009). Fracture characterization at multiple scales using borehole images, sonic logs, and walk around vertical seismic profile. *AAPG Bull* 93(11):1503–1516. <https://doi.org/10.1306/08250909019>.
- Purba, J. C., Gilbert, H., & Dettmer, J. (2021). Structure and dynamics of the southern Rocky Mountain Trench near Valemount, British Columbia, inferred from local seismicity. *Seismological Research Letters*, 92(5), 3087–3099. <https://doi.org/10.1785/0220200350>
- Ramanathan, V., Boskovic, D., Zhmodik, A., Li, Q., Ansarizadeh, M., Perez Michi, O., & Garcia, G.(2015). A simulation approach to modelling and understanding fracture geometry with respect to well spacing in multi well pads in the Duvernay – a case study. Paper presented at the SPE/CSUR Unconventional Resources Conference, Calgary, Alberta, Canada, October 2015. doi: <https://doi.org/10.2118/175928-MS>
- Reinecker, J., Tingay, M., & Müller, B. (2003). Borehole breakout analysis from four-arm caliper logs. World Stress Map Project.

- Reiter, K., & Heidbach, O. (2014). 3-D geomechanical–numerical model of the contemporary crustal stress state in the Alberta Basin (Canada). *Solid Earth Discussions*, 6, 2423–2494. [10.5194/sed-6-2423-2014](https://doi.org/10.5194/sed-6-2423-2014).
- Reiter, K., Heidbach, O., Schmitt, D., Haug, K., Ziegler, M., & Moeck, I. (2014). A revised crustal stress orientation database for Canada. *Tectonophysics*, 636, 111–124. <https://doi.org/10.1016/j.tecto.2014.08.006>
- Riazi, N., & Eaton, D. W. (2020). Anatomy of a buried thrust belt activated during hydraulic fracturing. *Tectonophysics*, 795, 228640. <https://doi.org/10.1016/j.tecto.2020.228640>
- Rice, J. R. (1968). Mathematical analysis in the mechanics of fracture. Pp. 192–311 in *Fracture*, vol. 2, H. Liebowitz, ed. New York: Academic Press. National Academies of Sciences, Engineering, and Medicine. 1996. *Rock Fractures and Fluid Flow: Contemporary Understanding and Applications*. Washington, DC: The National Academies Press. <https://doi.org/10.17226/2309>.
- Ristau, J., Rogers, G.C., and Cassidy, J.F., 2007, Stress in western Canada from regional moment tensor analysis: *Canadian Journal of Earth Sciences*, v. 44, p. 127–148, doi:10.1139/e06-057.
- Roddick, J. A. (1967). Tintina Trench. *J. Geol.* 75:23–33.
- Rokosh, C.D., Lyster, S., Anderson, S.D.A., Beaton, A.P., Berhane, H., Brazzoni, T., Chen, D., Cheng, Y., Mack, T., Pana, C. & Pawlowicz, J.G. (2012): Summary of Alberta's shale- and siltstone-hosted hydrocarbon resource potential; Energy Resources Conservation Board, ERCB/AGS Open File Report 2012-06, 327 p., URL <http://www.ags.aer.ca/publications/OFR_2012_06.html> [June 2017].
- Root, K.G. (2001). Devonian Antler fold and thrust belt and foreland basin development in the southern Canadian Cordillera: Implications for the Western Canada Sedimentary Basin: *Bulletin of Canadian Petroleum Geology*, v. 49, p. 7–36, <https://doi.org/10.2113/49.1.7>.
- Ross, G. M., Eaton, D. W., Boerner, D. E., & Miles, W. (2000). Tectonic entrapment and its role in the evolution of continental lithosphere: An example from the Precambrian of western Canada. *Tectonics*, 19(1), 116–134. <https://doi.org/10.1029/1999TC900047>
- Sami, T. T., & James, N. P. (1993). Evolution of an early Proterozoic foreland basin carbonate platform lower Pethei Group Great Slave Lake northwest Canada *Sedimentology*, v. 40, p. 403–430.

- Savoy, L. E., & Mountjoy, E. W. (1995). Cratonic-margin and Antler-age foreland basin strata (Middle Devonian to Lower Carboniferous) of the southern Canadian Rocky Mountains and adjacent plains. SEPM (Society for Sedimentary Geology).
- Schaef, H. T., Davidson, C. L., Owen, A. T., Miller, Q. R. S., Loring, J. S., Thompson, C. J., Bacon, D. H., Glezakou, V. A., & McGrail, B. P. (2014). CO₂ utilization and storage in shale gas reservoirs: Experimental results and economic impacts. *Energy Procedia*, 63, 7844–7851. <https://doi.org/10.1016/j.egypro.2014.11.819>
- Schieber, J. (1998). Developing a sequence stratigraphic framework for the w Chattanooga Shale of the southeastern USA: relevance for the Bakken Shale. Williston Basin Symposium.
- Schmitt, D. R., Currie, C. A., & Zhang, L. (2012). Crustal stress determination from boreholes and rock cores: Fundamental principles. *Tectonophysics*, 580, 1–26.
<https://doi.org/10.1016/j.tecto.2012.08.029>
- Schultz, R., Wang, R., Gu, Y. J., Haug, K., & Atkinson, G. (2017). A seismological overview of the induced earthquakes in the Duvernay play near Fox Creek, Alberta. *Journal of Geophysical Research: Solid Earth*, 122(1), 492–505. <https://doi.org/10.1002/2016jb013570>
- Schultz, R., Skoumal, R. J., Brudzinski, M. R., Eaton, D., Baptie, B., & Ellsworth, W. (2020). Hydraulic Fracturing-Induced Seismicity. *Reviews of Geophysics*, 58(3), e2019RG000695.
<https://doi.org/10.1029/2019RG000695>
- Schultz, R., & Wang, R. (2020). Newly emerging cases of hydraulic fracturing induced seismicity in the Duvernay East Shale Basin. *Tectonophysics*, 779, 228393.
<https://doi.org/10.1016/j.tecto.2020.228393>
- Scotese, C.R. (2016). Some Thoughts on Global Climate Change: The Transition for Icehouse to Hothouse Conditions. PALEOMAP Project.
- Serra, O. (1989). Formation micro scanner image interpretation. Schlumberger Education Services, Houston.
- Serra, O., & Serra, L. (2004). Well logging: data acquisition and applications. France, N.P.
https://www.osti.gov/etdeweb/biblio/20559_043
- Shaw, D.J. (2020). Sequence stratigraphic analysis of the Duvernay Formation, Kaybob area, Alberta, Canada. MSc Thesis, Department of Earth and Atmospheric Sciences, University of Alberta, 342 p.

- Shaw, D. J., & Harris, N. B. (2022). Facies and systems tracts at high-resolution in an organic-rich mudstone: The Duvernay Formation, Kaybob area, Alberta, Canada. *Sedimentary Geology*, 436. <https://doi.org/10.1016/j.sedgeo.2022.106157>
- Shen, L. W., Schmitt, D. R., & Haug, K. (2019). Quantitative constraints to the complete state of stress from the combined borehole and focal mechanism inversions: Fox Creek, Alberta. *Tectonophysics*, 764, 110–123. <https://doi.org/10.1016/j.tecto.2019.04.023>
- Sibson, R. (2000). Fluid involvement in normal faulting *Journal of Geodynamics* 29 469 499 10 1016 /S 0264 3707 99 00042 3
- Siddique, A., Abid, S., Shafiq, F., Nawab, Y., Wang, H., Shi, B., Saleemi, S., & Sun, B. (2019). Mode I fracture toughness of fiber-reinforced polymer composites: A Review. *Journal of Industrial Textiles*, 50(8), 1165–1192. <https://doi.org/10.1177/1528083719858767>
- Simpson, R. W. (1997). Quantifying Anderson's fault types: *Journal of Geophysical Research*, 102, no. B8, 17909–17919, <https://doi.org/10.1029/97JB01274>.
- Smith, D. G. (1994) Chapter 17. Paleogeographic evolution of the Western Canada Sedimentary Basin. In: Geological Atlas of the Western Canada Sedimentary Basin, Mossop, G. & Shetsen, I. compilers. Canadian Society of Petroleum Geologists and Alberta Geological Survey, p. 277-296.
- Soltanzadeh, M., Davis, G., Fox, A., Hume, D., & Rahim, N. (2015). Application of mechanical and mineralogical rock properties to identify fracture fabrics in the Devonian Duvernay Formation in Alberta. Proceedings of the 3rd Unconventional Resources Technology Conference. <https://doi.org/10.15530/urtec-2015-2178289>
- Souza, J., Martínez, G., Leon, M., Azadpour, M., & Atashbari, V. (2021). Pore pressure and wellbore instability. 10.1016/B978-0-12-817236-0.00014-5.
- Spencer, C. W. (1987). Overpressured reservoirs in Rocky Mountain region: *AAPG Bulletin*, v. 67, p. 1356–1357.
- Spratt, D. A., Dixon, J. M., & Beattie, E. T. (2004). Changes in structural style controlled by lithofacies contrast across transverse carbonate bank margins —Canadian Rocky Mountains and scaled physical models, in K. R. McClay, ed., Thrust tectonics and hydrocarbon systems: *AAPG Memoir* 82, p. 259–275
- Stacey, J., Hollis, C., Corlett, H., & Koeshidayatullah, A. (2020). Burial dolomitization driven by modified seawater and basal aquifer-sourced brines: Insights from the middle and upper

- Devonian of the Western Canadian Sedimentary Basin. *Basin Research*, 33(1), 648–680.
<https://doi.org/10.1111/bre.12489>
- Stearns, D. W. (1968). Certain aspects of fracture in naturally deformed rocks. In: Rieker, R. E. (ed.) National Science Foundation Advanced Science Seminar in Rock Mechanics. Special Report, Air Force Cambridge Research Laboratories, Bedford, Mass., AD66993751, 97-118.
- Stoakes, F. A. (1980). Nature and control of shale basin fill and its effect on reef growth and termination: Upper Devonian Duvernay and Ireton Formations of Alberta, Canada. In *Bulletin of Canadian Petroleum Geology (Vol. 28, Issue 3)*.
http://pubs.geoscienceworld.org/cspg/bcpg/article-pdf/28/3/345/4951345/cspg_1980_0028_0003_0345.pdfences
- Stoakes, F. A., & Creaney, S. (1985). Sedimentology of a carbonate source rock: The Duvernay Formation of Alberta Canada. *Rocky Mountain Carbonate Reservoirs*, 343–375.
<https://doi.org/10.2110/cor.85.07.0343>
- Strapoć, D., Mastalerz, M., Schimmelmann, A., Drobniak, A., & Hasenmueller, N. R., (2010). Geochemical constraints on the origin and volume of gas in the New Albany Shale (Devonian–Mississippian), eastern Illinois Basin: *AAPG Bulletin*, v. 94, no. 11, p. 1713–1740, doi:10.1306/06301009197.
- Streit, J.E. & Hillis, R.R. (2004). Estimating fault stability and sustainable fluid pressures for underground storage of CO₂ in porous rock, *Energy* 29, 1445-1456
- Swarbrick, R.E., Osborne, M.J., & Yardley, G.S. (2002). Comparison of overpressure magnitude resulting from the main generating mechanisms. A.R. Huffman, G.L. Bowers (Eds.), *Pressure Regimes in Sedimentary Basins and Their Prediction*, AAPG, Tulsa (2002), pp. 1-12
- Switzer, S.B., Holland, W.G., Christie, D.S., Graf, G.C., Hedinger, A.S., McAuley, R.J., Wierzbicki, R.A., & Packard, J.J. (1994). The Woodbend-Winterburn strata of the Western Canada Sedimentary Basin. In: G.D. Mossop and I. Shetsen (comps), *Geological Atlas of the Western Canada Sedimentary Basin. Geological Survey of Canada*, (Chapter 12).
- Tingay, M., Hillis, R., Swarbrick, R., Morley, C., & Damit, A. (2008). Origin of overpressure and pore-pressure prediction in the Baram Delta province, Brunei: *AAPG Bulletin*, v. 93, p. 51–74.

- Tissot, B. P., & Welte, D. H. (1978). *Petroleum Formation and Occurrence: A New Approach to Oil and Gas Exploration*, xviii+538 pp., 243 figs, 70 tables. Berlin, Heidelberg, New York: Springer-Verlag. ISBN 3 540 08698 6.
- Tokhmchi, B., Memarian, H., Rezaee, M.R. (2010). Estimation of the fracture density in fractured zones using petrophysical logs. *J Petrol Sci Eng* 72(1–2):206–213
- Twiss, R.J. and Moores, E.M. (1992) *Structural Geology*. W.H. Freeman and Company, New York, 532.
- Tyiasning, S., & Cooke, D. (2016). Anisotropy signatures in the Cooper Basin of Australia: Stress versus fractures. Interpretation. 4. SE51-SE61. 10.1190/INT-2015-0131.1.
- Ukar, E., Laubach, S. E., & Hooker, J. N. (2019). Outcrops as guides to subsurface natural fractures: Example from the Nikanassin Formation tight-gas sandstone, Grande Cache, Alberta foothills, Canada. *Marine and Petroleum Geology*, 103, 255–275.
<https://doi.org/10.1016/j.marpetgeo.2019.01.039>
- Venieri, M., Pedersen, Per K., & Eaton, D.W. (2019). A New Well Log-Based Method To Quantify Compositional And Geomechanical Heterogeneity In Organic-Rich Mudstones: Implications For Reservoir Potential Prediction In The Devonian Duvernay Formation, Alberta, Canada. Willian C. Gussow geoscience conference, Banff, Canada.
- Venieri, M., Harazim, D., Pedersen, P.K., Eaton, D.W., (2021a). Vertical and lateral facies variability in organic-rich mudstones at the reservoir scale: A case study from the Devonian Duvernay formation of Alberta, Canada. *Marine and Petroleum Geology*, 132, 105-232.
<https://doi.org/10.1016/j.marpetgeo.2021.105232>.
- Voight, B., & St Pierre, B. H. P. (1974). Stress history and rock stress. In *Advances in rock mechanics*. Proceedings of the Third Congress of the International Society for Rock Mechanics (Vol. 2, pp. 580-582)
- Voorn, M., Exner, U., Barnhoorn, A., Baud, P., & Reuschlé, T. (2015). Porosity, permeability and 3D fracture network characterization of dolomite reservoir rock samples. *J Petrol Sci Eng* 127:270–285. <https://doi.org/10.1016/j.petrol.2014.12.019>
- Vrolijk, P. J. (1994). Dating clay-rich thrust faults. In *Abstracts with Programs*, Geol. Soc. Amer., 1994 Annual Meeting (Vol. 466).
- Waldron, J. W. F., A. J. Locock, and A. Pujadas-Botey (2016). Building an Outdoor Classroom for Field Geology: The Geoscience Garden. *Journal of Geoscience Education* 64, 215-230.

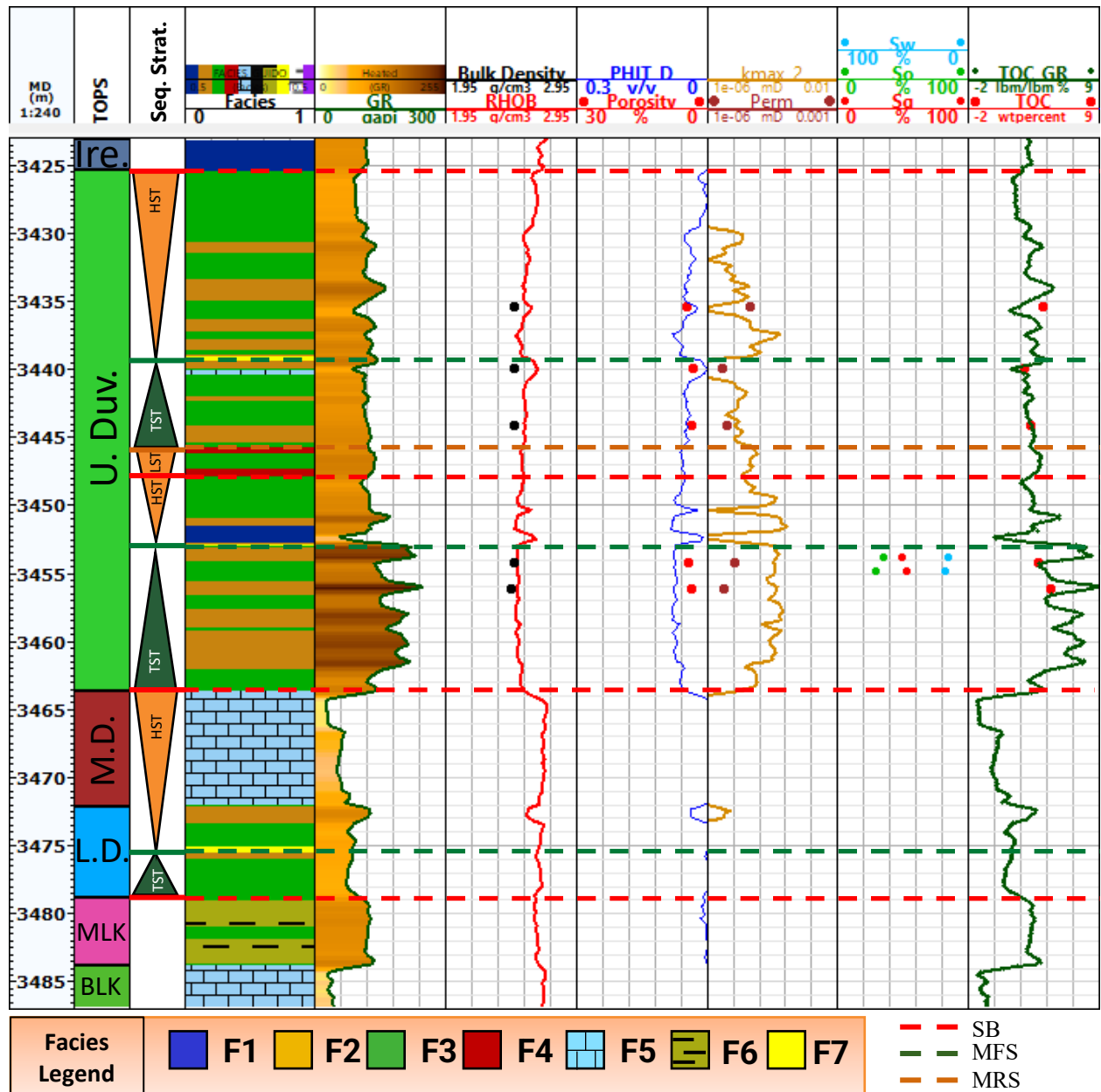
- Wang, X. (2005). Stereological Interpretation of Rock Fracture Traces on Borehole Walls and Other Cylindrical Surfaces. PhD dissertation, Virginia Polytechnic Institute and State University, Blacksburg, Virginia (September 2005).
- Wang, R., Gu, Y. J., Schultz, R., Zhang, M., & Kim, A. (2017). Source characteristics and geological implications of the January 2016 induced earthquake swarm near Crooked Lake, Alberta. *Geophysical Journal International*, 210(2), 979–988.
<https://doi.org/10.1093/gji/ggx204>
- Wang, P., Chen, Z., Jin, Z., Jiang, C., Sun, M., Guo, Y., Chen, X., & Jia, Z. (2018). Shale Oil and gas resources in organic pores of the Devonian Duvernay shale, western Canada Sedimentary Basin based on Petroleum System Modeling. *Journal of Natural Gas Science and Engineering*, 50, 33–42. <https://doi.org/10.1016/j.jngse.2017.10.027>
- Wang, J., Li, T., Gu, Y. J., Schultz, R., Yusifbayov, J., & Zhang, M. (2020). Sequential fault reactivation and secondary triggering in the March 2019 red deer induced earthquake swarm. *Geophysical Research Letters*, 47(22). <https://doi.org/10.1029/2020gl090219>
- Waters, G. A., Lewis, R. E., & Bentley, D. C. (2011). The effect of mechanical properties anisotropy in the generation of hydraulic fractures in organic shales. SPE Annual Technical Conference and Exhibition.
- Welch, M. J., Luthje, M., & Glad, A. C. (2019). Influence of fracture nucleation and propagation rates on fracture geometry: Insights from Geomechanical modelling. *Petroleum Geoscience*, 25(4), 470–489. <https://doi.org/10.1144/petgeo2018-161>
- Wendte, J.C. & Stoakes, F.A. (1982). Evolution and corresponding porosity distribution of the Judy Creek reef complex, Upper Devonian, central Alberta: In: Canada's Giant Hydrocarbon Reservoirs. W.G. Cutler, (ed.). Canadian Society of Petroleum Geologists Core Conference Manual, p. 63-81.
- Weng, X., Kresse, O., Cohen, C., Wu, R., & Gu, H. (2011). Modeling of Hydraulic Fracture Network propagation in a naturally fractured formation. *All Days*.
<https://doi.org/10.2118/140253-ms>
- Weng, Xiaowei. (2015). Modeling of complex hydraulic fractures in naturally fractured formation. *Journal of Unconventional Oil and Gas Resources*, 9, 114–135.
<https://doi.org/10.1016/j.juogr.2014.07.001>

- Wikel, K. (2011). Geomechanics: Bridging the gap from geophysics to engineering in unconventional reservoirs: *First Break*, 29, 71–80.
- Withjack, M.O., Olson, J. & Peterson, E. (1990). Experimental models of extensional forced folds. *American Association of Petroleum Geologists Bulletin*, v. 74, p. 1038-1054.
- Wong, P. K., Weissenberger, J. A. W., Gilhooly, M. G., Playton, T. E., & Kerans, C. (2016). Revised regional Frasnian sequence stratigraphic framework, Alberta outcrop and subsurface. *New Advances in Devonian Carbonates: Outcrop Analogs, Reservoirs, and Chronostratigraphy*, 49(1), 37-85.
- Woodland, D.C. & Bell, J.S. (1989). In situ stress magnitudes from mini-frac records in Western Canada, *J. Can. Pet. Technol.*, 28.
- Workum, R.H. & Hedinger, A.S. (1992). Devonian Frasnian stratigraphy, Rocky Mountain Front Ranges, Crowsnest Pass to Jasper, Alberta. *Geological Survey of Canada*, Open File 2509, 182 p.
- Weissenberger, J.A.W. (1994). Frasnian reef and basinal strata of West Central Alberta: a combined sedimentological and biostratigraphic analysis: *Bulletin of Canadian Petroleum Geology*, v. 42, p. 1-25.
- Wright, G. N., McMechan, M. E., Potter, D. E. G., Mossop, G. D., & Shetsen, I. (1994). Structure and architecture of the Western Canada sedimentary basin. *Geological atlas of the Western Canada sedimentary basin*, 4, 25-40.
- Wüst, R. A., Ziarani, A. S., & Cui, A. X. (2020). Interbedded carbonate and calcareous shales of the Devonian Duvernay Formation of Alberta, Canada: Implications for completion due to high variability of geomechanical properties. *Day 3 Wed, September 30, 2020*.
<https://doi.org/10.2118/200011-ms>
- Xiao, W., & Unsworth, M. (2006). Structural Imaging in the Rocky Mountain Foothills (Alberta) using Magnetotelluric Exploration. *AAPG Bulletin*, 90(3), 321–333.
<https://doi.org/10.1306/10150504140>
- Yang, S., Harris, N., Dong, T., Wu, W., & Chen, Z. (2015). Mechanical properties and natural fractures in a Horn River Shale core from well logs and hardness measurements. *All Days*.
<https://doi.org/10.2118/174287-ms>

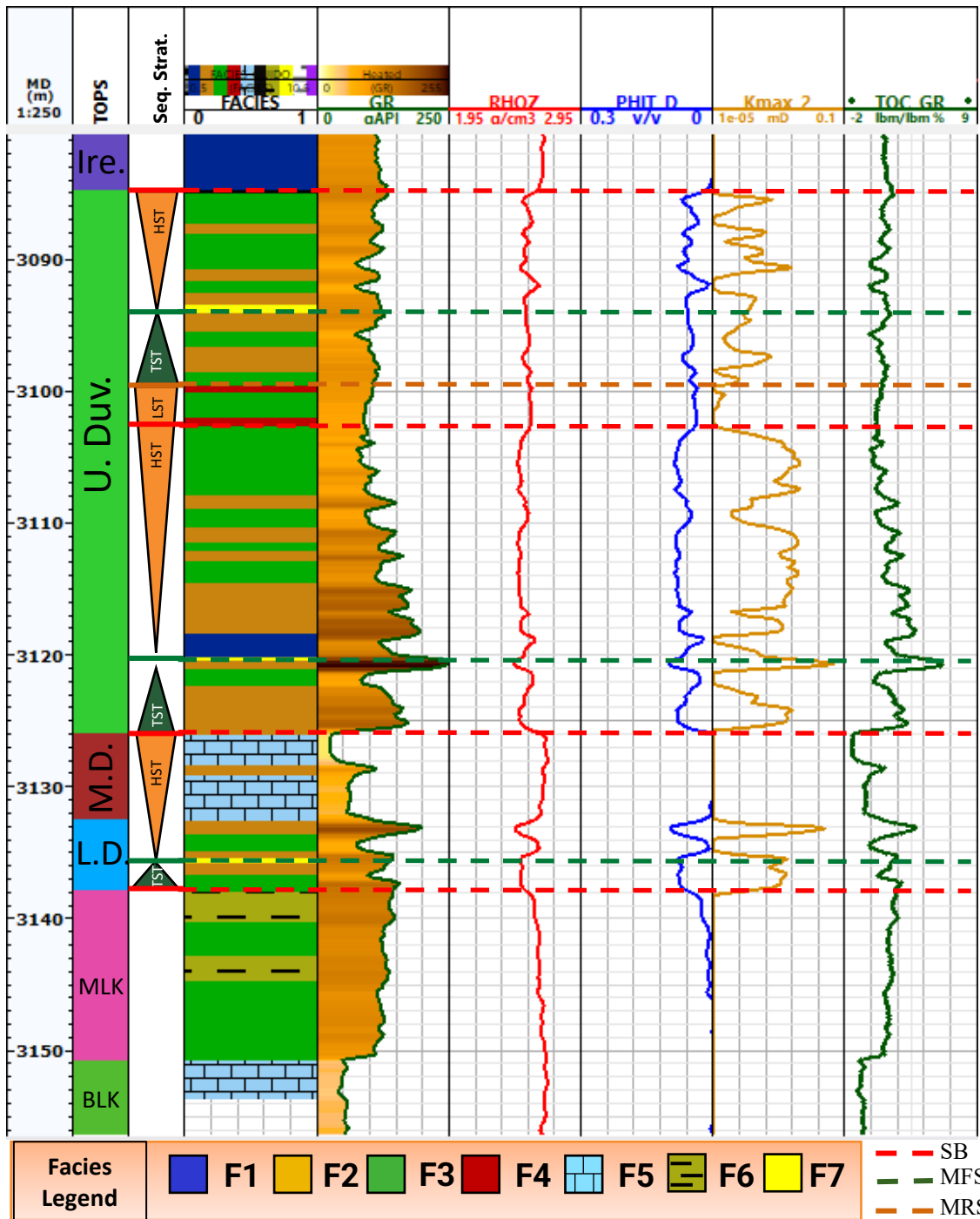
- Yassir, N. & Addis, M.A. (2002). Relationships between pore pressure and stress in different tectonic settings. A.R. Huffman, G.L. Bowers (Eds.), *Pressure Regimes in Sedimentary Basins and Their Prediction*. AAPG, Tulsa (2002), 79-88.
- Yeates, D. W., Hockaday, W. C., Atchley, S. C., Rau, E. G., & Thorson, A. M. (2022). Maturity trends for the late devonian duvernay formation and identification of the Willesden-Green Maturity High. *Marine and Petroleum Geology*, *145*, 105894.
<https://doi.org/10.1016/j.marpetgeo.2022.105894>
- Yenugu, M. (2010). "Ultrasonic measurements of Anisotropy of Shales." School of Geology and Geophysics, University of Oklahoma, USA.
- Younes, A. I., Moore, H., Suumeyer, N., Smith, P., Driskill, B., Bartsch, E. & Garbowicz, A. (2011), Sweet spotting the Haynesville-Bossier Shale Gas Play, Northwestern Louisiana, an integrated study: AAPG Search and Discovery article 90122:
http://www.searchanddiscovery.com/pdfz/abstracts/pdf/2011/hedberg-texas/abstracts/ndx_younes.pdf.html (accessed February 1, 2017).
- Yuan, W., Chen, Z., Kong, B., & Zhao, G. (2023). Hybrid geothermal energy and hydrocarbon resources production by repurposing horizontal wells in shale gas reservoirs in Horn River Basin, British Columbia, Canada. *Geoenergy Science and Engineering*, *227*, 211913.
<https://doi.org/10.1016/j.geoen.2023.211913>
- Zahmatkesh I., Aghli G., & Mohamadian R. (1994). Systematic fractures analysis using image logs and complementary methods in the Marun Oilfield SW Iran. *J Geopersia* 5(2):139–150
- Zhang, L., Currie, C., & Schmitt, D. (2010). Drilling Induced Core Fractures and Crustal Stress, GeoCanada 2010.
- Zhang, X. (2015). Devonian Shale Petrophysical Study and Modelling (Master's thesis, University of Calgary, Calgary, Canada). Retrieved from <https://prism.ucalgary.ca>
doi:10.11575/PRISM/25696
- Zhou, X., Wang, R., Du, Z., Wu, J., Wu, Z., Ding, W., Li, A., Xiao, Z., Cui, Z., & Wang, X. (2022). Characteristics and main controlling factors of fractures within highly-evolved Marine Shale Reservoir in strong deformation zone. *Frontiers in Earth Science*, *10*.
<https://doi.org/10.3389/feart.2022.832104>

- Ziegler, P.A. (1967). International Symposium on the Devonian System, Guidebook for Canadian Cordilleran Field Trip. Alberta Society of Petroleum Geologists, Map: Upper Devonian 345-359 m.y., p. 13.
- Zoback, M.D., Moos, D., Mastin, L.G., & Anderson, R.N., (1985). Well-bore breakouts and in situ stress: *Journal of Geophysical Research*, v. 90, p. 5523-5530.
- Zoback, M. D., Barton, C. A., Brudy, M., Castillo, D. A., Finkbeiner, T., Grollimund, B. R., Moos, D. B., Peska, P., Ward, C. D., & Wiprut, D. J. (2003). Determination of stress orientation and magnitude in deep wells. *International Journal of Rock Mechanics and Mining Sciences*, 40(7–8), 1049–1076. <https://doi.org/10.1016/j.ijrmms.2003.07.001>
- Zoback, M.D. (2010). Reservoir Geomechanics, Cambridge Univ. Press.

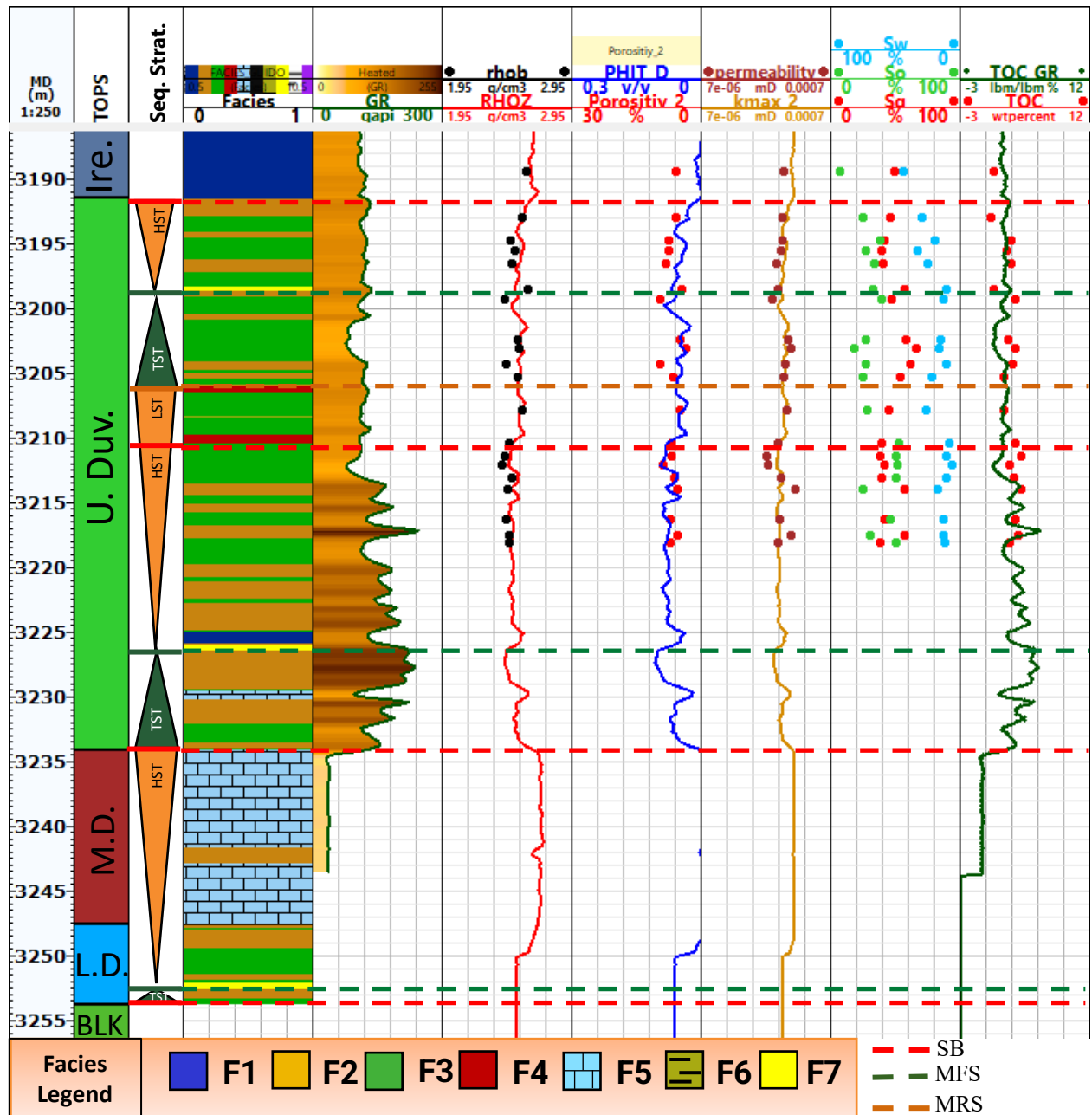
Appendix A: Additional petrophysical logs



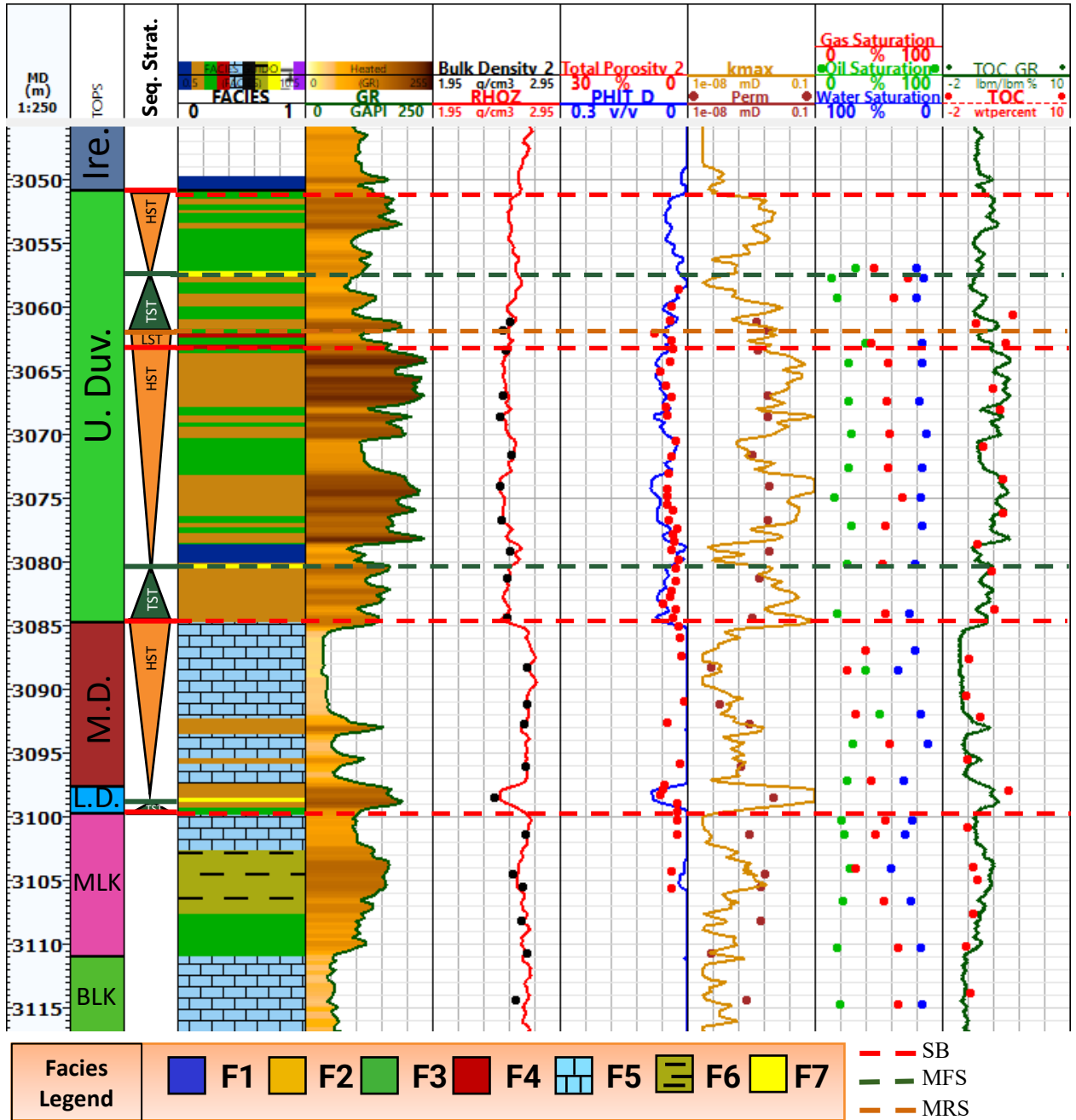
Sequence stratigraphy boundaries, lithofacies, gamma ray (GR), bulk density (RHOB) logs, estimated profiles of petrophysical parameters (solid lines) and XDR core testing data (dots) in well 1 (see Tables 3.1, 4.1, Fig. 4.6). PHIT, total porosity; kmax, horizontal permeability; TOC, total organic carbon; Sg, So and Sw, fluid saturation. Formation tops: Ire., Ireton; U. Duv., Upper Duvernay; M.D., Middle Duvernay; L. Duv., Lower Duvernay; MLK., Majeau Lake; BLK., Beaverhill Lake. SB, sequence boundary, MFS; maximum flooding surface; MRS, maximum regressive surface.



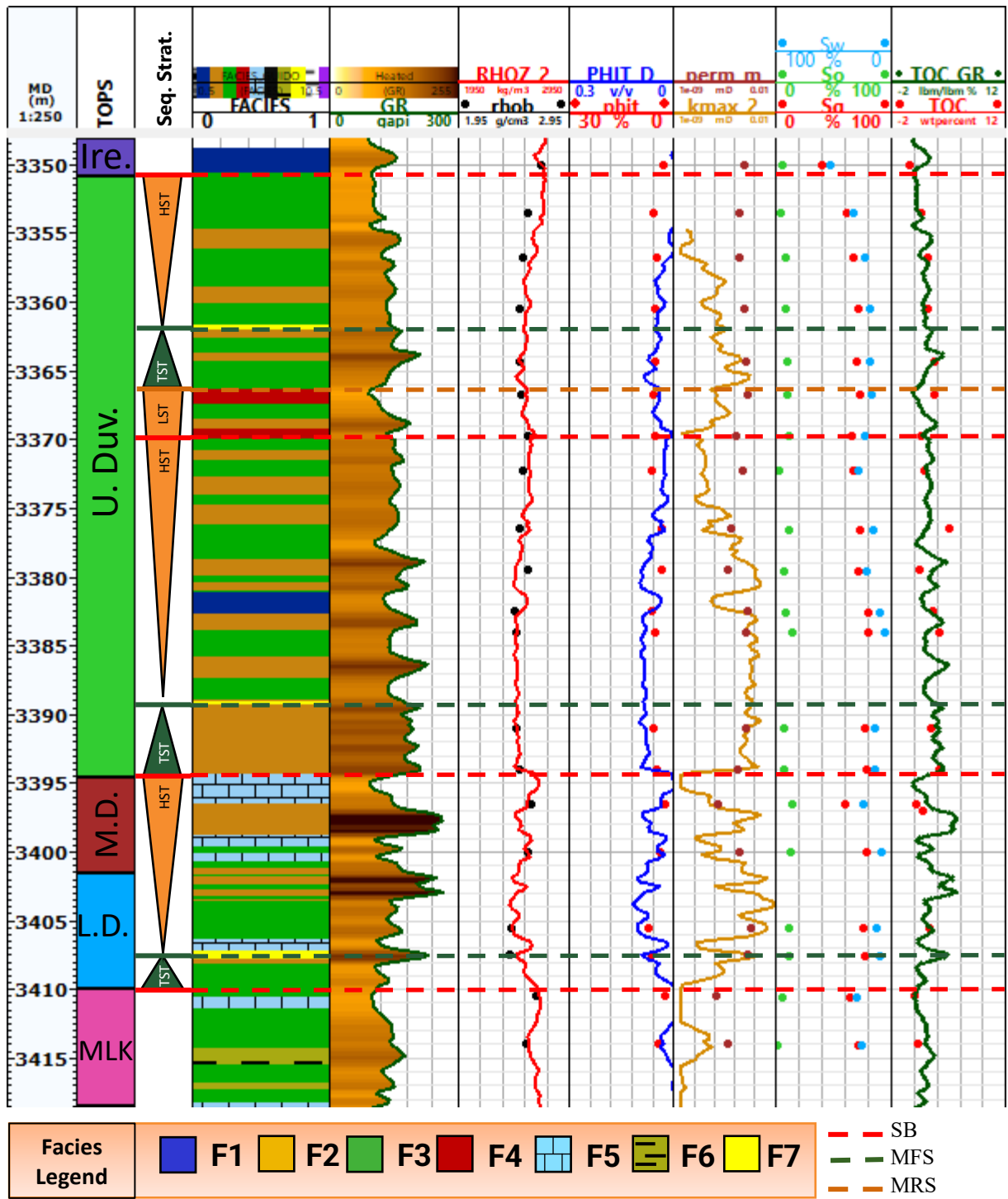
Sequence stratigraphy boundaries, lithofacies, gamma ray (GR), bulk density (RHOZ) logs and estimated profiles of petrophysical parameters (solid lines) in well 2 (see Tables 3.1, 4.1, Fig. 4.6). PHIT, total porosity; kmax, horizontal permeability; TOC, total organic carbon. Formation tops: Ire., Ireton; U. Duv., Upper Duvernay; M.D., Middle Duvernay; L. Duv., Lower Duvernay; MLK., Majeau Lake; BLK., Beaverhill Lake. SB, sequence boundary, MFS; maximum flooding surface; MRS, maximum regressive surface.



Sequence stratigraphy boundaries, lithofacies, gamma ray (GR), bulk density (RHOZ) logs, estimated profiles of petrophysical parameters (solid lines) and XDR core testing data (dots) in well 4 (see Tables 3.1, 4.1, Fig. 4.6). PHIT, total porosity; kmax, horizontal permeability; TOC, total organic carbon; Sg, So and Sw, fluid saturation. Formation tops: Ire., Ireton; U. Duv., Upper Duvernay; M.D., Middle Duvernay; L. Duv., Lower Duvernay; BLK., Beaverhill Lake. SB, sequence boundary, MFS; maximum flooding surface; MRS, maximum regressive surface.

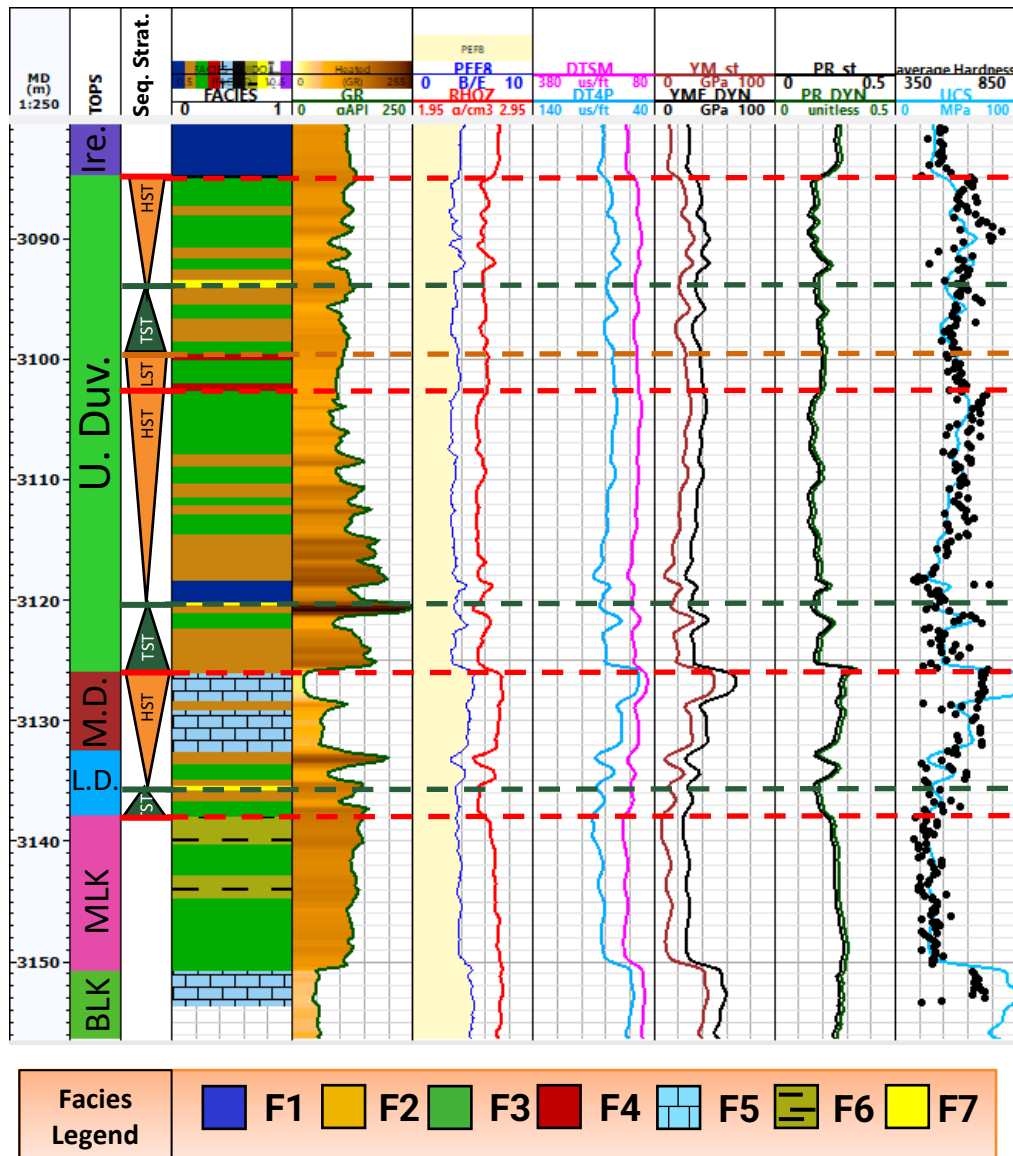


Sequence stratigraphy boundaries, lithofacies, gamma ray (GR), bulk density (RHOZ) logs, estimated profiles of petrophysical parameters (solid lines) and XDR core testing data (dots) in well 5 (see Tables 3.1, 4.1, Fig. 4.6). PHIT, total porosity; kmax, horizontal permeability; TOC, total organic carbon. Formation tops: Ire., Ireton; U. Duv., Upper Duvernay; M.D., Middle Duvernay; L. Duv., Lower Duvernay; MLK., Majeau Lake; BLK., Beaverhill Lake. SB, sequence boundary, MFS; maximum flooding surface; MRS, maximum regressive surface.



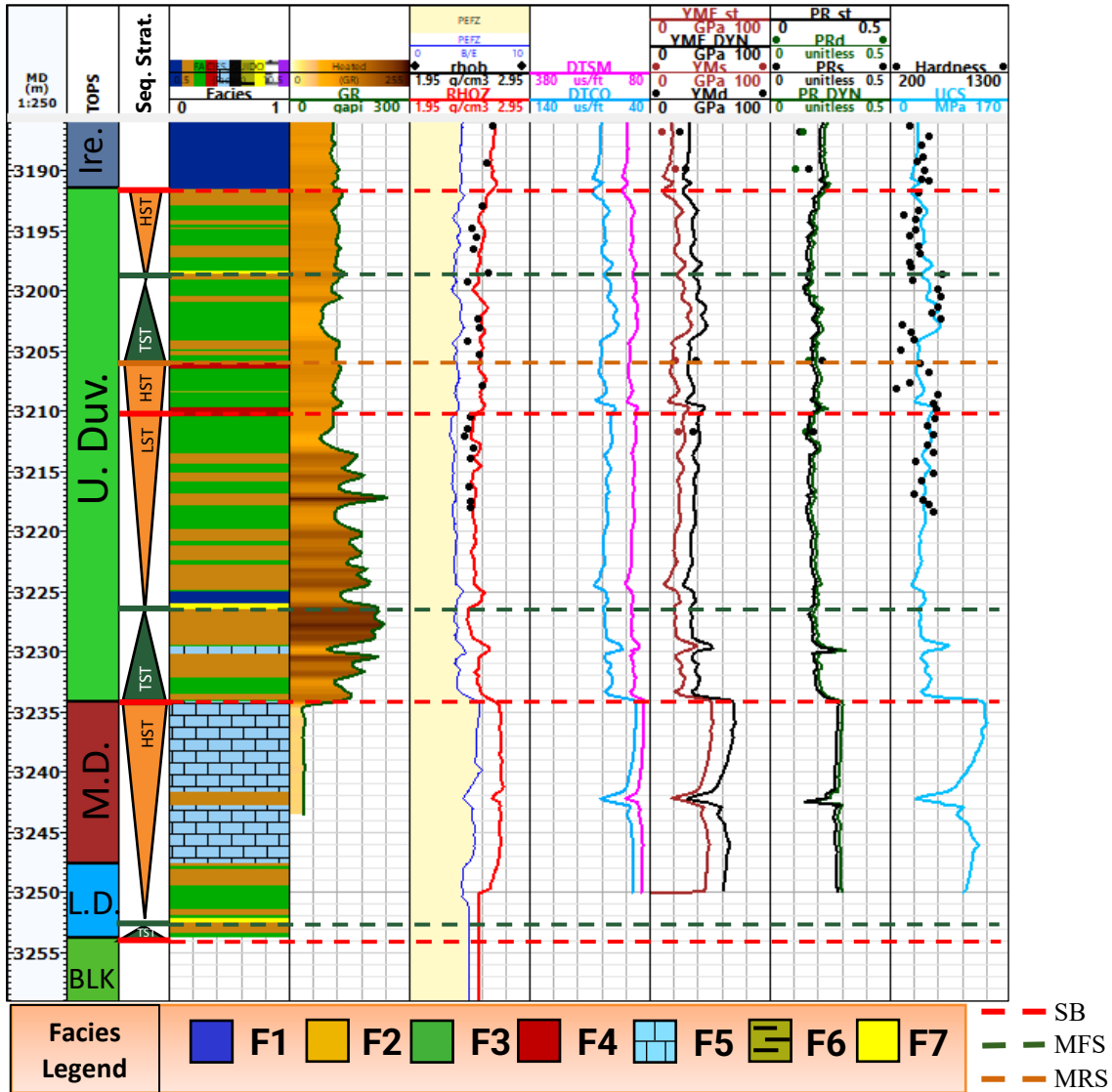
Sequence stratigraphy boundaries, lithofacies, gamma ray (GR), bulk density (RHOZ) logs, estimated profiles of petrophysical parameters (solid lines) and XDR core testing data (dots) in well 6 (see Tables 3.1, 4.1, Fig. 4.6). PHIT, total porosity; kmax, horizontal permeability; TOC, total organic carbon; Sg, So and Sw, fluid saturation. Formation tops: Ire., Ireton; U. Duv., Upper Duvernay; M.D., Middle Duvernay; L. Duv., Lower Duvernay; MLK., Majeau Lake. SB, sequence boundary, MFS; maximum flooding surface; MRS, maximum regressive surface.

Appendix B: Elastic and strength parameters for additional wells

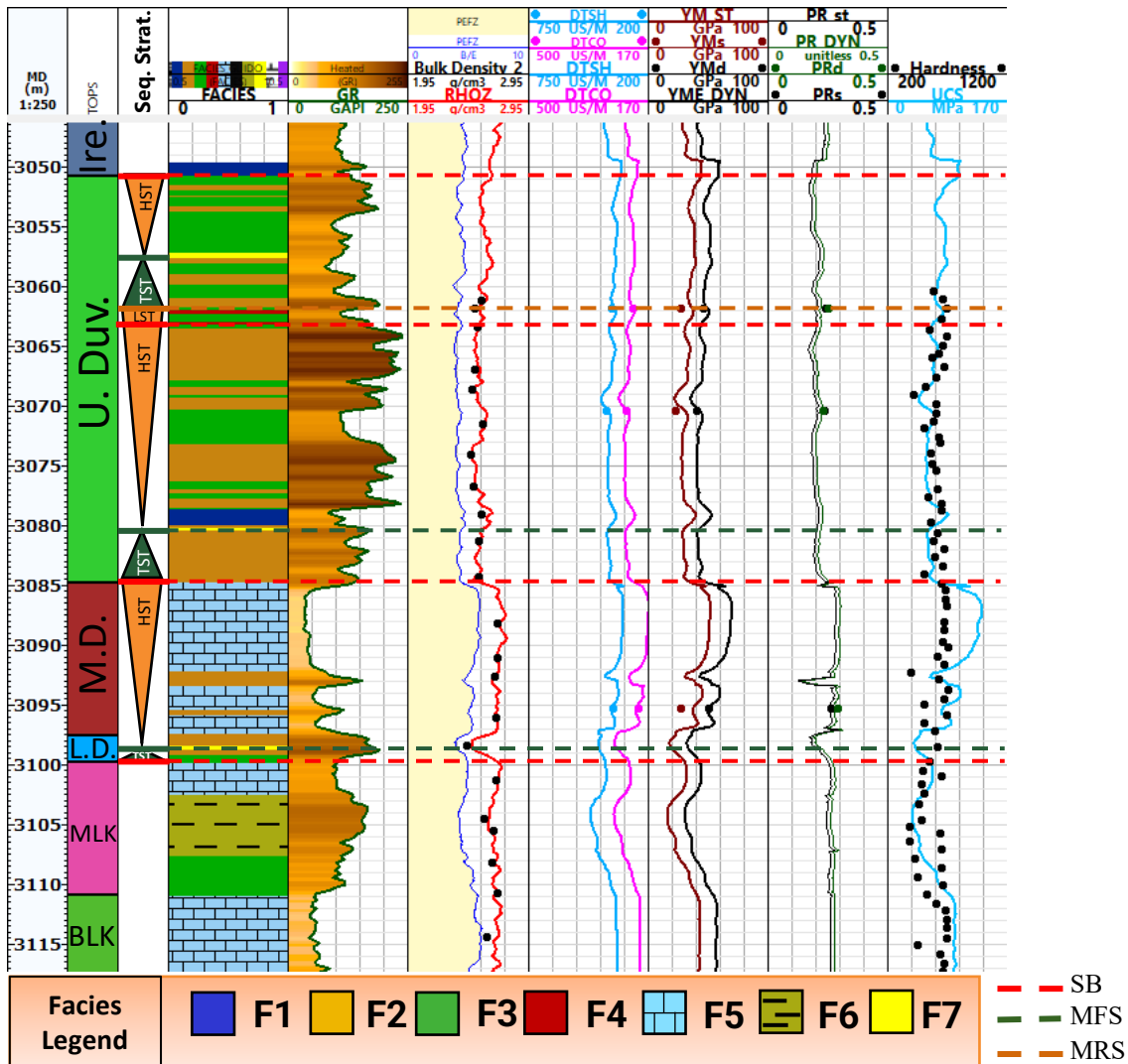


Well 2. Lithofacies, sequence stratigraphy boundaries, well logs of Gamma Ray, Photoelectric Factor (PEF8), Bulk Density (RHOZ), Shear (DTSM) and Compressional (DT4P) Slowness, and estimated profiles of Young's Modulus (YM), Poisson's Ratio (PR), Unconfined Compressive Strength (UCS) and Hardness measurements in the mudrocks of the Duvernay Formation.

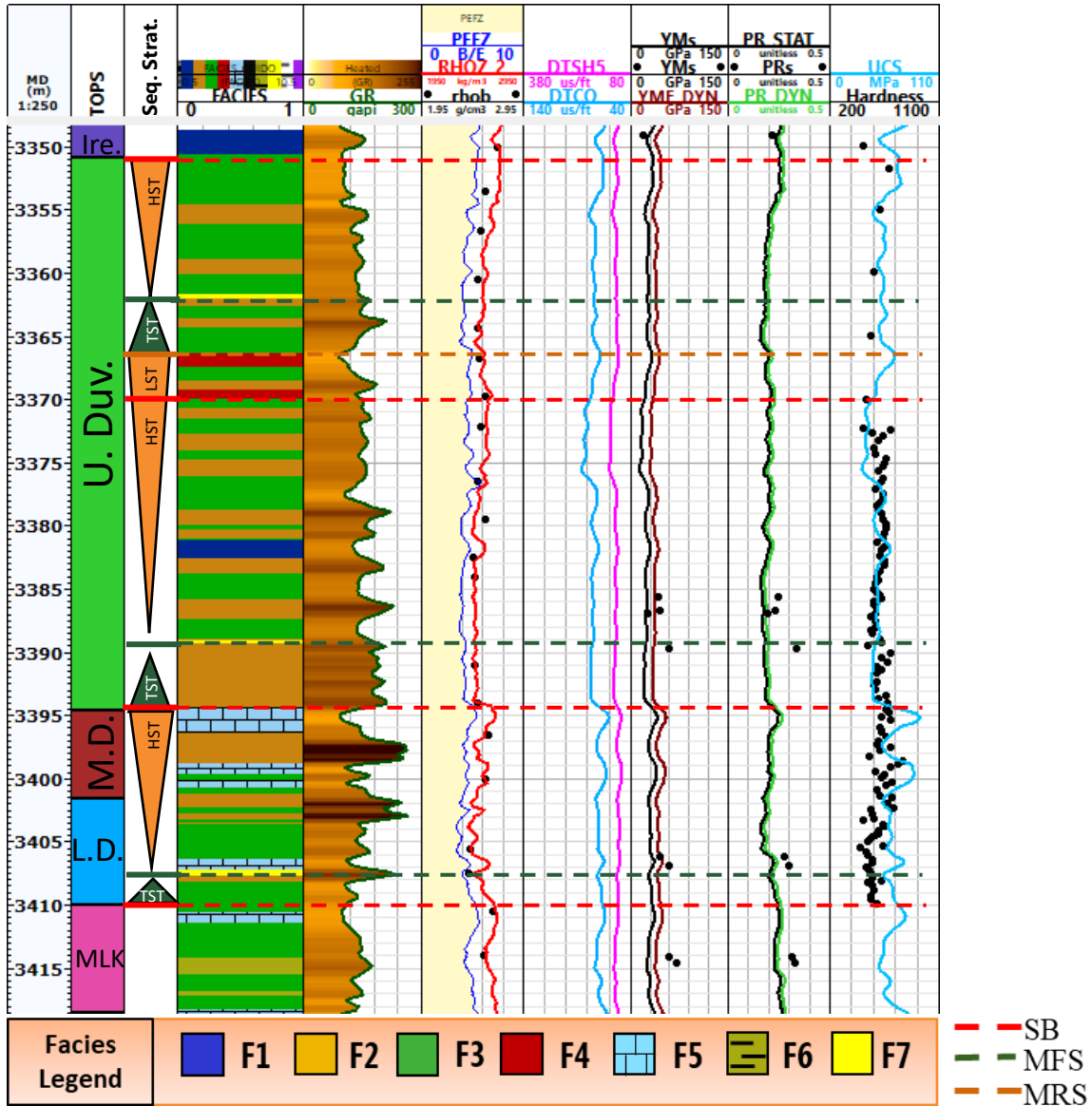
Labels: DYN, dynamic; s, static. Formation tops: Ire., Ireton; U. Duv., Upper Duvernay; M.D., Middle Duvernay; L. Duv., Lower Duvernay; MLK., Majeau Lake; BLK., Beaverhill Lake. SB, sequence boundary, MFS; maximum flooding surface; MRS, maximum regressive surface. See Fig. 4.6 and Table 3.1 for the name and location of the wells.



Well 4. Lithofacies, sequence stratigraphy boundaries, well logs of Gamma Ray, Photoelectric Factor (PEFZ), Bulk Density (RHOZ), Shear (DTSM) and Compressional (DTSCO) Slowness, and estimated profiles of Young's Modulus (YME), Poisson's Ratio (PR), Unconfined Compressive Strength (UCS) and Hardness measurements in the mudrocks of the Duvernay Formation. Labels: d, dynamic; s, static. Formation tops: Ire., Ireton; U. Duv., Upper Duvernay; M.D., Middle Duvernay; L. Duv., Lower Duvernay; BLK; Beaverhill Lake. SB, sequence boundary, MFS; maximum flooding surface; MRS, maximum regressive surface. See Fig. 4.6 and Table 3.1 for the name and location of the wells.



Well 5. Lithofacies, sequence stratigraphy boundaries, well logs of Gamma Ray, Photoelectric Factor (PEFZ), Bulk Density (RHOZ), Shear (DTSH) and Compressional (DTCO) Slowness, and estimated profiles of Young's Modulus (YM), Poisson's Ratio (PR), Unconfined Compressive Strength (UCS) and Hardness measurements in the mudrocks of the Duvernay Formation. Labels: d, DYN, dynamic; s, ST, static. Formation tops: Ire., Ireton; U. Duv., Upper Duvernay; M.D., Middle Duvernay; L. Duv., Lower Duvernay; MLK., Majeau Lake; BLK., Beaverhill Lake. SB, sequence boundary, MFS; maximum flooding surface; MRS, maximum regressive surface. See Fig. 4.6 and Table 3.1 for the name and location of the wells.



Well 6. Lithofacies, sequence stratigraphy boundaries, well logs of Gamma Ray, Photoelectric Factor (PEFZ), Bulk Density (RHOZ), Shear (DTSH5) and Compressional (DTSCO) Slowness, and estimated profiles of Young's Modulus (YM), Poisson's Ratio (PR), Unconfined Compressive Strength (UCS) and Hardness measurements in the mudrocks of the Duvernay Formation. Labels: DYN, dynamic; s, STAT, static. Formation tops: Ire., Ireton; U. Duv., Upper Duvernay; M.D., Middle Duvernay; L. Duv., Lower Duvernay; MLK., Majeau Lake. SB, sequence boundary, MFS; maximum flooding surface; MRS, maximum regressive surface. See Fig. 4.6 and Table 3.1 for the name and location of the wells